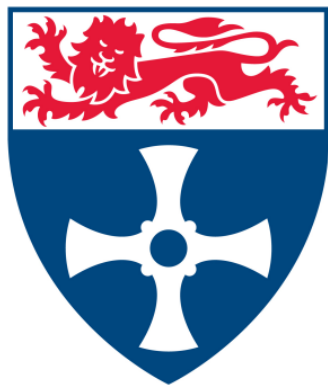


The p-type Project- Development of Alternative Sensitisers and p-type Materials for Integration into Tandem Devices.

Heather Victoria Flint

A thesis submitted for the degree of
Doctor of Philosophy in Chemistry



School of Natural and Environmental Sciences
Newcastle University
March 2022

Abstract

Photovoltaics are a key player in the push to provide the world with energy from sustainable sources. Tandem dye-sensitised solar cells are one approach to the integration of PV generation into daily life, but efficiency of these devices is limited by the properties of the photocathode. By replacing the thin-film NiO semiconductor with a material with better transparency, charge transport capabilities, or lower valence band potential, some of the problems with this technology can be addressed.

The aim of this work is to define an appropriate sensitising material for high-throughput materials screening during the development of alternative p-type semiconductors for tandem DSSCs. The work in this thesis encompasses a range of sensitisers for light harvesting within dye and quantum dot sensitised solar cells.

The introductory Chapters, 1 and 2, highlight the importance of photovoltaics in the context of the world's energy demand and provide background and insight into the state of the field. They also illustrate some of the most important techniques used throughout the course of these projects, and the experimental details for the fabrication of DSSCs.

In Chapter 3, two classes of sensitisers are integrated into n-type DSSCs and optimised. Firstly, an iridium (III) complex with panchromatic absorption response up to 700 nm is investigated as an alternative to ruthenium-based dyes. After optimisation using blocking and scattering layers on the TiO₂, an efficiency of 0.49 % was achieved for these devices. However, the application and poor sustainability of iridium-based dyes was a drawback for these devices, and a second approach was taken. The sensitisers derived from natural products, namely the seeds of the Peruvian-native prickly pear (*Opuntia Soehrensii*), were applied to the previously optimised TiO₂ thin films and tested in devices. Promising efficiencies were then improved via the addition of citric acid to stabilise the photosensitive dye, and an efficiency of 1.41 % was achieved with current output remaining stable after 7 days. Upon testing in low-light conditions, the devices also produced a PCE of 4 %.

Within Chapter 4, dyes for p-type DSSCs were investigated. Collaborators produced a series of dyes based on triarylamine cores, indolium acceptors and pyridine anchors. Each of these dyes were integrated into p-DSSCs, and the architecture combining two indolium acceptor groups with a phenyl pyridine anchor resulted in devices with the best

performance of the series ($\eta = 0.097\%$). While the performance was attributed to the absorption profile of the dye extending to almost 700 nm, the poor dye loading limited the absorption capability of the devices, and therefore the performance. Another study was undertaken using a further red-shifted BODIPY dye (RJ3) synthesised by colleagues. This dye was optimised for absorption onto NiO using two carboxylic acid anchoring groups and was highly emissive. Champion p-DSSCs containing this dye reached efficiencies over 0.1 %, allowing preliminary tandem devices to be constructed using a D35-sensitized TiO₂ photoanode. While poor current matching limited the output of the tandem cells, RJ3 was shown to be a promising dye for application in p-type devices.

The final results Chapter covers the development of quantum dot sensitiser for the screening of alternative p-type materials. Initial tests with PbS quantum dots synthesised ex-situ in a hot injection process gave poor results, due to low loading, so a new approach was taken in which CdS nanofilms were deposited directly onto films via SILAR. This process was then automated using robots constructed with low-cost and widely available LEGO pieces, allowing for in-laboratory upscale of film production. The CdS-sensitized NiO films were incorporated into devices containing a polysulphide gel-based electrolyte and a new counter electrode material, nickel foam. CdS films were also co-sensitised with the RJ3 dye investigated in Chapter 4 in order to extend the spectral response of the photocathode, which improved the device efficiency to over 1 %. Work with collaborators from IITH is also discussed in this chapter, in which new materials were introduced via SILAR onto NiO films, which were subsequently integrated into tandem devices.

Chapter 6 summarises the key findings in this thesis and discusses the scope for continuation of the work.

Acknowledgements

They say it takes a village to raise a child, and I think to make a scientist, it also takes a community of others to challenge, inspire or uplift them. I am grateful to everyone who has helped shape me during this work for the lessons and influence that I will take into the rest of my life.

Firstly, to Dr Elizabeth Gibson, who has taught me the importance of integrity and resilience, and who has inspired me to be the best scientist I can be. Thank you for the opportunities you have enabled me to take and for giving me the confidence to speak out for myself. For those around the world who have welcomed me into their countries, labs and homes, thank-you for the hospitality, experiences, and opportunities. To Prof. Maria Quintana of the Universidad Nacional de Ingeniería and her group, particularly Harry Tito and Tony Huamán, thank you. I am also grateful to Prof. Melepurath Deepa for insight and her welcome to IIT Hyderabad, and especially Ankita Kolay, who started out as an inspirational colleague, and ended up as a true friend. Closer to home, thanks go to Pietro Maiello at Northumbria University for showing me the ropes with the SEM. Thanks also go to the other members of staff at Newcastle University, in particular Dr Fabio Cucinotta, Dr Daniel Cole and Dr Eimer Tuite for their insight and support. Thanks to Justina Heslop for the great company and for letting me get stuck in. Thanks as well to the support staff, estates, cleaners, and administrators, all of whom made day to day life so much friendlier.

None of this would have been possible without the other members of the Gibson group, past and present. Their support, company, and uplifting spirit has been the most valuable aspect of the past four years and I will cherish the times I have had with them. I want to thank; Nils for making me believe I could do it, Nathan for the quantum dots and coffee, Abby, Jayne and Amy for keeping me sane and smiling, Dr John Mallows for the airmiles, Dr Josh Karlsson for teaching me patience, and Richard for absolutely everything else.

To Rob and Anaélle, who have helped me more than they know; je suis tellement reconnaissant. Thanks to my first coach, Richard Gill, for lifting my confidence and helping me aim truly. And thankyou to Dr Robert Craig, who has inspired me from the start and is a true mentor and friend.

And lastly, to my family. There are no words that can embody the gratitude, pride, and love I have for you all. You've lifted me up to the stars.

Table of Contents

Abstract	i
Acknowledgements	iii
Table of Contents	v
Publications	ix
List of Abbreviations	x
Chapter 1 Introduction	1
1.1 The need for Renewable Energy.....	1
1.2 Photovoltaics.....	3
1.2.1 Foundations and Semiconductors.....	3
1.2.2 1 st Generation PV.....	4
1.2.3 2 nd Generation PV.....	6
1.2.4 The solar spectrum and the Shockley Queisser limit.....	6
1.2.5 3 rd Generation PV.....	8
1.3 Dye Sensitized Solar Cells.....	8
1.3.1 Grätzel Cells.....	9
1.3.2 p-type DSSC.....	12
1.3.3 Tandem DSSC.....	13
1.4 Thesis Aims.....	17
1.5 References.....	18
Chapter 2 Theory and Experimental Techniques for the Study of DSSC	21
2.1 Device Properties.....	21
2.1.1 Current and Voltage.....	21
2.1.2 Power Output and Efficiency.....	22
2.1.3 IPCE.....	23
2.1.4 Dark Current.....	24
2.1.5 Charge Lifetime and Transport.....	25
2.2 Optical and Electrochemical Characterisation.....	28
2.2.1 Absorbance and Fluorescence.....	28
2.2.2 Cyclic Voltammetry.....	30
2.3 Computational Analysis.....	32
2.4 Morphological Characterisations.....	33
2.4.1 SEM and EDX.....	33

2.4.2 p-XRD	34
2.5 General Procedures	36
2.5.1 Preparation of glass substrates.....	36
2.5.2 Pt Counter electrode preparation.....	36
2.5.3 TiO ₂ film preparation	36
2.5.4 NiO film preparation	37
2.5.5 Liquid-junction device assembly.....	38
2.6 References.....	39
Chapter 3 Alternative Sensitisers for DSSC	41
3.1 A Panchromatic Iridium complex for near-IR absorbance in n-DSSC	42
3.1.1 Background	42
3.1.2 Results.....	50
3.1.3 Conclusions	60
3.2 A sensitizer derived from nature	61
3.2.1 Background	61
3.2.2 Results.....	68
3.2.3 Conclusions	79
3.3 Experimental.....	81
3.3.1 Procedures for section 3.1	81
3.3.2 Procedures for section 3.2	82
3.4 References.....	84
Chapter 4 Red-Shifted Dyes for p-DSSCs	89
4.1 Triphenylamine-based donor-acceptor dyes for DSSCs.....	89
4.1.1 Background	89
4.1.1.1 Push-Pull dyes.....	89
4.1.1.2 Simple Organic Donor-Acceptor Dyes in p-Type Devices.....	93
4.1.2 Results.....	98
4.1.2.1 Optical and Electrochemical Properties.....	99
4.1.2.2 Dye Loading.....	101
4.1.2.3 P-type devices	102
4.1.3 Conclusions	105
4.2 A near-IR absorbing near-IR BODIPY dye for p-DSSC.....	106
4.2.1 Background	106
4.2.1.1 BODIPY Dyes as Near-IR Absorbers	106

4.2.1.2 The Pentafluorosulfanyl Group.....	111
4.2.2 Results.....	112
4.2.2.1 Synthetic Procedures.....	112
4.2.2.2 Optical properties.....	114
4.2.2.3 Electrochemistry.....	115
4.2.2.4 Computational Analysis.....	116
4.2.2.5 Solid state Properties and Dye Loading.....	120
4.2.2.6 P-type devices.....	122
4.2.2.7 Preliminary Tandem devices.....	125
4.2.3 Conclusions.....	131
4.3 Experimental.....	132
4.4 References.....	133
Chapter 5 Alternative Architectures for Efficient Tandem Quantum Dot Sensitized Solar Cells.....	137
5.1 Background.....	137
5.1.1 Quantum Dot Principles and Applications.....	137
5.1.2 Synthesis of Quantum Dot Materials.....	139
5.1.3 Integration of QDs into QDSSC.....	139
5.1.3.1 In-situ growth.....	140
5.1.3.2 Ex-situ synthesis.....	141
5.1.4 Optimisation of QDSSC.....	143
5.1.4.1 Requirements for the Electrolyte and CE for QDSSC.....	143
5.1.4.2 Modification of QD structures.....	144
5.1.5 Aims for this Chapter.....	146
5.2 Direct Deposition of PbS Quantum Dots.....	147
5.2.1 Synthesis and Characterization of PbS.....	147
5.2.2 Device Results.....	149
5.2.2 Integration into Anodes for Photo-Electrochromic Devices.....	151
5.3 Automation of CdS nanocrystal deposition via SILAR.....	153
5.3.1 Automation of SILAR technique.....	153
5.3.2 Material Properties.....	155
5.3.3 Device Results.....	158
5.3.4 Examination of CE materials.....	160
5.3.5 Co-sensitization with RJ3.....	162

5.4 Investigation of Alternative Architectures and Materials	165
5.4.1 Synthesis and Characterisation of Bi ₂ S ₃	165
5.4.2 Single junction device and preliminary tandem device results.....	168
5.4.3 Integration of AgBiS ₂ into tandem devices.....	176
5.5 Conclusions and Future Outlook.....	178
5.6 Experimental.....	180
5.7 References.....	183
Chapter 6 Conclusions and Future Outlook.....	187
References	191

Publications

The following publications contain work by the author which is included in this thesis.

- 1) Hierlinger, C.; Flint, H.; Bradford-Cordes, D.; Slawin, A. M. Z.; Gibson, E. A.; Jacquemin, D.; Guerschais, V.; Zysman-Colman, E. A Panchromatic, Near Infrared Ir(III) Emitter Bearing a Tripodal C^NC ligand as a Dye for Dye-Sensitized Solar Cells *Polyhedron*. **2018**, *140*, 109-115.
- 2) Kolay, A.; Flint, H.; Gibson, E. A.; Deepa, M. Efficient Charge Separation and Transport in a Tandem Solar Cell with Photoconducting Se sub-Microtubes and AgBiS₂ Quantum Dots *Chemical Engineering Journal*. **2022**, *437*
- 3) Kolay, A.; Flint, H.; Gibson, E. A.; Deepa, M. Self-switching photoelectrochromic device with low cost, plasmonic and conducting Ag nanowires decorated V₂O₅ and PbS quantum dots *Solar Energy Materials and Solar Cells*, **2022**, *239*
- 4) Marri, A. R.; Flint, H.; Gibson, E. A.; Fielden, J. Pyridyl Anchored Indolium Dyes for the p-Type Dye Sensitized Solar Cell *Dyes and Pigments*, **2022**, *202*

List of Abbreviations

a.u.	arbitrary units
BODIPY	Boron dipyrromethane
CB	conduction band
CBD	chemical bath deposition
CV	cyclic voltammetry
DCM	dichloromethane
DI	de-ionised water
DSSC	dye-sensitized solar cell
E_{CB}	conduction band energy
E_F	Fermi level energy
E_g	band gap energy
E_{VB}	valence band energy
FF	fill factor
FTO	fluorine-doped tin oxide
HOMO	highest occupied molecular orbital
Or	High Resolution Electrospray Ionisation Mass Spectrometry
IPCE	incident photon-to-current conversion efficiency
IR	Infra- red
J_{sc}	photocurrent density
KPFM	Kelvin probe force microscopy
LUMO	lowest unoccupied molecular orbital
MPA	mercaptpropionic acid

NMR	nuclear magnetic resonance
PV	photovoltaic
p-XRD	powder X-ray diffraction
QD	quantum dot
QDSSC	quantum dot-sensitised solar cell
RT	room temperature
SEM	Scanning electron microscopy
SILAR	successive ionic layer adsorption and reaction
TOP	Tri-Octyl Phosphine
UV	ultra-violet
VB	valence band
V _{oc}	open-circuit photovoltage
XPS	X-ray photoelectron spectroscopy
η_{cc}	charge collection efficiency
η_{inj}	charge injection efficiency

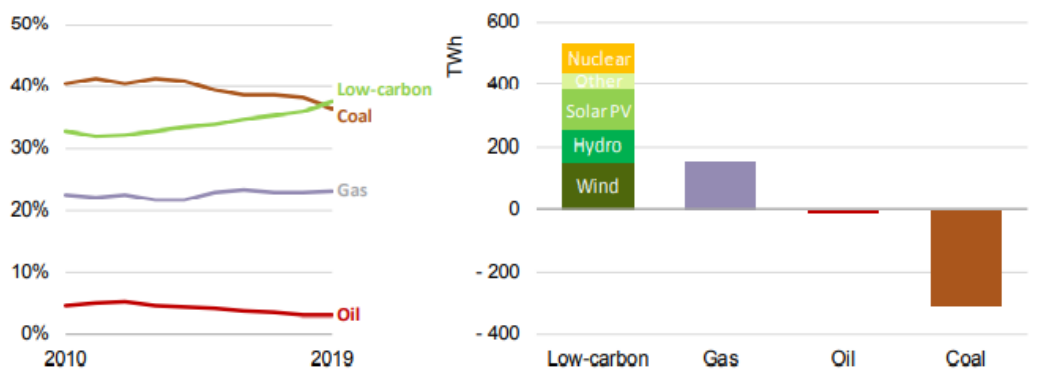
Chapter 1 Introduction

1.1 The Need for Renewable Energy

The world is at a tipping point. The forests are burning, islands of plastic float in the oceans, and the ice at the poles is melting. Human impact on the planet is wide ranging, long term, and devastating. Since the Industrial Revolution, human innovation has accelerated, thanks to our use of the energy trapped within fossil fuels. However, the burning of these fossil fuels has also contributed to the rise in global temperature. ^{1,2}

In this anthropogenic age, we must reduce our reliance on non-renewable sources of energy and find sustainable ways of meeting the worlds energy requirements. This can be achieved in several ways, including;

- Reduction of greenhouse emissions released upon burning non-renewable fuels.
- Elimination of environmental scarring caused by fuel extraction and processing.
- Balance financial and socioeconomic disparities caused by the localization of energy resources.



IEA 2020. All rights reserved

Figure 1: a) Percentage change in energy demand between 2010 and 2019 by source b) Relative change in energy usage in TWh across the same period. Image reproduced from IEA 2020 report. ⁴

Projections of energy demand in 2050 estimate that up to 30 TW of power could be required globally. ³ Alternative methodologies for energy production include wind, solar, tidal, nuclear, geothermal and biomass. Figure 1, from an IEA report in 2020, illustrates the change in global energy demand by source. As of 2019, demand for low carbon fuel sources, including nuclear and solar PV, surpassed that catered for by the burning of coal. ⁴ Additionally, the coal industry showed a marked decrease in energy output, meaning that the replacement of these environmentally damaging fuels is not just a concept for the future, it is a reality now. ⁴ Solar energy is an extremely good candidate to help cater for the changing global demand. ⁵ Between 2018 and 2019, the global demand for solar photovoltaic electricity generation increased by 22.3 %.

1.7×10^5 TW of solar energy strikes the earth's surface, and with appropriate infrastructure, we could capture around 600 TW. If we utilised fully the potential of commercial solar modules, most of which have efficiencies topping $\sim 10\%$, we could have the capability to supply 60 TW of power. ⁶ Not only is this method of energy harvesting beneficial for energy production, but it also has a place in day-to-day life. Energy can also be harvested in a localised manner by both countries and corporations, reducing costs and decreasing reliance on centralised reserves. Through the integration of PV into product design, there is also the capability to power smaller devices, lessening their overall energy demand. Integration of PV into smaller smart devices could expand the range of technologies in what is known as the Internet of Things (IoT) and make our everyday lives a little easier. ⁷

1.2 Photovoltaics

As a cornerstone to photosynthetic processes, solar energy is fundamental to life on this planet. It is therefore fitting that the Sun will help sustain human development in years to come. To utilise solar resources, the energy provided by the Sun must be converted to a different form. Conversion strategies include solar thermal (sunlight to heat), solar thermal electric (sunlight to heat, then converted to electricity), biomass (sunlight to biofuel) and photovoltaics (sunlight to electricity).⁸

In 1954, Bell Laboratories demonstrated the first ‘practical’ solar cell, a silicon p/n junction with a measured efficiency of 6 %.^{9,10} The development of PV technologies before this point was sporadic and, in some cases, accidental. Yet after this point, research in the field accelerated, and now, terrestrial device efficiencies have surpassed 40 %, via the use of multi-junctions and solar concentrators.¹¹

1.2.1 Foundations and Semiconductors

Semiconductors are materials with a finite energy gap (E_g) in their range of excitation energies. As opposed to conventional molecular or metallic bonding, their energy levels can be separated into a conduction band and valence band. The valence band is the charge filled state of the material, which is populated by electrons. When photons of at least the minimum energy $h\nu = E_g$ excite electrons, they may be promoted into the conduction band. For the electron to return to the valence band, it must first decay to the band edge (via rapid stepwise generation of phonons), and subsequently, lose energy equivalent to that of the bandgap all in one step through the emission of a photon. Electrons can therefore have a lifetime of microseconds (or yet longer in indirect bandgap materials) in the conduction band, making it possible to harvest and utilise them to produce electrical energy.

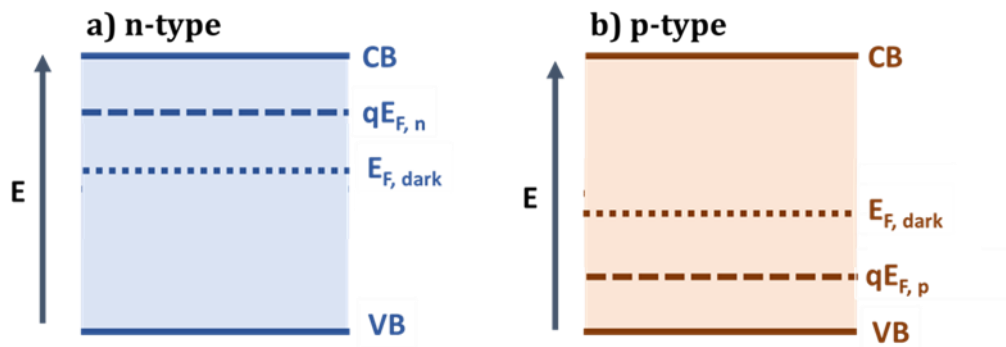


Figure 2: Energy level diagram of Fermi (E_F) and quasi-Fermi (qE_F) level energies of a) an n-type and b) a p-type semiconductor in the dark and upon illumination.

'Fermi levels' are values dictated by the probability density of electrons and holes in a semiconductor under thermal equilibrium, which describes the potential of the electrons or holes. Semiconductors can be categorised into two groups: Intrinsic semiconductors are those composed of materials such as silicon and germanium, with internal defects, while extrinsic semiconductors are those doped with other elements to modify their Fermi levels for use in optoelectronic applications. Impurities can either donate electron density into the conduction band to increase the Fermi level (as in n-type) or withdraw electron density from the valence band to decrease the Fermi level (as in p-type). Under illumination or other applied bias, the thermal equilibrium within the semiconductor is disturbed, which can 'split' the established Fermi level into two quasi-Fermi levels.¹² Quasi Fermi levels describe the relative quantities of electrons and holes in the conduction and valence bands respectively when the populations of charge carriers are displaced from the equilibrium and are shown in Figure 2. For example, if the rate of hole recombination is slower than the equilibration of the separated charges, the quasi-Fermi level will tend towards the valence band. Alternatively, any electron accepting defects within the bulk material will increase the population of holes in the valence band. This means that the majority carriers are holes, and the material will be p-type.

1.2.2 1st Generation PV

What is known as the first generation of photovoltaic technologies includes both monocrystalline and polycrystalline silicon solar cells (c-Si). These devices are composed of highly pure, highly crystalline silicon wafers with thicknesses ranging between 0.2 –

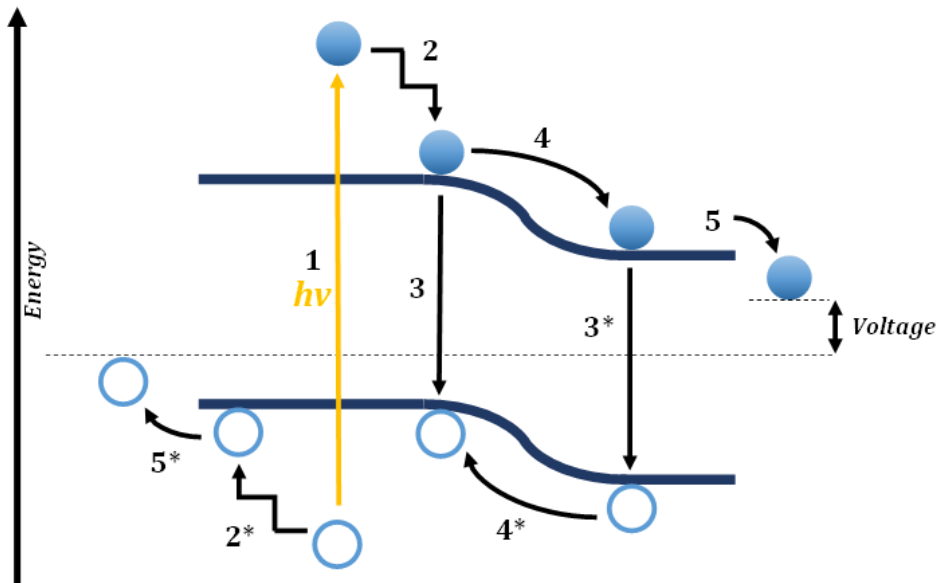


Figure 3: Relative energy levels and charge transfer mechanisms within a pn-junction solar cell. 1) Light absorption; 2,2*) thermal relaxation; 3,3*) recombination losses; 4,4*) junction loss; 5,5*) contact loss.

0.5 mm. The wafers are doped with either phosphorous or boron, leading to both n-type and p-type silicon domains respectively. The interface between these regions forms a p-n junction, at which photons can be absorbed and then separated into an electron-hole pair. These charges are collected at contacts at the front and the back of the material. The processes involved within a pn-junction solar cell are shown in Figure 3. Photons are absorbed at the pn-junction and an electron-hole pair is generated (1). Thermal relaxation of the electron and hole (2/2*), or recombination processes (3) can then occur. The electric field at the junction helps to separate electrons and holes (4/4*) and the charges are then collected at front and back contacts (5/5*).

Since the integrity of the material is key for the light harvesting and charge extraction processes, any defects in the bulk phase will drastically decrease the overall efficiency of the device. Since the crystalline silicon also has an indirect band gap, large quantities of material are required to absorb enough light to reach their high efficiencies (>25 %).¹³ This made initial production of Si devices prohibitively expensive. Yet with developments in manufacturing upscale and increased uptake in both the commercial and residential sectors, solar modules containing mono- and poly- crystalline Si wafers are now commonplace in daily life.¹⁴

1.2.3 2nd Generation PV

While silicon solar modules have established their place as the workhorses of solar energy production, they are limited in their application due to the manufacturing infrastructure required for production. The second generation of PV technology spans thin film technologies such as amorphous silicon (a-Si), cadmium telluride (CdTe) and copper indium gallium selenide (CIGS, an alloy of CuInSe₂ and CuGaSe₂).¹⁵⁻¹⁸ These devices also work via p-n junctions, and since the materials all have direct bandgaps, they have improved light harvesting capabilities and can be produced at a sub millimetre scale rather than using bulk material. The production of thin film devices opposed to bulk crystalline wafers reduces overall production costs and even allows for the design of flexible PV systems. However, the inclusion of rare elements, such as indium and tellurium, is a concern in terms of viability for sustainable upscale, and intrinsic limitations to efficiency of first- and second-generation devices could eventually limit applicability.

1.2.4 The solar spectrum and the Shockley Queisser limit

By understanding the light that we are provided with, we can tailor the working region of our devices to specific regions of the solar spectrum. Conversion of solar energy into

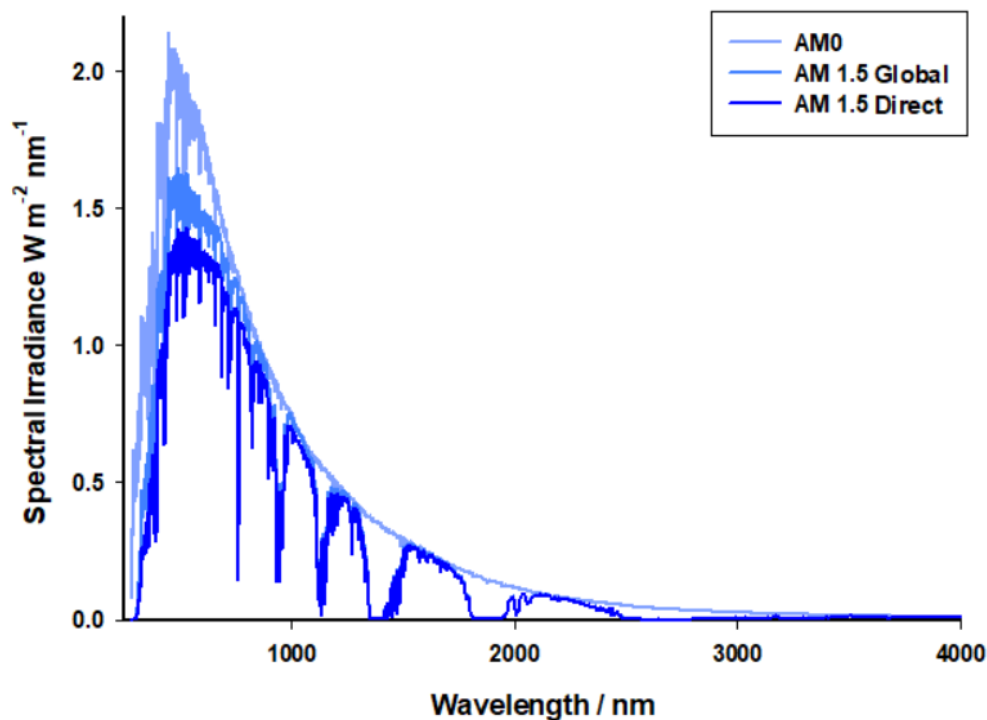


Figure 4: Plot of solar irradiance spectrum against wavelength. Reproduced from data sourced by NREL.¹⁹

current can be considered to take place in two steps- initial absorption of solar radiation and conversion to chemical energy, followed by transformation into electrical energy by producing current and voltage. The output of the cell can be measured in several ways, with most literature focussing on the efficiency of the cell which provides a point of comparison between a variety of cells created by different groups and allows us to determine which components have yielded better results. Most testing for PV devices is conducted at AM 1.5 Global (AM1.5G) illumination, often using a solar simulator. This provides a spectrum of incoming photon energies like that shown in Figure 4.¹⁹

When designing and producing solar cells, both the V_{oc} (open circuit voltage) and J_{sc} (short circuit current density) are aimed to be maximised to increase output power, since $P=IV$ (current (Amps) \times voltage (Volts) = power (Watts)). Theoretically, for a DSSC, the maximum voltage generated by the device is the difference between the quasi-Fermi level of the semiconductor and the redox potential of the electrolyte. Therefore, adjusting the bandgap of the sensitiser for a large energy difference is important to maximise V_{oc} .

However, since J_{sc} is dictated by the rate of flow of electrons, a lower bandgap is needed to increase the number of incident photons that can excite the sensitiser and generate current. This modification to improve current comes at the expense of voltage, leading to a trade-off that limits the amount of output to be gained from a cell. The optimal bandgap for an absorber was found to be ~ 1.4 eV, leading to a maximum theoretical cell efficiency of 33.4 %. This is known as the Shockley-Queisser limit, and to develop DSSCs that could be used practically, novel solutions must be devised to overcome it.²⁰ Multi junction cells surpass this limit by absorbing photons of varying wavelength, leading to an increase in maximum theoretical efficiency. For two junctions, this limit becomes around 45 %, reaching up to 68.7 % for an infinite number of cells.²¹⁻²³

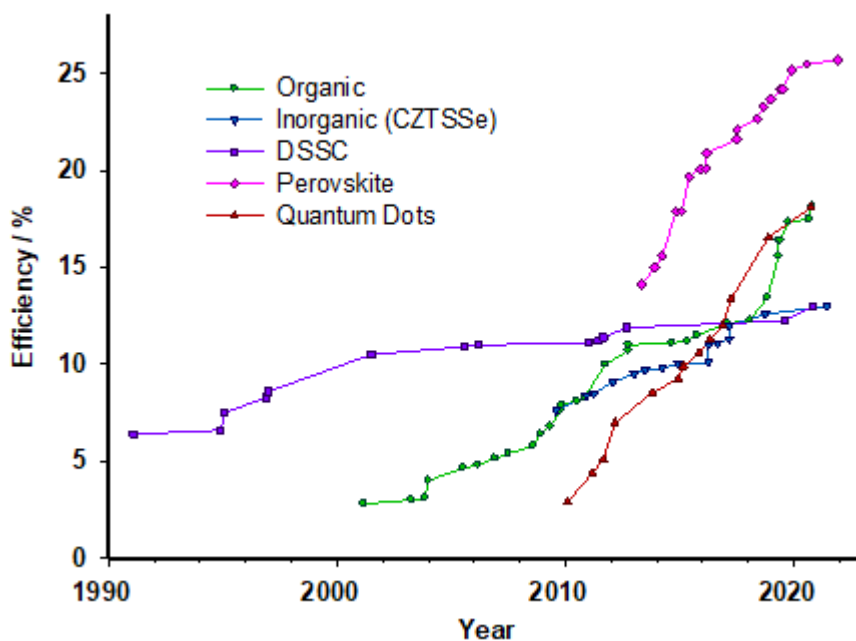


Figure 5: Record research cell efficiencies in emerging PV technologies, adapted from data collated and verified by NREL. ²⁴

1.2.5 3rd Generation PV

The third generation of photovoltaics include multi-junction systems such as those described above, as well as emerging technologies that can be produced at low cost. ²⁴ They often involve thin film or novel materials and architecture that is helping to reinvent the energy landscape and encourage assimilation of solar technologies into our everyday lives. Lower manufacturing costs, the use of novel and easy-to process materials and cutting-edge developments make this group of PV technologies an exciting frontier of development. Three notable examples of these devices include perovskite solar cells, dye-sensitised solar cells (DSSC) and quantum dot solar cells (QDSC). Each contain molecular or composite absorber materials with their own benefits and drawbacks. Current record efficiencies of these cells range from ~15 % for DSSCs up to 25.8 % for perovskite solar cells. ^{25,26} Hybrid devices such as QD- sensitised solar cells or perovskite QD solar cells have also reached efficiencies of 15.5 % and 16.6 % respectively. ^{27,28}

1.3 Dye sensitized Solar Cells

While DSSCs present low efficiencies in comparison to their QD and perovskite counterparts, their versatility makes them particularly promising for use in architectural design, ambient light harvesting, or within the IoT.

1.3.1 Grätzel Cells

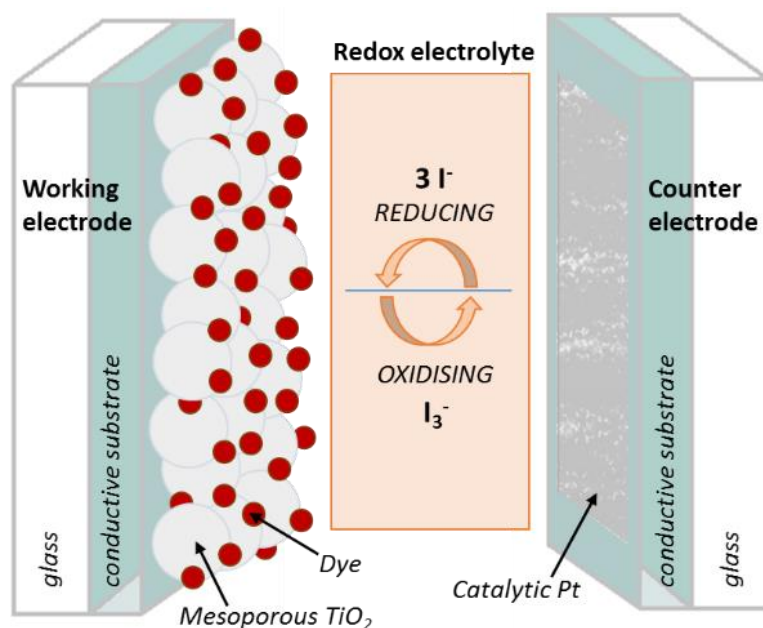


Figure 6: Simplified schematic of the principal components of a DSSC.

The first working dye sensitised solar cells (DSSCs) were produced by Grätzel et al. in 1991.²⁹ The principal components of a DSSC include the dye, electrolyte, semiconductor, and counter electrode, as seen in Figure 6. DSSCs utilise dyes to absorb photons of specific wavelength and inject the resulting excited electrons into the conduction band of the semiconductor to cause charge to flow and generate a photocurrent. The redox electrolyte reduces and regenerates the dye by shuttling electrons from the counter electrode. Since the semiconductor components in the devices are nanocrystalline, charge separation within the material is dependent on diffusion rates to the front and back contacts in the device. DSSCs also perform relatively well in diffuse light conditions and high temperatures, with limitless possibilities for integration and application into everyday life due to their varied colours, shapes and transparency.³⁰

Figure 7 outlines the productive electron transfer pathway through the n-type DSSC, through to charge extraction within the circuit. The electron transfer mechanism begins when the sensitizer (S) undergoes photoexcitation to an excited state (S*).



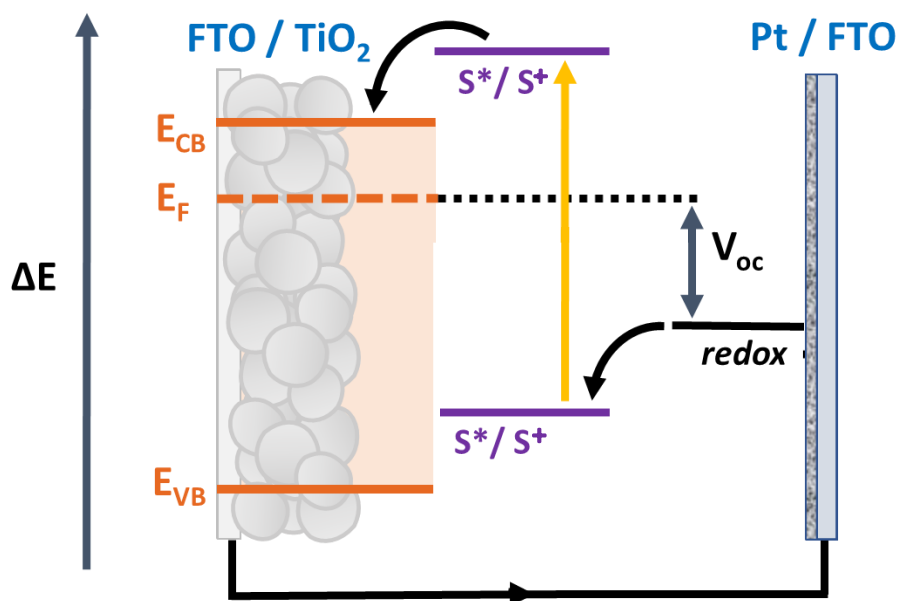
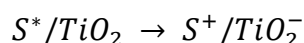


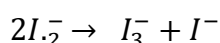
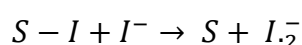
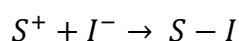
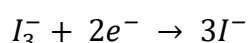
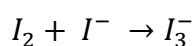
Figure 7: Relative energy levels and direction of electron transfer in an *n*-DSSC.

If the energy level of the excited state of the sensitizer is sufficiently high enough, there will be enough Gibbs free energy to facilitate electron injection of the photoexcited electron from the sensitizer to the conduction band of the titanium dioxide, TiO₂. Upon injection of the electron, the sensitizer is oxidised and forms the charge separated state.

31

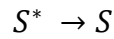


The electron then diffuses through the semiconductor to reach the back contact where it is collected and then transferred through the circuit. The sensitizer is regenerated to its ground state via a redox electrolyte, in this case, an iodide / triiodide redox couple. The formation of iodide ions and mechanism of regeneration is thought to take place in the following manner: ^{30,32}

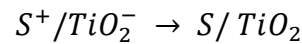


In the electrolyte solution, both iodine and iodide ions combine to form triiodide, which diffuses to the counter electrode. Electrons on the platinised CE reduce the triiodide species to iodide once more, which can be used to regenerate the oxidised dye.

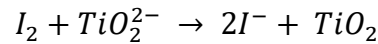
Regeneration of the dye forms the radical species, which through a disproportionation reaction reforms the iodide and triiodide pair. These favourable forward transfer processes in the n-DSSC contribute to the generation of photocurrent in a device yet are hindered by unfavourable recombination mechanisms. These include:



relaxation of the excited sensitiser to its ground state, preventing the transfer of the excited electron to the TiO_2 conduction band,



recombination of the charge separated state after injection of the excited electron, or



recombination of the negative charges within the semiconductor with iodide species, which subverts the sensitiser entirely. This recombination is one of the key limitations to n-DSSC performance, and can be reduced with modifications to the sensitiser properties, semiconductor morphology, or electrolyte composition.³³ This recombination is also the source of dark current within the device, the reduction of which corresponds to an increase in open circuit photovoltage (V_{OC}), and a decrease in semiconductor-electrolyte recombination. Where photocurrent arises from the success of these electron transfer processes, the V_{OC} of the device is equal to the difference in potential between the quasi Fermi level of an electron injected into the semiconductor and the redox potential of the electrolyte;

$$V_{OC} = qE_{F,n} - E_{redox}$$

For n-type devices, each component has been extensively studied and optimised to align with the structural and electronic properties of the TiO_2 material. While there have been some modifications made to the design of the devices since their original iterations, the working principles and components have remained mostly unchanged. Discussion of several varieties of sensitisers used in n-DSSC can be found in Chapter 3.

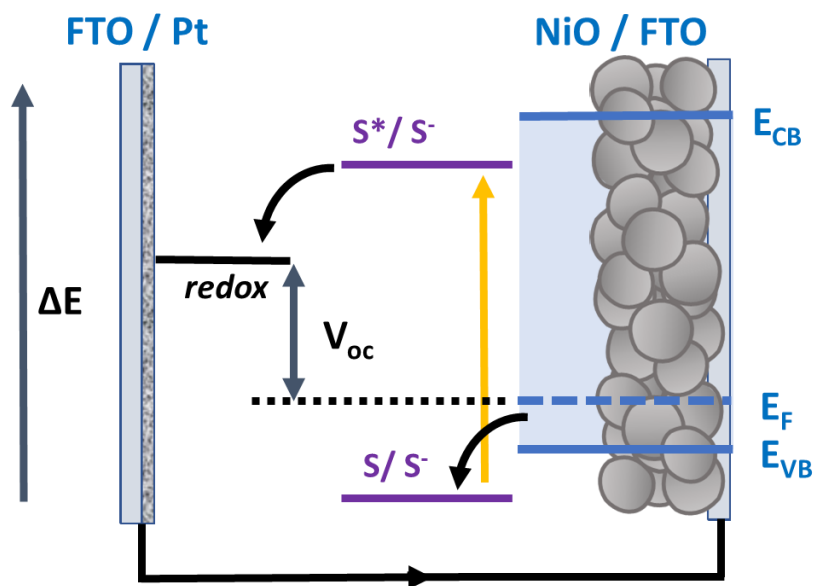
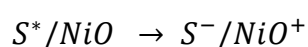


Figure 8: Relative energy levels and direction of electron transfer in a p-DSSC

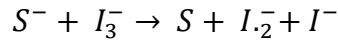
1.3.2 p-type DSSC

In contrast to the n-type semiconductors described above, p-type materials undergo carrier transport through hole injection into the valence band. NiO is a very common, wide band gap material (3.6-4.0 eV, depending on number of Ni (III) sites),³⁴ which is used in p-type systems due to its stability and transparency.

The p-type DSSC works in a similar way to the n-type, but with a reversal in the direction of electron transfer, as seen in Figure 8. Upon excitation of the sensitizer and production of an electron-hole pair, the redox electrolyte is reduced by the promoted electron, which is replaced again in the ground state by an electron from the valence band of the NiO. However, low power conversion efficiencies are often reported for p-type NiO DSSCs. These are attributed to the low V_{oc} (resulting from the small potential difference between the electrolyte redox potential and the quasi-Fermi level in the NiO photocathode) and J_{sc} (which stems from rapid hole recombination in the NiO with the reduced sensitizer). The steps generating current in the device are listed below, beginning when the sensitizer is illuminated, and an electron promoted to the excited state. Next, an electron is transferred from the valence band of the NiO to the excited sensitizer. This creates a charge separated state that includes a reduced sensitizer and a hole in the VB of the NiO;

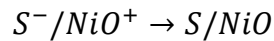


The hole diffuses to the back contact of the device for extraction, while the sensitiser is regenerated by the triiodide species,

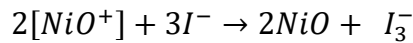


The triiodide is then regenerated at the CE via another electron transfer reaction.

After the absorption of light, radiative and non-radiative decay processes within the sensitiser may cause the excited electron and hole pair to recombine. The positive charge of hole density in the NiO also can combine with the excited state electron of the sensitiser.



This is an intrinsic problem with NiO semiconductors and is one of the key limitations to p-DSSCs.^{32,35} This can be overcome by forcing spatial separation between the excited state of the sensitiser and the NiO surface. Additionally, the redox couple could undergo oxidation by the NiO surface if its electron is not collected by the back contact.



Preventing this process can be achieved via the use of blocking layers or by preventing contact between the redox electrolyte and the bulk NiO surface. Work to mitigate the effects of recombination processes has been varied but have not yet improved the efficiencies of p-DSSCs to the level of the n-type devices. Photovoltage in these devices arises from the potential difference between the quasi-Fermi level at the semiconductor valence band (VB) edge and the redox potential of the electrolyte, and can be calculated in the following way:

$$V_{OC} = qE_{F,p} - E_{redox}$$

Alternative dye systems, electrolyte configurations and material optimisation are all approaches to improving the performance of these devices.³⁶ Further discussion and investigation of alternative dye systems utilised in this type of DSSC can be found in Chapter 4.

1.3.3 Tandem DSSC

High-efficiency DSSCs generate photocurrent via electron injection from a dye sensitiser into a n-type semiconductor (n-DSSCs). By using a p-type semiconductor, the inverse operation occurs where electrons are transferred from the material (typically NiO) to a photoexcited dye molecule (p-DSSCs). Tandem cell structures (pn-DSSCs) can be built by combining two photoactive electrodes connected in series, which together have a

maximum theoretical efficiency of up to 43 %, much greater than the Shockley-Queisser limit. The resulting photocurrent is therefore limited by the photoelectrode with lowest current, whereas the photovoltages of the two cells are combined. To match the photocurrent, semiconductor film thicknesses can be adjusted to control optical absorption on both sides. While n-DSSCs have been shown to reach verified efficiencies of over 15 %, the p-DSSC systems still have low current output, reaching ~ 2.5 % at their upper limits,³⁷ and are therefore the limiting factor to performance of previously reported pn-DSSCs. Further development into the working of the p-type photoelectrode can allow us to improve the overall efficiency of tandem devices.³⁸

The steps shown in Figure 9 show the direction of electron transfer when both electrodes are photoactive. **A-** Upon excitation via an incident photon, an electron is promoted to the LUMO of sensitiser 2. **B-** The excited electron reduces the electrolyte. **C-** The electrolyte oxidises sensitiser 1. **D-** Excitation of sensitiser 1 promotes an electron to the LUMO. **E-** Electrons are donated to the conduction band of the n-photocathode. Charge can then flow from this electrode back to the p-photoanode via an electrical circuit to begin the cycle again, leading to **F-** Electrons are injected into the HOMO of sensitiser 2 from the p-

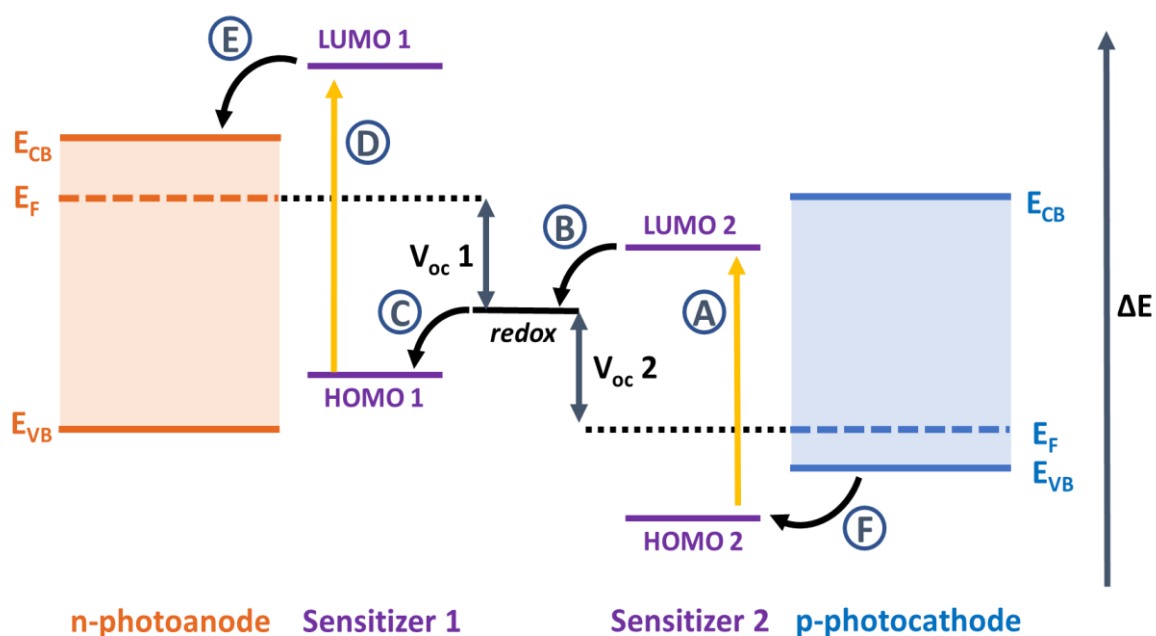


Figure 9: Relative energy levels and direction of electron transfer in a tandem DSSC.

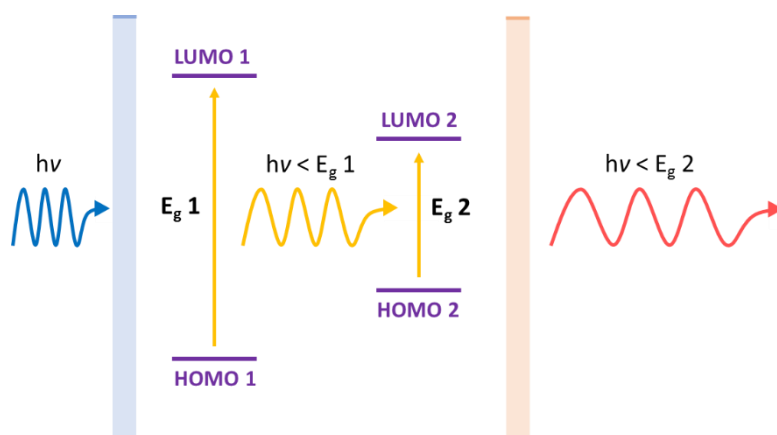


Figure 10: Simplified diagram describing the relative band-gap energies in the optimal tandem cell orientation for photon absorption.

semiconductor. In designing these cells, care must be taken to tune the band gaps of the sensitizers to maximise V_{oc} , promote current flow and help prevent recombination of charge.

Multi junction solar cells can be used to increase the number of photons that can be used by the cell by using sensitizers of different bandgaps to absorb over multiple wavelength regions and therefore maximise absorption. In tandem cells, the most efficient orientation of absorbers is to have the material with the highest optical bandgap at the front (the illuminated side). Therefore, $E_{g1} > E_{g2}$. As shown in Figure 10, high energy photons with $h\nu > E_{g1}$ will be absorbed by the first layer of material in the tandem cell. The second layer, with the lower energy bandgap E_{g2} , will absorb photons with an energy between the values of E_{g1} and E_{g2} , as well as any that the first layer has failed to trap. In this orientation, the photon energies are used more efficiently, and both sides can work to their full potential range.³⁹ Tandem devices such as these can have low energy conversion efficiencies, but will overall still exceed the efficiencies of their components tested individually.⁴⁰ The typical dye found in an n-DSSC converts photons reaching around to 600 nm in wavelength. To maximise output of a tandem device, spectral overlap between sensitizers on the n- and p- electrodes should be reduced to fully utilise the entire solar spectrum available. Therefore, for p-DSSCs to complement the established n-type systems, the sensitizers used in these devices must harvest light in the unused portion of the spectrum beyond 600 nm.

As expanded below and in Figure 9, the V_{oc} of the tandem devices is equal to the sum of the V_{oc} for each individual device. Since the redox potential of the electrolyte is the same,

and the n- and p- type devices are connected in series, the maximum V_{oc} of a tandem device is equal to the potential difference between the quasi fermi levels of NiO and TiO₂.

$$(1)V_{OC} = qE_{F,n} - E_{redox}$$

$$(2)V_{OC} = qE_{F,p} - E_{redox}$$

$$(Tandem)V_{OC} = qE_{F,n} - qE_{F,p}$$

Given the position of the quasi-fermi levels of TiO₂ and NiO at -0.5 V vs NHE and 0.54 V vs NHE respectively, the maximum V_{oc} for a tandem device using these materials would be approximately 1.04 V.

By lowering the potential of the fermi level of the photocathodic semiconductor, the overall V_{oc} of the device can be increased. Intrinsic problems with NiO, including the opacity of synthesised nanoparticles and poor electron transport properties can be addressed by replacement with an appropriate material. By increasing charge transport rates within the p-semiconductor, recombination processes between excited sensitizer or electrolyte with the material will be averted and overall current output will also increase. This will improve current matching between the p- and n-type halves of the device and increase performance.

The p-type project undertaken in the Energy Materials group at Newcastle University aims to design and investigate different p-type semiconductors for efficient solar energy capture, conversion and storage.⁴¹ The group is currently working on a high-throughput reactor setup that can generate tuneable and reproducible samples of p-type materials with varying properties, in order to discover a viable replacement to NiO. In order to assess each materials' viability within devices, rapid screening methodologies are required. By doing this, the group aims to combat problems in the current p-type DSSCs such as small ΔE , recombination and back-electron transfer through the implementation of new semiconductors. The work in this thesis contributes towards this goal by highlighting sensitizers that enable the testing and integration of new materials into tandem DSSCs.

As discussed previously, sensitizers must absorb in the near-infrared region of the solar spectrum to attain good spectral coverage and increase transparency within the tandem DSSC. As discussed in Chapter 4, the limited commercial availability of NIR-absorbing

dyes suitable for this screening application, as well as the uncertainty in discerning binding mechanisms and chemical compatibility of the dye to each synthesised material, make it difficult for a dye to act as a 'one size fits all' candidate. While this does create an opportunity to design an appropriate candidate, in the meantime, alternative sensitiser beyond the traditional dye motif should be employed. In this case, quantum dot sensitising materials could be used to functionalise the synthesised semiconductor library as light absorbers.

1.4 Thesis Aims

The key aim of this work is to facilitate the investigation of alternative sensitising materials for tandem solar cells. This will be achieved through a multi-faceted approach that covers both a thorough study of the various sensitiser available for use in DSSCs, as well as a review of QDs as sensitiser for p-QDSC. Firstly, alternative sensitiser will be integrated into TiO₂ based DSSC in an effort to understand the role that both synthetic and natural dyes can play in the field in terms of their sustainability and application. Secondly, NiO-based p-DSSC will be investigated, and a study of red shifted dyes based on TPA and BODIPY cores will be undertaken. These dyes will ideally have absorption responses beyond 600 nm to better fit into a tandem device. If successful in single junction p-DSSCs, the dye sensitised NiO photocathodes will be integrated into tandem devices using complementary dye-sensitised TiO₂ photoanodes. Finally, quantum dots will be investigated as sensitiser materials. QDs have highly competitive properties as sensitiser for solar cell applications, such as their tuneability, sufficient photostability, and high molar extinction coefficients.⁴² Methods for sensitisation, coupling to counter electrodes, the design of electrolyte systems and the optimisation of devices are more commonly tested in n-type cells, so will be adapted for p-type applications. Performances of NiO DSSCs sensitised with various absorbers will be used to evaluate the QDs as sensitiser candidates in a high-output process for the screening of alternative p-type semiconductors. Successful p-QDSSC will also be integrated into tandem devices alongside other n-QDSSC.

1.5 References

- 1 S. A. Hill, Y. Ming and M. Zhao, *J. Clim.*, 2006, **31**, 9793–9814.
- 2 S. Manabe and R. T. Wetherald, *J. Atmos. Sci.*, 1967, **24**, 241–259.
- 3 A. Zaban, O. I. Mii, B. A. Gregg and A. J. Nozik, *Langmuir*, 1998, **14**, 3153–3156.
- 4 IEA, *Global Energy Review 2019 - The latest trends in energy and emissions in 2019*, 2020.
- 5 S. Rühle, M. Shalom and A. Zaban, *ChemPhysChem*, 2010, **11**, 2290 – 2304.
- 6 D. Sharma, R. Jha and S. Kumar, *Sol. Energy Mater. Sol. Cells*, 2016, **155**, 294–322.
- 7 V. Pecunia, L. G. Occhipinti and R. L. Z. Hoye, *Adv. Energy Mater.*, 2021, **11**, 31.
- 8 R. L. Hulstrom, *Solar Resources*, MIT Press, 1989.
- 9 United States Patent Office, 2780765, 1954, 3.
- 10 D. M. Chapin, C. S. Fuller and P. Pearce, *J. Appl. Phys.*, 1954, **25**, 1–3.
- 11 J. F. Geisz, R. M. France, K. L. Schulte, M. A. Steiner, A. G. Norman, H. L. Guthrey, M. R. Young, T. Song and T. Moriarty, *Nat. Energy*, 2020, **5**, 326–335.
- 12 J. Nelson, *The Physics of Solar Cells*, Imperial College Press, 2003.
- 13 S. Almosni, A. Delamarre, Z. Jehl, D. Suchet, L. Cojocar, M. Giteau, B. Behaghel, A. Julian, C. Ibrahim, L. Tetry, H. Wang, T. Kubo, S. Uchida, H. Segawa, N. Miyashita, R. Tamaki, Y. Shoji, K. Yoshida, N. Ahsan, K. Watanabe, T. Inoue, M. Sugiyama, Y. Nakano, T. Hamamura, T. Toupance, C. Olivier, S. Chambon, L. Vignau, C. Geffroy, E. Cloutet, G. Hadziioannou, N. Cavassilas, P. Rale, A. Cattoni, S. Collin, F. Gibelli, M. Paire, L. Lombez, D. Aureau, M. Bouttemy, A. Etcheberry, Y. Okada and J. F. Guillemoles, *Sci. Technol. Adv. Mater.*, 2018, **19**, 336–369.
- 14 A. Blakers, N. Zin, K. R. McIntosh and K. Fong, in *Energy Procedia*, Elsevier B.V., 2013, vol. 33, pp. 1–10.
- 15 M. Stuckelberger, R. Biron, N. Wyrsh, F. Haug and C. Ballif, *Renew. Sustain. Energy Rev.*, 2017, **76**, 1497–1523.
- 16 T. Sinha, D. Lilhare and A. Khare, *J. Mater. Sci.*, 2019, **54**, 12189–12205.

- 17 J. Ramanujam and U. P. Singh, *Energy Environ. Sci.*, 2017, **10**, 1306–1319.
- 18 I. A. Rauf and P. Rezai, *Renew. Sustain. Energy Rev.*, 2017, **73**, 408–422.
- 19 N. R. E. Laboratory, Reference Air Mass 1.5 Spectra, <https://www.nrel.gov/grid/solar-resource/spectra-am1.5.html>, (accessed 1 March 2022).
- 20 W. Shockley and H. J. Queisser, *J. Appl. Phys.*, 1961, **32**, 510–519.
- 21 C. Yan Dai, X. Liang Zhang, E. Chuang Wang, Z. Liu, M. Hui Li and C. Mei Liu, *Advanced Materials Research*, 2013, **601**, 437–448.
- 22 C. H. Henry, *J. Appl. Phys.*, 1980, 4494–4500.
- 23 J. He, H. Lindstrom, A. Hagfeldt and S.-E. Lindquist, *Sol. Energy Mater. Sol. Cells*, 2000, **62**, 265–273.
- 24 National Renewable Energy Laboratory, Best Research-Cell Efficiency Chart, <https://www.nrel.gov/pv/cell-efficiency.html>, (accessed 1 March 2022).
- 25 D. Zhang, M. Stojanovic, Y. Ren, Y. Cao, F. T. Eickemeyer, E. Socie, N. Vlachopoulos, J. E. Moser, S. M. Zakeeruddin, A. Hagfeldt and M. Grätzel, *Nat. Commun.*, 2021, **12**, 2–11.
- 26 H. Min, D. Y. Lee, J. Kim, G. Kim, K. S. Lee, J. Kim, M. J. Paik, Y. K. Kim, K. S. Kim, M. G. Kim, T. J. Shin and S. Il Seok, *Nature*, 2021, **598**, 444–450.
- 27 M. Hao, Y. Bai, S. Zeiske, L. Ren, J. Liu, Y. Yuan, N. Zarrabi, N. Cheng, M. Ghasemi, P. Chen, M. Lyu, D. He, J. H. Yun, Y. Du, Y. Wang, S. Ding, A. Armin, P. Meredith, G. Liu, H. M. Cheng and L. Wang, *Nat. Energy*, 2020, **5**, 79–88.
- 28 H. Song, Y. Lin, Z. Zhang, H. Rao, W. Wang, Y. Fang, Z. Pan and X. Zhong, *J. Am. Chem. Soc.*, 2021, **143**, 4790–4800.
- 29 B. O'Regan and M. Gratzel, *Nature*, 1991, **353**, 737–740.
- 30 A. Hagfeldt, G. Boschloo, L. Sun, L. Kloo and H. Pettersson, *Chem. Rev.*, 2010, **110**, 6595–6663.
- 31 A. Listorti, B. O'Regan and J. R. Durrant, *Chem. Mater.*, 2011, **23**, 3381–3399.

- 32 F. Odobel, Y. Pellegrin, E. A. Gibson, A. Hagfeldt, A. L. Smeigh and L. Hammarström, *Coord. Chem. Rev.*, 2012, 256, 2414–2423.
- 33 A. B. Muñoz-García, I. Benesperi, G. Boschloo, J. J. Concepcion, J. H. Delcamp, E. A. Gibson, G. J. Meyer, M. Pavone, H. Pettersson, A. Hagfeldt and M. Freitag, *Chem. Soc. Rev.*, 2021, 101.
- 34 J. He, H. Lindström, A. Hagfeldt and S.-E. Lindquist, *J. Phys. Chem. B*, 1999, **103**, 8940–8943.
- 35 E. A. Gibson, A. L. Smeigh, L. Le Pieux, J. Fortage, G. Boschloo, E. Blart, Y. Pellegrin, F. Odobel, A. Hagfeldt and L. Hammarström, *Angew. Chemie - Int. Ed.*, 2009, **48**, 4402–4405.
- 36 M. Bonomo and D. Dini, *Energies*, 2016, **9**, 32.
- 37 E. a. Gibson, A. L. Smeigh, L. Le Pleux, J. Fortage, G. Boschloo, E. Blart, Y. Pellegrin, F. Odobel, A. Hagfeldt and L. Hammarström, *Angew. Chemie*.
- 38 E. Benazzi, J. Mallows, G. H. Summers, F. A. Black and E. A. Gibson, *J. Mater. Chem. C*, 2019, 7, 10409–10445.
- 39 B. Minnaert and P. Veelaert, *Materials (Basel)*., 2012, **5**, 1933–1953.
- 40 C. J. Wood, G. H. Summers and E. A. Gibson, *Chem. Commun. Chem. Commun*, 2015, 3915–3918.
- 41 X. Zhang, G. E. Eperon, J. Liu and E. M. J. Johansson, *Nano Energy*, 2016, **22**, 70–78.
- 42 M. Kouhnavard, S. Ikeda, N. A. Ludin, N. B. Ahmad Khairudin, B. V. Ghaffari, M. A. Mat-Teridi, M. A. Ibrahim, S. Sepeai and K. Sopian, *Renew. Sustain. Energy Rev.*, 2014, **37**, 397–407.

Chapter 2 Theory and Experimental Techniques for the Study of DSSCs

In this section, fundamental theory and some key techniques for the study of DSSCs and their components are described. General experimental details are outlined and apply to all work done in this thesis, except when indicated otherwise.

2.1 Device Properties

2.1.1 Current and Voltage

The overall efficiency of DSSCs can be evaluated by measuring a photovoltage vs photocurrent density curve. When a DSSC is illuminated, a bias is applied to the device. At zero bias, with negligible external load, the device is said to be at short circuit, and the maximum current output is known as the short-circuit current (J_{sc}). When connected and under an infinite load, there is negligible flow of current and the device is at open-circuit. The build-up of charge within the device produces a potential difference through the device, which at its maximum is known as the open circuit voltage (V_{oc}). By sweeping a potential range across the device and modifying the applied load, changes in current output can be measured and a photovoltage vs photocurrent density curve (JV) can be generated, like that shown in Figure 1.

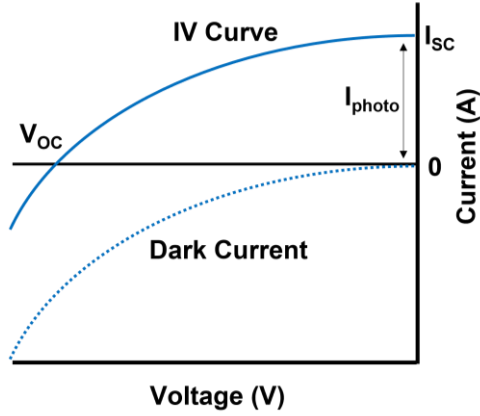


Figure 1: Sample JV curve (solid line) and dark current curve (dashed line) for a p-DSC.

The shape of the curve can be described by the diode equation;

$$I = I_{SC} - I_0 \left(e^{\frac{qV}{kT}} - 1 \right)$$

In which I is equal to the output current, I_0 is the diodes' dark leakage current, V is the input voltage, q is the absolute charge of the carrier, k is the Boltzmann constant, and T is the temperature.

In this work, an Ivium CompactStat potentiostat was used to take IV measurements of devices in both the dark and under AM 1.5 simulated sunlight from a Xenon light source (Newport, 300 W) calibrated to 100 mW cm^{-2} with a Si diode. The device working area was masked with a black aperture. Applied voltage was swept between appropriate potentials for each experiment (generally between open circuit and short circuit), at scan rates between 5 and 50 mV s^{-1} .

2.1.2 Power Output and Efficiency

The power output and efficiency of devices are derived from both the photovoltage, and photocurrent per unit area. Maximum power output (P_{\max}) occurs at the point where the product of the current and voltage is highest. The fill factor (FF) is the ratio of the actual maximum power output to the theoretical maximum power (the product of V_{OC} and J_{SC}). The fill factor is a good parameter in evaluating a cells performance, since those with a low internal resistance tend to have a high FF, as less produced current is lost in recombination processes.

The equation below is used to calculate η and arises from the ratio between P_{max} and the power of the incident light upon the cell ($P_{in} = 1000 \text{ W m}^{-2}$).

$$\eta = \frac{P_{max}}{P_{in}} = \frac{J_{sc}V_{oc}FF}{P_{in}}$$

Since device efficiency takes into account all parameters measured, as well as the working area of the device, it is one of the best ways of comparing the overall performance of PV technologies between studies. However, to evaluate the applicability of a PV device, the power output is key.

2.1.3 IPCE

Another parameter by which cells can be compared is the incident photon-to-current conversion efficiency (IPCE). IPCE values as a function of wavelength can be calculated as follows: ¹

$$IPCE = \frac{J_{sc}(\lambda)}{e\phi(\lambda)} = \frac{J_{sc}(\lambda)}{\lambda P_{in}(\lambda)}$$

Where ϕ is the photon flux, P_{in} is the power density of the incoming light, and λ is the wavelength of light. The spectrum created when running this experiment indicates a devices' photocurrent response at different wavelengths, making it crucial to facilitate the design of tandem PV. By analysing the spectral response of the photoanode and photocathode individually, it can be determined whether the two will either compete for light in the device or complement each other.

Incident photon to current conversion efficiency (IPCE) measurements were conducted by passing light from a Xenon source lamp through a monochromator (Oriel Cornerstone 130 1/8 m) at 5 nm increments between 400-800 nm and measuring the current output of the device, calibrated against the output of a Si photodiode.

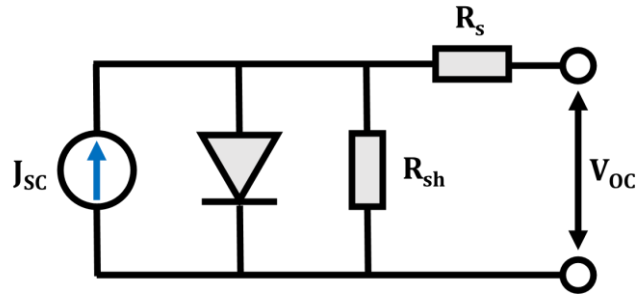


Figure 2: Simplification of DSSC as a diode circuit, where R_s is series resistance and R_{sh} is shunt resistance.

2.1.4 Dark Current

The interface between electrolyte and semiconductor can be modelled as a simple diode, as shown in Figure 2.² When measuring a JV curve for a device in the dark, the produced current is known as dark current, and follows the diode equation shown above. Dark current flows in the negative direction to the photocurrent, and at open circuit voltage, the dark current matches the opposing photocurrent, resulting in a net current of 0.³

Comparison of the dark current of devices is a good way of comparing recombination processes between electrolyte and semiconductor within a DSSC, as shown in Figure 3. Lower potential onset is an indication of increased recombination within the device.

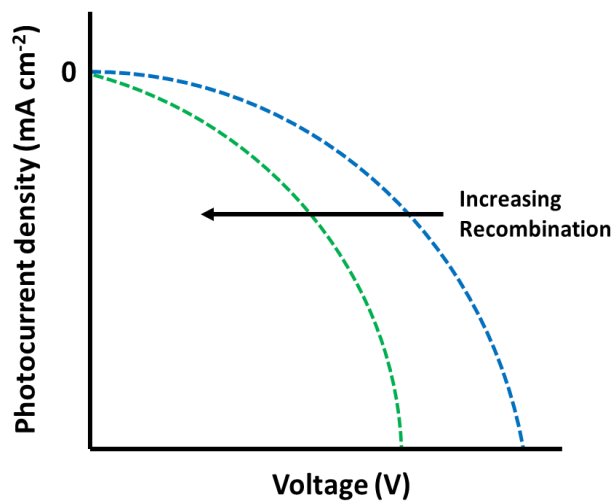


Figure 3: Samples of two dark current curves.

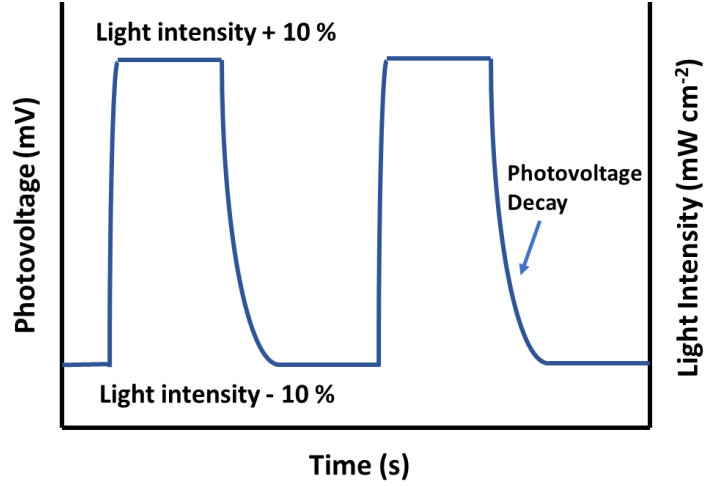


Figure 4: Sample photovoltage response of a SSWMPV experiment.

2.1.5 Charge Lifetime and Transport

Observation of the decay of photovoltage in a p-type device can provide information about the lifetime of charges (in this case holes (h^+)) within the device as well as the rate of recombination of these charges. The quasi-Fermi level of the NiO is dependent on the concentration of injected charge, therefore a change in charge concentration will alter the photovoltage of the device. Through the modulation of applied light, changes in photovoltage can be observed, in a small square wave modulated photovoltage experiment (SSWMPV) as shown in Figure 4. ⁴

The applied light is modulated by $\pm 10\%$ to ensure the response is tailored to that of the working conditions of the device. The relationship between the quasi-Fermi (qE_F) level and charge concentration (n_{VB}) is described in the equation below; ⁵

$$n_{VB} = N_{VB} e^{-\left(\frac{qE_F - E_{VB}}{kT}\right)}$$

Where N_{VB} and E_{VB} are the density of states and energy of the valence band respectively. T is temperature, and k is the Boltzmann constant. This can be rearranged to produce the quasi-Fermi level as so:

$$qE_{F,p} = E_{VB} + kT \ln \frac{N_{VB}}{n_{VB}}$$

As the photovoltage is directly related to the quasi-Fermi level of the p-semiconductor, there is an exponential relationship between the measured photovoltage and the concentration of charge. Therefore, the change in photovoltage (ΔV) during modulation

(where $V_{OC,0}$ is the initial measured photovoltage) can be fit to a 1st order exponential decay to produce the resulting charge lifetime (τ_h):

$$V_{OC} = V_{OC,0} + \Delta V e^{\left(\frac{-t}{\tau_h}\right)}$$

Over a range of light intensities, usually starting at 1 sun and decreasing in intensity, resulting in a range of values for $V_{OC,0}$. As light intensity and $V_{OC,0}$ decrease, the charge lifetime increases, suggesting that there is less charge available in the NiO that can undergo recombination.

In order to quantify the charge density, charge extraction experiments can be undertaken. By illuminating the device at open circuit, charge is allowed to accumulate in the device and photovoltage increases. When the light is switched off, the photovoltage then begins to decay as accumulated charge recombines with the redox electrolyte. The experiment begins when the device is switched to short circuit, at which point the current ‘spikes’.

Figure 5 illustrates an example of the extraction experiment, where the ‘spike’ in current is integrated to extract the charge. By varying the time delay as the photovoltage decays, the current response can be measured for a range of photovoltages.

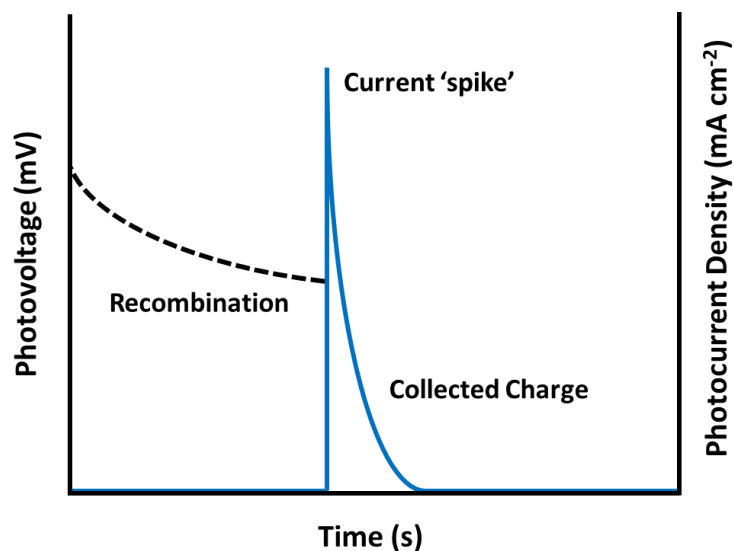


Figure 5: Sample charge extraction experiment. The dashed line represents the photovoltage, while the blue solid line shows the photocurrent response.

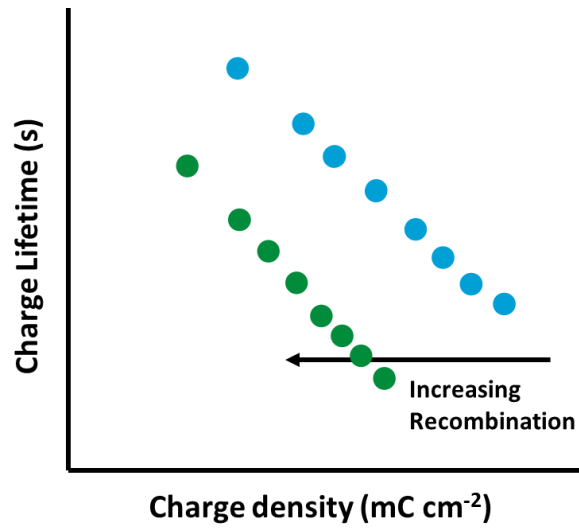


Figure 6: Sample charge density vs lifetime result for two devices.

By matching the photovoltages from each of these two experiments, the corresponding measured charge density and calculated charge lifetimes can be plotted against one another, as shown in Figure 6.

2.2 Optical and Electrochemical Characterisation

2.2.1 Absorbance and Fluorescence

Ultraviolet-visible spectroscopy elucidates electronic transitions, providing an absorption profile that quantifies the relative proportion and absolute quantity of light absorbed by a material. Visible light can be used to evaluate valence electron transitions (such as from p, d and π -orbitals) and rotational and vibrational changes when a material is irradiated. The wavelength of an absorption corresponds to a measure of energy separation between electronic states, so a change in bandgap, or shift in HOMO-LUMO energy can cause a shift in a materials' absorption onset. This measurement is pertinent to the design of tandem devices in that the spectral overlap of dyes and materials can be evaluated. The molar absorption coefficient is indicative of the ability of a material or molecule to absorb light, and is defined in the Beer-Lambert equation:

$$A = \log \frac{I_0}{I} = \epsilon cl$$

Where I_0 and I are the intensities of both the incident and transmitted light respectively, ϵ is the molar absorption coefficient, c is the concentration of the sample in solution, and l is the path length of the sample. In most cases, the path length refers to the cuvette in which a liquid sample is held, but for thin films this may refer to the thickness of the film.

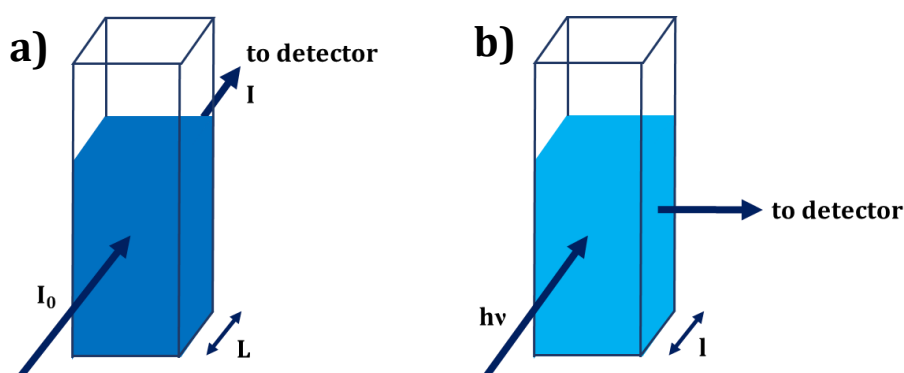


Figure 7: Schematic for the experimental setup of both a) an absorption and b) an emission spectral measurement. Arrows represent the direction of light.

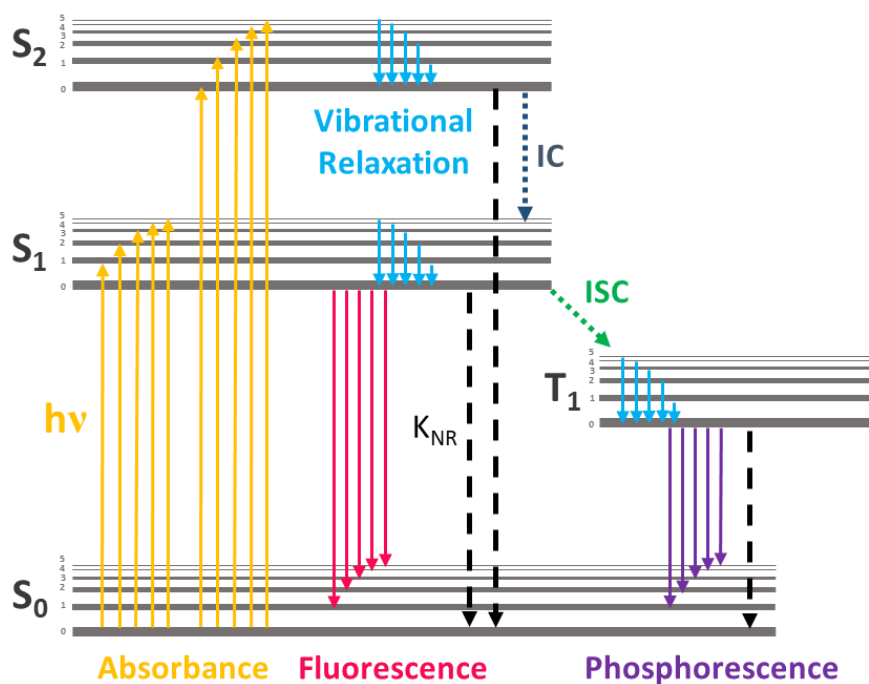


Figure 8: Jablonski diagram highlighting processes upon photoexcitation. S_0 denotes the ground state, while S_1 and S_2 are excited singlet states. T_1 is an excited triplet state. k_{NR} indicates the non-radiative decay constant, while IC and ISC represent internal conversion and intersystem crossing transitions respectively.

UV-Visible absorption spectroscopy is useful for determining the energy associated with absorption of light, yet there are multiple processes that occur within a molecule upon excitation. Once a photon is absorbed, an electron from the ground state is promoted to

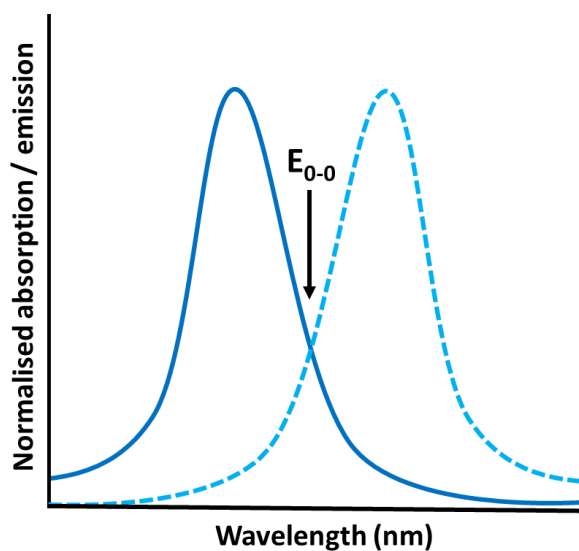


Figure 9: Normalised absorption (solid line) and emission (dashed line) spectra plots, demonstrating the elucidation of E_{0-0} from the intersection of the two.

the higher energy singlet excited state, which is then released via radiative and non-radiative decay processes to relax back down to the ground state. The Jablonski diagram in Figure 8 illustrates the relative energy level of each excited state, as well as the electron transitions between these states upon excitation.

Since most processes within a DSSC rely on the photogenerated excited states of dyes and other materials, fluorescence spectroscopy is an important tool used to evaluate their radiative decay processes. Kasha's rule dictates that any measurable fluorescence emission will usually have yielded from the lowest excited state, focussing our attention onto this energy level for these experiments. The wavelength at which the absorption and fluorescence emission profiles intersect, as shown in Figure 9, corresponds to the energy difference between the singlet s_1 and ground s_0 states, also known as the E_{0-0} .

2.2.2 Cyclic Voltammetry

In order to understand the electronic properties of dyes, electrolytes and other components used in DSSC, cyclic voltammetry can be used. In this experiment, a setup using three electrodes, as shown in Figure 10, is used to determine redox potentials. Potentials are applied through the working electrode at a variety of user-defined values, scanning between two voltages in forward and reverse directions, recording current values. These potentials are relative to a reference electrode, and the current measured is that flowing between the working and counter electrodes, through a supporting electrolyte that often contains the analyte. The measurement results in a cyclic voltammogram, and example of which can be seen in Figure 11. The redox potential of a

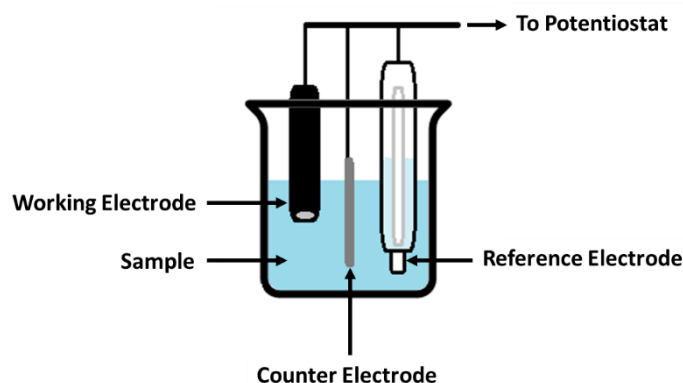


Figure 10: Schematic for the experimental setup of cyclic voltammetry of a sample in solution.

species at the working electrode can be calculated using the Nernst equation:

$$E = E_{redox}^{O'} - k_B T \ln \left(\frac{C_{ox}}{C_{red}} \right)$$

Where E and $E_{redox}^{O'}$ are the electrode potential and the redox formal energy, k_B and T are the Boltzmann constant and temperature, and C_{ox} and C_{red} are the concentrations of the oxidised and reduced species respectively.

Upon scanning towards positive potential, charging processes are observed. The current increases slowly until the $E_{redox}^{O'}$ is reached, at which point faradaic processes at the electrode begin, and the current starts to increase rapidly. Continuing to scan positively brings the anodic current to a peak, until the species at the electrode is consumed, the processes begin to tail off, and the current decreases once more. For reversible reductions, subsequent reversal of the scanning direction will cause the analyte to be re-oxidised, and a cathodic current will arise. For electrolytes, the redox potentials are key for determining the alignment of potential energies within a device. For dyes studied withing this thesis, the redox potentials correspond to electron transfer processes and relative HOMO-LUMO energy. The oxidation potential is the potential required to remove an electron from the dyes' HOMO, while the reduction indicates the potential at which an electron is accepted into the LUMO of the dye. By corroborating cyclic voltammetry with data acquired with UV-vis or emission spectroscopy, the redox potentials of a dyes excited state could be estimated.

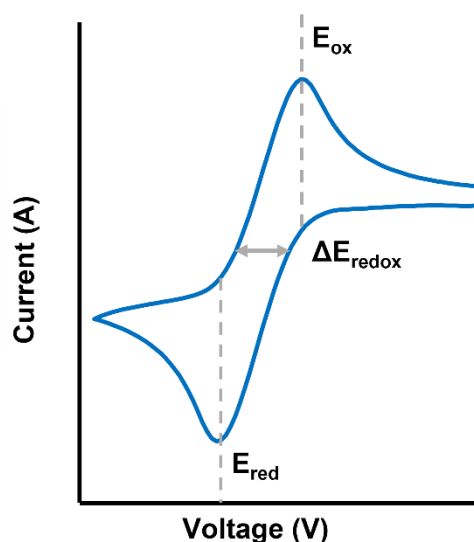


Figure 11: Representation of a reversible reduction process measured via cyclic voltammetry. E_{red} and E_{ox} are the reduction and oxidation peak potentials, and ΔE_{redox} is the difference in voltage between these peaks.

2.3 Computational Analysis

While physical experimentation remains imperative for scientific study, theoretical models are important for understanding both results from experiments and the performance of dyes in devices. Computational experiments were undertaken by colleagues and collaborators to complement the work done on dyes used in this thesis, specifically in Chapters 3 and 4. Credit is given to Claus Hierlinger for performing computational calculations in Section 3.1.2, and to Richard James for performing calculations for Sections 3.2.2 and 4.2.2.4. With the development of high-performance computing and the availability of these techniques becoming more widespread, computational analysis has become a staple in the study of DSSCs. Features of dyes such as energy levels, locations of the HOMO and LUMO and charge transfer properties can be calculated, and therefore the driving forces within a device can be predicted.^{6,7} Since large structures can be computationally expensive to model, large amounts of time and resources must be used. So, to study the range of complex dye molecules for DSSCs, the less computationally expensive density functional theory (DFT) is employed. This produces isodensity plots that overlay the expected electron densities on a molecule. For charge transfer mechanisms within DSSCs, time dependent density functional theory (TDDFT) can also be used to calculate the energies of electronic transitions within the dye molecule in question. By assigning these transitions to experimentally obtained spectra, further information about the behaviour of the dye molecule under irradiation can be obtained. Additionally, the relative contribution of each electronic transition can be ascertained to provide information about the type of molecular transitions to be expected within the molecule. Use of the B3LYP hybrid functional is one of the most used methods of calculating these transitions, as they are less likely to underestimate the energy of the 'charge transfer' transitions compared to a pure Hartree-Fock or DFT calculation.⁸⁻¹¹

2.4 Morphological Characterisation

2.4.1 SEM and EDS

Scanning electron microscopy (SEM) is a technique used to analyse the physical properties and morphology of materials with a resolution of up to 1 nm.¹² To probe the surface, an electron beam is scanned across the surface, and the interactions between these electrons and the material are detected and processed. The beam is produced by applying voltage through a filament, and then extracting the electrons by accelerating them towards an anode. They are then focussed using magnets to produce the scanning probe. Figure 12 highlights just some of the interactions that the material undergoes upon bombardment by the scanning beam. As the electron beam hits the surface, they are either reflected, absorbed, or interact with the sample's atoms. Secondary electron imaging is the most common imaging process and is therefore known as the standard detection mode. In this mode, the microscope can produce images of high resolution (up to 1 nm for some microscopes) of the samples surface, which is achieved by the collection

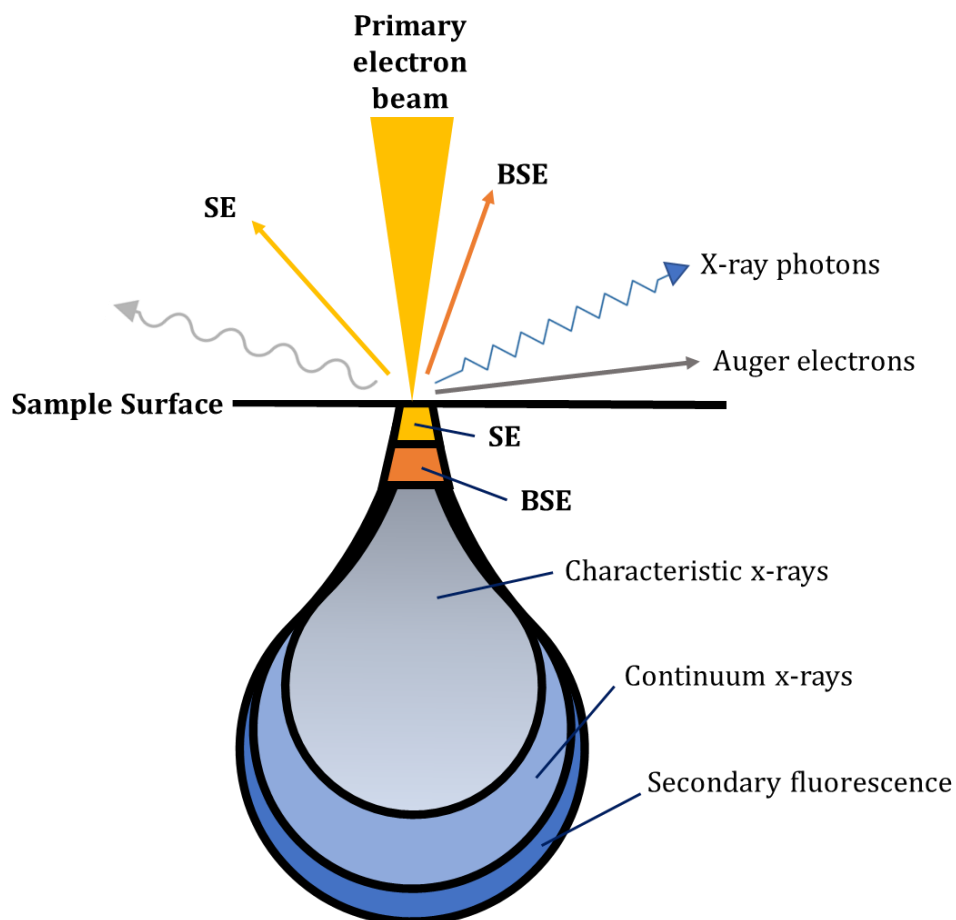


Figure 12: Cross sectional representation of electron interactions within a material during SEM.

of low-energy electrons ejected from atoms within the sample. The low energy of these electrons means that they cannot escape from anywhere but the very surface of the sample and are localised to the point of the electron beam. Those that are reflected via elastic scattering are referred to as back scattered electrons (BSE) and are of much higher energy than the secondary electrons. Since they are higher energy, they can emerge from deeper within the sample and across a broader area, therefore detection of these electrons is at lower resolution.

If the electron beam manages to remove an inner-shell electron from an atom in the sample, then a higher energy electron may move down and take its place, emitting a characteristic X-ray (known as the Auger effect). EDS (energy-dispersive X-ray spectroscopy) is a measurement of the relative abundance of these emitted X-rays versus their energy. A specialised solid-state detector absorbs the X-rays and eventually converts them to a voltage measurement. The relative energies of each element of the sample (all of which will release X-rays of varying wavelengths) produce a spectrum that can be analysed to determine a materials' elemental composition.

2.4.2 *p*-XRD

Powder X-ray diffraction is a branch of X-ray crystallography that explores the material compositions of powders or microcrystals. Samples are placed into a diffractometer, which directs X rays towards the powder. The beam is then either reflected from the surface or will enter the lattice to be diffracted from atoms within the sample. The diffracted waves are detected by the instrument and form a diffraction pattern in accordance with the spacing between atoms in the sample. Braggs law describes the interactions between the source radiation and the relative positions of the atoms, and can be summarised as thus:

$$n\lambda = 2d \sin \theta$$

for atoms arranged with a separation distance d , the diffracted waves will interfere constructively only when the difference in path length ($2d\sin\theta$) is equal to a multiple of the wavelength. These interactions will produce maxima in the diffraction pattern.

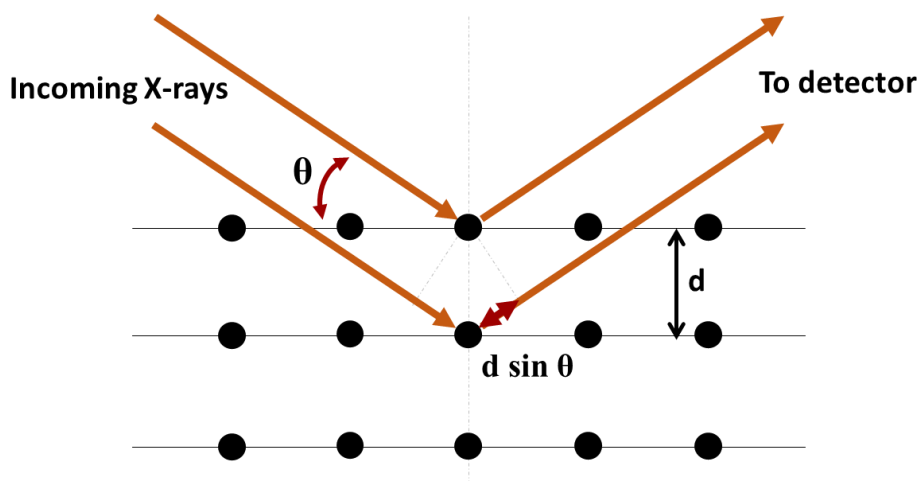


Figure 13: Representation of the interaction of X-rays within a crystal lattice, incident at angle θ .

Conversely, any points where the diffracted x-rays are out of phase will result in destructive interference and a decrease in intensity in the resulting diffraction pattern.

Powdered samples are considered theoretically as isotropic systems, meaning that statistically all orientations of the crystalline phase of the material are represented equally in a randomised sample. However, in practice the powder is often rotated inside the diffractometer to overcome any imbalance and represents equally all orientations within the sample. This rotational averaging results in a series of diffraction rings around the beam axis collected by the detector, the angle of which is denoted as the scattering angle, 2θ . Fourier transformation of the acquired signals allows us to describe the three-dimensional structure of the crystals in a single dimension, providing a trace that describes the material structure as a function of intensity against scattering angle. Databases of structural data facilitate the comparison of results against established control samples to allow for the identification and quantification of results.

2.5 General Procedures

As each chapter in this thesis focusses on a different area of DSSC or QDSSC development, specific experimental techniques for each section are found at the end of the relevant chapter. However, there are many techniques that overlap between most chapters, and so are summarised below.

2.5.1 Preparation of glass substrates

Blank FTO glass substrates (Pilkington TEC 15 for working, TEC 8 for counter) were prepared by first cutting to size (18 x 15 mm) followed by cleaning in an ultrasonic bath with soapy water, 0.1 M HCl in ethanol, and lastly ethanol only. After cleaning, the glass surface was treated with ozone (using a Novascan PSD Series Digital UV Ozone System) for 15 minutes before application of the electrode material.

2.5.2 Pt Counter electrode preparation

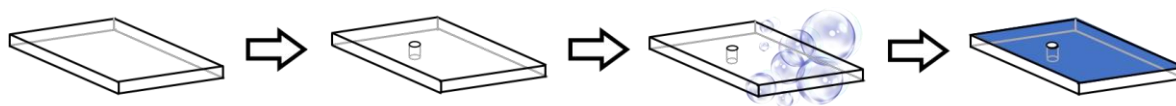


Figure 14: Steps for the preparation of a platinised counter electrode; 1) cutting glass, 2) drilling the hole 3) washing the substrate and 4) deposition of Pt.

Counter electrodes were prepared by drilling a small hole (approximately 1 mm \emptyset) into the substrate before cleaning to allow for electrolyte to be added post-assembly. Platisol-T solution (0.2 mL cm⁻², SOLARONIX) was added dropwise to the conductive surface of the glass and annealed at 450 °C for 15 minutes in a Nabertherm B150 Chemical Oven to give a platinised counter electrode.

2.5.3 TiO₂ film preparation

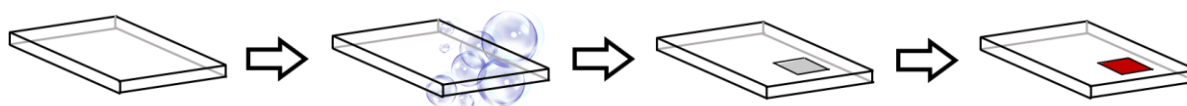


Figure 15: Preparation of a sensitised semiconductor film for DSSCs; 1) cutting glass, 2) washing the substrate, 3) deposition of semiconductor and 4) sensitisation of film with dye.

TiO₂ films were prepared by a doctor blading method in which a transparent TiO₂ paste (DSL 18NR-T, Dyesol) was deposited by spreading with a glass rod. Masks to determine thickness and film size (0.25 cm²) were made using Scotch Magic Tape. The films were dried by heating to 80 °C on a hotplate for 5 minutes, and the procedure repeated until the desired number of layers were achieved. Alternatively, a screen printing methodology can be used to deposit these layers, as described below in section 2.5.4.

2.5.4 NiO film preparation

Several methodologies have been developed during the course of this thesis for the investigation of NiO thin films, but the following two are those used predominantly. Each method was chosen for its suitability for the context of each study.

Method 1: Sol gel NiO precursor was prepared by dissolving anhydrous NiCl₂ (1 g) and a tri-block co-polymer, F108 (poly(ethylene glycol)-block-poly(propylene glycol)-block-poly(ethylene glycol)) (1 g) in a mix of EtOH (6 ml) and deionised water (5 ml). The solution is left to age for 14 days and centrifuged to remove remaining solids before use. To prepare the electrodes, the doctor blade method was used to apply the precursor solution over a Scotch Magic tape spacer to form films with an active area of 0.2 cm². The films were sintered in a Nabertherm B150 Chemical Oven in air at 450 °C for 30 minutes, and the process is repeated using additional layers of precursor solution to increase layer thickness, giving 3-layer NiO films with an average thickness of 1.2 μm (measured with Dektak³ST Surface Profile Measuring System).

Method 2: Screen-printing is a technique completed by a mesh used to transfer material onto a substrate, except in areas made impermeable by the blocking stencil. The stencil was designed to produce a grid of 6 x 6 films. The screen printer is an effective tool to produce multiple thin films at a time. It requires greater quantities of material from the onset but produces less waste. A commercial paste of NiO (Solaronix) was used to screen print NiO films onto conductive substrates. The substrates are cut to a grid of 6 x 6 pieces before printing. In short, a blade or squeegee is moved across the screen (73 thread mesh) to fill the open apertures with paste, and a second, firm stroke of the squeegee deposits the material. Once the films are deposited, the grids are kept in an atmosphere of ethanol for 5 minutes to allow the film to flatten, before drying on a hotplate at 80 °C for 5 minutes. This process was repeated until the required number of layers were

deposited. The films were then sintered in a Nabertherm B150 Chemical Oven in air at 450 °C for 30 minutes.

2.5.5 Liquid-junction device assembly

The as-prepared counter electrode and photocathode are sandwiched together using a thermoplastic frame (Surlyn, 60 μm thickness) as a spacer. Liquid electrolytes were introduced into the device via vacuum backfilling through the pre-drilled hole. Another Surlyn piece and a glass cover slip were then used to seal the cell.

2.6 References

- 1 A. Hagfeldt, G. Boschloo, L. Sun, L. Kloo and H. Pettersson, *Chem. Rev.*, 2010, **110**, 6595–6663.
- 2 H. Choi, T. Hwang, S. Lee, S. Nam, J. Kang, B. Lee and B. Park, *J. Power Sources*, 2015, **274**, 937–942.
- 3 F. Odobel, Y. Pellegrin, E. A. Gibson, A. Hagfeldt, A. L. Smeigh and L. Hammarström, *Coord. Chem. Rev.*, 2012, 256, 2414–2423.
- 4 A. D. S. Gonçalves, M. R. Davolos, N. Masaki, S. Yanagida, S. Mori and A. F. Nogueira, *J. Appl. Phys.*, 2009, **106**, 10803–10807.
- 5 A. Listorti, B. O'Regan and J. R. Durrant, *Chem. Mater.*, 2011, 23, 3381–3399.
- 6 P. Salvatori, G. Marotta, A. Cinti, C. Anselmi, E. Mosconi and F. De Angelis, *J. Phys. Chem. C*, 2013, **117**, 3874–3887.
- 7 D. Alonso-Álvarez, T. Wilson, P. Pearce, M. Führer, D. Farrell and N. Ekins-Daukes, *J. Comput. Electron.*, 2018, **17**, 1099–1123.
- 8 S. Karamshuk, S. Caramori, N. Manfredi, M. Salamone, R. Ruffo, S. Carli, C. A. Bignozzi and A. Abbotto, *Energies*, 2016, **9**, 1–10.
- 9 Y. Derin, R. F. Yilmaz, İ. H. Baydilek, V. E. Atalay, A. Özdemir and A. Tutar, *Inorganica Chim. Acta*, 2018, **482**, 130–135.
- 10 M. K. Nazeeruddin, F. De Angelis, S. Fantacci, A. Selloni, G. Viscardi, P. Liska, S. Ito, B. Takeru and M. Grätzel, *Renew. Energy Four Vol. Set*, 2018, **2–4**, 227–251.
- 11 A. K. Pal, D. B. Cordes, A. M. Z. Slawin, C. Momblona, E. Ortí, I. D. W. Samuel, H. J. Bolink and E. Zysman-Colman, *Inorg. Chem.*, 2016, **55**, 10361–10376.
- 12 J. Liu and J. M. Cowley, *Ultramicroscopy*, 1993, **52**, 335–346.

Chapter 3 Alternative Sensitisers for DSSC

The absorption and subsequent conversion of solar energy into electrical potential is the foundation of PV technologies. What makes DSSCs unique is the depth and range of sensitisers available for exploitation. As developments are continuously arising to this end, projects were undertaken to explore and become familiar with the vastness of the field. In section 3.1, a panchromatically absorbing iridium complex is integrated into TiO₂ DSSC and optimised to produce devices with ~0.5 % efficiency. While this is a low output compared to established ruthenium-based sensitisers for n-DSSC, the primary concern during this study was the use of rare metals in what should be a sustainable technology. Section 3.2 addresses this with the use of sensitisers derived from natural products. Optimised TiO₂ DSSC sensitised with dye extracts from a native species of Peruvian prickly pear and stabilised with citric acid produced efficiencies of over 2 %.

3.1 A Panchromatic Iridium complex for near IR absorbance in n-DSSC

With thanks to Claus Hierlinger of the University of St Andrews for providing the as synthesised and characterised complex **1**. Device preparation, optimisation and characterisation were performed by the author of this thesis.

3.1.1 Background

After the publication of the landmark DSSC paper in 1991, ¹ ruthenium complexes as sensitisers largely dominated the dye landscape. Their broad absorption and long excited state lifetimes have highlighted their suitability as photosensitisers. By modifying the ligand structure surrounding the metal centre, these properties of the complex can be tuned to fit specification. This concept has been thoroughly investigated for ruthenium-based complexes, ²⁻⁴ and the record for the efficiency of devices containing ruthenium sensitisers has surpassed 10 %, allowing them to be upscaled and trialled in commercial settings. ⁵

These investigations have highlighted that increased separation distance of the dye from the semiconductor surface limits charge recombination pathways. However, dyes (such as cyclometalated ruthenium complexes) that have injecting excited states with MLCT (metal to ligand charge transfer) character have their injection efficiencies reduced as they are further separated from the surface. ^{6,7} Iridium dyes have been shown to use majority LLCT (ligand to ligand charge transfer) pathways to transfer electrons from the excited dye to TiO₂. ⁸ Because of this, dyes can be still effectively distanced from the surface while maintaining charge injection efficiency, thereby reducing recombination between the dye and surface. ⁹

Iridium (III) complexes are commonly used as high-performance emitters in electroluminescent devices. Due to the cyclometallating ligands around the third-row metal ion, spin orbit coupling between the singlet and triplet excited states results in reducing the Stokes shifts between the absorption and emission bands of the complex. Iridium (III) complexes also boast good stability and reduced access to MLCT states. These properties lend themselves to the application of these complexes as photo-reductants, sensors, biological labelling agents, and photovoltaic devices. ¹⁰ Yet, iridium complexes have previously not performed well in DSSCs. The performance of iridium devices is very low in comparison to the established 11.18 % for ruthenium complexes.

¹¹ This is primarily because most iridium (III) complexes are not panchromatic, having absorption spectra that tail off by 550 nm. This produces low short circuit currents in DSSCs and consequently poor overall efficiencies.

The first application of iridium complexes in DSSCs was by Gray et al. in 2006.¹⁰ They reported results for two representative iridium (III)dyes; $[\text{Ir}(\text{ppz})_2(\text{dcbpy})]^+$ (**a**) and $[\text{Ir}(\text{ppz})_2(\text{dcbq})]^+$ (**b**) (where ppz=phenylpyrazolyl, dcbpy = 4,4'-dicarboxybipyridine and dcbq = 4,4'-dicarboxy-2,2'-biquinoline) with PF_6^- counterions. Both dyes were shown to exhibit LLCT from the cyclometalating ligand to the bipyridine or biquinoline ligands by investigating their weak absorption band in the visible region using density functional theory (DFT). Additionally, the complexes had both ground-state formal reduction potentials (E'_{D/D^-}) that were sufficiently positive to oxidize the I_3^-/I^- redox couple, and excited-state formal reduction potentials ($E'_{\text{D}^*/\text{D}^-}$) similar to the ruthenium analogue. This indicated them as ideal dyes for injection into TiO_2 . Both gave reasonable performances compared to the ruthenium analogue $[\text{Ru}(\text{ppz})_2(\text{dcbpy})]^{2+}$ (with efficiencies of 0.65, 0.5 and 1 % for dyes **a**, **b** and the Ru analogue respectively) and demonstrated the use of iridium (III) complexes and solar converters using LLCT state injection. The authors argued that these kinds of complexes could be synergised with other dyes that use MLCT injection pathways for a dual-sensitised device.

Further development of the complexes focussed on two pathways: spatial separation of the dye from the semiconductor, and extension of the absorption spectrum beyond the visible region. Baranoff et al. began to investigate spatial separation of the dye using a series of complexes with bipyridine ancillary ligands, two of which were extended with a carboxy-styrene moiety (**c** and **d**).¹² They found that extending the anchoring groups so that the dye was separated from the surface increased V_{oc} but cut the current output drastically. Keeping the more efficient of the two anchoring ligands, the phenyl-pyridine ligand was modified as in structure **e**. This reduced the overall voltage with little change in current. A new dye (**f**) with extended absorption up to 900 nm (compared to 600 nm for structure **e**) was prepared and gave greatly increased performance, with the device spectral response extending past 550 nm and efficiency reaching 1.87 %. Extension of the dye spectral response was concluded to be imperative for improving device output.

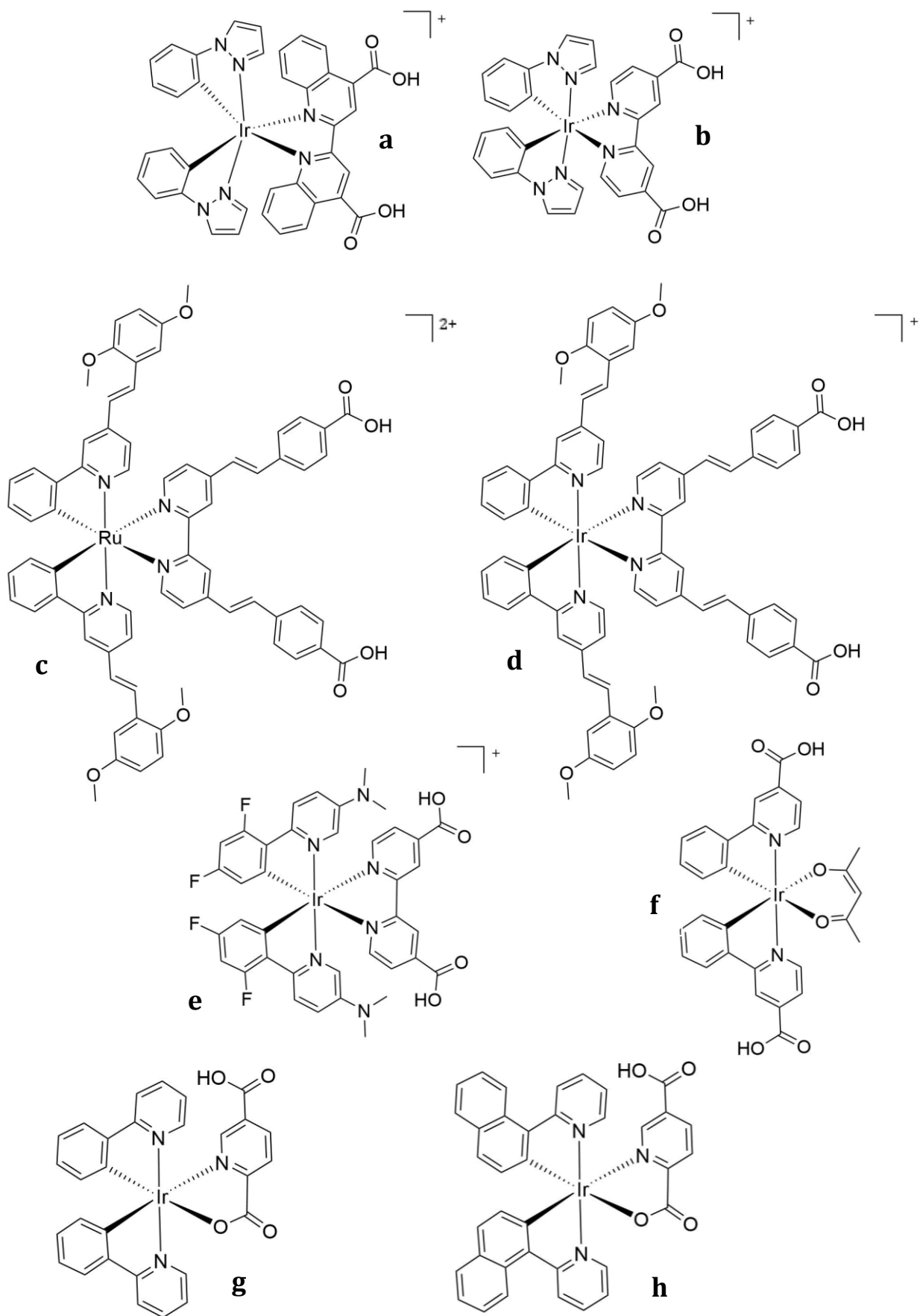


Figure 1: Structures of dyes **a-h** discussed in this section. ^{10,12,13}

Concurrently, work was released by Ning et al. describing iridium (III) dyes containing carboxyl pyridine ligands (**g** and **h**). The device spectral responses extended to 600nm and gave reasonable performances of almost 2 %.¹³ Dye **g** had much higher V_{oc} compared to that of **h**, which was thought to be due to the compact structure of **g**, allowing for greater dye loading on the TiO_2 surface. Since increased coverage of the electrode can reduce charge recombination between the electrolyte and semiconductor, a co-adsorbent, deoxycholic acid, was used to fill in the gaps. For dye **h**, a small increase in voltage was achieved, yet overall efficiency did not change markedly. In comparison, competition with the deoxycholic acid meant that device performance for **g** decreased.

A recurrent theme in these findings is that the relationship between a complex's structural features and final device performance should be carefully considered in dye choice for PV applications. In 2014, Yuan et al. investigated light-harvesting iridium (III) complexes in the context of hydrogen photogeneration, as well as applied to DSSCs.¹⁴ By keeping the 2,2'-bipyridine-4,4'-dicarboxylate binding ligand constant and modifying the substitution of the ancillary ligand skeleton, structure-activity relationships were established. The 2-phenylbenzothiazole skeleton provides an extended π -conjugation length and boasts high chemical and photophysical stability in comparison with conventional phenylpyridine, so was an ideal candidate for the study. The addition of trifluoromethyl (CF_3) groups (as in dyes **i1**, **i2**, **i4** and **i5**) increases electrophilicity, resulting in a small shift in absorption. When this group is situated on the phenyl moiety, as in **i1** and **i2**, this is a 10 nm red shift; however, when located at the 5-position of the benzothiazole ring, as in **i4**, it leads to a blue-shift. Dye **i5** has a completely different absorption profile to the rest of the series with an intense band at 438 nm, which was thought to arise from LLCT between the amino-substituted ancillary ligand to the binding ligand. The electronic effects of the CF_3 substituent also increases the complex's oxidation potentials due to decreased electron density around the metal centre. In devices, complexes **i2** and **i5** performed well but were surpassed by **i3**. The higher HOMO of dyes **i3** and **i5** allowed for improved regeneration of the oxidised dye and therefore increased current output, while the rest of the series' electronegative CF_3 groups acted as a hindrance to electron transfer from the dye to the TiO_2 surface. **i5**'s performance was improved by its increased spectral response compared the rest of the series, but poor dye

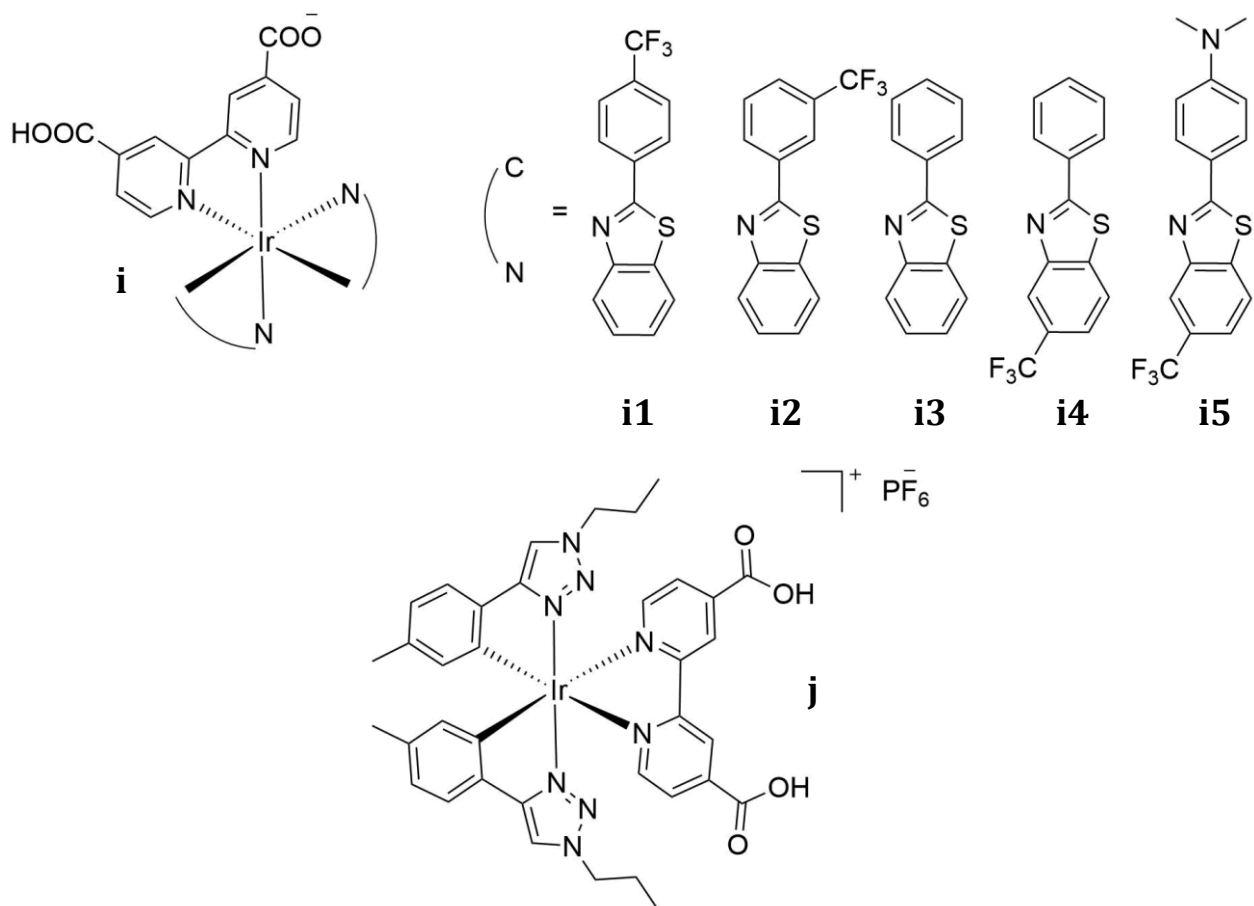


Figure 2: Structures of dyes **i** and **j** discussed in this section, as well as the ligands used for the variations to dye **i**.^{14,15}

loading compared to **i3**, which was sterically smaller and more compact, limited the devices light-harvesting capability.

The most recent work on these complexes in TiO₂ DSSCs was released in 2017 by Sinopoli et al. The groups' series of iridium (III), biscyclometalated aryltriazole complexes utilised the high energy triazole moiety to help localise the LUMO of the complex onto the binding ligand.¹⁵ The ligands were also argued to be easy to make or sourced from readily available feedstocks. However, the absorption spectra of the dyes were comparatively blue shifted compared to previously reported complexes, and the most successful of the series, dye **j**, gave a reasonable efficiency of 0.6 %.

Compound	Reference	$J_{sc} / \text{mA cm}^{-2}$	V_{oc} / V	FF	$\eta / \%$
a	10	2.24	0.44	0.67	0.65
b	10	1.99	0.38	0.66	0.5
c	12	0.27	0.46	0.75	0.09
d	12	2.70	0.50	0.69	0.94
e	12	2.70	0.41	0.72	0.79
f	12	4.30	0.59	0.74	1.87
g	13	6.31	0.55	0.53	1.84
h	13	6.53	0.48	0.55	1.77
I1	14	2.26	0.50	0.73	0.82
I2	14	2.23	0.51	0.72	1.76
I3	14	3.72	0.50	0.74	1.39
I4	14	2.35	0.49	0.72	0.82
I5	14	3.02	0.49	0.74	1.09
j	15	2.40	0.43	0.60	0.62

Table 1: Parameters of n-type devices constructed using dyes discussed in this section.

Iridium (III) complexes had also been briefly investigated for p-type devices by the same group, as applied to NiO DSSCs. Since one focus on the development of dyes for p-type is the lengthening of the charge separated state, the intrinsic CT excited state character of the heteroleptic iridium (III) complexes makes them a possible candidate. The dye was designed with the detrimental recombination of the injected hole with the excited electron in mind. To prevent this process, the carboxylate anchoring groups were placed on the electron donating aryl groups. This means that the anionic anchoring group, the region closest to the NiO surface, has a localised HOMO surrounding it, allowing for efficient hole injection to its valence band. Combining this with a

Compound	Reference	$J_{sc} / \text{mA cm}^{-2}$	V_{oc} / V	FF	$\eta / \%$
k	16	1.12	0.10	0.37	0.043
l	17	0.14	0.35	0.44	0.021
m	17	0.25	0.51	0.54	0.068
n	17	0.37	0.38	0.44	0.061

Table 2: Parameters of p-type devices constructed using dyes discussed in this section.

neutral electron accepting ancillary ligand, trans to the anchoring aryl carboxylate rings, localises the LUMO away from the anchoring groups, maximising the necessary charge separation. Absorption of dye **k** stretched to 550 nm and produced an efficiency of 0.043 % when tested in p-type devices. This is significantly lower than performance of n-type devices, which is expected. Compared to the work by Gennari et al. in p-type devices two years before, the performance falls short again. While the newer paper used an iodine-based electrolyte in their devices, the French group managed to utilise dyes with longer charge-separated states, which enabled the use of a Co (II)/(III) redox couple.¹⁷ Cobalt redox electrolytes are sometimes slow to accept electrons due to their lower diffusion coefficients, but devices containing them have the benefit of a greatly increased open-circuit voltage. This factor led to large V_{oc} up to 508 mV, and therefore the better performance of this series. Low J_{sc} values were attributed to reduced light harvesting, since the series did not absorb very far into the visible region. It was noted that through the series of **l**, **m** and **n**, as the maximum absorption wavelength increased, J_{sc} increased also.

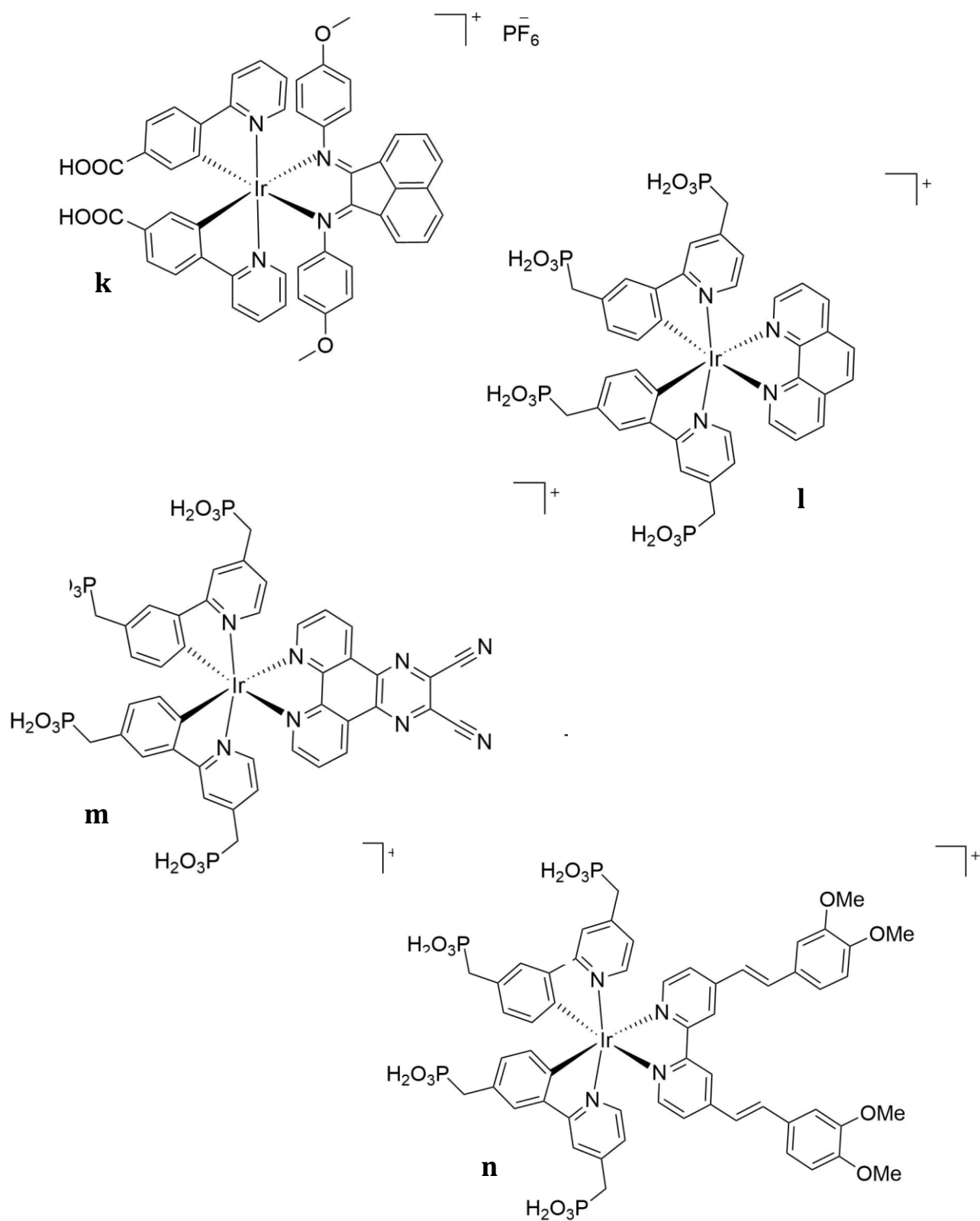


Figure 3: Structures of dyes **k** to **n** discussed in this section. ^{16,17}

It is clear that a sufficiently red shifted, iridium (III) complex with extended charge separated state is required to unify the findings of the literature and consolidate our understanding of the chemistry of these dyes in DSSCs.

The work in this section describes the PV performance of an iridium (III) complex containing both a previously reported tripodal C[^]N[^]C ligand, 2-benzhydrylpyridine,¹⁸ and an electron-poor ancillary ligand in diethyl [2,2'-bipyridine]-4,4'-dicarboxylate (deeb). The C[^]N[^]C ligand coordinates to iridium, forming three six-membered chelate rings through a double C–H bond activation, while combination with the bidentate diimine ligand produces an orange-to-red emitting complex. The complex was simple to synthesise and boasted panchromatic absorption up to 650 nm. The electron withdrawing capacity of the anchoring ligand lends itself to the transfer of electrons to the semiconductor, so this dye was used in n-type, TiO₂ based devices.

3.1.2 Results

Ligand **L1**¹⁸ and diethyl [2,2'-bipyridine]-4,4'-dicarboxylate (deeb)¹⁹ were prepared using reported methods as shown in Figure 4. A two-step, one pot method was employed to obtain **Complex 1**, wherein a mixture of L1 and IrCl₃.H₂O in 2-ethoxyethanol/H₂O (3:1) was heated to reflux for 19 hours, after which, deeb was added and the reaction left for a further 6 hours (shown in Figure 4). Complex **1** was obtained with 52% yield as a black solid, and characterised by ¹H and ¹³C NMR spectroscopy, HR-ESI mass spectrometry, elemental analysis and melting point determination.

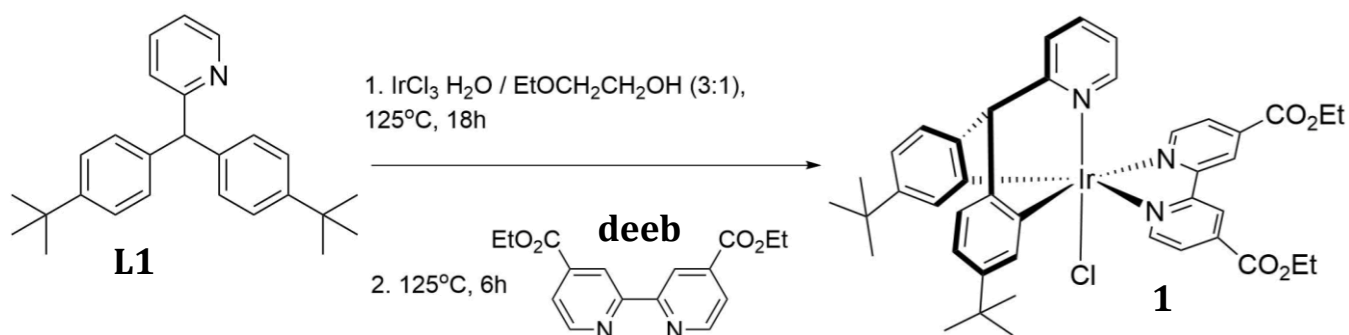


Figure 4: Reaction scheme for the synthesis of complex **1**.

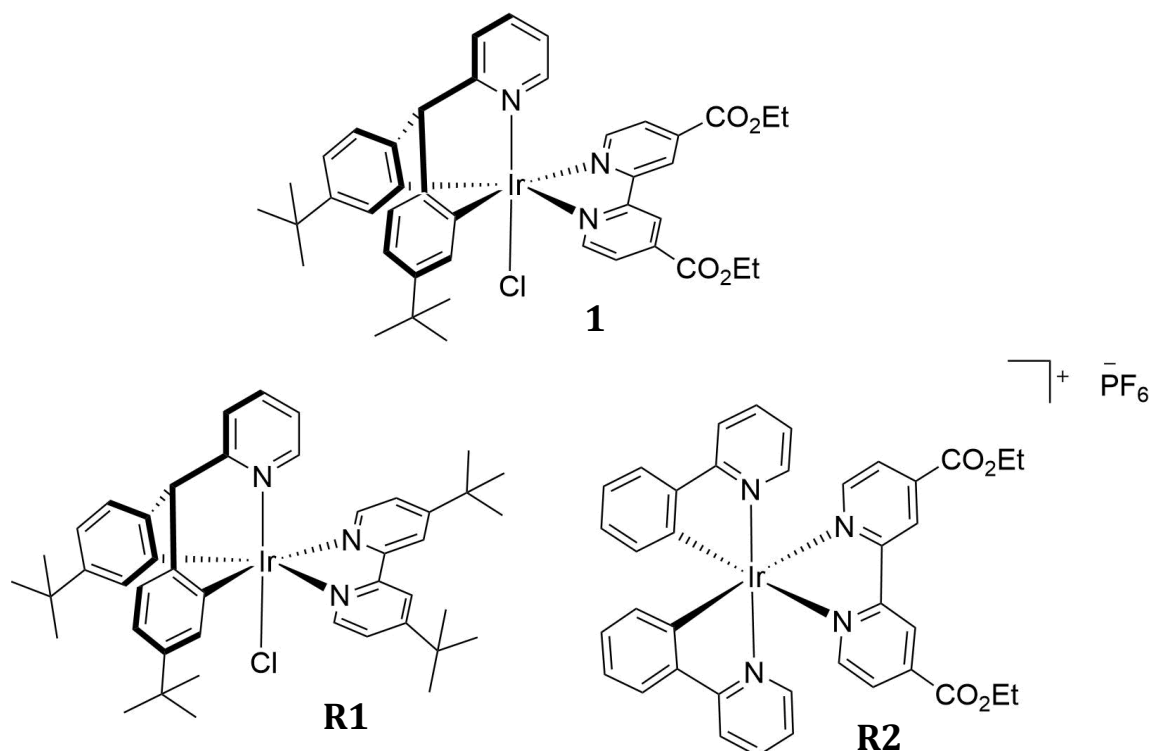


Figure 5: Structure of complex **1**, as well as the reference complexes **R1** and **R2** discussed in this section.

Structural morphology was determined via single-crystal X-ray diffraction, which showed that the pyridyl ring of L1, iridium (III) center, and chloride were all aligned directly along a mirror plane through the complex. The electrochemical properties of **1** were established via cyclic voltammetry (CV) and differential pulse voltammetry (DPV). The properties of reference complexes **R1** ($[\text{Ir}(\text{L1})(\text{dtBubpy})\text{Cl}]$) and **R2** ($[\text{Ir}(\text{ppy})_2(\text{deeb})]\text{PF}_6$) were also considered to establish the contribution of the **L1** or the deeb ligand respectively. The data is shown in Table 3, complex **1** exhibits a quasi-reversible single electron oxidation wave at 1.21 V, which stems from the Ir (III)/Ir (IV) redox couple, with contributions from both the two phenyl rings of **L1** and the chloride. Compared to **R1** ($E_{\text{D}/\text{D}^+} = 1.04$ V vs. NHE),¹⁸ the oxidation potential of **1** is shifted anodically by 170 mV, which highlights the change in electron density on the iridium centre upon inclusion of the electron withdrawing ethyl ester groups of the deeb ligand. However, this oxidation potential is lower than that of **R2** ($E_{\text{D}^*/\text{D}^-} = 1.57$ V in deaerated MeCN vs NHE, where ppy is 2-phenylpyridinato).²⁰

	$E_{1/2}^{\text{ox}}$	ΔE_p	$E_{1/2}^{\text{red}}$	ΔE_p	ΔE	E_{HOMO} (eV)	E_{LUMO} (eV)
1	1.21	88	-0.97	99	2.18	-5.31	-3.13

Table 3: Selected electrochemical properties of complex **1** in degassed CH_2Cl_2 solution at 298 K at a scan rate of 100 mV s^{-1} using Fc/Fc^+ as the internal reference and referenced with respect to NHE (0.70 V vs. NHE).

Complex **1** shows a single quasi-reversible reduction wave at -0.94 V upon scanning to negative potentials. Upon comparison to **R1** ($E_{\text{D}/\text{D}^+} = -1.58 \text{ V vs NHE}$), an anodic shift of 610 mV by the reduction wave can be attributed to the electron-withdrawing nature of the ethyl ester groups on the anchoring ligand. To establish the impact of the deeb ligand on the reduction potential, the properties of the **R2** complex were analysed. **R2** showed two reversible reduction waves; the first, assigned to the reduction of the deeb ligand at -0.76 V, and the second at -1.30 V from the reduction of the phenylpyridinato group. The reduction of the deeb ligand in **1** is cathodically shifted by 210 mV compared to the same ligand reduction in **R2**.

DFT calculations were performed by C. Hierlinger. Kohn-Sham electron density plots of **R1** indicate that both the HOMO and HOMO-1 are both close in energy and involve the iridium centre, chloride, and the two phenyl rings of **L1**.¹⁸ As can be seen in Figure 6, the same electron density distribution is found in **1**. It was also shown that in **1**, that the three lowest unoccupied orbitals are exclusively localized on the deeb ligand, while in **R1** the LUMO+1 is found primarily on the pyridyl of **L1**. This highlights the stronger accepting character of the deeb anchor. From estimates for the relative energy levels of the dye, both charge injection from the excited dye into TiO_2 and regeneration by the electrolyte are thermodynamically favourable.

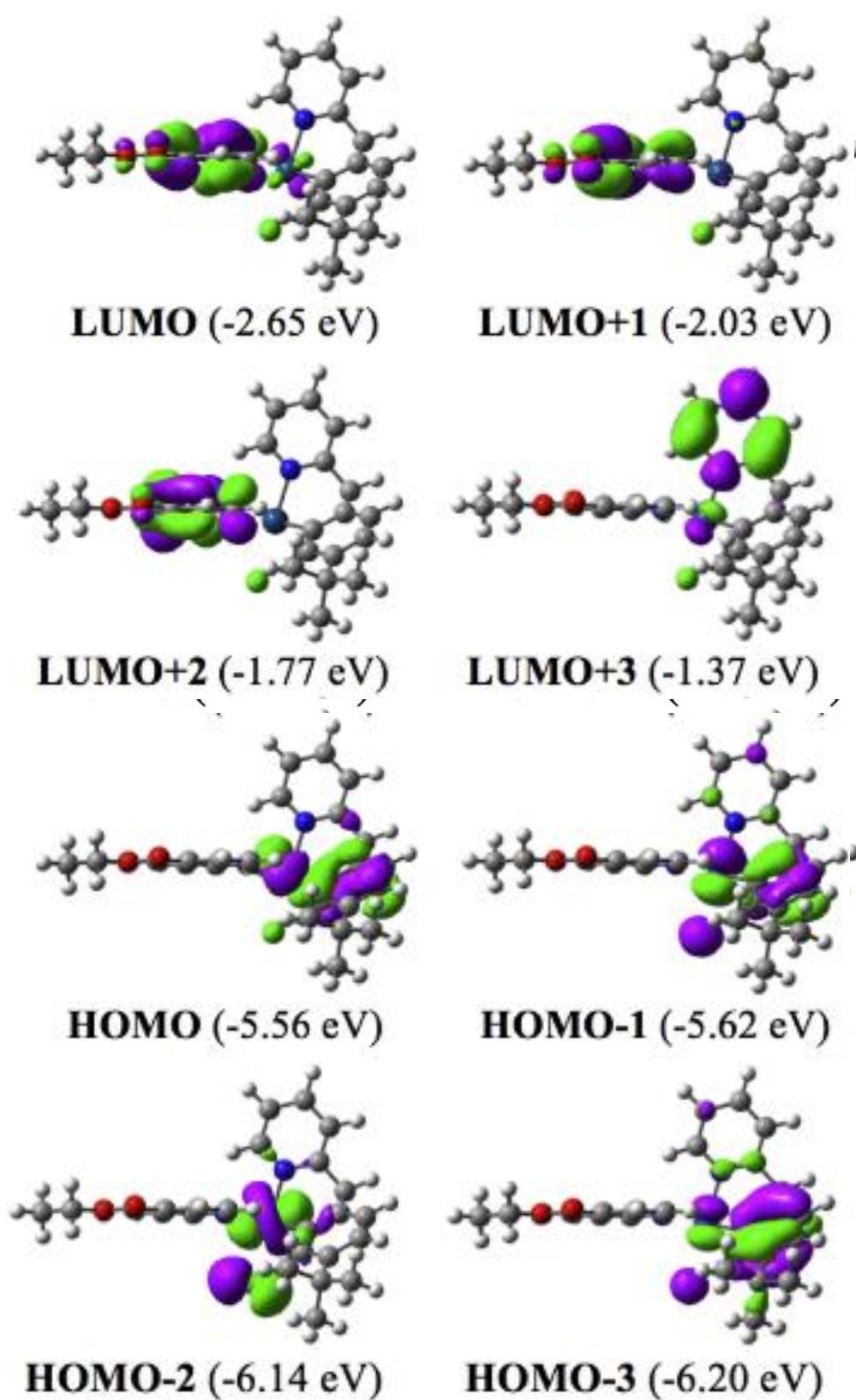


Figure 6: Calculated molecular orbitals of 1 computed via DFT (M06 functional, see Section 3.3 for details) and represented using a contour threshold of 0.03 au.

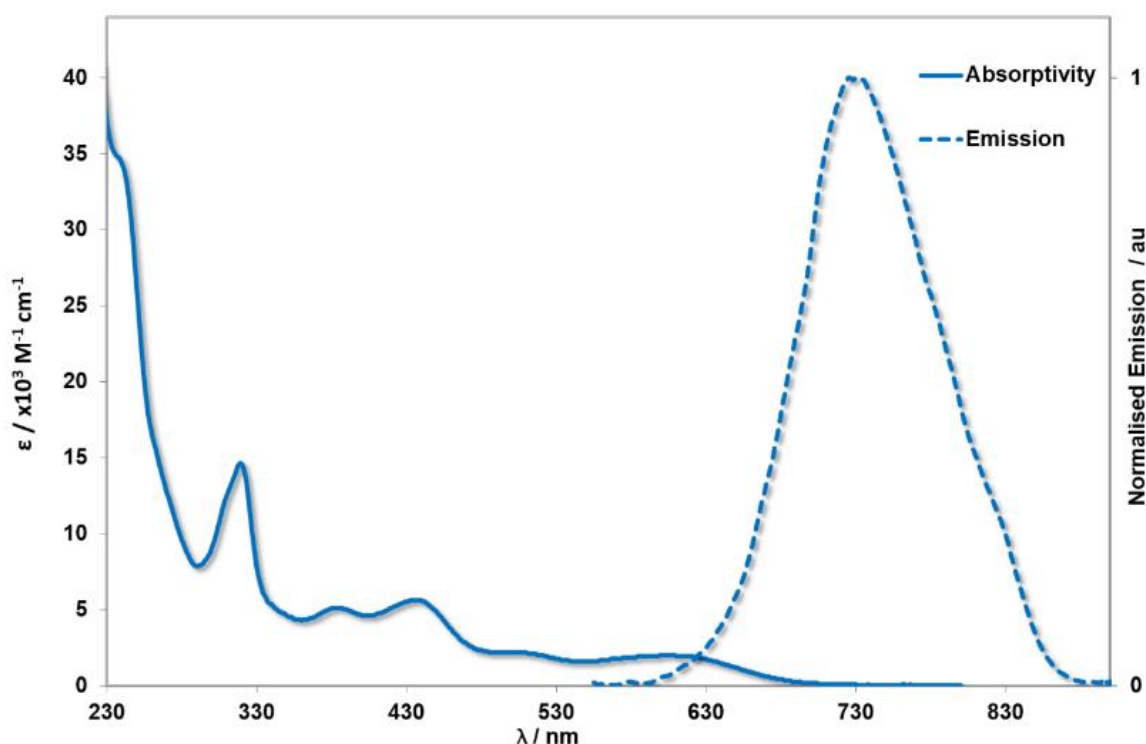


Figure 7: The absorptivity (solid line) and photoluminescence spectra (dotted line) of **1** in CH_2Cl_2 at 298 K. Reproduced from Paper 1.

Photophysical measurements of **1** in CH_2Cl_2 were performed and assignments were confirmed by TD-DFT calculations. The absorbance spectrum of **1** shows intense high-energy bands below 250 nm, which are assigned to ligand-centred transitions localized on the deeb ligand. The next, moderately intense band at 319 nm shows a ligand-centred (LC) excitation from a low-lying orbital on the deeb, with small CT character towards the LUMO, which is also centred on the deeb. Weaker bands between 380–440 nm and tailing off through 500–600 nm can be attributed to a mixture of MLCT and LLCT transitions involving the deeb ligand. The two lowest computed single states at 623 and 611 nm correspond respectively to both the HOMO-1 to LUMO and HOMO to LUMO transitions. Figure 6 illustrates these transitions as mixed CT processes from the metal and the phenyl rings of the $\text{C}^{\wedge}\text{N}^{\wedge}\text{C}$ ligand towards the deeb. TD-DFT also predicted significant vertical absorption peaks at 496 nm, 456 nm and 443 nm, and assigned to HOMO-2 to LUMO, HOMO to LUMO+1 and HOMO-1 to LUMO+1 transitions respectively. All of these transitions are seen to involve intense CT character in the direction of the deeb moiety.

Additionally, complex **1** emits a broad, featureless profile with a maximum at 731 nm upon photoexcitation at 420 nm, indicative of an emission with mixed CT character. This is significantly redshifted in comparison to **R1** (which emits at 630 nm¹⁸) and **R2** (which emits at 680 nm²⁰), due to the presence of the electron accepting deeb ligand. The measured photoluminescence quantum yield (PL) of **1** is naturally lower than complexes **R1** and **R2**, with values of 0.5 %, 6 %, and 5 % respectively. The DFT calculations return an emission from the T1 state at 762 nm, close to the experimental value, which confirms emission from the lowest triplet excited state. Due to this triplet emission pathway, the dye boasts a long excited-state lifetime (~36 ns), which is hugely beneficial for application in devices.

Since the evidence provided overwhelmingly shows that the direction of electron transfer tends towards the deeb, then the effectiveness of the dye within an n-DSSC was investigated. Sandwich solar cells were assembled using sensitised nanocrystalline TiO₂ as the working electrode, platinized conducting glass as the counter electrode and iodide/triiodide redox couple (0.6 M TBAI, 0.03 M I₂, 0.1 M guanidinium thiocyanate and 0.5 M t-butyl pyridine) in acetonitrile as the electrolyte. More details are given in section 3.3. Since the complexes **R1** and **R2** were not available to the author, the benchmark ruthenium sensitiser N719 was used to determine **1**'s relative performance in devices.

Additionally, the TiO₂ photoanodes were optimised using both a TiCl₄ treatment and the addition of a scattering layer. TiCl₄ treatments are used to coat the glass substrate both before and after applying the TiO₂ semiconductor in order to prevent recombination between the electrolyte and FTO,^{21,22} while addition of a scattering layer can increase light harvesting and therefore increase performance.²³ Experimental details for these optimisations are given in section 3.3. The photocurrent density- photovoltage curves were analysed, and the resulting photovoltaic performances of solar cells based on **1** and **N719** are summarized in Table 4.

Dye	Film Treatment	J_{sc} / mA cm ⁻²	V_{oc} / V	FF	η / %
1	None	0.12	-0.594	0.617	0.04
1	Scattering	0.70	-0.67	0.75	0.35
1	TiCl ₄	0.41 x 10 ⁻⁴	-0.04	0.26	0.43 x 10 ⁻⁶
N719	None	6.05	-0.79	0.64	3.06
N719	Scattering	6.79	-0.772	0.59	3.13
N719	TiCl ₄	4.29	-0.811	0.69	2.43

Table 4: Photovoltaic parameters, including open circuit voltage (V_{oc}), short circuit current (J_{sc}), fill factor (FF) and efficiency (μ) of development devices using N719 and compound **1** and using two different film treatments; a **TiCl₄** based blocking layer applied both before and after film deposition, and a Ti-nanoxide **scattering** layer applied post TiO₂ deposition. Further experimental details can be found in Section 3.3.

The work by Ning et al. described earlier highlighted the addition of chenodeoxycholic acid (known as CDCA) as a co-adsorbant.¹³ Work by previous groups that included this molecule in both the dye absorption stage via the dye bath or through addition to the electrolyte found that the CDCA worked as an insulating layer on the TiO₂ surface and improved performance of devices using N719 sensitizers.²⁴ However, integrating CDCA in the optimisation experiments did not yield improved uptake or performance for complex **1**. For controlled comparison, no additives were added to either dye bath, so performance of the N719 DSSC will be naturally slightly lower than that typically obtained in fully optimized devices.

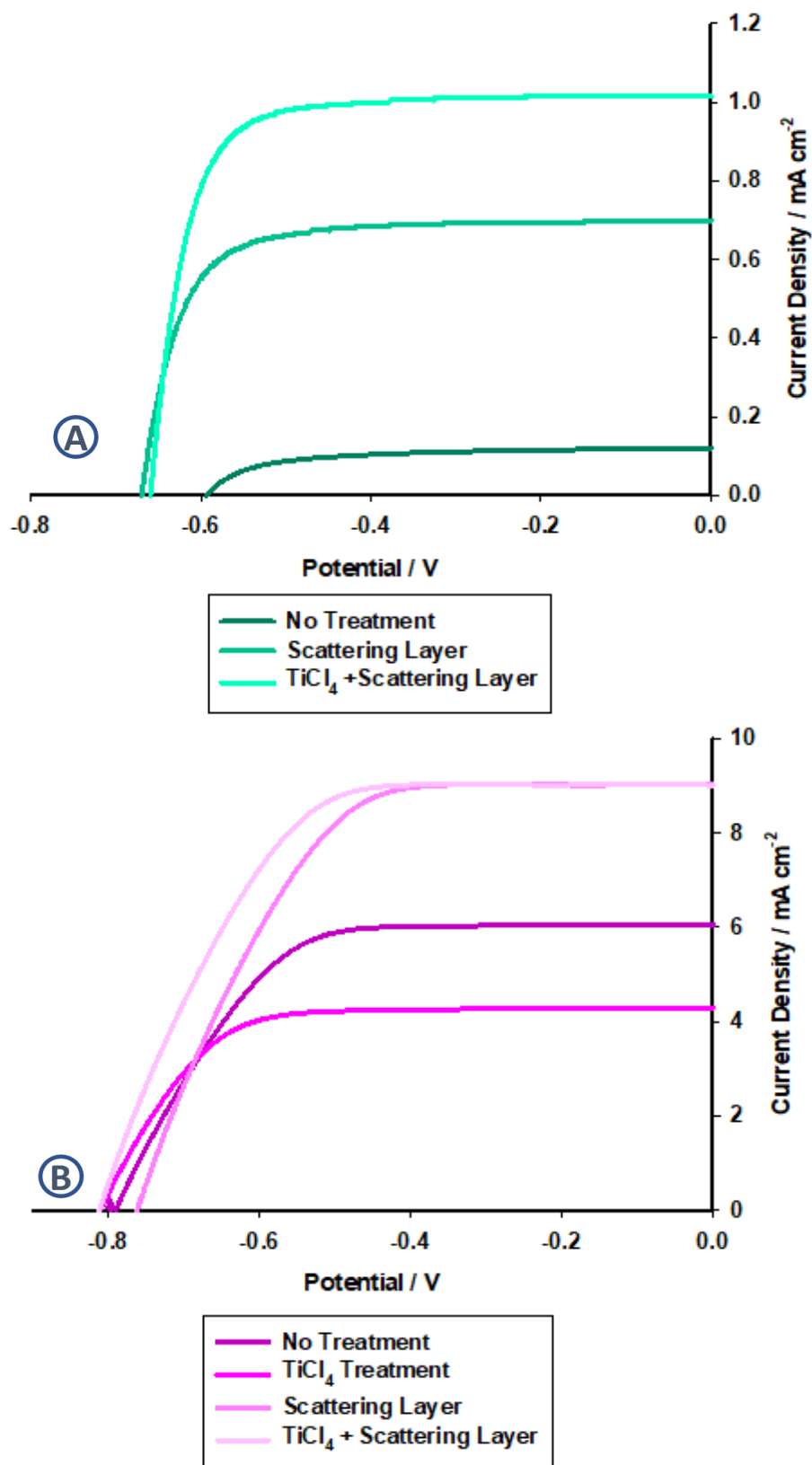


Figure 8: Current-voltage curves for DSSCs constructed using **a)** Ir complex 1 (green) and **b)** N719 (purple) dyes with various substrate configurations. Results for Iridium + TiCl₄ only were negligible and have been omitted. Electrolyte composition: 0.6 M TBAI, 0.03 M I₂, 0.1 M guanidinium thiocyanate and 0.5 M *t*-butyl pyridine in MeCN

Figure 8 shows the current–voltage characteristics of devices containing the dyes under AM 1.5 simulated sunlight (100 mW cm^{-2}). Preliminary, non-optimised devices using **1** gave low efficiency due to poor J_{sc} values. Interestingly, the V_{oc} values reached almost 0.6 V, roughly 20 % higher than all previously reported in the literature. Upon addition of the scattering layer, current and photovoltage for devices containing **1** increased by nearly tenfold. In contrast, the marginal increase in efficiency of **N719** devices upon addition of the scattering layer could highlight the poor light harvesting effect of **1**. The TiCl_4 treatments of the FTO were less promising, with a decrease in performance. This could be attributed to two factors: the blocking layer may be suppressing any current contributed by electrolyte side-reactions, or, more likely, the integrity of the TiO_2 layer has been compromised. Many film samples prepared with the treatment became flaky and unstable, perhaps due to poor adhesion between each material layer.

Subsequently, devices with both treatments were produced and gave the greatest performance for each dye. The champion devices containing the iridium (III) complex achieved only low photovoltaic efficiency ($\eta = 0.49 \%$), but the outcome is consistent with previous reported results for iridium (III) sensitizers. The high FF of devices using **1** indicates reduced interface resistance, but the low efficiency of **1** compared to **N719** could be attributed to the poor absorption in the visible region. IPCE measurements of the champion device architecture are shown in Figure 10. These were compared to the absorption spectrum of the dye once bound to the semiconductor surface. The absorption spectrum of the TiO_2 electrode after immersion in the dye solution omits the details of

Dye	Film treatment	$J_{sc} / \text{mA cm}^{-2}$	V_{oc} / V	FF	$\eta / \%$
1	Both scattering and TiCl_4	0.995	0.67	0.74	0.49
N719	Both scattering and TiCl_4	8.84	0.81	0.61	4.4

Table 5: Photovoltaic parameters, including open circuit voltage (V_{oc}), short circuit current (J_{sc}), fill factor (FF) and efficiency (μ) of champion devices using **N719** and compound **1** with both **scattering/TiCl₄** treatments). Further experimental details can be found in section 3.3.

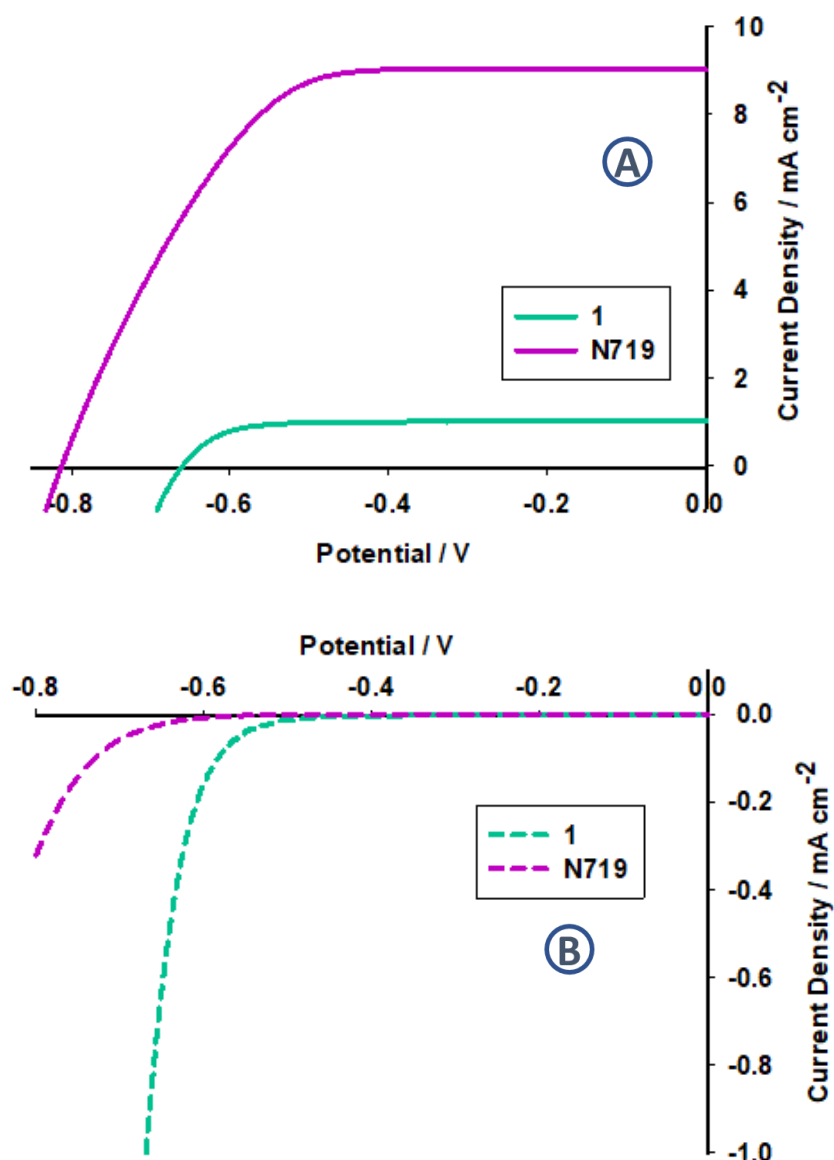


Figure 9: Current-voltage curves for DSSCs constructed using Ir complex **1** (green) and N719 (purple) in **a**) simulated sunlight (solid lines, AM1.5, 100 mW cm⁻²) and in the **b**) dark (dashed lines). Electrolyte composition: 0.6 M TBAI, 0.03 M I₂, 0.1 M guanidinium thiocyanate and 0.5 M *t*-butyl pyridine in MeCN.

the latter absorption peak at 430 nm, while the IPCE highlights the spectral response of the dye more precisely. A current response beyond 600 nm was measured, but with such poor light-harvesting at $\lambda > 620$ nm, it is extremely low (IPCE < 2 %). While the dyes do absorb broadly across the visible spectrum, the low absorption coefficients ($\epsilon \sim 2,000$ M⁻¹ cm⁻¹) compared to ruthenium dyes ($\epsilon > 10,000$ M⁻¹ cm⁻¹) is a great limitation to their solar cell performance. Analysis of the lower energy regions of the spectrum, such as sub 330 nm, will yield higher IPCE, but will be masked by the absorption effects of the TiO₂

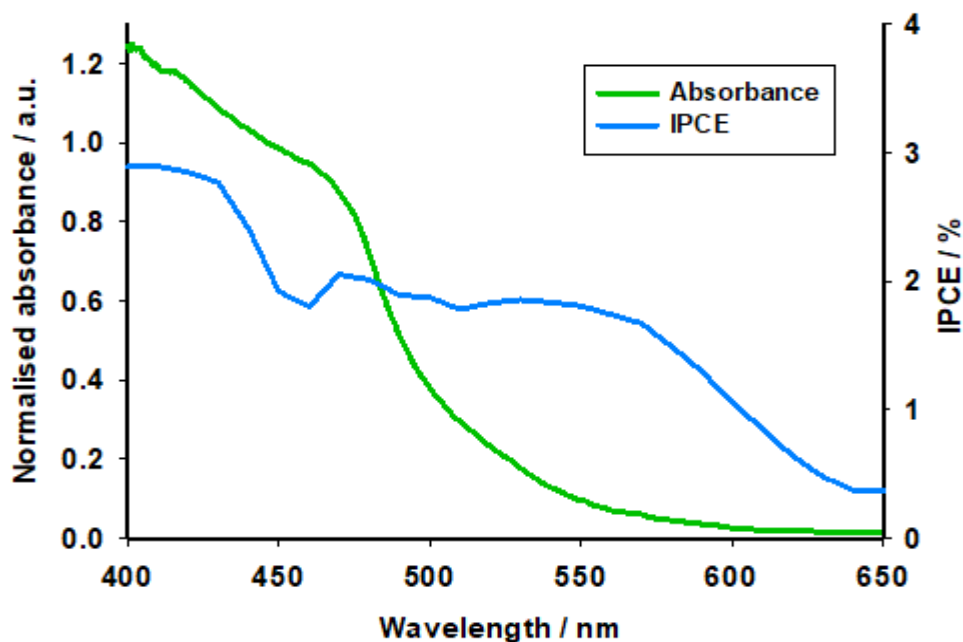


Figure 10: IPCE response of devices containing complex 1 compared to a normalised absorption spectrum.

and iodine redox couple. It is imperative to increase dye loading on the film, and to improve ϵ in the visible region to fully take advantage of the increased absorption range.

3.1.3 Conclusions

A new panchromatically absorbing, NIR luminescent iridium (III) complexes bearing a tripodal tris-(six-membered) chelate ligand was synthesised and characterized. The absorption spectrum tailed off at 700 nm, much further than most neutral iridium complexes, while the emission was significantly shifted into the NIR, with a maximum at 731 nm. DSSCs using **1** as the dye achieved efficiency of 0.49 %, which is comparable to other iridium (III) dyes reported in similar conditions.¹⁵ This was attributed to the modest absorption coefficient, which leads to weak light harvesting of the film in the visible region, and low short-circuit current. This highlights the importance of anchoring group design and utilisation in the application of new sensitisers to DSSC. The dye is a good emitter but use in the context of solar energy harvesting is restricted and other, more sustainable avenues should be explored. Iridium is one of the rarest metals in the Earth's crust and sourcing these materials have ethical, environmental and long-term impacts in the countries of origin. There are more sustainable alternatives to heavy-metal complexes that should be considered in the overall picture of device design and implementation.

3.2 A sensitiser derived from Nature.

With thanks to Harry Tito and Antony Huaman of Universidad Nacional de Ingeniería (UNI) Lima, for undertaking FTIR, solution absorption and lifetime experiments.

This section focusses on a collaborative project undertaken with the National University of Engineering in Lima, which was established to attempt to use native Peruvian flora and their extracts to harness light from the sun. The extracts from four candidate materials (yellow rose, red quinoa, molle leaves, and ayrampo seeds) were subjected to initial tests, where the ayrampo seeds were found to have most promise in this application. Further work was done to optimise the extraction process of the ayrampo pigment and develop devices using the natural dye as a sensitiser.

3.2.1 Background

Over 3 million people in Peru do not have direct access to electricity, many of whom live in remote regions with no access to the mainline power grid. Installation of off-grid energy sources such as solar panels, or the replacement of widely used oil lamps with LEDs, could help reduce energy poverty and could assist in the improvement of the general health and amenities available to those living in rural areas in Peru. Yet, there are ancient traditions that are practised widely by artisans in Peru and Bolivia that can tie directly into the manufacture of DSSC. Weavers use ancient practices handed down through the generations to dye sheep and alpaca wool using simple methods and easy to find mordants. These mordants help to set the dye into the fibre and can traditionally include lemon juice, alum, ferrous sulfate, copper sulfate, or even urine. The solvent is



Figure 11: Image of dried raw ayrampo seeds.

usually water, and the dyeing process is often in large batches with minimal waste. The colour of the resulting wool products will be dependent on factors including the natural pH of the dye material, the temperature, and the type of mordants used. However, much knowledge surrounding natural dyeing processes is not recorded quantitatively. Information is passed with a 'common sense' approach and there is very little exact data to be found in what is, culturally, an art form.

Unlike artificial sensitisers, which are often designed with specific charge transfer or absorption properties, dyes from vegetation have developed with the organism in mind. This means that the focus of research in 'natural' DSSC is not in the optimisation of the dye molecules, but rather the selection of sources and extraction of dye components, followed by extensive optimisation of the systems surrounding the dye (including but not limited to the semiconductor morphology, electrolyte composition, pH and concentrations). Yet due to their versatility and photochemical properties, natural products in photovoltaic devices have been studied before, using beets, grapes, blackberry, hibiscus, and other natural products as the source material for the photosensitisers.²⁵ Now, sensitisers from nature are used to demonstrate the principles of DSSC and renewable energy sources in classrooms and teaching labs around the world.

26

Most natural dyes can be categorised into 4 groups; anthocyanins, betalaines, carotenoids and chlorophylls.²⁷ Most work has focussed on the more common anthocyanin and chlorophyll dyes. The former dyes are a compound family found in the leaves, flowers and fruits of many plants, and are responsible for the red, blue or purple colouring of many common fruit and flowers.²⁸ Anthocyanins fulfil a biological photoprotective function, reducing the photoinhibition and photobleaching of chlorophyll under intense light conditions. Extended π conjugation through the molecules core, a 2-phenyl-benzopyrylium chromophore (known as flavylium) allows the anthocyanin family to absorb light in the visible region, while the number of hydroxyl and methoxyl groups, type of sugar, and the nature of bound acidic groups determines the intensity, wavelength and stability of the dye's absorption spectrum.

Basic Structure of anthocyanins using flavylum cation			
Name (abbreviated)	Substituent		λ_{\max} in MeOH- HCl / nm
	R1'	R3'	
Pelagoridin (Pg)	H	H	520
Cyanidin (Cy)	OH	H	535
Delphinidin (Dp)	OH	OH	546
Peonidin (Pn)	OCH ₃	H	532
Petunidin (Pt)	OCH ₃	OH	543
Malvidin (Mn)	OCH ₃	OCH ₃	542

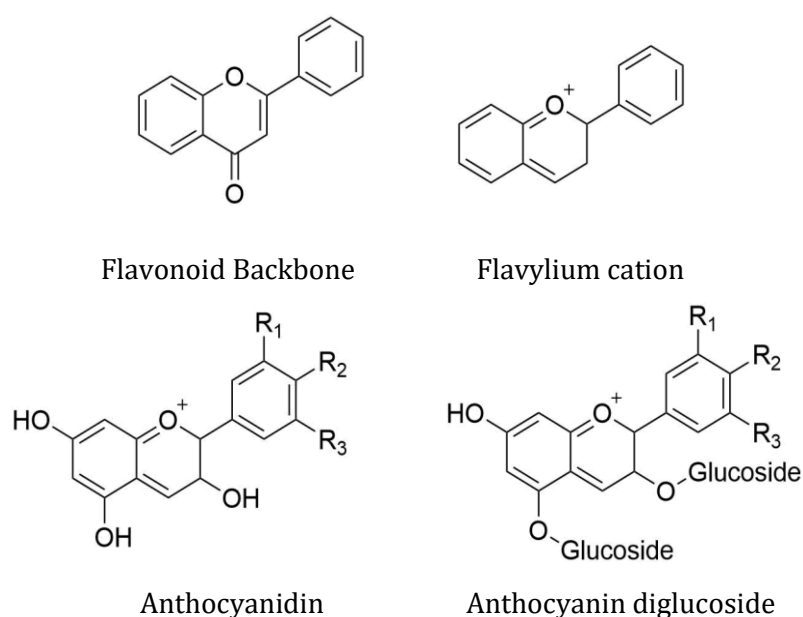


Figure 12: Structures of anthocyanins based on the flavylium cation backbone, with accompanying table highlighting the R-configuration of common anthocyanin molecules.

The dyes are known to be stabilised by acidic conditions, since above pH 2, the flavylium cation is known to undergo deprotonation or hydration reactions, resulting in the yellow or colourless forms of the anthocyanin.^{29,30} Another investigated property of anthocyanins is molecular co-pigmentation, in which the stabilising mechanism between a molecule and its co-pigment increases longevity of the dye solution.^{28,31} The electron-poor flavylium ion in the anthocyanin can associate with electron rich systems, such as naturally-occurring polyphenols and flavones, as well as other organic acids, metallic ions, or even other anthocyanins (known as self-association). N-type devices containing anthocyanin reported in literature reach almost 2 % efficiency using raw extracts, with

good results found using citric acid as a solvent and/or stabilizer in some instances.²⁹ Losses in the efficiency were attributed by Zhang et al. to either increased dye aggregation on the films, or electron recapture by the redox electrolyte, but these observations could be also attributed to most natural (or indeed synthetic) dye systems, not just the anthocyanins studied.³²

The second group, chlorophylls, are famous for their role in photosynthetic processes and are commonly green in colour. Chlorophylls are structurally related to porphyrins, in that they are based on a cyclic tetrapyrrole. Yet this class of dyes have reduced pyrrole rings and a phytol group, which is a long chain, hydrophobic alcohol that is esterified into an acid side chain. Chl-*a* (C₅₅H₇₂O₅N₄Mg, cyan), Chl-*b* (C₅₅H₇₀O₆N₄Mg, yellow-green) and Chl-*c* (C₃₅H₂₈O₅N₄Mg, blue-green) are proposed to be the most common structures found naturally in the chlorophyll family and are shown in Figure 13. These structures have an extensive array of highly stable conjugated architecture, ideal for delocalization of orbitals and therefore for their application as photosensitisers.³³ Derivatives of these molecules have been used as luminescent materials and dyes in the food, cosmetic and textile industries due to their low cost and environmentally-friendly synthesis and purification pathways, another advantage over their porphyrin cousins.

Extensive analysis of chlorophyll derivatives used in TiO₂ based-DSSC was carried out by Kay and Graetzel in 1993, where Chl-*a* was found to bind to the TiO₂ surface only poorly

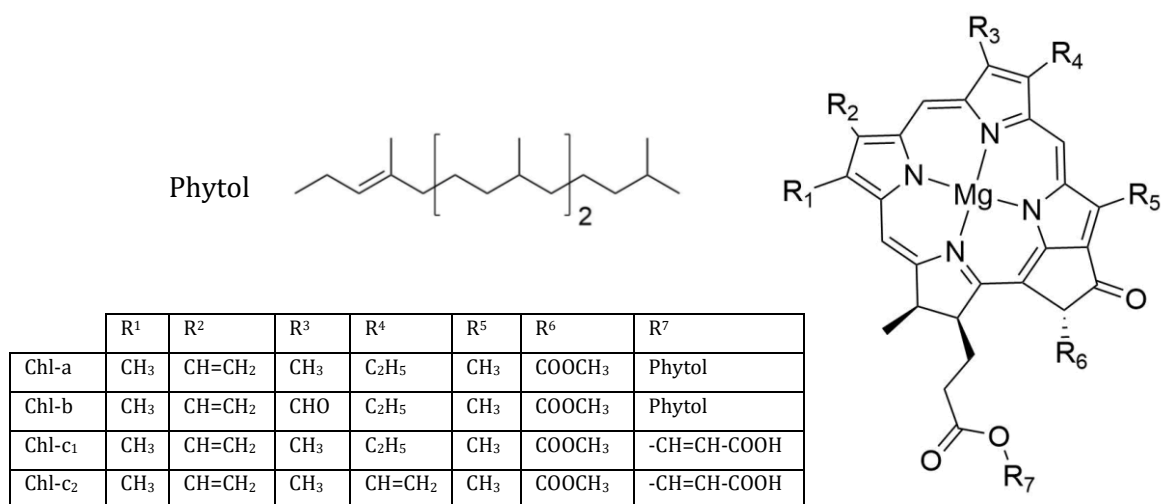


Figure 13: Structure of the core cyclic configuration of chlorophyll, with accompanying table of the R group configurations of the three Chl- complexes discussed in this section.

due to the weak interaction of its ester and keto carbonyl groups with the hydrophilic oxide layer. Use of solvents with lower polarity such as hexane or diethyl ether improved dye absorption significantly, but a strong broadening and red shift of the film's absorption spectrum compared to the dye in solvent suggested that there was aggregation of the dye on the surface.³⁴ Further investigations concluded that only chlorophyll sensitizers bearing carboxylic acids directly conjugated to π -electrons of the chromophore could exhibit an effective electron injection into the TiO₂ electrode. Wang et al. investigated the common chlorophyll variants from wakame seaweed extracts, and their findings agreed that reduced dye aggregation due to the favourable configuration of the peripheral vinyl carboxyl group was instrumental in reaching the high ($\eta \sim 3.4 - 4.6\%$) efficiencies achieved.³⁵ However, most investigation into the compounds' properties have been in highly purified or synthetic samples and not with raw extracts.

The focus of this work is a family of molecules known as betalains, which are mainly classed into two types: betaxanthins (often yellow in colour) and betacyanins (usually purple). Both share the same chromophore backbone, an immonium derivative of betalamic acid with substituent R groups extending from the nitrogen. The structure of the R group determines where the molecule falls in its classification, as shown in Figure 14, where betacyanins are thought to be product of condensation between the backbone and *cyclo-DOPA*, and condensation of the backbone with amines or other amino acids gives rise to the betaxanthins. Generally, these dyes have orange and red colour, mostly depending on prevailing dye content: betacyanin or betaxanthin. For example, prickly pear contains betanin and indicaxanthin (proline-betaxanthin) and is orange, while the Bonel variety of red beet contains betanin and vulgaxanthin (glutamine-betaxanthin), which exhibits an intense red coloration with high absorption coefficients.³⁶

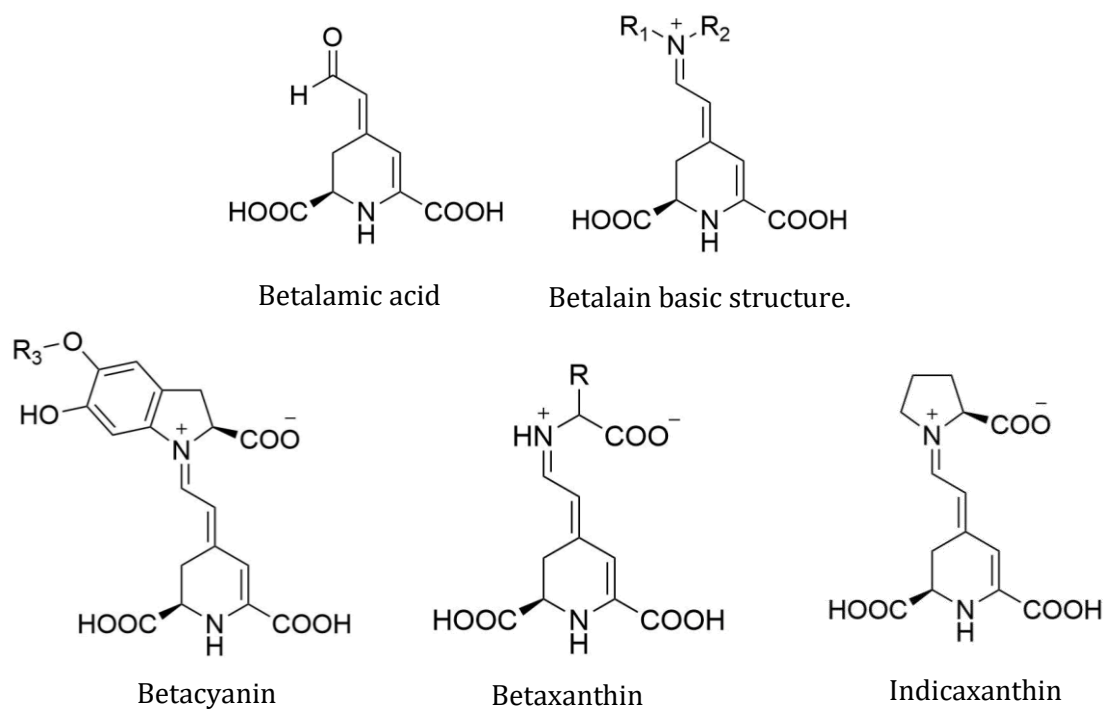


Figure 14: Structural classification of both betacyanins and betaxanthins according to the configurations of groups R_1 and R_2 . The R_3 group within betacyanin further classifies the molecule; $R_3 = H$ denotes a betanidin, while $R_3 = \beta\text{-D-glucose}$ indicates a betanin.

The red-shift in absorption of betacyanins in comparison to the betaxanthins can be attributed to the extended aromatic structure in the cyclo-DOPA condensate. Due to these strong absorption capabilities in the visible spectrum, betalains have promise as photocurrent converters in devices. Additionally, the carboxyl functional groups are key to binding the dyes to the semiconductor nanostructure, and many betalain structures host multiple acid moieties. The molecules are also stable in the pH range 2-7, which makes them useful in mildly acidic and neutral conditions, and they are also more resistant to hydrolysis, making them an ideal dye system for green solvent use.

There are significantly fewer varieties of betalains compared to the anthocyanins, and a corresponding lack of research dedicated to their application in DSSC. Red beet was considered the only edible source of betalain dye for a long time, which limited the amount of attention the family received, yet in recent years betalains have been analysed and extracted from other sources such as *Bougainvillea*, amaranth, prickly pear, dragon fruit, and beetroot.^{37,38}

Betalain pigments in one fruit of the prickly pear genus (Sicilian Prickly Pear, *Opuntia ficus-indica*) have been characterised by different groups, and the fruit found to contain both betanins and betaxanthins.³⁹ The betaxanthin known as indicaxanthin was found to be a major compound in the fruit, followed by betanin and isobetanin. The lack of betanin side products in some studies were attributed to gentle work-up conditions and led to higher purity betanin samples.³⁶ Calogero et al. achieved an efficiency of 1.26 % using an optimised TiO₂ thin film as the photoanode substrate and purple extract from Sicilian prickly pear.⁴⁰ Zhang et al investigated uptake of dye from red beet onto TiO₂ films, with limited success, by 'purifying' the dye extract via column chromatography to remove the yellow betaxanthins, efficiency of their device increased. It was only upon the utilisation of an acidic pre-treatment on the TiO₂ that uptake increased, yet devices failed to surpass 1 % efficiency.⁴¹ Sandquist and McHale proposed that separation of the red/purple betanin from the yellow indicaxanthin would improve dye uptake, since they had discovered that the yellow dye preferentially binds to TiO₂. By boosting the concentration of strongly photoactive molecules (in this case, the betanins from red beet root) then an increase in light harvesting and therefore efficiency will result. Their efforts to optimise the DSSC to reduce recombination, alongside their purification steps via MPLC resulted in devices reaching 2.7 % efficiency.

This work focusses on 'Ayrampo' fruit, from a prickly pear species (*Opuntia soehrensii*) native to South America, specifically Peru. The flesh and seeds are known to be a good natural source of betalains, and they work as a powerful antioxidant against pyroxyl and nitric oxide radicals.⁴² Along with their intense red colouring, this has led to their use as natural pigment for textiles, in natural remedies, and as a fashionable ingredient of gourmet food. With little research in the efficacy of betalains in DSSCs, the Ayrampo seeds have potential as a native source of sensitisers for DSSCs produced in Peru.

3.2.2 Results

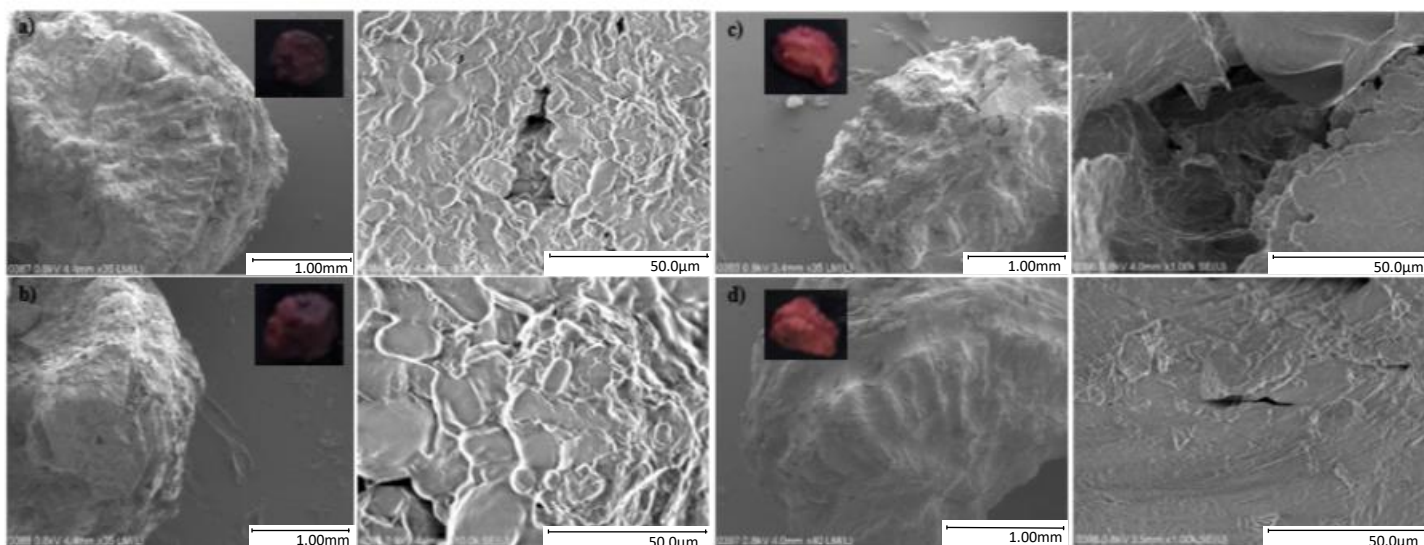


Figure 15: Images of ayrampo seeds obtained by scanning electron microscopy (SEM) before and after being subjected to the pigment extraction process.

Experimental details outlining the preparation of the seed material and extraction of pigment samples are outlined in the Section 3.3. In short, three extract samples, labelled **AY1-3** were obtained, and a fourth extract, designated as **raw** ayrampo extract was used as a reference. Images (inset, Figure 15) of the ayrampo seeds both before and after extraction show the visible color change to the seed cuticle from deep purple to pink/yellow. The central husk is covered by a hard lignin coating that has negligible pigment content in comparison to the surrounding flesh. This is the reason why vigorous ultrasound treatment of the seeds to extract pigment is too harsh. The protective lignin layer of the seed may become damaged by the ultrasound and will release unwanted flavonoids and phenolic compounds from the husk into the dye solution. The loss of pigmentation from the seed coating demonstrated good dye extraction using the gentle water treatment. The SEM images illustrate the breakdown of the porous fleshy layer, leaving the smoother internal husk surface behind. This demonstrates that the seed husk itself plays no part in the extraction of dye material, and only the remnant flesh of the fruit around it contains the vibrant pigment.

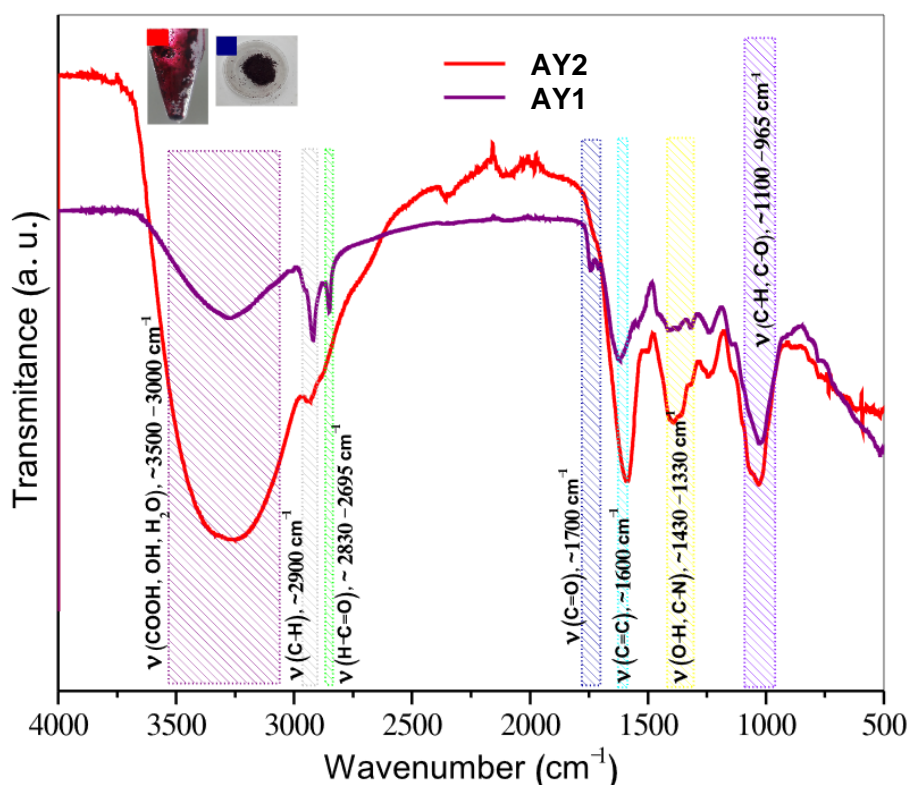


Figure 16: FTIR spectroscopy of samples AY1 and AY2 with key regions corresponding to functional groups highlighted with colour.

ν cm^{-1}	Bond types	AY1	AY2
~1100 - 965	C-H, C-O	✓	✓
~ 1430 - 1330	O-H, C-N	✓	
~ 1600	C = C	✓	✓
~ 1700	C = O		✓
~ 2830 - 2695	H-C = O		✓
~ 2900	C-H	✓	✓
~ 3500 - 3000	COOH, OH, H ₂ O	✓	✓

Table 6: Summarised peak data from Figure 16.

The precipitated material **AY2** has a tacky texture and viscosity not seen in the suspended and dried material, due to excessive amounts of water in the sample. Repeated washing and drying steps did not lead to improvement. FTIR characterization in ATR mode (Figure 16, Table 6) shows the different vibrational frequencies for the samples **AY2** and **AY1**. The **AY2** sample contains an amine functional group peak (C-N, $\nu = 1335 \text{ cm}^{-1}$) not observed in the powder sample spectrum, as well as an intense peak for the alkene functional group (C = C, $\nu = 1600 \text{ cm}^{-1}$). However, **AY1** contains peaks absent in the viscous sample, such as those denoting carboxyl groups (C = O, $\nu = 1700 \text{ cm}^{-1}$) and aldehydes (H-C = O, $\nu = 2700 \text{ cm}^{-1}$).

UV-vis spectrophotometry of the separated fractions of **AY3** gives the absorption wavelengths of these extracts, seen in Figure 17. With key peaks between 250-300 nm denoting the disaccharide and cDOPA groups, a small peak expected around 480 nm for the indicaxanthin, and a broad absorption at 540 nm stemming from the betanin molecules. The concentrations of these molecules can be seen to coincide with the depth of colour of the fractions of solution, with deeper colour observed in samples with higher betanin concentrations. However, after one month in direct sunlight, the concentrations of each fraction were evaluated, finding a decay in the characteristic peak for the betanin and indicaxanthin (Figure 18). The betanin was only then found in fractions 4 and 5, while the absorption peaks of both the disaccharides and cDOPA are maintained. This indicated

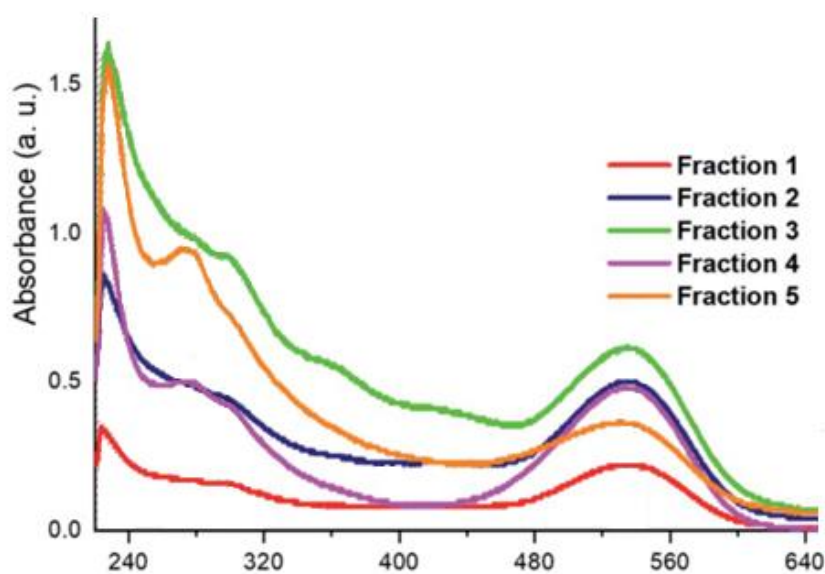


Figure 17: Smoothed UV-Vis spectra of AY3 fractions in DI water

that the only remaining photoactive compounds in the series are likely the betacyanins, and their absorbance profile, and therefore structure, remains intact after this time. Upon submersion of TiO₂ films in the raw extract, a similar trend was observed in the absorption spectra. The absorption peak around 450 nm representing the presence of indicaxanthin recedes after only 24 hours and gives way to the betalain peaks.

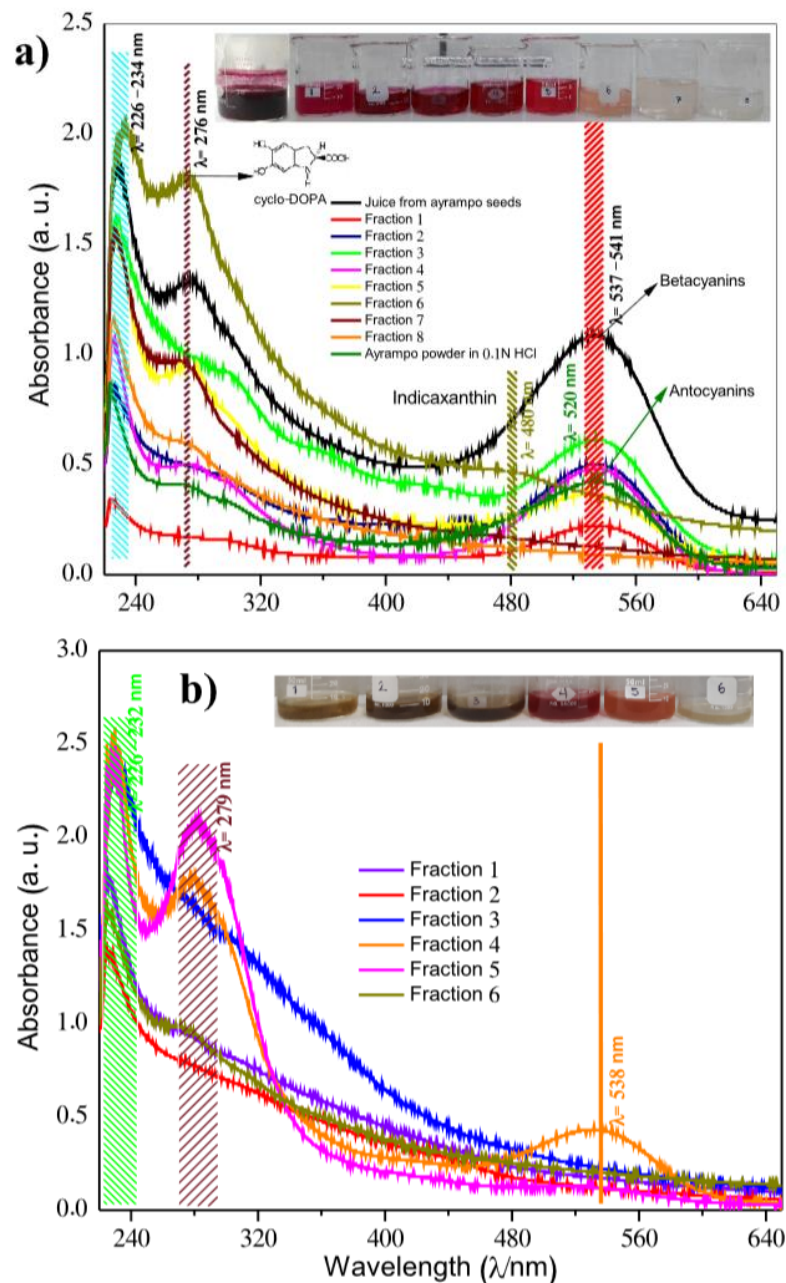


Figure 18: UV-Visible spectra of both *raw* and *AY3* fractions a) before and b) after exposure to 1 month of ambient light with key components of the mixtures annotated.

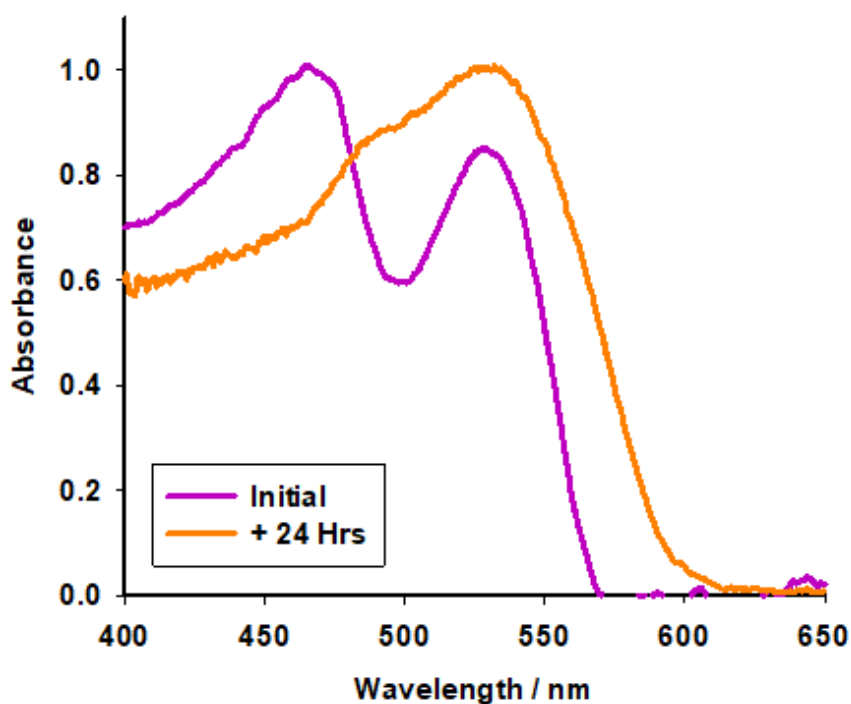


Figure 19: UV-Visible spectra of AY1 samples in DI water before and after 24 hours of exposure to ambient light.

However, raw extract samples do boast this long-term retention of color. Either the components of the raw juice are in a synergistic relationship with each other to prevent or slow degradation, or there is another, non-optically active component that facilitates retention of the mixtures' optical characteristics. This indicates that the methodology for sample and dyebath preparation from the raw extract has a large impact on the resulting molecules that are obtained. More advanced separation and characterization techniques (such as HPLC or LC-MS) would need to be used to fully appreciate the role of each molecule in the seeds' composition. Taking into account practical considerations, if devices are to be created in a non-laboratory environment, then advanced chromatographic separation is not a viable way of optimizing devices.

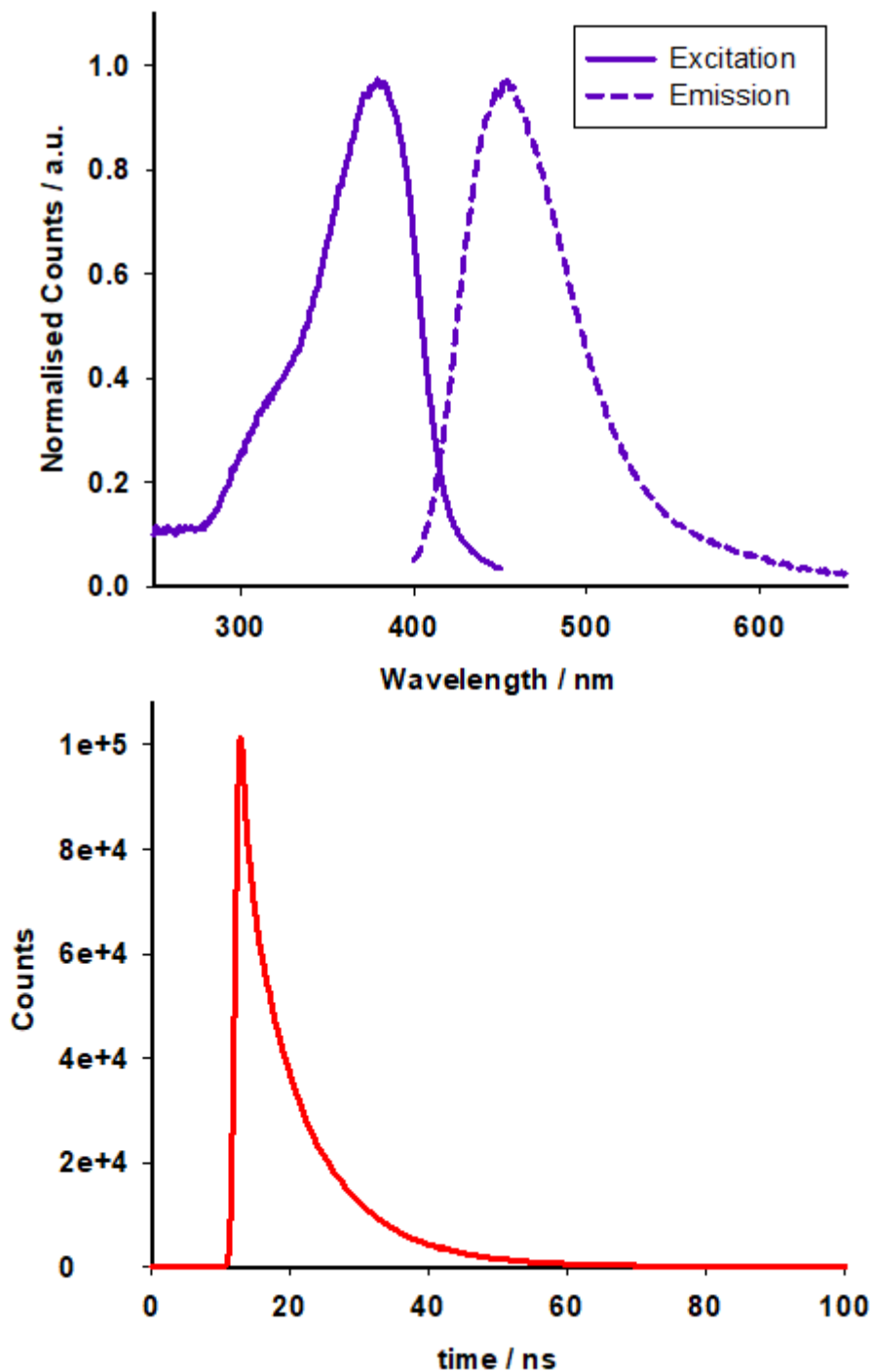


Figure 20: a) Excitation and Emission spectra of AY2 in H₂O b) Lifetime decay trace of AY2.

Fluorescence spectroscopy of the **AY2** extract gives an excitation peak maximum around 380 nm and emission peak redshifted by roughly 100 nm. The emission peak lacks the vibronic shoulder seen in the excitation. The lifetime of the excited dye solution was calculated to be 9 ns, in a single exponential decay, which indicates singlet fluorescence.

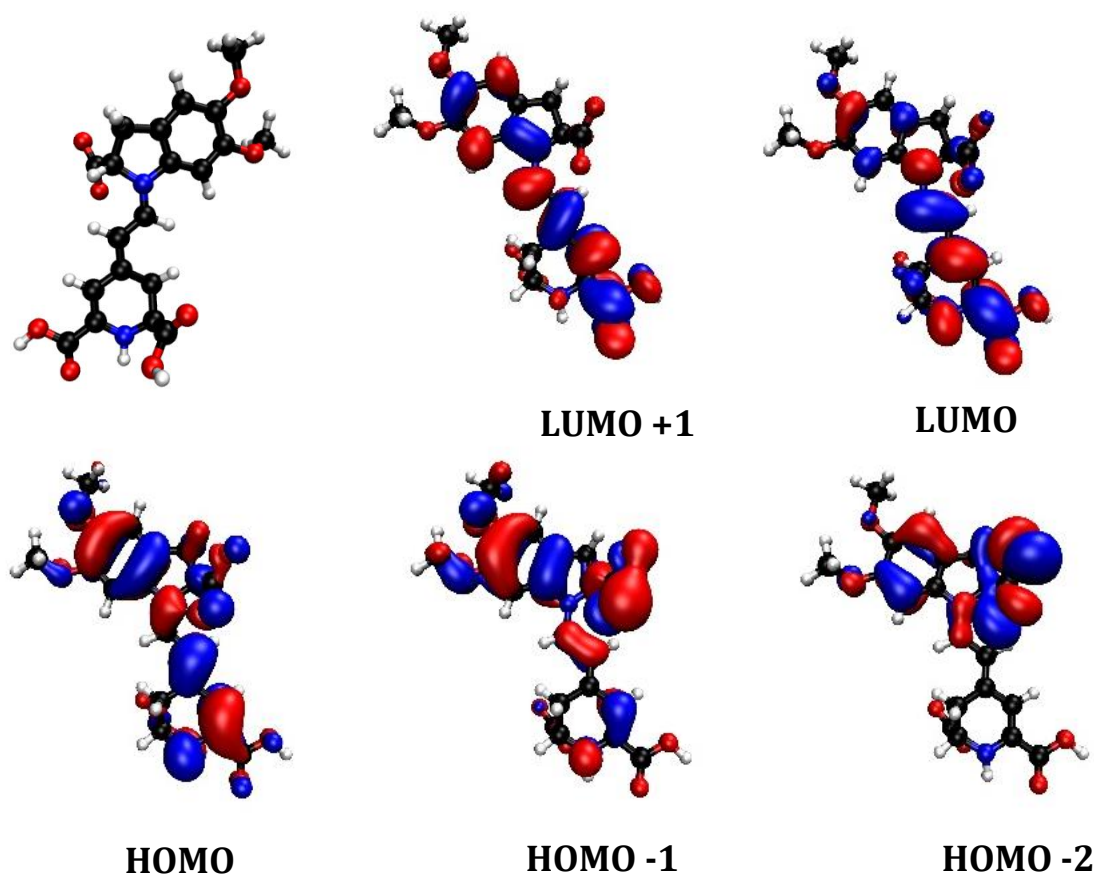


Figure 21: Ground state structure and calculated molecular orbitals for the proposed key betalain component of the AY samples.

Excited State	Transition	Contribution	Absorbance /nm	Energy / eV	Oscillator strength
1	HOMO to LUMO	100%	532	2.3302	1.1172
2	HOMO-1 to LUMO	98%	447	2.7717	0.0645
	HOMO-3 to LUMO	2%			
3	HOMO-2 to LUMO	100%	430	2.8838	0.0054

Table 7: Table of calculated absorption peaks and associated orbital transitions within the betalain, as well as the relative contribution of each calculated transition to the peak.

To ratify these findings and investigate the optical and orbital properties of the betalain component, time dependent density functional theory was utilised. The structure was simplified to reduce computational costs by substitution of the sugar rings of the betanin with methoxy groups. The geometry of the molecule was calculated in vacuum and the energy calculations were run in acetonitrile to represent the interaction of the dye with electrolyte, using the IEFPCM solvent model. The basis set for both optimisation and energy was B3LYP 6-311g ++ (d,p), to attain a good balance between depth of the calculation and computational cost. Due to these compounds not displaying any phosphorescence, only the singlet energy levels were calculated, and are summarised in Table 7. The first excited state is an intense HOMO-LUMO π to π^* transition with a small amount of charge transfer character and an absorbance of 532 nm. The LUMO shows more electron density around the carboxylic acid group. This calculated HOMO-LUMO transition agrees with the experimentally measured UV-Vis absorption peak found in Figure 19. The second excited state, corresponding to a transition at 447 nm, is much weaker with an oscillator strength of 0.0645. This transition has two components; HOMO-1 to LUMO with a 98% contribution, and HOMO-3 to LUMO making up the rest. As seen in Figure 21, the HOMO-1 shows more electron density around the aromatic ring. The third calculated transition of HOMO-2 to LUMO was calculated but not considered, since the oscillator strength is low enough to discount its impact. Samples of **AY1** and **raw**, as well as **N719** as a reference dye, were subsequently used to produce DSSCs in order to assess the capability of ayrampo extracts as sensitisers. A series of experiments were performed to elucidate the optimal device configuration, which is described in Section 3.3. In short, devices presented in this section comprised of an optimised 3 layer TiO₂ photoanode with both a spin-coated blocking layer and a compact scattering layer. The electrolyte used for these devices was an iodine-based electrolyte and all devices were completed with a platinised counter electrode. Once an architecture was established, further experiments were carried out to deduce the effects of the natural dye sample preparation on the performance of the resulting DSSC.

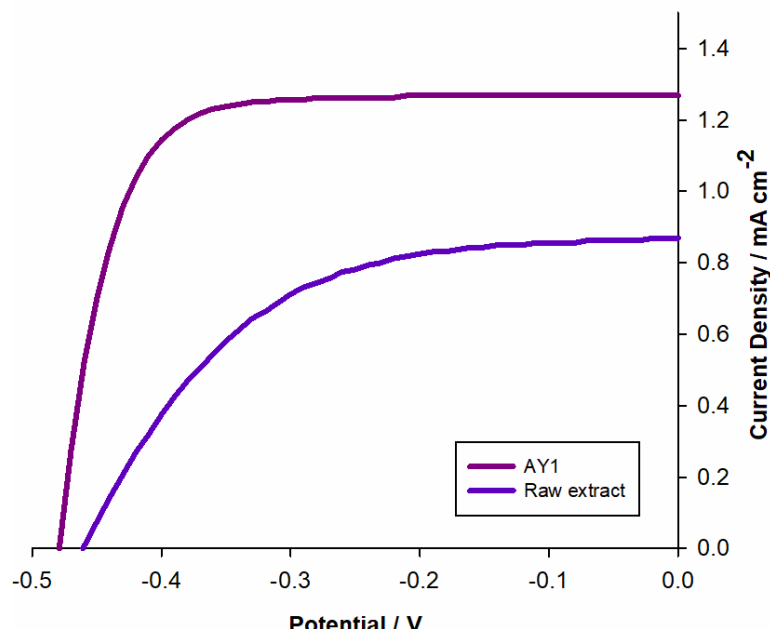


Figure 21: Current-voltage curves for DSSCs constructed using containing **AY1** and **raw** extract under illumination (AM 1.5G, 100 mW cm^{-2}) composition: 0.05 M I_2 , 1 M 1,2 , dimethyl-3-propylimidazolium iodide, 0.5 M LiI , 0.5 M TBP in MeCN.

In the first round of testing, the **raw** extract was compared with **AY1**. As expected, the **AY1** devices gave improved performance compared to the **raw** extract and the performances of these devices are summarised in Table 8. Greater power output is likely due to improved dye loading, from less competition between the dye and unwanted materials in the crude material. The removal of the yellow band of indicaxanthin during the filtration step for **AY1** may also account for the increased uptake of dye.

Sensitiser	V_{oc} / V	$J_{sc} / \text{mA cm}^{-2}$	FF	$\eta / \%$
Raw	0.485	0.88	0.68	0.29
AY1	0.48	1.27	0.75	0.45
AY1 + citric acid	0.39	7.21	0.5	1.41
N719	0.56	15.39	0.55	4.75

Table 8: Photovoltaic parameters, including open circuit voltage (V_{oc}), short circuit current (J_{sc}), fill factor (FF) and efficiency (η) of the n-type devices tested in this section, with **N719** dye as a reference. Natural dye extracts include the raw sample, the cleaned **AY1**, as well as **AY1** treated with citric acid. Further experimental details can be found in section 3.3.

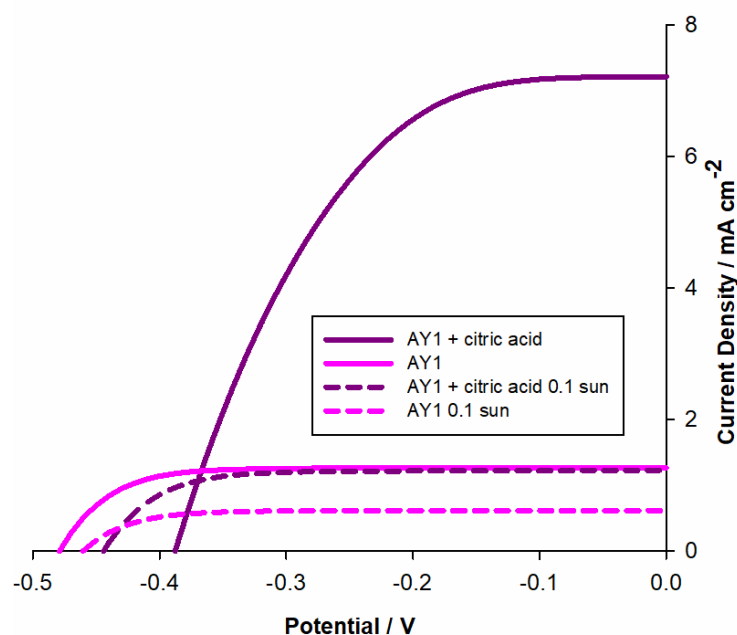


Figure 22: Plot of current density against voltage for illuminated devices containing both **AY1** and **AY1** with citric acid under full illumination (solid lines) and 10% illumination (dashed lines).

While the V_{OC} and FF values of the Ayrampo cells were reasonable, low current output limited the overall device performance. The next step was to improve this without hindering the sustainability of the device. Both the work of Prabavthy with anthocyanins²⁹ and Calogero's prickly pear devices⁴⁰ used acidic solvents or treatments to the TiO_2 film in order to increase current output. This was considered, from a sustainability point of view, no different than the established processes of dyeing fibres with acidic or basic additives, known colloquially as 'mordants'. As shown in Figure 22, the addition of 0.01 M citric acid to the aqueous dye bath solution drastically increased the J_{SC} , and therefore the overall efficiency of the devices tested. Tests with ascorbic, hydrochloric and citric acid additives were conducted, and citric acid was the most promising in terms of current improvement, with the added benefits of being cheap, widely available and non-toxic. The pH of the dyebath dropped upon addition of the acid to a value of around 2-3, making it ideal for the stability of the betalains.

Sensitiser	V_{oc} / V	$J_{sc} / \text{mA cm}^{-2}$	FF	$\eta / \%$
AY1	-0.47	0.61	0.72	2.1
AY1 + citric acid	-0.45	1.23	0.74	4.1

Table 9: Photovoltaic parameters, including open circuit voltage (V_{oc}), short circuit current (J_{sc}), fill factor (FF) and efficiency (μ) of n-type devices containing **AY1** and the citric acid stabilised **AY1** sensitiser under 10% AM 1.5G illumination.

The efficiency of the device using **AY1** and citric acid reached 1.41 %, which is comparable to the state of the art for betalains, and surpasses the efficiency of many natural chlorophyll and anthocyanin dyes found in literature.²⁵ Additionally, decreasing the light intensity to 10 % of its normal value is more representative of the amount of light that reaches the floor of rainforests, which are unsurprisingly lacking in power infrastructure. It was then found that upon testing the device under low light conditions, these efficiencies reach up to 4 % for the citric acid treated device. Investigation of the device longevity over a week period was undertaken. Each sample was measured under 1 sun intensity in intervals of 0, 1 and 7 days. The devices that dried out or were otherwise compromised during the time period were excluded from subsequent measurements. The N719 device exhibited an expected decrease in both V_{oc} and J_{sc} after 1 day, followed by a plateau in performance. Both the **raw** ayrampo sample and the pure **AY1** devices showed steady decline in performance over the week. However, the acid-stabilised device retained most of its high performance past its initial degradation after the week, even after continued exposure to sunlight. It is thought that the acid group could act as a stabiliser by decreasing breakdown of the dye via hydrolysis mechanisms.

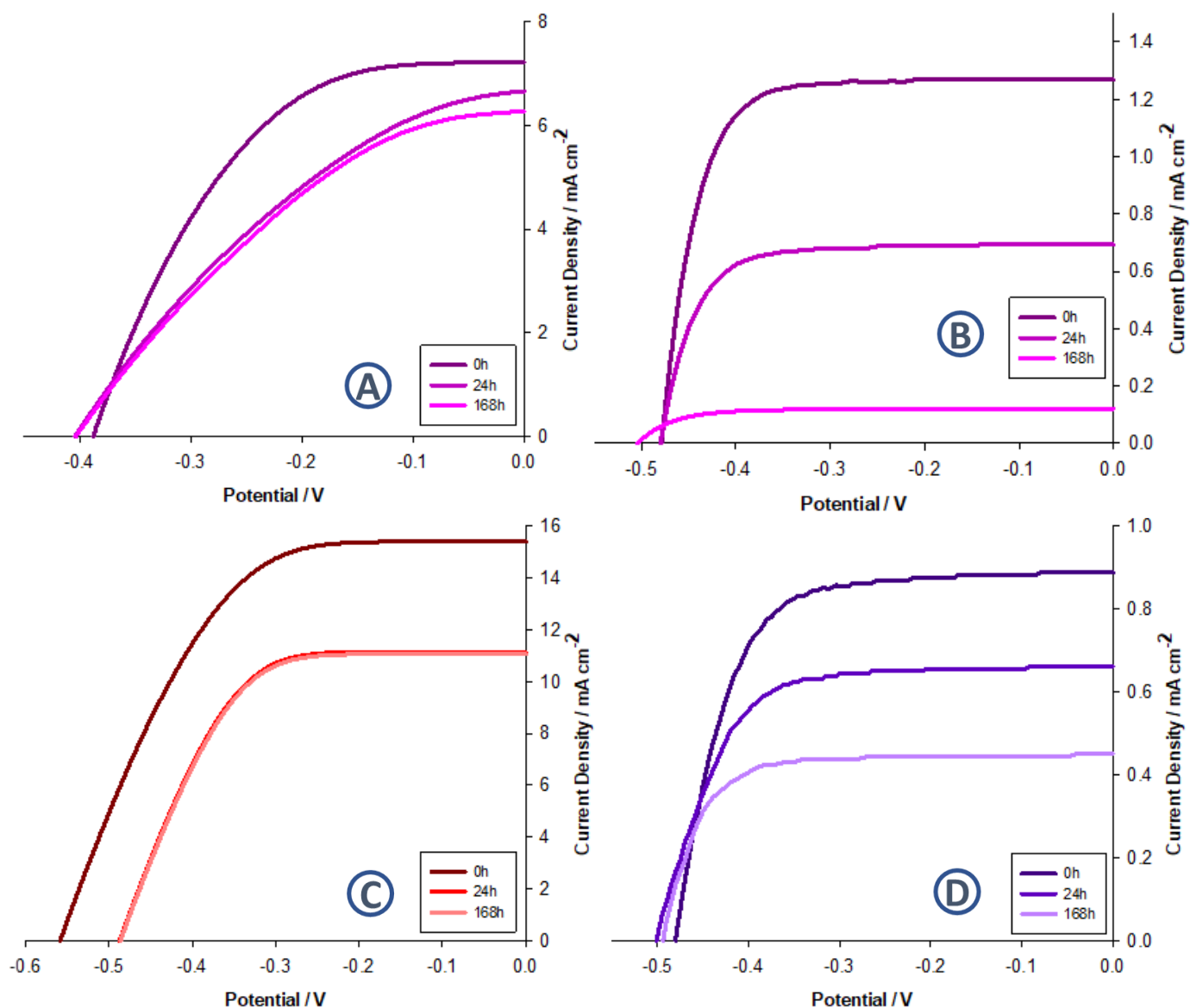


Figure 23: Plots of current density against voltage for devices containing a) citric acid stabilised AY1, b) non-stabilised AY1, c) N719 dye, d) raw dye extract, tested repeatedly over several days.

Further investigation onto the stability of these devices is required to identify the processes, whether physical or chemical, behind the loss of pigmentation.

3.2.3 Conclusions

Due to the interest in looking for new sources of natural pigments, Ayrampo seeds hailing from native Peruvian flora are presented as a good alternative which has previously only been used in preliminary studies. In Peru, native traditions and customs have shaped the way that modern citizens live and see themselves in day-to-day life. However, cultural citizenship of those in indigenous populations is not as well developed, as societies

struggle against cultural discrimination, violence, or economic abuse from the state. By utilising technology that takes inspiration from, and is adapted alongside tradition, avenues are provided for devices to be produced internally, by less developed communities, without a jarring contrast between tradition and technology. This therefore facilitates sustainable growth. To generate long lasting or permanent benefits, two pathways could be adopted:

- Reduction of device fabrication and supply costs by using local, abundant or natural materials.

- Construction of a dual knowledge-technology capacity in Peru, through exchange and collaboration.

This work has focussed on only one of the vast arrays of photoactive sensitiser available in the natural world. Findings from this section not only highlight the potential of natural sensitiser in DSSCs but helped us understand that simple extraction and gentle handling methods can contribute to improved device performance. It has also highlighted the capability of the devices in low light conditions, with up to 4 % efficiency reached for the citric acid stabilised **AY1** sample in diffuse light, with only small losses in the device performance over an extended period. However, several assumptions have been made to reach these conclusions, as limitations in the characterisation of the dye molecule reduce our understanding of the chemistry involved in both the sensitisation and excitation processes. Since the completion of this work, collaborators published a follow-on paper using these findings in order to prove the use of ayrampo dye in OLED devices.⁴³ This highlights the varied utility of the dye found in just one species of plant, with the betalain dye surpassing the power output of the commonly used anthocyanin sources.

The use of natural sensitiser can be beneficial in the investigation of aqueous electrolytes due to their inherent tolerance to water.⁴⁴ Improvements in the use of aqueous electrolytes and reduction of manufacturing costs is the next phase of development of what have been dubbed 'biophotovoltaics'.⁴⁵ Even though the performance of these devices is lower than that of their synthetic counterparts, natural products still have a place in the study of DSSC.

3.3 Experimental

To measure the photovoltaic parameters of devices, an Ivium CompactStat potentiostat was used in conjunction with a Xenon light source (Newport, 300 W) calibrated to 100 mW cm^{-2} with a Si diode. A black aperture was used to mask the device working area and the current was measured at applied bias between 0.1 V and -0.05 V at a rate of 5 mV s^{-1} . Incident photon to current conversion efficiency (IPCE) measurements were conducted by filtering the source lamp through a monochromator (Oriel Cornerstone 130 1/8m) and measuring the current output at 5 nm increments between 400-800 nm, using a Si photodiode as a baseline. For all devices, standard procedures were followed to prepare glass substrates and perform analyses unless otherwise stated.

3.3.1 Procedures for section 3.1

For the working electrode, a TiCl_4 blocking layer was first deposited by immersing the substrates into 20 mM TiCl_4 solution and heating to $75 \text{ }^\circ\text{C}$ for 30 minutes, then washing with water and ethanol. TiO_2 films were prepared by a doctor blading method in which a transparent TiO_2 paste (DSL 18NR-T, Dyesol) was deposited by spreading with a glass rod. Masks to determine thickness and film size (0.25 cm^2) were made using Scotch Magic Tape. The films were dried by heating to $80 \text{ }^\circ\text{C}$ on a hotplate for 5 minutes. In some cases, TiO_2 scattering layer (Ti Nanoxide R/SP, Solaronix) was applied. The films were sintered ($450 \text{ }^\circ\text{C}$, 30 min, 30 min ramp time) and upon cooling, another TiCl_4 treatment was applied. The films were placed into dye baths containing 0.3 mM of Complex **1** and left in the dark for 24 hours before testing. The dye bath solvent was MeCN, which gave a pale yellow/green solution. Further investigation of the MeCN dyebath to improve performance included submerging films in EtOH for 5 minutes before immersion into the dyebath, or the inclusion of chenodeoxycholic acid (0.01 M) into the solution.

Control dyebaths contained 0.3 mM N719 in a 1:1 ratio of t-butanol and acetonitrile. Cells were constructed using the as-prepared films sandwiched with a Pt-coated FTO glass counter electrode (TEC 8), using $60 \text{ }\mu\text{m}$ Surlyn as a spacer. An iodine redox electrolyte composed of 0.6 M TBAI, 0.03 M I_2 , 0.1 M guanidinium thiocyanate and 0.5 M t-butyl pyridine in MeCN was introduced into cells via vacuum and the cells were then sealed.

3.3.2 Procedures for section 3.2

Raw ayrampo seeds were purchased in the central market in Cusco, Peru. They were stored in dark, sealed bags in a refrigerator at 15 °C to avoid contamination and discoloration until used for further experimentation.

Use of solvents such as mercaptopropionitrile (MPN), dichloromethane (DCM), or acetonitrile (MeCN) to run columns or perform any kind of extraction not only gave instant colour changes to the dyebath, but also would not be a sustainable alternative and would not be suitable for upscale in rural areas. Therefore, only solvents such as water or ethanol were used for the extraction and dyeing processes. To fully analyse the natural dye potential in devices, a compromise was reached to optimise both speed of extraction and the cleanliness of the resultant liquor. To minimize the time taken to extract the dye and reduce losses, a short plug column of silica was used to clean the raw extract, remove large particles, and potentially reduce the betaxanthin concentration in the sample. This partially purified solution was labelled **AY1** and was taken on for further testing.

To further separate and extract the pigments, seeds were first dried overnight at 60 °C. 4 g of the dried seeds were added to 20 ml DI water and shaken. The final solution was filtered to produce a raw, highly pigmented solution. This was designated as **raw ayrampo**, and the solution was then further separated in two different ways:

- a) 5 ml of this solution was separated and an acetone anti-solvent was added, and the mixtures centrifuged at 6000 rpm for 20 minutes, obtaining a precipitate and a supernatant, which were then dried at 50 °C for 6 hours (**AY2**). This resulted in a sticky residue left for further testing.
- b) The remaining 15 ml was separated into 8 distinct fractions via column chromatography with DI H₂O. Solvent was then removed from each fraction using a rotary evaporator (**AY3**).

Surface morphology and cuticle degradation of the ayrampo seed was characterized both visually and using SEM (HITACHI model SU8230). Pigments obtained from the ayrampo solution in the forms of precipitate, supernatant or solution were characterized via UV-Vis spectrometry (Ocean Optics, USB 4000 equipped with a UV-VIS-NIR light source model DH-2000-BAL) and FTIR (Fisher Scientific Nicolet iS10 FT-IR spectrometer).

For devices produced in this section, the iodolyte electrolyte included 0.05M I₂, 1M 1,2, dimethyl-3-propylimidazolium iodide, 0.5 M LiI, 0.5 M TBP in MeCN.

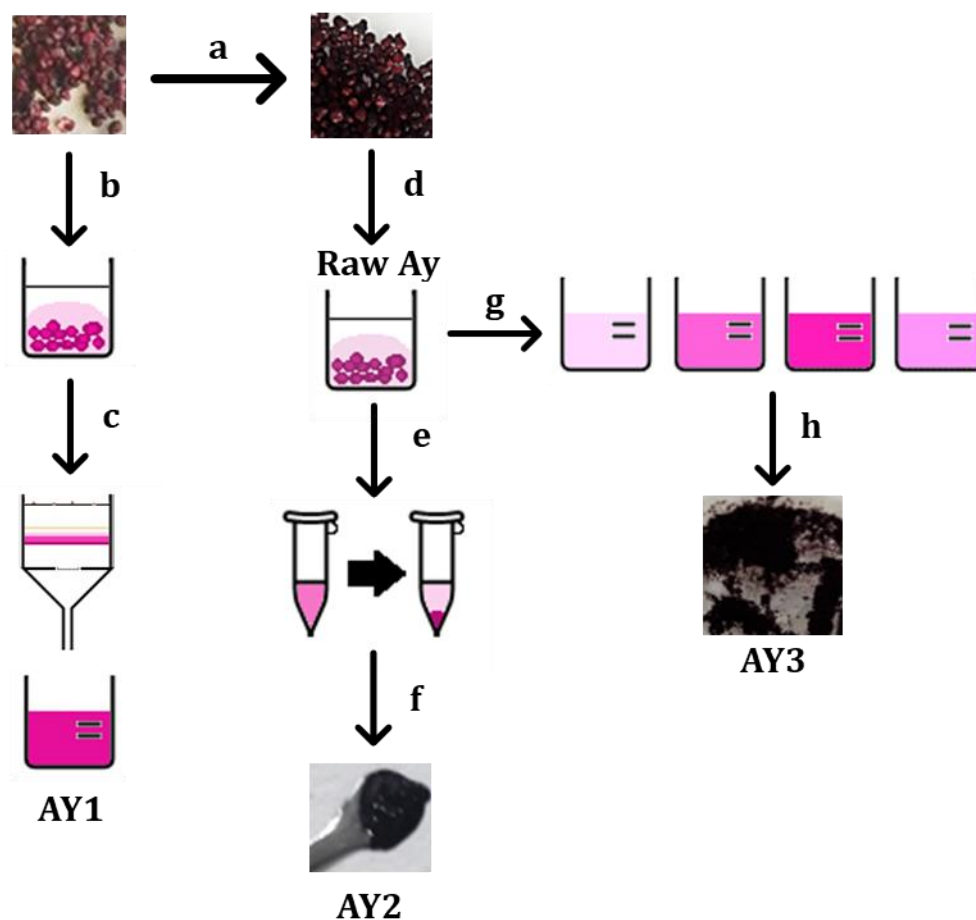


Figure 24: Schematic of extraction processes described in this section. Processes labelled with each arrow are as follows; a) drying for 12 hours b) submersion of seeds in DI H₂O c) filtration purification of solution with silica plug d) submersion of dried seeds in DI H₂O e) centrifugation f) drying of precipitate g) separation via column chromatography h) removal of solvent via rotary evaporation.

3.4 References

- 1 B. O'Regan and M. Gratzel, *Nature*, 1991, **353**, 737–740.
- 2 B. Pashaei, H. Shahroosvand, M. Graetzel and M. K. Nazeeruddin, *Chem. Rev.*, 2016, **116**, 9485–9564.
- 3 M. K. Nazeeruddin and S. Aghazada, *Inorganics*, 2018, **6**, 34.
- 4 S. Aghazada, P. Gao, A. Yella, G. Marotta, T. Moehl, J. Teuscher, J. Moser, F. De Angelis and M. Gra, *Inorg. Chem.*, 2016, **55**, 6653–6659.
- 5 M. K. Nazeeruddin, P. Péchy, T. Renouard, S. M. Zakeeruddin, R. Humphry-Baker, P. Cointe, P. Liska, L. Cevey, E. Costa, V. Shklover, L. Spiccia, G. B. Deacon, C. A. Bignozzi and M. Grätzel, *J. Am. Chem. Soc.*, 2001, **123**, 1613–1624.
- 6 C. Dragonetti, A. Valore, A. Colombo, S. Righetto and V. Trifiletti, *Inorganica Chim. Acta*, 2012, **388**, 163–167.
- 7 E. I. Mayo, K. Kils, T. Tirrell, P. I. Djurovich, A. Tamayo, M. E. Thompson, N. S. Lewis and H. B. Gray, *Photochem. Photobiol. Sci.*, 2006, **5**, 871–873.
- 8 E. A. M. Geary, L. J. Yellowlees, L. A. Jack, I. D. H. Oswald, S. Parsons, N. Hirata, J. R. Durrant and N. Robertson, *Inorg. Chem.*, 2005, **44**, 242–250.
- 9 Y. Shinpuku, F. Inui, M. Nakai and Y. Nakabayashi, *J. Photochem. Photobiol. A Chem.*, 2011, **222**, 203–209.
- 10 E. I. Mayo, K. Kilså, T. Tirrell, P. I. Djurovich, A. Tamayo, M. E. Thompson, N. S. Lewis and H. B. Gray, *Photochem. Photobiol. Sci.*, 2006, **5**, 871–873.
- 11 M. K. Nazeeruddin, F. De Angelis, S. Fantacci, A. Selloni, G. Viscardi, P. Liska, S. Ito, B. Takeru and M. Grätzel, *Renew. Energy Four Vol. Set*, 2018, **2–4**, 227–251.
- 12 E. Baranoff, J. H. Yum, M. Graetzel and M. K. Nazeeruddin, *J. Organomet. Chem.*, 2009, **694**, 2661–2670.
- 13 Z. Ning, Q. Zhang, W. Wu and H. Tian, *J. Organomet. Chem.*, 2009, **694**, 2705–2711.
- 14 Y. Yuan, J. Zhang, Z. Yu, J. Feng, W. Luo, J. Ye and Z. Zou, *Inorg. Chem.*, 2012, **51**, 4123–4133.

- 15 A. Sinopoli, C. J. Wood, E. A. Gibson and P. I. P. Elliott, *Inorganica Chim. Acta*, 2017, **457**, 81–89.
- 16 A. Sinopoli, C. J. Wood, E. A. Gibson and P. I. P. Elliott, *Dye. Pigment.*, 2017, **140**, 269–277.
- 17 M. Gennari, F. Légalité, L. Zhang, Y. Pellegrin, E. Blart, J. Fortage, A. M. Brown, A. Deronzier, M. N. Collomb, M. Boujtita, D. Jacquemin, L. Hammarström and F. Odobel, *J. Phys. Chem. Lett.*, 2014, **5**, 2254–2258.
- 18 C. Hierlinger, T. Roisnel, D. B. Cordes, A. M. Z. Slawin, D. Jacquemin and E. Zysmancolman, *Inorg. Chem.*, 2017, **56**, 5182–5188.
- 19 W. Y. He, J. M. Fontmorin, P. Hapiot, I. Soutrel, D. Floner, F. Fourcade, A. Amrane and F. Geneste, *Electrochim. Acta*, 2016, **207**, 313–320.
- 20 D. N. Chirdon, C. E. McCusker, F. N. Castellano and S. Bernhard, *Inorg. Chem.*, 2013, **52**, 8795–8804.
- 21 S. Ito, P. Liska, P. Comte, R. Charvet, P. Pechy, U. Bach, L. Schmidt-Mende, S. M. Zakeeruddin, A. Kay, M. K. Nazeeruddin and M. Grätzel, *Chem. Commun.*, 2005, 4351–4353.
- 22 M. K. Nazeeruddin, A. Kay, E. Miiller, P. Liska, N. Vlachopoulos, M. Gratzel, C.-Lausanne and R. April, *J. Am. Chem. Soc.*, 1993, **115**, 6382–6390.
- 23 S. W. Lee, K. S. Ahn, K. Zhu, N. R. Neale and A. J. Frank, *J. Phys. Chem. C*, 2012, **116**, 21285–21290.
- 24 P. Salvatori, G. Marotta, A. Cinti, C. Anselmi, E. Mosconi and F. De Angelis, *J. Phys. Chem. C*, 2013, **117**, 3874–3887.
- 25 G. Calogero, A. Bartolotta, G. Di Marco, A. Di Carlo and F. Bonaccorso, *Chem. Soc. Rev.*, 2015, **44**, 3244–3294.
- 26 G. P. Smestad and M. Grätzel, *J. Chem. Educ.*, 1998, **75**, 752–756.
- 27 N. T. R. N. Kumara, A. Lim, C. M. Lim, M. I. Petra and P. Ekanayake, *Renew. Sustain. Energy Rev.*, 2017, **78**, 301–317.
- 28 A. BAKOWSKA-BARCZAK, *Polish J. food Nutr. Sci.*, 2005, **14**, 107–116.

- 29 N. Prabavathy, S. Shalini, R. Balasundaraprabhu, D. Velauthapillai, S. Prasanna, P. Walke and N. Muthukumarasamy, *J. Mater. Sci. Mater. Electron.*, 2017, **28**, 9882–9892.
- 30 K. Torskangerpoll and Ø. M. Andersen, *Food Chem.*, 2005, **89**, 427–440.
- 31 A. J. Davies and G. Mazza, *J. Agric. Food Chem.*, 1993, **41**, 716–720.
- 32 N. J. Cherepy, G. P. Smestad, M. Grätzel and J. Z. Zhang, *J. Phys. Chem. B*, 1997, **101**, 9342–9351.
- 33 W. H. Lai, Y. H. Su, L. G. Teoh and M. H. Hon, *J. Photochem. Photobiol. A Chem.*, 2008, **195**, 307–313.
- 34 A. Kay and M. Grätzel, *J. Phys. Chem.*, 1993, **97**, 6272–6277.
- 35 X. F. Wang, C. H. Zhan, T. Maoka, Y. Wada and Y. Koyama, *Chem. Phys. Lett.*, 2007, **447**, 79–85.
- 36 F. C. Stintzing, A. Schieber and R. Carle, *J. Agric. Food Chem.*, 2002, **50**, 2302–2307.
- 37 H. Zhou, L. Wu, Y. Gao and T. Ma, *J. Photochem. Photobiol. A Chem.*, 2011, **219**, 188–194.
- 38 N. S. Ramli, P. Ismail and A. Rahmat, *Sci. World J.*, 2014, **2014**, 7.
- 39 J. A. Fernández-López and L. Almela, *J. Chromatogr. A*, 2001, **913**, 415–420.
- 40 G. Calogero, G. Di Marco, S. Cazzanti, S. Caramori, R. Argazzi, A. Di Carlo and C. A. Bignozzi, *Int. J. Mol. Sci.*, 2010, **11**, 254–267.
- 41 D. Zhang, S. M. Lanier, J. A. Downing, J. L. Avent, J. Lum and J. L. McHale, *J. Photochem. Photobiol. A Chem.*, 2008, **195**, 72–80.
- 42 D. Butera, L. Tesoriere, F. Di Gaudio, A. Bongiorno, M. Allegra, A. M. Pintaudi, R. Kohen and M. A. Livrea, *J. Agric. Food Chem.*, 2002, **50**, 6895–6901.
- 43 H. A. Rivera Tito, G. Hernández-Sosa, C. Romero-Nieto, E. Regulska, N. Jürgensen, J. Zimmermann, K. Salazar-Salinas and M. E. Quintana Caceda, *RSC Adv.*, 2020, **10**, 36695–36703.
- 44 F. Bella, C. Gerbaldi, C. Barolo and M. Grätzel, *Chem. Soc. Rev.*, 2015, **44**, 3431–3473.

45 H. Hug, M. Bader, P. Mair and T. Glatzel, *Appl. Energy*, 2014, **115**, 216–225.

Chapter 4 Red-Shifted Dyes for p-DSSCs

4.1 Triphenylamine-based donor-acceptor dyes for DSSCs

With thanks to Anil Reddy Mari from the Fielden Group at the University of East Anglia, for provision of as-synthesised dyes **JF1**, **JF2** and **JF3** as well as their corresponding electrochemical characterisations. All other work was undertaken by the author of this Thesis.

4.1.1 Background

4.1.1.1 Push-pull dyes

As discussed previously, dyed photocathodes used in tandem devices must harvest light in the upper wavelengths of the visible light spectrum (>650 nm) in order to reduce spectral overlap with their n-type counterparts. Alongside this, other design criteria must be considered, such as high molar absorption coefficients, suitable redox potentials, and improved charge separation. These criteria can be satisfied by designing the dye structure to encompass these features. Some of the earliest organic dyes designed for photocathodes were perylene based, one of which was functionalised with an NDI

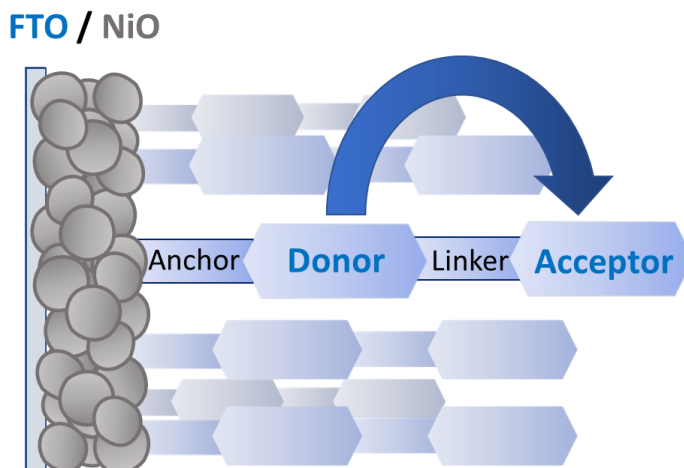


Figure 1: Representation of the principal components of a donor-acceptor dye bound to a NiO surface. The blue arrow represents the direction of electron transport through the dye.

acceptor group. Between dyes **A** and **B**, a long-lived charge-separated state was discovered upon addition of the electron acceptor moiety. This extended lifetime reduces the charge recombination between the dye and NiO valence band. The device parameter measurements for this proof-of-concept dye series were not published, but the APCE values demonstrated an increase from 15 to 45 % with the addition of the NDI.¹

This preliminary work was critical in highlighting the effect of an acceptor moiety on performance, affecting the future of the design and integration of p-type dyes. This development in p-type dye design demonstrated a ‘push-pull’ system, in which both electron withdrawing and electron donating species are incorporated into dye structures in order to define the charge separated states. Another example of this has already been described in Chapter 3, but for p-type dye systems the direction of the charge separated state is reversed. As shown in Figure 1, the donor- π -acceptor (D- π -A) system draws electron density from the semiconductor surface, rather than the electrolyte. Several D- π -A systems have already been described in literature, with the highest performing NiO devices based on dual-purpose carboxylic acid modified triphenylamines working as both the electron donor and the anchoring group, as shown above. Most p-type dyes are based on the TPA moiety and utilise π conjugated linkers to establish a charge separated excited state. The acceptors for these dyes range from large complex chromophores down to simple units such as vinyl cyano moieties. The dye **P1** is one example, discussed below, and is used as a baseline in both this section, and other work presented in this thesis.^{2,3}

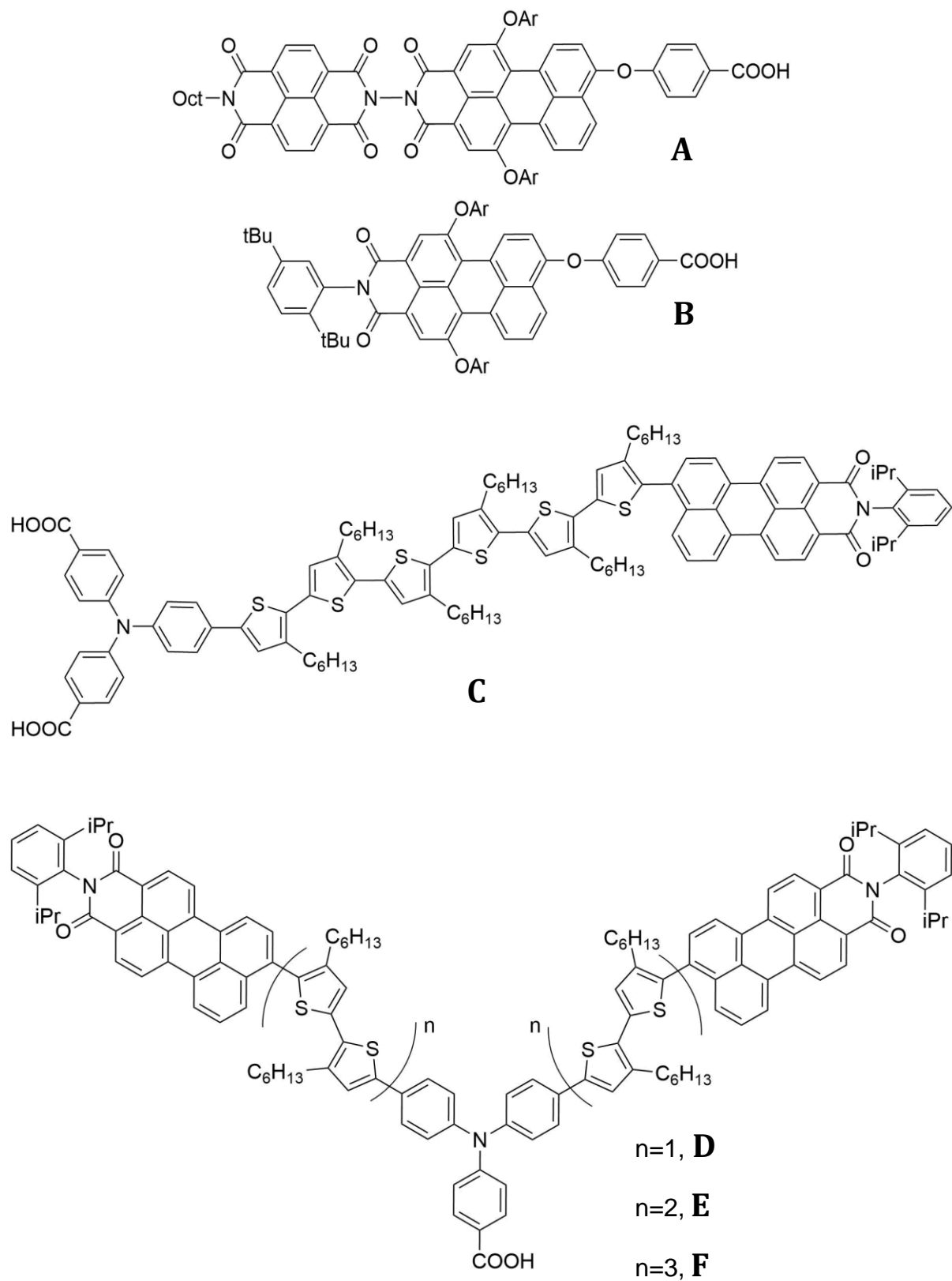


Figure 2: Structures of p-type dyes **A-F** containing perylene acceptor groups.

Dye	Literature Name	Reference	$J_{sc} / \text{mA cm}^{-2}$	V_{oc} / mV	FF	$\eta/\%$
C	PM1-6T-TPA	4	7.65	645	0.51	2.51
	I ₂ electrolyte		6.26	243	0.39	0.60
D	BH2	5	4.3	97	0.31	0.13
E	BH4	5	7.4	128	0.30	0.28
F	BH6	5	4.4	95	0.31	0.13
G	P1	3	2.51	110	0.29	0.08
H	O2	6	1.43	94	0.37	0.05
I	O7	6	1.74	90	0.38	0.06
J	QT-1	7	8.2	120	0.34	0.33
K	CAD 1	8	3.32	87	0.33	0.09
L	CAD 2	8	3.25	96	0.33	0.10
M	CAD 3	9	8.21	101	0.31	0.25
N	GS1	9	5.87	106	0.31	0.20

Table 1: Summary of the performances of the p-type devices using dyes described in this section.

The perylene backbone described above was adopted as an acceptor group by Bach et. al, using a triphenylamine donor with two carboxylic acid anchoring groups, as well as a varying amount of oligothiophene spacer units. ⁴ By increasing the length of the linker unit, the separation between the donor and acceptor moieties increased, which extended the lifetime of the charge separated state, and therefore the performance of the devices increased. Dye **C** is known as PMI-6T-TPA, indicating the presence of the PMI acceptor, six thiophene unit linkers, and TPA donor. This dye was investigated further and a landmark paper was published in 2015 presenting a NiO p-DSSC with an efficiency of 2.51%. ⁴ This record efficiency was achieved via the application of the [Fe(acac)₃]^{0/1-} electrolyte, which increased the photocurrent output of the device to 7.65 mA cm⁻². Table

1 also lists the performance of dye **C** upon application with a simple I_2/I_3^- electrolyte, in order to facilitate comparison with the work in this thesis.

The success of the TPA donor group lies in its functionality. It can serve as a skeleton that can be modified with additional groups using simple chemistry. The TPA can be functionalised with combinations of anchoring, linker or acceptor groups in order to satisfy the 'design criteria' for the dye. For example, the dye may contain two acceptors and one anchoring group, or two anchor and one acceptor. The record PMI-6T-TPA dye was used as a basis for TPA-donor, double-acceptor analogues in a series of dyes with extended thiophene chains. By adding two acceptor groups, the molar extinction coefficients were increased compared to dye **C**, and the extension of thiophene chain length further compounded this effect through the series ($\epsilon = 64,580, 89,830, \text{ and } 99,980$ for Dyes **D**, **E** and **F** respectively).⁵ Comparison of device performance between the two publications is not straightforward due to the use of different redox electrolyte environments, as the favourable energetic alignment of the $[Fe(acac)_3]^{0/1-}$ redox potentials boosted photovoltage using dye **C** to over 600 mV.⁴ The work by Click et al. found that there was a trade-off between increasing the absorption of the dye and improving dye loading.⁵ While the single anchoring group was deemed sufficient for dye uptake by the NiO surface, the large steric bulk of the dyes became a limiting factor in efforts to dye the film. Additionally, the chain length may have an impact in determining recombination rates between the acceptor and the NiO surface. Longer chain lengths of six oligothiophenes could also allow for higher degrees of rotational freedom in terms of molecular orientation, possibly leading to contact between the acceptor and surface. Conversely, a shorter chain may not be sufficient to shield the NiO surface from interaction with the redox couple. Both scenarios are detrimental to device efficiency, so a compromise of four linker units is thought to be optimal.

4.1.1.2 Simple Organic Donor-Acceptor Dyes in p-Type Devices

Perylene acceptors are well established as key dye components in high-performing devices. However, other electron accepting groups have been investigated to pair with the TPA donor to make perylene-free p-type dyes. The first of these alternatives is Dye **G**, known as P1. Developed by Sun et al. in 2008, it incorporated the TPA donor, two oligothiophene spacers, and a pair of dicyanovylene acceptors.³ At the time, this dye produced unprecedented IPCE values of around 35 % at wavelengths between 450 - 600

nm. The dye served as a start point for push-pull dye systems and demonstrated that simple, well considered dye designs can perform in p-type devices. After the work with dye **G**, the single acceptor, double anchor analogue was published by Ji et al. three years later. ⁶ The analogue dye **H** performed similarly in devices to those containing unoptimized **G** with overall efficiencies reaching 0.05 %. The effect of the linker on device performance was the key focus of this paper, therefore optimisation of other device parameters was not undertaken in this case. However, investigation of the dye **I**, an analogue containing a 3,4-ethoxythiophene (EDOT) linker, uncovered increased IPCE and therefore overall J_{sc} values due to the increased driving force for regeneration of the dye by electrolyte. In the same year, Zhang et al modified Dye **H** by substituting the thiophene linker with a quinoidal thiophene bridge to produce dye **J**. The reasoning was that the bridge would force the dye into a rigid, planar π system with good separation of the donor and acceptor. The small steric bulk of the dye also allowed more of the dye to load on the NiO surface than Perylene based dyes. The dye performed well in devices, with an increase in reported current up to 8.2 mA cm^{-2} using an optimised iodine electrolyte, leading to an overall efficiency of 0.33 %, values attributed to the increased intramolecular charge transfer yielding high molar absorptivity. ⁷ In 2014, two near-IR absorbing dyes were produced and tested by Wood and collaborators. Cationic acceptor dyes **K** and **L** had absorption peaks at 558 and 586 nm respectively making them ideal sensitizers for use in tandem devices. However, they both had similar performances. While Dye **L** had a marginal increase in photocurrent density, the steric bulk of the dye decreased dye loading and therefore impaired the light harvesting capability of the photocathode. However, the increased bulk is beneficial for reducing charge recombination between the electrolyte and the NiO, making up for this deficit. ⁸ Development of these dye structures by Wood et al. used an additional indolium acceptor to attempt to push the photoresponse of the dye system towards red.

Dye loading of **M** was still lower than that of dye **G** due to its steric bulk, but the overall performance of the individual p-DSSC was promising with a photocurrent response of 8.2 mA cm^{-2} . ⁹ A fourth dye was also synthesised as a single-acceptor analogue to **M**. The new dye in the study, **N**, utilised a dicarboxypyrrole moiety along with a single indolium acceptor, and found that while dye loading effectively doubled, the recombination rate for this analogue was much higher than that of dye **M**. This served to provide some

evidence that the increased performance for **M** was due to the limitation of recombination pathways through dye design.¹⁰

Previous to the work in this thesis, a series of dyes with both pyridinium and dicyano acceptors were synthesised and their p-type device parameters characterised in order to systematically investigate both the effects of the number of anchors and acceptors, and the nature of the acceptor group itself. A pyridyl functionalized triaryl amine is used as both the foundation and anchoring group for the dyes. Dye **O** was previously synthesised in work by Cui et al,¹¹ and the dicyano acceptor group was used in the first series. A set of analogues with a pyridinium moiety was also prepared. The dyes included the two moieties (either dicyano or pyridinium) incorporated in three ways: a pair directly upon the triarylamine (Dyes **O** and **R**), a pair separated by a phenyl group (Dyes **P** and **S**), or a mono-acceptor with two phenyl pyridine binders (Dyes **Q** and **T**).¹²

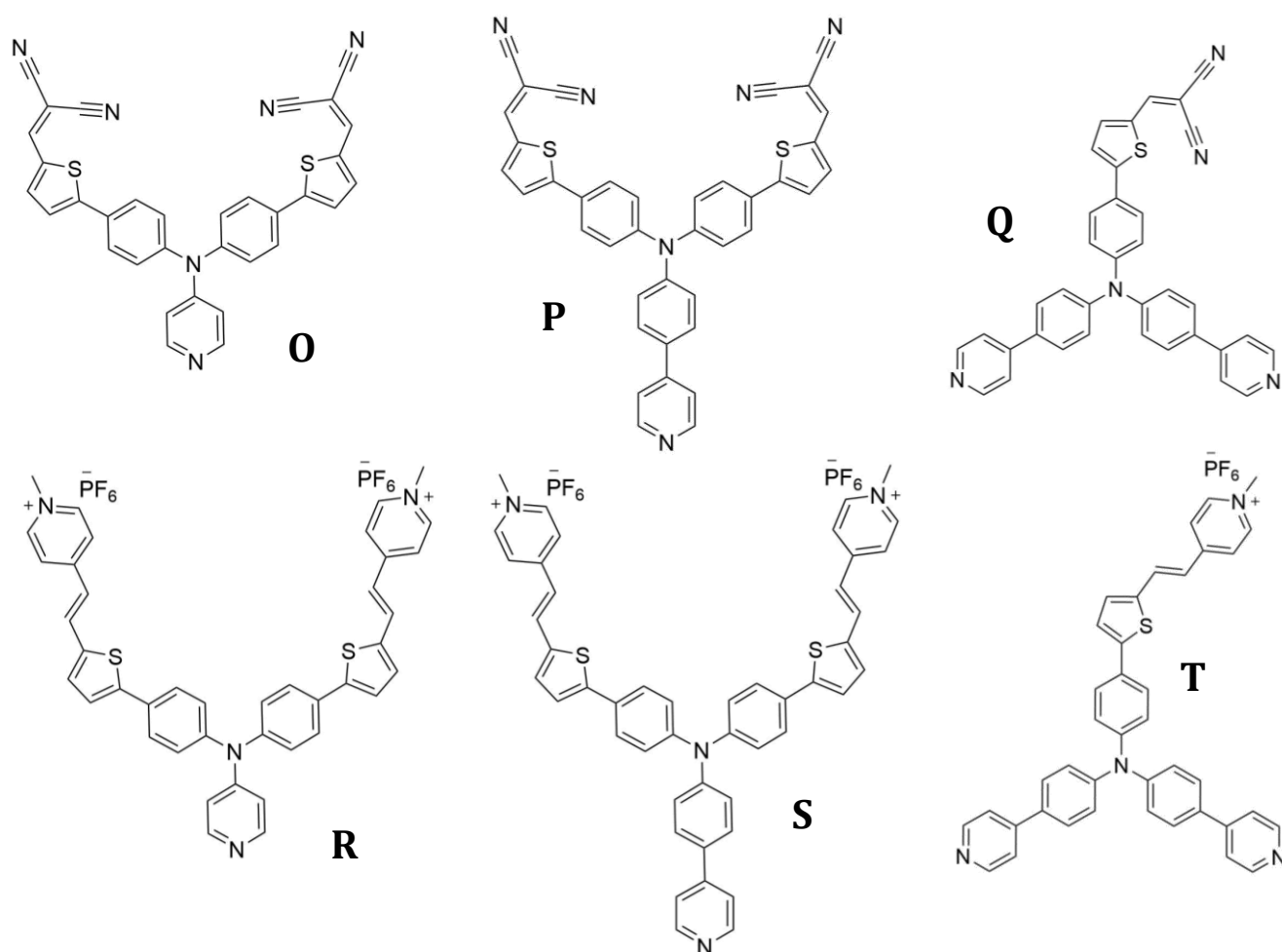


Figure 4: Structures of TPA-based dyes produced by Fielden et. al, including both pyridinium and dicyano acceptor analogues.¹²

A summary of the device performances using these dyes can be seen in Table 2. The pyridinium series gave increased extinction coefficients had broader absorption spectra, allowing for greater light harvesting. DFT calculations also suggested better spatial separation of the HOMO and LUMO, therefore indicating improved charge separation. This allowed the dyes **R** and **T** to produce identical PCE to the equivalent dicyano systems **O** and **Q**, despite lower dye uptake. However, the best performance ($\eta = 0.06\%$) arose from the previously studied bis-dicyano, mono-pyridyl architecture of dye **P**. It was thought that the bulky, doubly cationic pyridinium dye limited the dye loading of **S**, reducing the device output. However, the APCE measurements of **S** showed that the pyridinium acceptor could be used in simple to synthesise molecules, as long as they were paired with a counterion to improve dye loading.¹²

The work described in this section is a continuation of the work with the indolium acceptors previously described, along with the TPA donor group and pyridine anchor skeleton established by collaborators.

Dye	$J_{sc} / \text{mA cm}^{-2}$	V_{oc} / mV	FF	$\eta/\%$
O	0.83	50	43	0.018
P	1.6	103	36	0.06
Q	0.87	49	32	0.014
R	0.83	66	33	0.018
S	1.11	86	37	0.036
T	0.84	70	23	0.014

Table 2: Summary of the performances of the p-type devices using dyes **O-T** previously published by Fielden et al.¹²

4.1.2 Results

The dyes **JF1-3** were synthesised using commercially available starting materials by A. R. Mari via established literature strategies.¹¹ In brief, for dye **JF1**, Knoevenagel condensation was used to connect diphenylamine to the indolium acceptor. Dyes **JF2** and **JF3** used the same method but utilised 4-bromotriphenylamine to produce the derivatised triarylamine moieties. The dyes were characterised using NMR, elemental analysis and mass spec, by A.R. Mari, London Metropolitan University, and the UK National Mass Spectrometry Service at Swansea University respectively. The properties of the dyes and their performances in NiO-based DSSCs is discussed below.

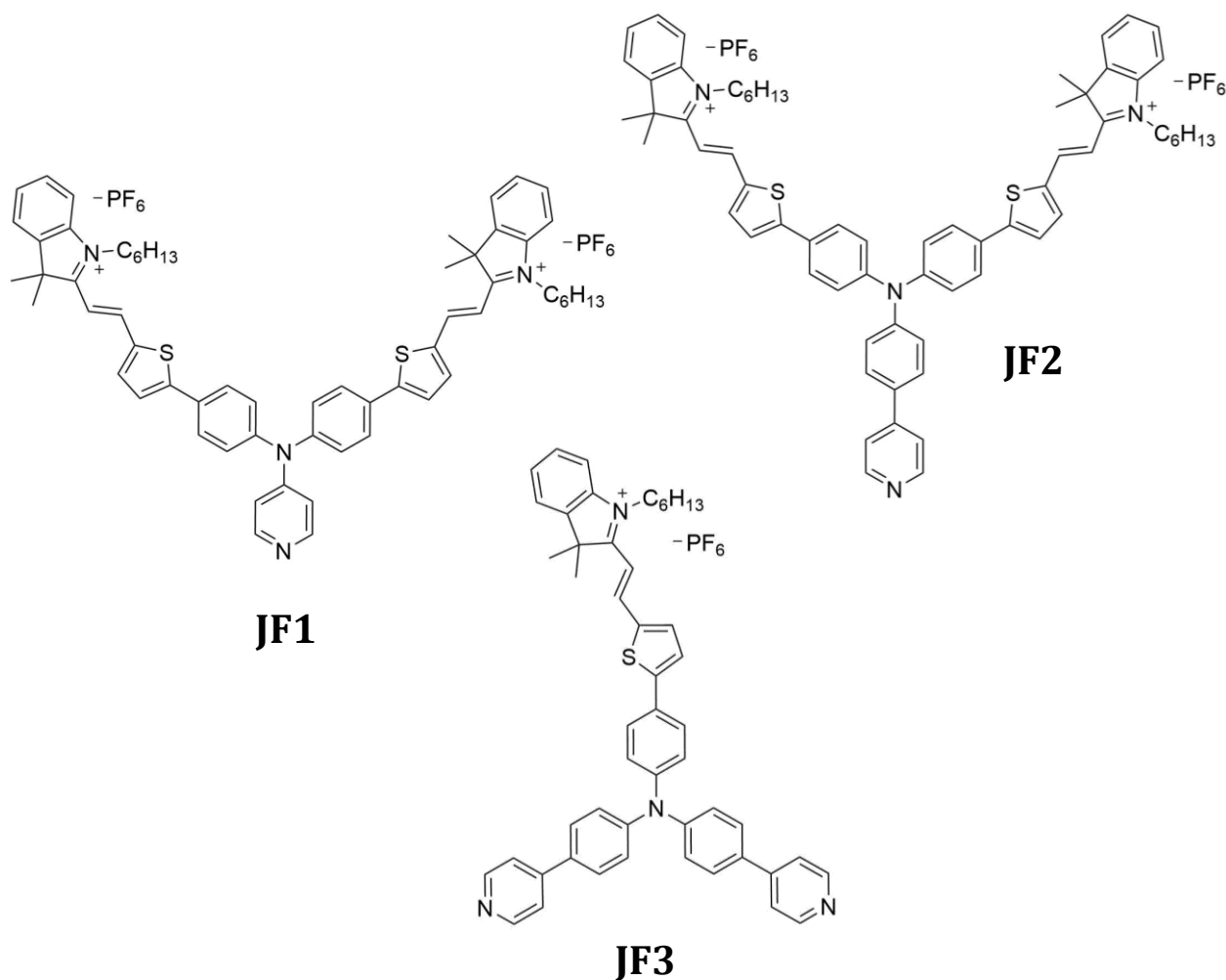


Figure 5: Structures of the dyes 1-3 examined in this work.

4.1.2.1 Optical and Electrochemical Properties

UV-Visible absorption spectra of the dyes in acetonitrile are shown in Figure 6 and full characterisation data of each dye is summarised in Table 3. All three dyes show intense, low energy absorption (ranging between 500-600 nm) that are assigned to intramolecular charge transfer (ICT) from the donor triarylamine group to the indolium acceptor. This peak undergoes a red shift of around 50 nm upon replacement of the pyridyl binding group of **JF1** with the phenyl pyridyl of **JF2**. Increasing the spatial separation between the components has led to a reduction of electron withdrawing capacity of the acceptor. In contrast, dye **JF3** is less red-shifted than **JF2** due to the cumulative effects of the two weakly electron withdrawing phenylpyridyl groups. The molar absorption coefficients associated to this intense band are larger in dyes **JF1** and **JF2** due to the presence of two acceptor groups, compared to the mono-acceptor dye **JF3**. In the higher energy regions, weaker absorptions assigned to π - π^* transitions can be observed. The peak at 350 nm is notably only observed in dyes **JF2** and **JF3**. With the intensity of the peak increased for the bis-phenylpyridyl dye **JF3**, which suggests the transition is due to the presence of the phenyl pyridine moieties. The dyes were found to be only weakly emissive with Stokes shifts of roughly 250 nm versus λ_{max} .

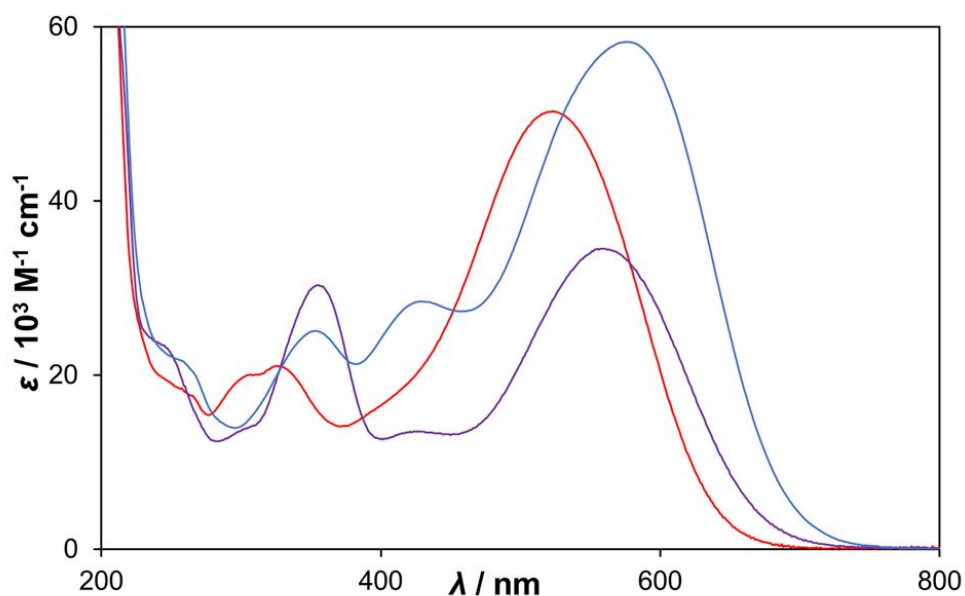


Figure 6: UV-Visible spectrum of dyes **JF1** (red), **JF2** (blue) and **JF3** (purple) in dry MeCN. Figure reproduced from Paper 4.

Electrochemical analysis of all the dyes in solution via cyclic voltammetry revealed irreversible reduction peaks at around -0.25 V vs NHE. These peaks were assigned to the indolium acceptor and are within range of previously reported indolium dyes.^{8,11,12} Since this value is significantly less negative than similar pyridinium and dicyano acceptor dyes, the acceptor strength of the imidazole is proven to be much stronger. Comparing the reduction potential within this series shows a decrease in potential from dyes **1** through to **3**. As the donor group becomes more electron rich, as is the case with the extended phenyl spacer reducing the withdrawing effect in dye **2**, the potential becomes more negative. Additionally, with only the single indolium acceptor unit such as in dye **3**, the reduction becomes yet more negative, indicating a weak influence of the donor upon the reduction potential of the acceptor.

The oxidation of the donor was found to be at much more positive potentials compared to dye systems with weaker acceptor groups and are all more positive than the VB of NiO, making them favourable for hole transfer to the semiconductor. However, the electron transfer from the dye acceptors to the iodine redox couple, while still favourable, provides significantly less driving force and will be pertinent to the analyses of the dyes in devices.

Dye	λ_{max} (nm)	λ_{em} (nm)	E_{0-0} (eV)	E_{pa} vs NHE (V)	E_{pc} vs NHE (V)	HOMO vs NHE (V)
JF1	523	745	2.02	1.54	-0.23	1.79
JF2	578	856	1.81	1.40	-0.24	1.57
JF3	561	852	1.85	1.44	-0.28	1.57

Table 4: A summary of energy transitions for the **JF** series. Absorption and emission maxima (λ_{max} and λ_{em}), with the E_{0-0} calculated (for **JF2** and **JF3**) from the intersection between the normalised absorption and emission spectra or (for **JF1**) from the midpoint between absorption and emission peaks. Electrochemical data including values for E_{pa} for E_{pc} obtained via cyclic voltammetry (1mM analyte, 0.1 M NBu_4BF_4 in MeCN against Fc/Fc^+ reference, scan rate of $100mV s^{-1}$) and converted to NHE using $Fc/Fc^+ = 0.69 V$ vs NHE.

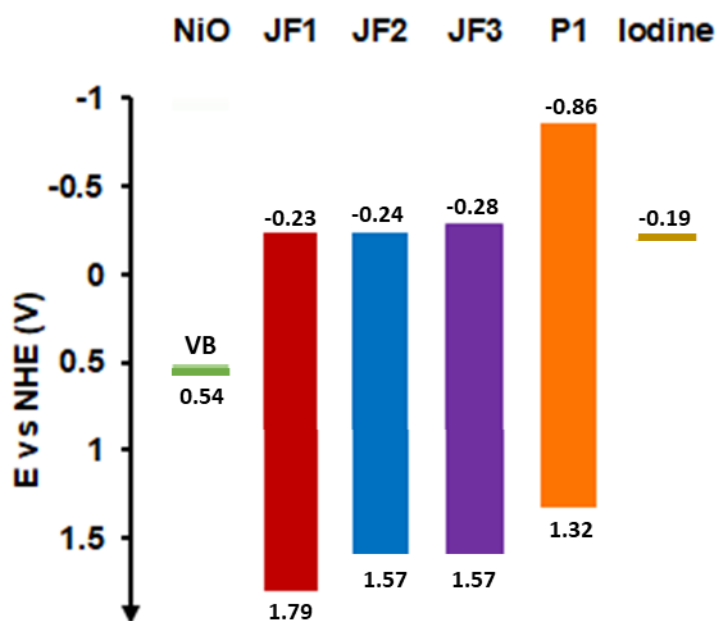


Figure 7: Relative potentials of the **JF** series HOMO and LUMO relative to the NiO valence band edge and I^-/I_3^- redox couple.

4.1.2.2 Dye Loading

Fig. 8 shows the absorption spectra of **JF1** to **JF3** on 3-layer NiO films after immersion for 48 hours. The intermolecular charge transfer peaks have broadened slightly compared to the solution spectra, but the transitions are still defined. By calculating dye loadings using the average change in absorbance of the dyebaths, it was shown that each of the cationic dyes **JF1** to **JF3** load poorly compared to **P1** (which is negatively charged upon deprotonation), which is consistent with repulsion from the positively charged NiO surface.

Dye	λ_{max} (nm)	ϵ ($M^{-1}cm^{-1}$)	Dye loading ($nmol\ cm^{-2}$)
JF1	523	49,900	6.31
JF2	578	58,300	4.32
JF3	561	34,300	6.46
P1	461	58,000 [17]	8.48

Table 5: Absorption maxima (λ_{max}), molar extinction coefficients (ϵ) and calculated loading quantities of dyes **JF1-3** onto 3 layer NiO films. Further details of dye loading experimental setup can be found in Section 4.3.

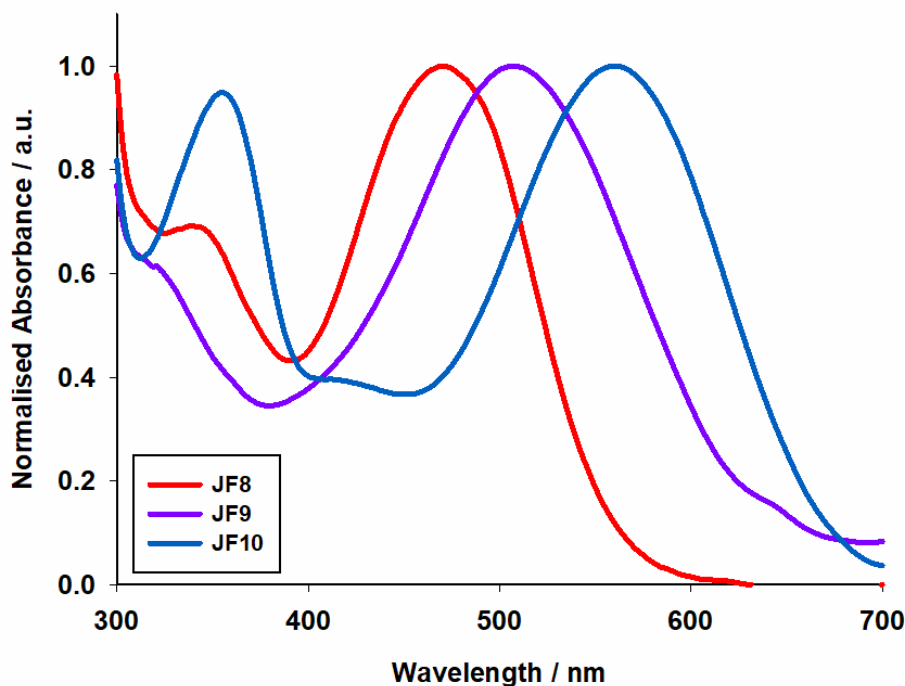


Figure 8: UV-vis spectra of 1 to 3 on 3-layer NiO films, with the spectral response of NiO taken as a background reading.

These results confirm previous findings that dye loading is an important limitation to the performance of p-DSSCs based on cationic dyes and suggest that a complex range of factors must influence loading, including the space required by the dye at the surface and the basicity of the pyridine anchoring group, and the molecular charge of the dye.

4.1.2.3 P-type Devices

The photovoltaic performance of the dye series **JF1-3**, as well as **P1** as the reference TPA-based dye, was assessed in NiO devices using an I_2/I_3^- redox mediator. J/V profiles of the champion devices resulting from this testing are shown in Figures 9 and 10, and the device parameters summarised in Table 6. It can be seen that all of the pyridine anchored dyes investigated here have high V_{oc} values relative to the **P1** reference. High V_{oc} has previously been found for pyridine anchored dicyano dyes, and understood as a consequence of the binding mechanism of the anchoring group to the NiO. The electron donating character of the pyridinium anchor will push the Fermi level of the NiO upwards towards the conduction band. This will increase the potential difference between the fermi level and the redox potential of the electrolyte. The increased V_{oc} , in conjunction with

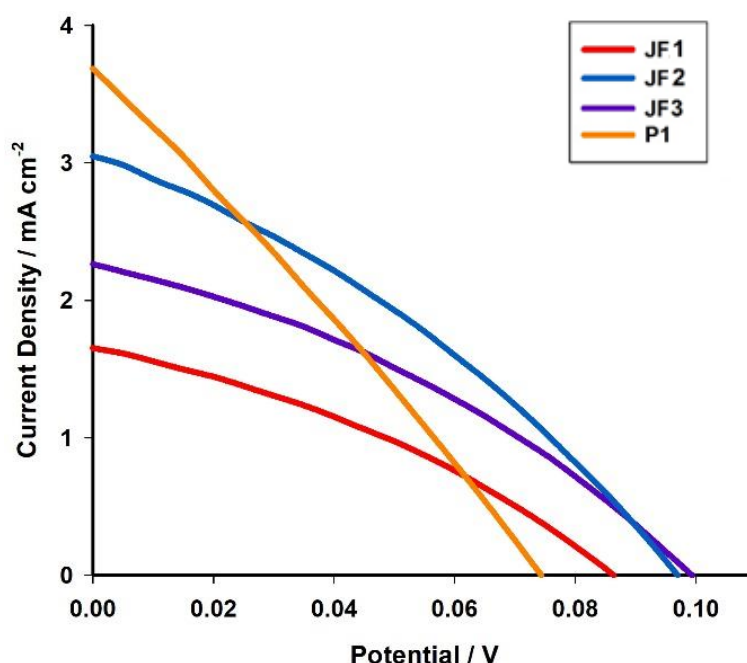


Figure 9: Plot of current density against voltage for illuminated devices containing dyes **JF1-3** and the reference dye **P1**. Electrolyte composition: 0.1 M LiI and 1 M I₂ in dry MeCN.

improved fill factors, enables the best performing indolium dye, **JF2**, to reach a higher power conversion efficiency (PCE, $\eta = 0.097\%$) than **P1**, despite lower J_{sc} . This phenylpyridyl *bis*-indolium dye's good performance is consistent with the findings described in section 4.1.1.2 for its dicyano (dye **P**) and pyridinium (dye **S**) analogues. However, key properties of the indolium have boosted the J_{sc} values of the devices to such a degree that the efficiency of the devices was improved by as much as 1.5 x and 3 x times more than its dicyano and pyridinium alternatives respectively. The improved J_{sc} values can be ascribed to improved and red-shifted light absorption properties of the indolium system, as well as reduced recombination at the dye interface due to the presence of the long alkyl chain acceptor.

As stated above, trends within this dye series reflect previous findings with the pyridinium analogues,¹² but with improved results for all structures using the new indolium acceptor. Between indolium dyes **JF1** and **JF2**, there is a more than 100 % increase in efficiency, attributed to the additional spacer units in the anchoring moiety reducing recombination pathways in the device and improving dye loading. While the pyridinium- and dicyano- acceptor analogues (dyes **Q** and **T** respectively) of the bis-

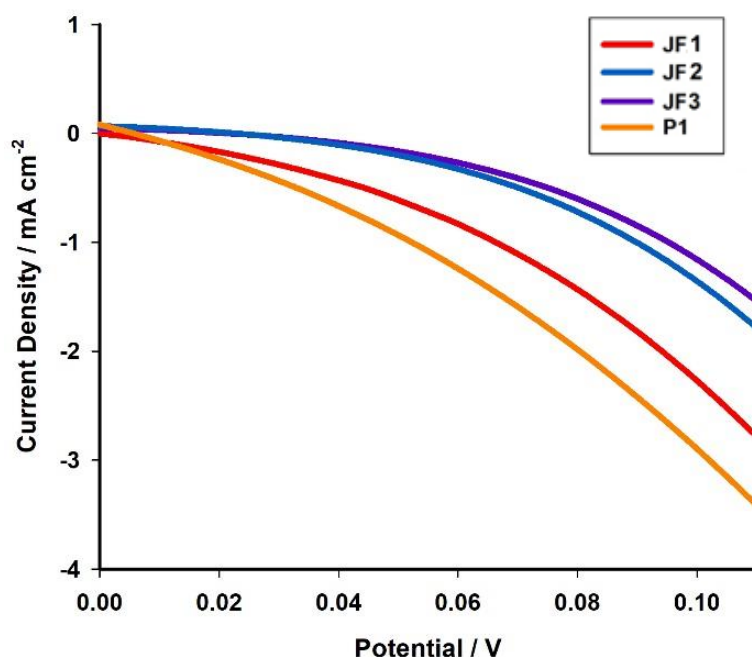


Figure 10: Plot of current density against voltage for devices in the dark containing dyes **JF1-3** and the reference dye **P1**. Electrolyte composition: 0.1 M LiI and 1 M I₂ in dry MeCN.

anchored dye **JF3** performed poorly, the indolium acceptor used in this work boosted performance when applied to devices. This could be due to several factors, including the marked increase in dye loading. The stronger indolium acceptor could also be facilitating unidirectional charge transfer within the molecule, yet TD-DFT calculations did not yield huge disparities between the excited state HOMO or dipole moment changes of dye **Q** and **JF3**. (Paper 4)

Dye	V _{oc} / mV	J _{sc} / mA cm ⁻²	FF / %	η / %
JF1	89	1.65	34	0.044
JF2	97	3.04	33	0.097
JF3	99	2.26	34	0.077
P1	71	3.82	27	0.079

Table 6: Summary of the performances of the p-type devices tested in this section, with **P1** dye as a reference.

In comparison to dyes **JF1** and **JF2**, the redox potential of **JF3** was measured to be 40 mV more negative, lowering the driving forces for electron transfer between the excited state dye and the reduced electrolyte. This could force a trade-off in the mono-acceptor indolium dyes, whereby reduced dye loading of **JF1** and **JF2** is compensated for with an increase in electron transfer driving forces. This demonstrates that while dyes with an indolium acceptor may produce significant improvements to performance compared to their pyridinium analogues, the strength of the acceptor is not the only factor for improving performance. Therefore, a tailored approach to the entire dye design is more suitable, with a balanced approach to the nature of the donor acceptor structure, absorption and redox chemistry required to secure the devices' success.

4.1.3 Conclusions

The effects of different electron acceptor moieties in simple organic dyes has been a focus of investigation in recent literature.^{12,13} A series of dyes based on triarylamine cores, indolium acceptors and pyridine anchors have been successfully synthesized and characterized by collaborators at the University of East Anglia. TD-DFT calculations indicated an ideal combination of strong donor-acceptor communication, and a high degree of charge separation in the excited state. This, along with the dyes' high extinction coefficients and extended absorption profiles made them promising candidates for investigation in p-DSSCs.

Prior work with dicyano- and pyridinium acceptors in a series of configurations followed a trend in device performance that was reflected in this work. Dye **JF2**, boasting an architecture combining two indolium acceptor groups with a phenyl pyridine anchor, resulted in devices with the best performance of the series, and indeed surpassed those in the previous study ($\eta = 0.097\%$). This is attributed the absorption profiles of this series of dyes extending to almost 700 nm, further than those examined in previous studies.¹² However, limitations to device performance arose through poor dye loading, which limited the absorption capability of the device, and weak driving forces for reduction of the electrolyte by the indolium acceptor. In comparison to a previously reported dye with an indolium acceptor that anchors through carboxylic acid group, the dye loading of this series is lower by a factor of 1000.⁸ It could be argued that the indolium dyes presented here demonstrate the upper limit of what can be improved via increasing acceptor

strength only, and for a step-change in efficiency, an overhaul of the entire dye design may be required.

4.2 A Near-IR absorbing BODIPY dye for p-DSSC

4.2.1 Background

As discussed in previous sections, dye properties have a great influence upon DSSC performance and longevity. The established donor-acceptor structure described previously in this chapter usually, for dyes in p-type devices, uses a functionalised TPA as a donor group. The findings in Section 4.1 show that to find simple absorber structures that perform well in devices, a new approach should be undertaken. One such approach is via a new dye architecture, using functionalised 4,4-difluoro-4-bora-3a,4a-diaza-s-indacene (BODIPY) absorbers.

4.2.1.1 BODIPY Dyes as Near IR Absorbers

BODIPY dyes are well established in terms of synthetic route and real-world applications, in areas such as fluorescent markers for therapy, commercial dyes, chemical sensing and OLEDs.^{14,15} The group lends itself to these applications due to its extremely high molar extinction coefficient, fluorescence quantum yields, vibrant colouring, and relative stability. The method for producing the BODIPY core (shown with annotations in Figure 11) remains mostly unchanged since its establishment by Treibs et al. in 1968.¹⁶ Briefly, the core is synthesised by acid-catalysed condensation of two pyrroles with an acid chloride or anhydride to form a dipyrromethene frame. Alternatively, an aldehyde can be used in the condensation and the intermediate subsequently oxidised using DDQ (2,3-Dichloro-5,6-dicyano-1,4-benzoquinone) or p-chloranil to produce the frame.¹⁷ The next steps for both cases is deprotonation, followed by chelation of the dipyrromethene with $\text{BF}_3 \cdot \text{Et}_2\text{O}$. By modifying the starting products, large structural changes can be made to the

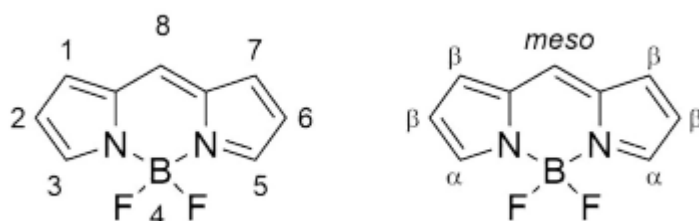


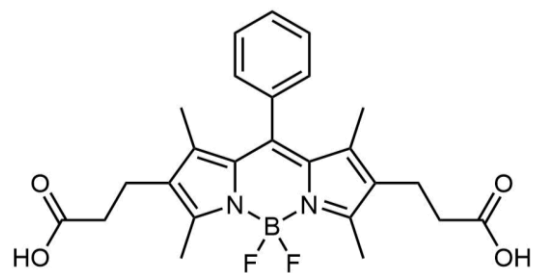
Figure 11: Structure of the 4,4-difluoro-4-bora-3a,4a-diaza-s-indacene (BODIPY) core described by both numeric and alphabetic notations.

resulting molecule without dramatic changes to the synthetic procedure. There have been very few examples of BODIPY based dyes used in photovoltaic applications. Over ten years ago, the first BODIPY dye (Figure 12) was integrated into n-type DSSCs by Fukuzimi et al.¹⁸ They demonstrated that photoexcitation of the fluorescent BODIPY moiety resulted in direct electron injection from the singlet excited state of the dye, which lead to the photocurrent generation. While performance was low, this proof-of concept inspired the development of BODIPY dyes optimised to this application.¹⁴ Kubo et al. produced a series of dyes containing thienyl-cyanoacrylic acid units with excellent light harvesting capabilities. They argued that this was the reason for the increased performance of their devices, in spite of the fact that their molecules contained no strong donor moiety.¹⁹ They demonstrated a step change in efficiency, doubling the then-record to just over 6%. However, the record n-type DSSC utilising BODIPY dyes was published later that year.

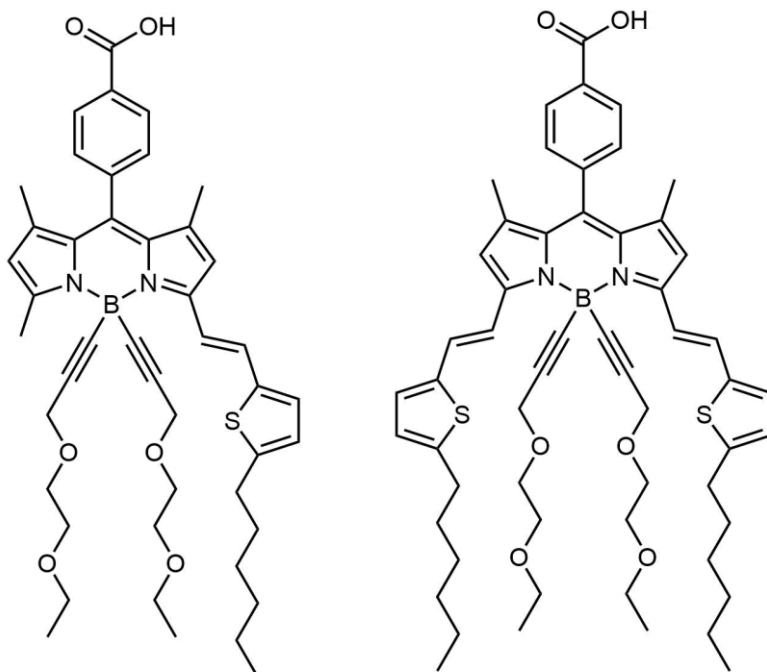
In 2014, Ziessel et al. demonstrated a series of NIR absorbing BODIPYs that included both long alkoxy groups stemming from the Boron atom, and extended styryl substituents in the α positions. One drawback of BODIPY sensitiser with their intense absorption peaks is the lack of broad light harvesting capabilities.

Dye Name	Reference		Abs λ_{max}	V_{oc} / mV	J_{sc} / mA cm ⁻²	FF / %	η / %
PHBDP- COOH	18	TiO ₂	524	464	0.49	0.71	0.16
T₂P₂A	20	TiO ₂	666	544	15.78	0.67	5.75
TP₂A	20	TiO ₂	581	526	11.40	0.71	4.26
T₂P₂A + TP₂A	20	TiO ₂	-	570	16.23	0.69	6.43
KUBO Dye 2	19	TiO ₂	660	540	19.02	0.59	6.06
P1BODIPY	21	NiO	540	79	3.15	0.31	0.08
GS1	9	NiO	565	106	5.87	0.31	0.20
BODIPY Acid	22	NiO	730	79	0.61	0.25	0.01

Table 7: Summary of key BODIPY-based photosensitisers described in this section, along with the substrate material tested on.

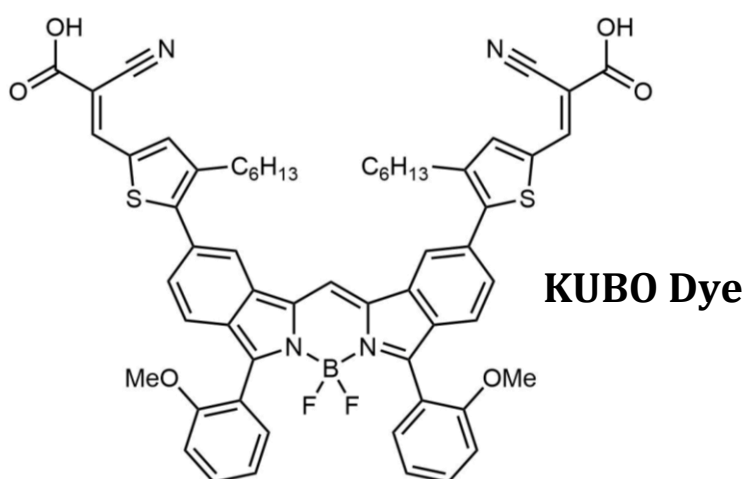


PHBDP-COOH



TP₂A

T₂P₂A



KUBO Dye

Figure 12: Structures of BODIPY sensitisers used in *n*-type DSSCs described in this section

Therefore, the group co-sensitised their photoanode with two complimentary dyes, and increased the devices' spectral response. This resulted in a device with an IPCE over 70% at 750 nm, narrowly surpassing the record set by Kubo and reaching an efficiency of 6.43%.¹⁹

From the established work in n-DSSCs, several properties have been highlighted that have indicated the BODIPY moieties' suitability for application in p-type devices. Their versatility, especially in terms of red-shifting absorption beyond 600nm, has been demonstrated, and modifications to the core can be done fairly simply, synthetically.

The first instance of p-type DSSC that utilised a BODIPY-based chromophore was published in 2014.²¹ Known as **P1-BODIPY**, it consisted of two fully substituted BODIPY cores, with a triphenylamine donor and anchoring group connected through the meso position (Figure 13). Using the TPA-based skeleton allowed for direct comparison to **P1**, and the dyes' molar extinction coefficient was almost double than that of **P1**. However, efficiency was almost half of that of **P1** devices in similar conditions.²³ This could be due to poor electronic communication between the donor and acceptor in the **P1-BODIPY** molecule, attributed to an electronically deactivated meso position. Rotation of the bond between the acceptor and linker causes the BODIPY and thiophene to become almost perpendicular, decoupling the orbitals involved in electron transfer, and blocking charge transport. To study this effect, a new analogue was produced where methyl groups in the 1,7 and 3,5 positions were replaced with hydrogen and phenyl rings respectively. The lack of steric hindrance in the 1,7 positions allow the molecule to align into a more planar orientation, facilitating charge transfer. The new molecule, named **GS1**, was bathochromically shifted in absorption and achieved a device efficiency of 0.2 %.⁹

In 2019, Kubo et al. produced an extremely red-shifted BODIPY, with anchoring groups stemming from the 3,5 positions.²² Extended pi-systems were added to the beta positions to push the absorption into the NIR. Tailing at 830 nm, it was an ideal NIR absorber, and the IPCE photocurrent response reflected this. However, overall device efficiencies were very low, due to the low band gap of the photosensitiser allowing for rapid recombination between the reduced dye and the NiO surface. The group suggested that a different redox electrolyte may improve performance, but in order to reduce the recombination between the semiconductor and dye, there may be other structural modifications of the dye to be made first.

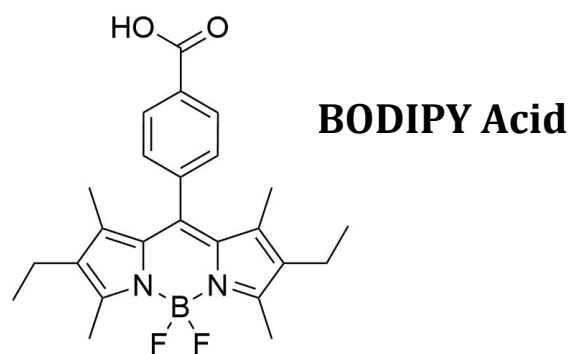
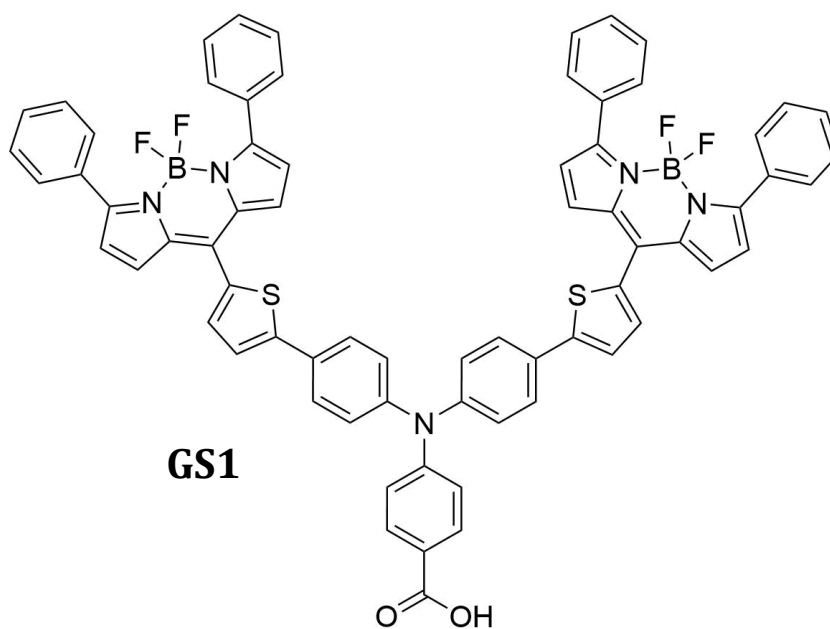
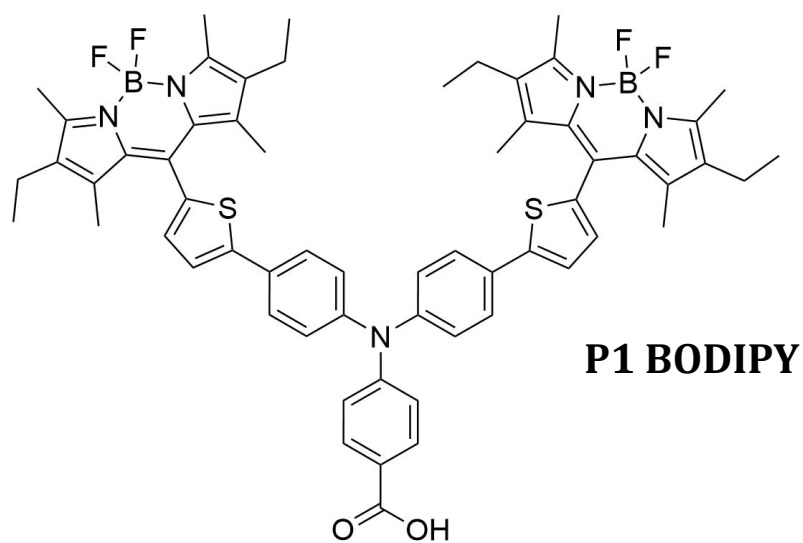


Figure 13: Structures of BODIPY sensitizers used in p-type DSSCs described in this section.

In order to create a red-shifted dye with extended charge separated lifetime, the BODIPY core will be incorporated into the donor- pi- acceptor configuration without the TPA donor, in order to streamline charge transfer. As discussed previously in this chapter, merely changing the donor group opens up little in terms of performance, at the cost of more complex synthetic routes and less- green reactions. In this work, a combined approach has been undertaken via the modification of a red-shifted BODIPY donor chromophore with a sterically bulky, electronegative SF₅ acceptor moiety.

4.2.1.2 The Pentafluorosulfanyl Group

The pentafluorosulfanyl functional group (SF₅) consists of a hypervalent sulfur (VI) in an octahedral configuration with five fluorine atoms and space to functionalise it with another molecule. Sheppard et al. first described the pentafluorosulfanyl moiety in the 1960s, ²⁴ yet the complex synthetic pathways and poor availability of the group commercially meant that its applications were not thoroughly explored. The SF₅ group boasts good chemical and thermal stability, large steric bulk, lipophilicity, and increased electronegativity. It was only in 2012 when Umemoto et al. managed to synthesise the moiety with a 78 % yield, ²⁵ and since, there has been an influx of research into the group with applications in a variety of research areas. ²⁶⁻²⁸

The beneficial properties and new ease of synthesis are why there have been several publications exploring both the chemistry and electron withdrawing effects of this group in chromophores. Golf et al. incorporated the pentafluorosulfanyl group into dipyrromethanes, porphyrins, corroles and BODIPY molecules, proving the groups' chemical stability and tolerance of a variety of reaction conditions. ²⁹ Collaborators from Chapter 3, Zysman-Colman et al., also investigated the groups effects on the phosphorescence of iridium complexes. They remarked that the steric bulk of the group reduced intermolecular interactions in the solid state and increased the solubility of the complex compared to equivalent fluoro- and trifluoromethyl ligands. The stronger electron-withdrawing capability also increased the oxidation potential of the complex and resulted in a hypsochromic shift in the phosphorescence. From 2018 to recently, Chan et al. have produced a series of papers investigating the effect of the SF₅ group in push-pull dye systems. Their seminal paper highlighted six dyes, all containing a triphenyl amine donor and a SF₅ acceptor separated by varied spacer groups. The dyes were analysed computationally, and the push-pull nature elucidated. The HOMO of the

dyes was located on the TPA donor, and the LUMO was found on the SF₅ acceptor.³⁰ Another study highlighted the potential of the SF₅ for application in two-photon acceptor molecules.³¹ Both cases stressed the capability of the SF₅ moiety and a good electron acceptor, making it a promising candidate for this work.

Research utilising this group is still in its infancy, and understandably, none of the current dyes have been reported for application in either n- or p- type DSSC's. In this section, a series of SF₅-BODIPY molecules were synthesised, and the final dye characterised for use in p-type DSSCs. The intermediate **RJ1** contains the electron withdrawing SF₅ moiety in the meso position, and the dye precursor **RJ2** expands this with an extended styryl group to red-shift the absorption. Deprotection of the ester produces carboxylic acid anchoring groups, and results in the final dye structure **RJ3**.

4.2.2 Results

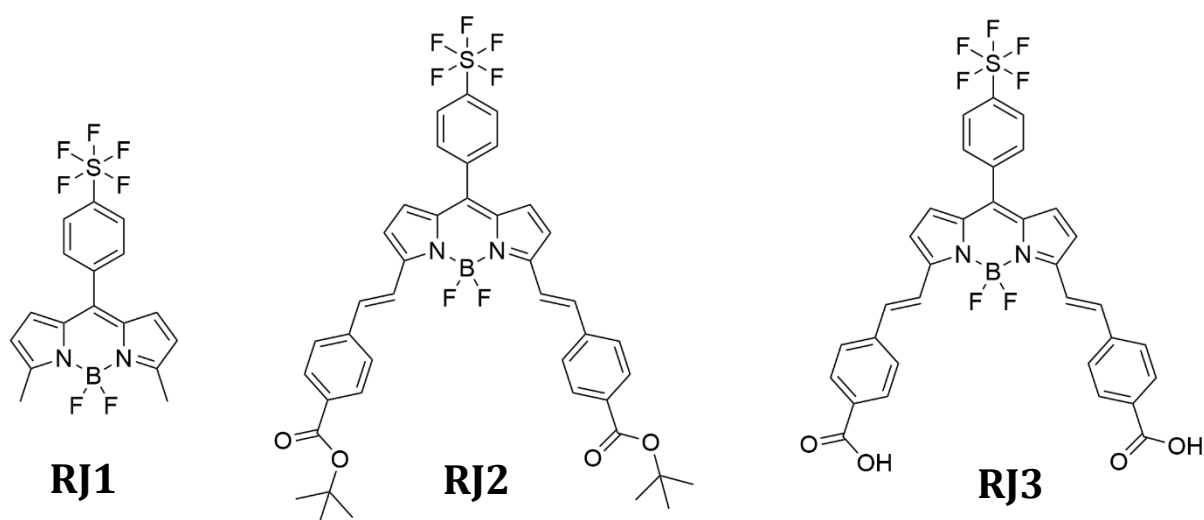


Figure 14: Chemical structures of the dyes **RJ1**, **2** and **3** synthesised in this work.

4.2.2.1 Synthetic Procedures

Figure 13 shows the structures of the three BODIPY compounds produced in this section. Synthesis of these dyes was performed by Richard James and is summarised below.

RJ1 The precursor 2-methyl pyrrole was obtained via literature procedure.³² This was reacted with 4-(pentafluorosulfanyl)benzaldehyde in an acid catalysed condensation reaction, followed by oxidation with p-chloranil. The subsequent deprotonation and chelation steps were performed using diisopropylethylamine and borotrifluoroetherate

respectively in a 1-pot reaction. The product **RJ1** was purified via column chromatography, made straightforward by the high steric bulk of the SF₅ group that reduced π - π stacking, which increased the solubility of the molecule.

To produce **RJ2**, piperidine and acetic acid were used to catalyse a room-temperature Knoevenagel condensation with tert-butyl 4-formylbenzoate over 4 hours. This unconventional room temperature synthesis can be achieved because of the reduced steric hindrance at the BODIPY's meso position, and the beneficial electronegativity of the SF₅ moiety. An analogue with only one styryl arm on the α position was observed as an intermediate during TLC but was not isolated, as the intermediate outcompetes the starting material in terms of reactivity and the condensation occurs preferentially on the intermediate. This resulted in a high-yielding reaction with only trace quantities of unreacted intermediate. Purification using column chromatography led to hydrolysis of **RJ2** by the acidic silica unless a fast column was run. Basifying the column with triphenylamine improved mobility and eliminated this problem. With the general molecular structure established, the addition of carboxylic acid anchoring groups was necessary to bind the molecule to the NiO surface.

Acid hydrolysis of **RJ2** was proceeded with excess tetrafluoroacetic acid which was stirred overnight to give quantitative yields of **RJ3**. The poor solubility of **RJ3** meant that purification by column was unsuitable, but unnecessary as the product spontaneously precipitated. The poor solubility also means that **RJ3** is excluded from most optical characterisation techniques in this section. All three dyes were characterised with NMR and mass spectrometry to confirm.

4.2.2.2 Optical properties

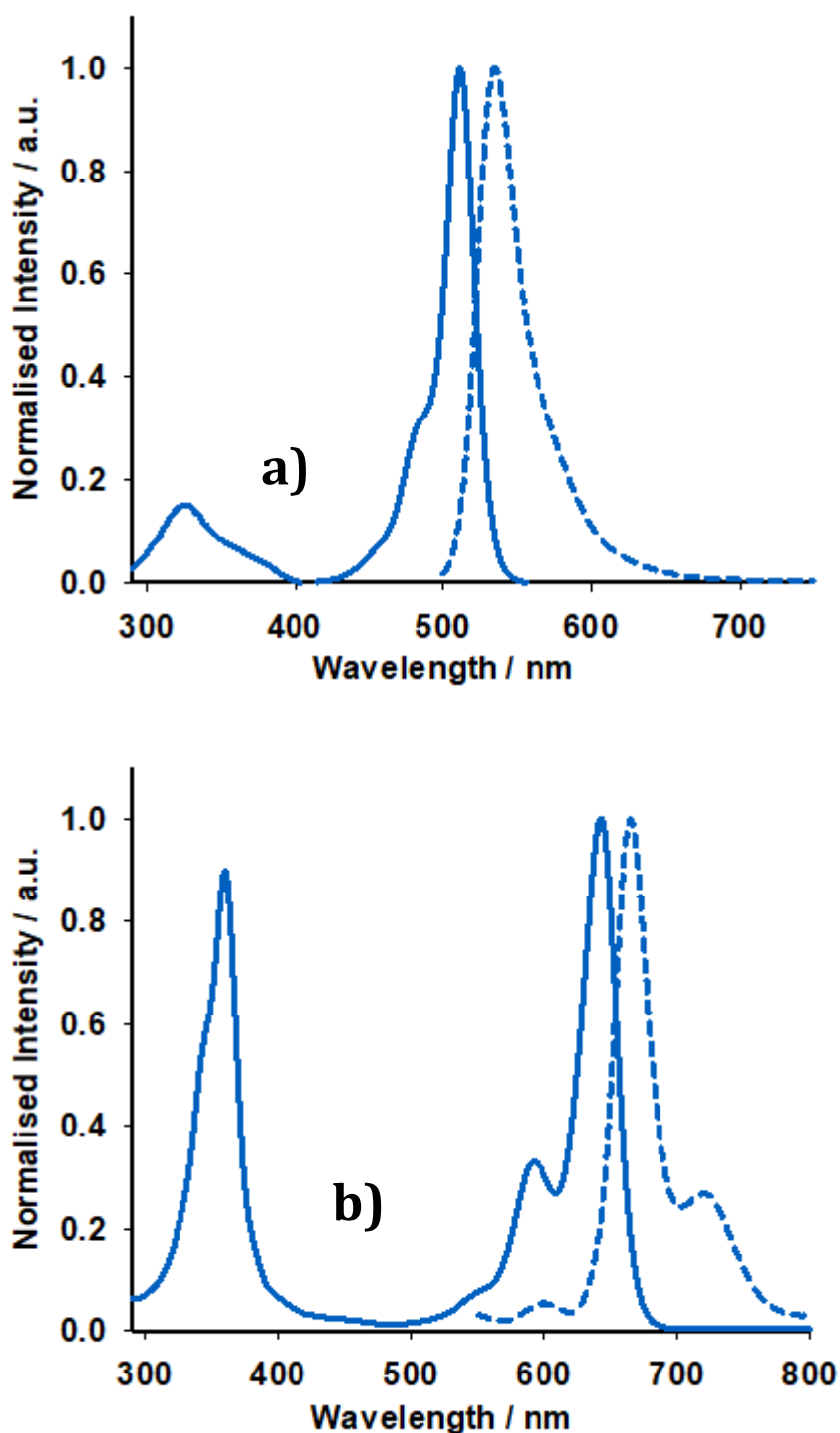


*Figure 15: UV-Vis and emission (511nm) of (a) **RJ1** and (b) **RJ2** in MeCN.*

UV-Visible and fluorescence spectroscopy of **RJ1** and **RJ2** produced the traces shown in Figure 15. The absorbance maxima at 511 nm and 642 nm for **RJ1** and **RJ2** respectively are assigned to the $S^0 \rightarrow S^1$ ($\pi \rightarrow \pi^*$) transition, with a red shift of 131 nm upon addition of the extended styryl moieties. Both also display a vibrational shoulder, with the **RJ1** peak

diminished in comparison to **RJ2**. Comparing the molar extinction coefficient of the dye, **RJ2** is also much higher than that of **P1** or **GS1** (79,354, 66,000 and 65,700 M⁻¹ cm⁻¹ respectively) ⁹ making it an ideal light harvester. Compared to these two dyes, it is also significantly red shifted, with λ_{\max} shifted by almost 100 nm compared to **GS1**. The high energy peak observed at around 350 nm for both BODIPY molecules and is the S⁰ to S² transition, with **RJ1** having a low molar extinction coefficient and **RJ2** being much more intense.

The emission of both dyes demonstrates a small Stokes shift, characteristic of BODIPY compounds. **RJ2** also produced a quantum yield of 0.57, increased versus that of **RJ1** (0.30) due to increased rigidity within the molecule. The decay of the excited state was measured to last 4.95 ns, also a longer lifetime than that of the starting dye **RJ1** (0.487). The larger quantum yield and reduced number of intra-molecular degrees of rotation could be the cause of this.

4.2.2.3 Electrochemistry

RJ1 undergoes three processes; a pseudo-reversible reduction, a non-reversible reduction, and an oxidation. The first process is expected for BODIPYs of this type. The second irreversible reduction is attributed to structural changes in the pentafluorosulfanyl group and has been reported previously. The final oxidation indicates that the molecules are reacting with each other via the formation of dyads through the unsubstituted β positions. Further investigation using Differential Pulse Voltammetry yielded values for these processes, as summarised in Table 8.

		RJ1	RJ2
E_{red}	V vs fc	-1.24	-0.97
	V vs NHE	-0.61	-0.34
E_{ox}	V vs fc	0.64	0.68
	V vs NHE	1.27	1.31
E_{0-0} eV		1.90	

Table 8: Electrochemical potentials of oxidation and reduction potentials of the **RJ1** and **RJ2** dyes measured in MeCN with 0.2 M TBAPF₆, glassy carbon working electrode and calomel electrode reference, where fc is the redox potential for ferrocene.

Upon addition of the styryl groups, the reduction potential of **RJ2** decreases in comparison to **RJ1**. Two irreversible reductions of both the BODIPY core and the SF₅ moiety were elucidated via square wave voltammetry. The unsubstituted 1,7 and 2,6 positions make the BODIPY core susceptible to oxidative reaction in both molecules, with little difference in the oxidative potential between the pair. Upon addition of the extended styryl groups, the π system extends, decreasing the difference between the HOMO and LUMO, bathochromically shifting the absorption of the dye.

4.2.2.4 Computational Analysis

In order to fully understand the optical and electrochemical properties of these dyes, computational analysis was employed. For dyes **RJ1** and **RJ2** the obtained crystal structures (discussion of which is beyond the scope of this thesis) were used to elucidate their starting geometry for the energy calculations. Due to the difference in both size and complexity of the molecules, slightly different base set methodologies were used for each dye. Both environments were calculated in vacuum using cam-B3LYP 6-311G ++ (d,p), considered in acetonitrile using an IEFPCM solvent model. Since the BODIPY molecule does not display phosphorescence and cannot access the triplet state, only the singlet excited states were considered.

For **RJ1**, the HOMO is found on the BODIPY core, and the LUMO shown to spread across both the core and the aryl ring. The absence of substituents in the 1,7 positions allows the aryl ring to be positioned at a 50° angle to the core, allowing for this electronic communication between the core and acceptor. The LUMO+1 orbital can be seen in Figure 17 to encompass the SF₅ group. However, it is not seen to contribute to the first three excited states within this molecule, as shown in Table 9. The HOMO to LUMO transition with the greatest oscillator strength corresponds to the S⁰ to S¹ transition. The S⁰ to S² is assigned to the HOMO-1 to LUMO transition, while the S⁰ to S³ is assigned to a combination of the HOMO-3 to LUMO and HOMO-2 to LUMO transitions, with the corresponding wavelength only 20 nm away from the S⁰ to S². The predicted wavelengths and relative intensities of the peaks correlate to the experimental absorption spectrum of the dye, albeit hypsochromically shifted.

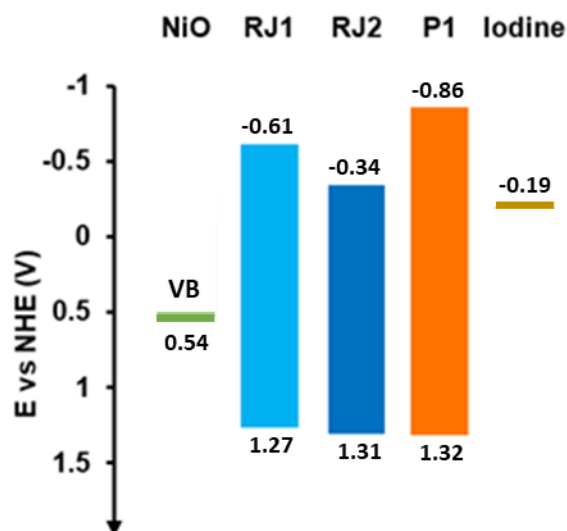


Figure 16: Relative potentials of the **RJ1** and **RJ2** HOMO and LUMO relative to P1, the NiO valence band edge and I_2/I_3^- redox couple.

For **RJ2**, the optimised molecular structure is planar, with the aryl rings of the styryl groups in line with the BODIPY core. The cause of the bathochromic shift of the absorption compared to **RJ1**, the π system is expected to be spread further, between the BODIPY core and the added styryl groups. The first excited state is therefore associated with the π - π^* transition from the HOMO to LUMO and is shown to have some small charge transfer characteristics through the movement of electron density from the styryl group to the aryl ring in the meso position. The second transition is a similar peak, however with greater oscillator strength and therefore, greater intensity. It corresponds to a combination of the HOMO-1 to LUMO (79 %) and HOMO to LUMO+2 (21 %) transitions. The two combine, as both the HOMO-1 and LUMO+2 have a large amount of electron density on the styryl groups, and less around the BODIPY core. The third excited state is a weak transition that includes both transitions described above, but with reversed intensities, and a minute contribution from the HOMO-1 to LUMO+3 transition. In the experimental absorbance spectrum, these values are reflected minus the third transition. This is, however, expected due to its low intensity.

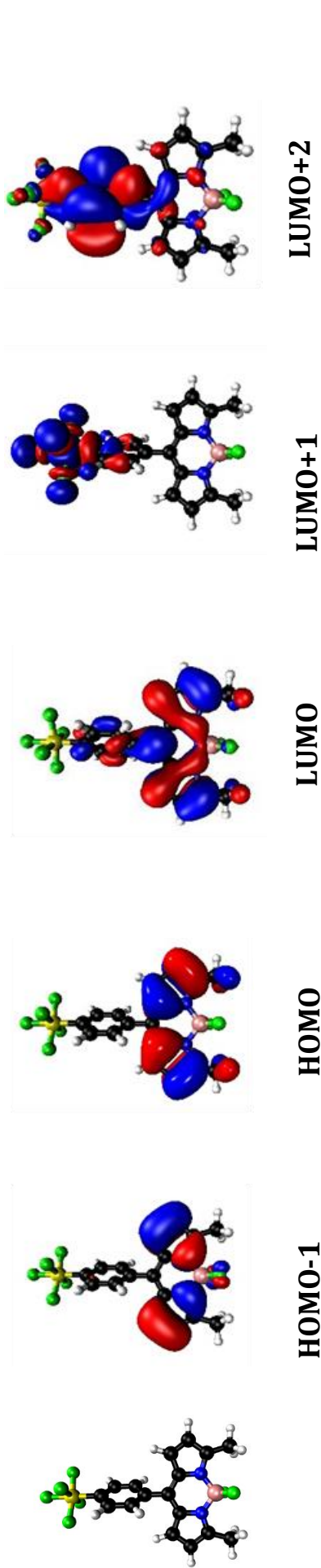


Figure 17: Calculated frontier molecular orbital configurations for each energy level for the RJ1 dye. Experimental details and basis set information can be found in the body text.

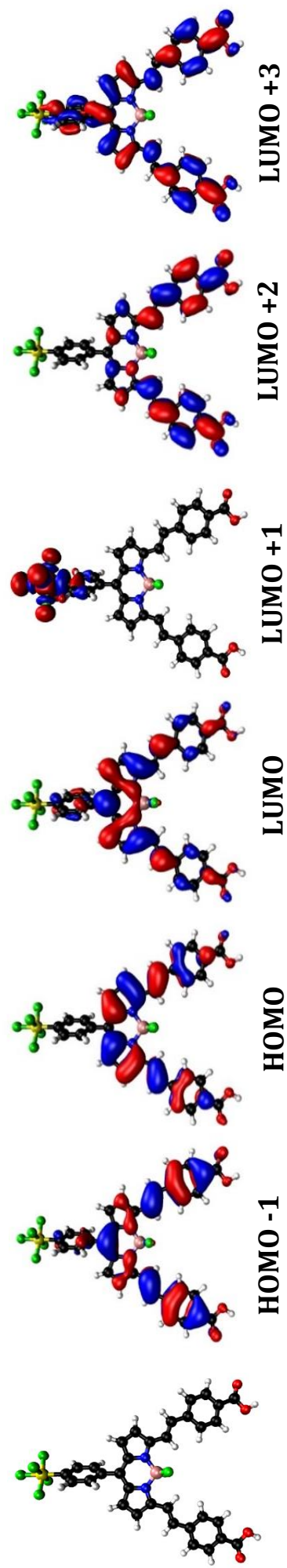


Figure 18: Calculated frontier molecular orbital configurations for each energy level for the RJ2 dye. Experimental details and basis set information can be found in the body text

Excited State	Transition	Contribution	Absorbance /nm	Energy / eV	Oscillator strength
1	HOMO to LUMO	100%	438	2.8276	0.5786
2	HOMO-1 to LUMO	100%	306	4.0520	0.0649
3	HOMO-3 to LUMO	93%	286	4.3284	0.1365
	HOMO-2 to LUMO	7%			

Table 9: Calculated singlet energy transitions for the first three excited states for **RJ**, as well as the relative contributions of each orbital transition.

Excited State	Transition	Contribution	Absorbance /nm	Energy / eV	Oscillator strength
1	HOMO to LUMO	100%	586	2.1166	1.1086
2	HOMO-1 to LUMO	79%	351	3.5367	2.1656
	HOMO to LUMO+2	21%			
3	HOMO-1 to LUMO	22%	338	3.6712	0.1365
	HOMO-1 to LUMO+3	4%			
	HOMO to LUMO+2	74%			

Table 10: Calculated singlet energy transitions for the first three excited states for **RJ2**, as well as the relative contributions of each orbital transition.

4.2.2.5 Solid State Properties and Dye Loading

Table 11 lists the λ_{\max} and corresponding absorption coefficients for the most red-shifted peak for each of the three dyes and the **P1** benchmark. To more precisely investigate the binding properties of the dye onto the NiO surface, optical characterisation of the dye on the film (**RJ3**) was compared to that of the dye in solution (**RJ2**). Additionally, **RJ3** was used to dye an inert material, an animal fibre based wool. The emission profiles are shown in Figure 19, and demonstrate a large difference in the spectra between the dye on the semiconductor and that on the inert wool. Even upon irradiation of the NiO sample with incredibly intense light (with slit widths increased from 1 and 2 mm to 5 and 10 mm for the excitation source and detector respectively) the emission is still dwarfed by that of the **RJ3** on wool. This is possible to observe visually, with even diffuse light sources causing a noticeable colour change to the wool and solvent samples. The decrease in intensity of the emission between the semiconducting and non-conductive substrates suggests that there is good electronic coupling between the BODIPY and the NiO, allowing the excited state of the dye to be quenched via charge transfer to the semiconductor. The emission profile of the dye on NiO includes a peak at 670 nm, while the dye on wool emits across two intense peaks at 680 nm and 745 nm. The additional peak may arise from aggregation of dye molecules on the surface, a phenomenon not observed in the NiO sample.

Dye	λ_{\max}	ϵ ($M^{-1}cm^{-1}$)	Concentration difference(μmol)	Dye loading ($nmol\ cm^{-2}$)
P1	481	57000	2.28	8.48
RJ1	511	69,500	-	-
RJ2	642	79,354	-	-
RJ3	642		1.54	2.87

*Table 11: Spectroscopic properties of dyes **RJ3** and **P1**, including the location of the λ_{\max} peak and molar extinction coefficients.*

System	Lifetime (ns)	X ²
RJ3 in MeCN	4.9	1.877
RJ3 on wool	3.2	1.334
RJ3 on NiO	4.1	1.295

Table 12: Tabulated lifetimes of **RJ3** bound to various substrates, measured with an excitation wavelength of 600 nm.

Excited state lifetimes of **RJ3** on NiO and wool were also measured and compared to that of **RJ2** in solution. In solution, the lifetime was longest at 4.97 ns and decayed with a single exponential profile. Upon binding of **RJ3** to the substrates, the decay was split into two exponential decay components- with the longest components lasting 3.22 ns and 4.08 ns for dyes bound to wool or NiO respectively. This is shorter than the dye in solution, possibly due to aggregated dyes on the surface undergoing self-quenching.

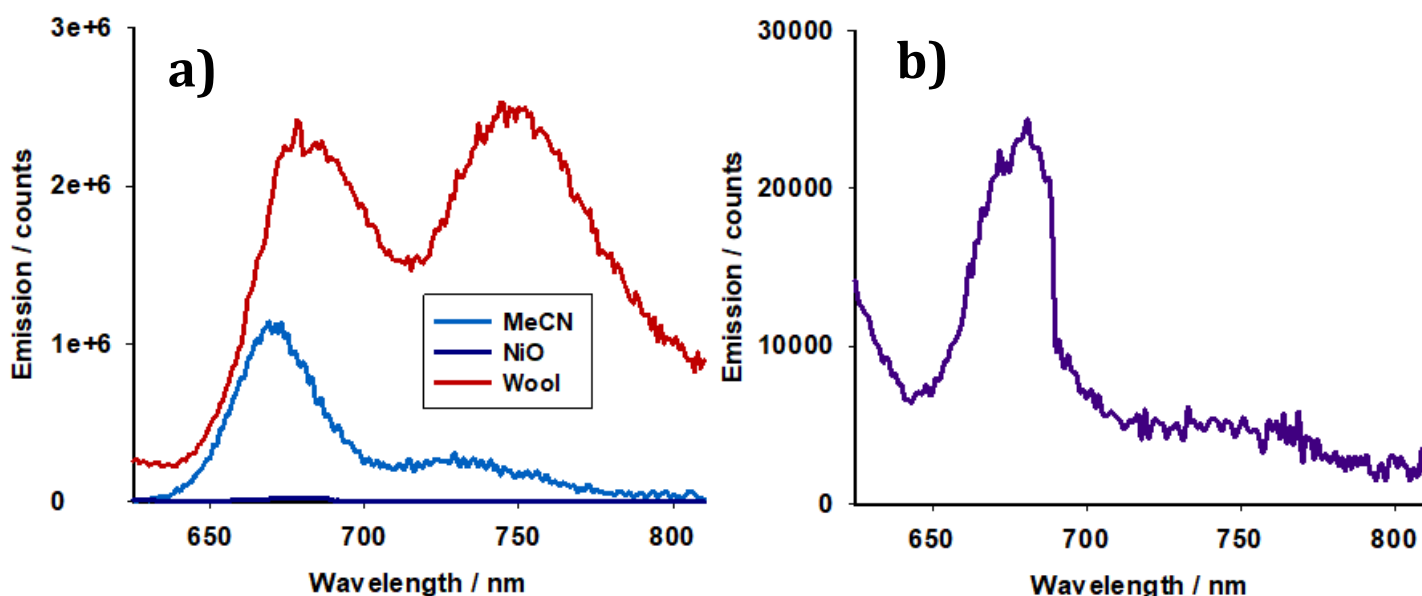


Figure 19: a) Emission spectrum of **RJ3** bound to various substrates, b) scaled up graph of NiO emission, with minimal response.

4.2.2.6 P-type devices

RJ3 was used for application in NiO-based devices due to its anchoring group functionality. P-type DSSCs were constructed using the methods described in section 4.3 and current-voltage curves were obtained in both the dark and under AM1.5 G illumination. As expected for the red-shifted **RJ3** dye, current output in devices was lower than the optimised triphenylamine-based **P1**. However, a higher fill factor, improved V_{oc} and reduced recombination in the dark current measurement indicates the efficacy of **RJ3** as a blue p-type dye. **RJ3** also has a greatly improved performance compared to other BODIPY-core dyes, such as those demonstrated by Summers et al.³³

The IPCE spectra of the NiO- DSSC shows a slightly (circa. 20 nm) red shifted peak in current output relative to the absorption spectra of the dye on the NiO film. While the IPCE is low compared to competing dyes, a secondary peak is estimated to arise due to the higher energy S^0-S^2 transition, a spectral region not captured by the measurement equipment and masked by the iodine absorption response.

While the dye loading of **RJ3** is lower than that of **P1**, the increased absorption coefficient and favourable electronic communication between the dye and the NiO film led to the promising efficiencies of > 0.1 % in AM 1.5 sunlight, as well as improved V_{oc} . The

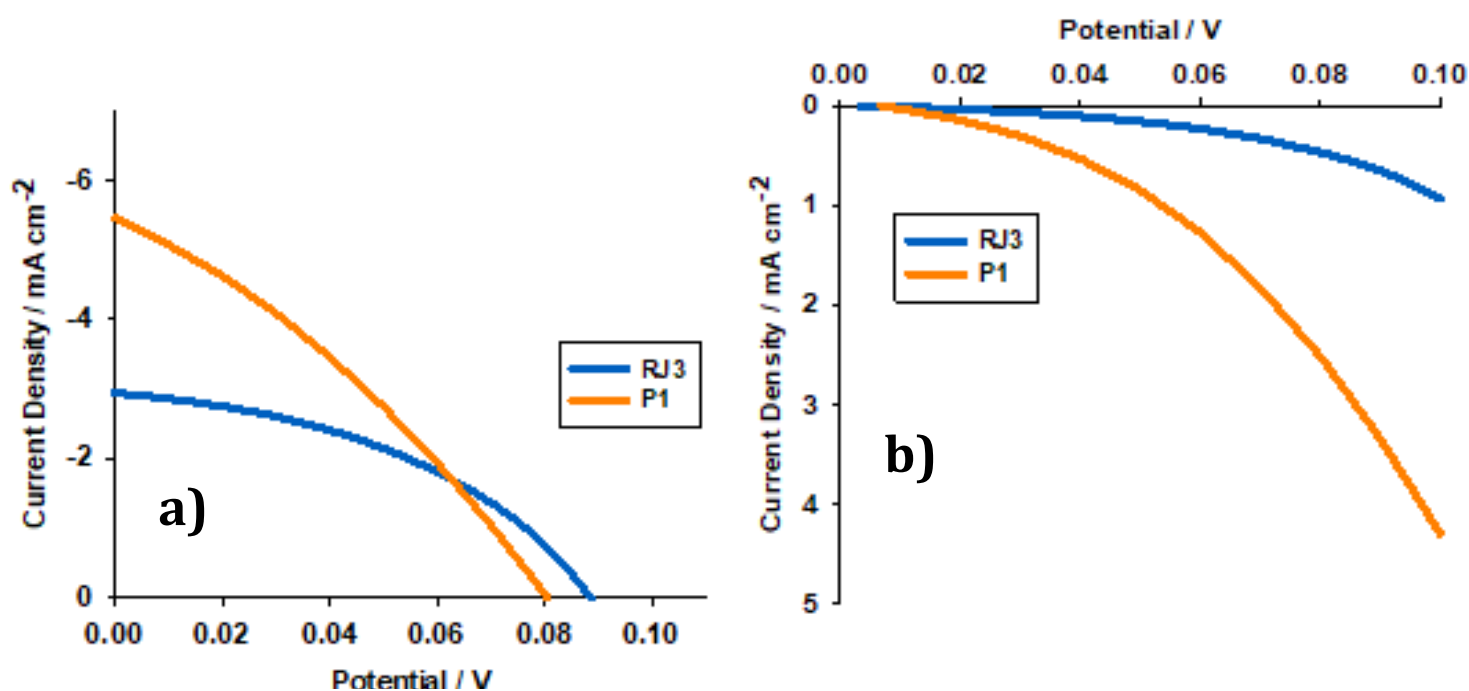


Figure 20: Plot of current density against voltage for illuminated devices containing dye **RJ3** and the reference dye **P1**. Electrolyte composition: 0.1 M LiI and 1 M I₂ in dry MeCN.

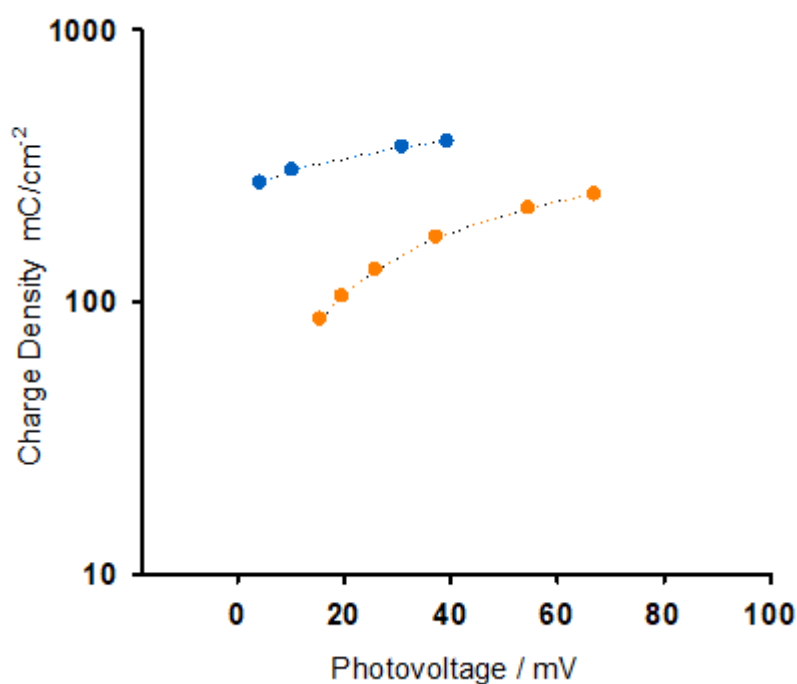


Figure 21: Extracted charge density vs photovoltage plots for *p*-DSSCs containing **P1** (orange) and **RJ3** (blue).

increased fill factor implies good electronic communication between the dye and NiO film, as well as reduced electrolyte interaction with the surface. The electronegativity and steric bulk of the SF₅ group can help reduce the interaction of the iodine electrolyte with the surface, decreasing recombination losses and improving performance.

Charge extraction and lifetime studies were undertaken to further investigate the effect of the **JF3** dye in devices. Experimental details for the study are outlined in section 4.3. Results for these measurements are shown in Figures 21 to 23.

Dye	V _{oc} / mV	J _{sc} / mA cm ⁻²	FF / %	η / %
RJ3	85	3.02	41	0.104
P1	80	5.45	31	0.135

Table 13: Photovoltaic parameters, including open circuit voltage (*V*_{oc}), short circuit current (*J*_{sc}), fill factor (*FF*) and efficiency (*μ*) of champion NiO *p*-DSSCs based on dyes **RJ3** and **P1**.

The charge lifetime is longer at similar charge density of for devices using **P1** then those sensitised with **RJ3**, resulting in higher device current. Within the higher operating potential range of the device, the longer lifetime is consistent with the improved J_{sc} measured for the **P1** device.

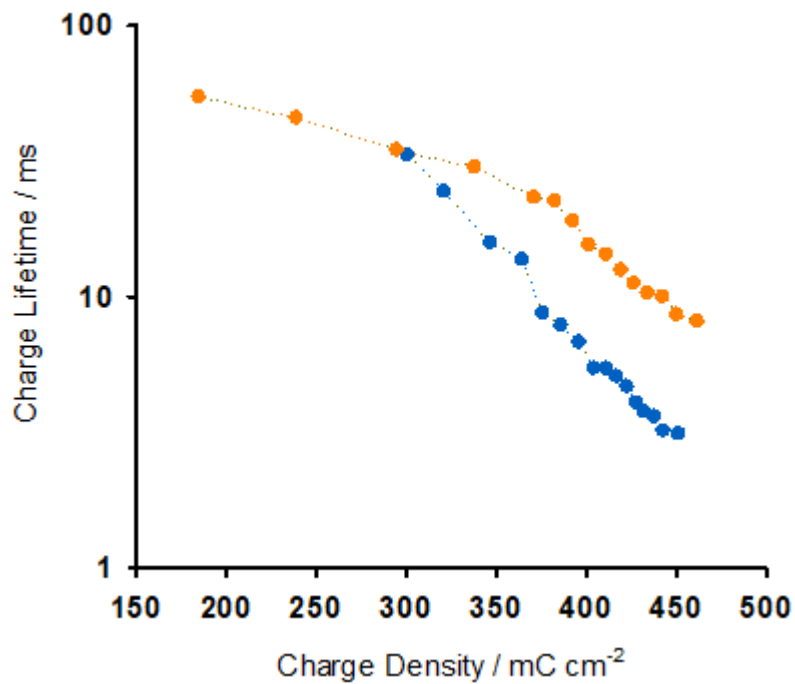


Figure 22: Charge lifetime vs extracted charge density plots for *p*-DSSCs containing **P1** (orange) and **RJ3** (blue).

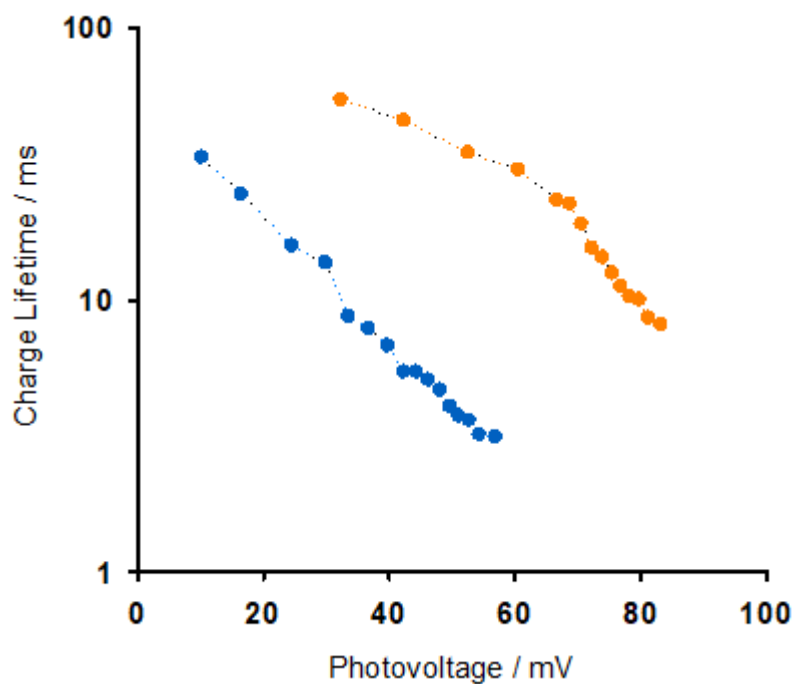


Figure 23: Charge lifetime vs photovoltage for *p*-DSSCs containing **P1** (orange) and **RJ3** (blue).

4.2.2.7 Preliminary Tandem Devices

By varying the number of layers of NiO in the p-type devices, the current output of the devices can be increased up to a point. While additional layers promote the loading of more dye and increase the amount of light harvested, thicker layers of NiO can also have

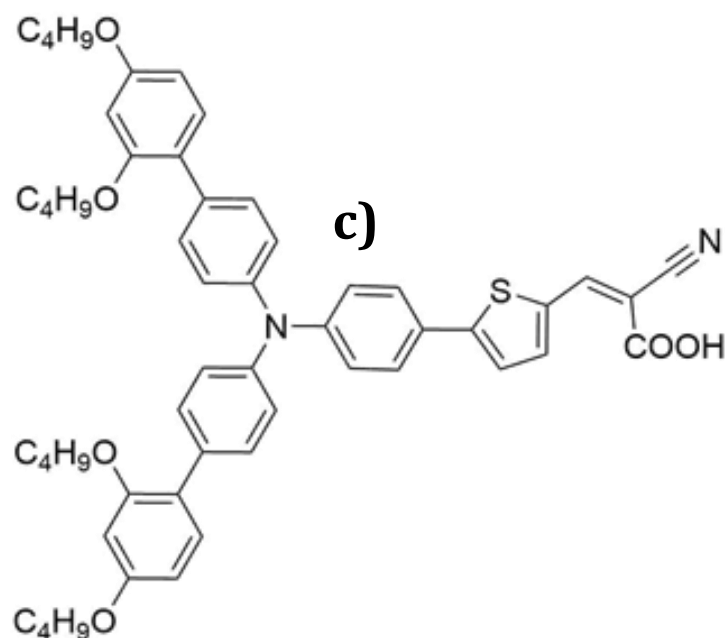
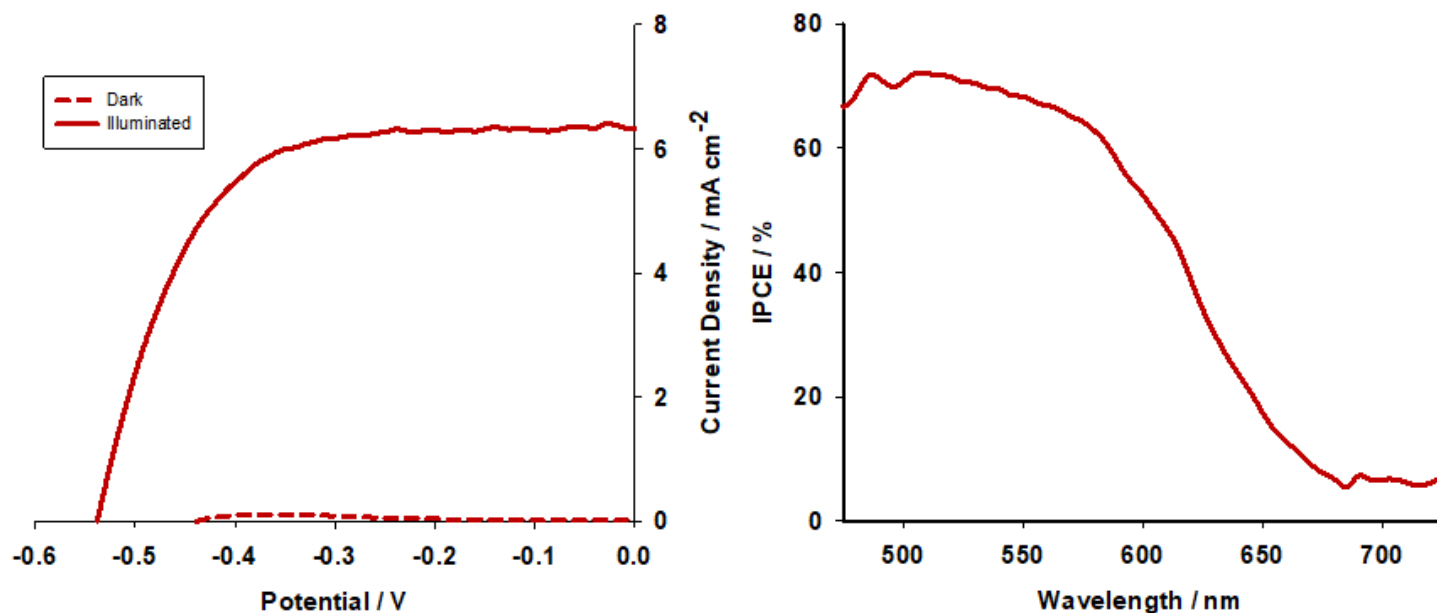


Figure 24: a) J/V curve of 2L TiO₂ single junction device containing **D35** dye (electrolyte composition: 0.1 M LiI and 1 M I₂ in dry MeCN), b) IPCE response of the same device, c) structure of **D35** dye used in this study.

detrimental effects, with the creation of additional recombination sites or defects in the nanoporous material. As seen in Figure 26, optimisation of **P1** yielded a cap between 4 and 5 layers of NiO deposition. Not only did performance massively drop after this point, but there is added risk in the synthesis of the layers as the material is more likely to flake away from the substrate or be contaminated or damaged between annealing cycles. **RJ3**, however, reaches this point after 3 layers, where the addition of a fourth or fifth layer does not yield any further improvement in device performance. Further study into the dye loading mechanisms may elucidate more information, but this could be a result of the dyes high absorption coefficient. If only the very top layers are absorbing photons, then the addition of extra layers of absorber may not provide any additional benefit.

Once the photocathode was optimised, the photoanode was prepared and tested individually before incorporation into the tandem device structure. For this application, the commercially available **D35** dye, which absorbs in the blue region with a $\lambda_{\max} = 444$ nm was selected to act as the absorber. Results for initial devices using this absorber with an unoptimized, 2-layer TiO₂ photoanode and the same electrolyte as p-DSSC testing can be seen in Figure 24 and Table 14. While the current output of the n-DSSC was still higher than either p-DSSC, it was deemed sufficiently low to produce preliminary tandem devices. While the design parameters of tandem DSSCs assume that the light will be incident on the photocathode, the devices were tested in both orientations.

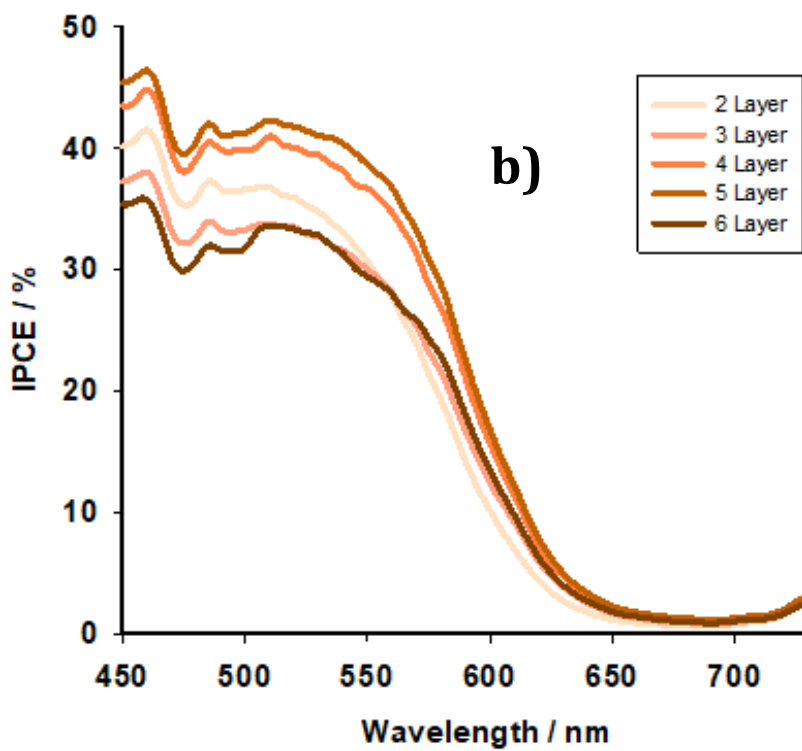
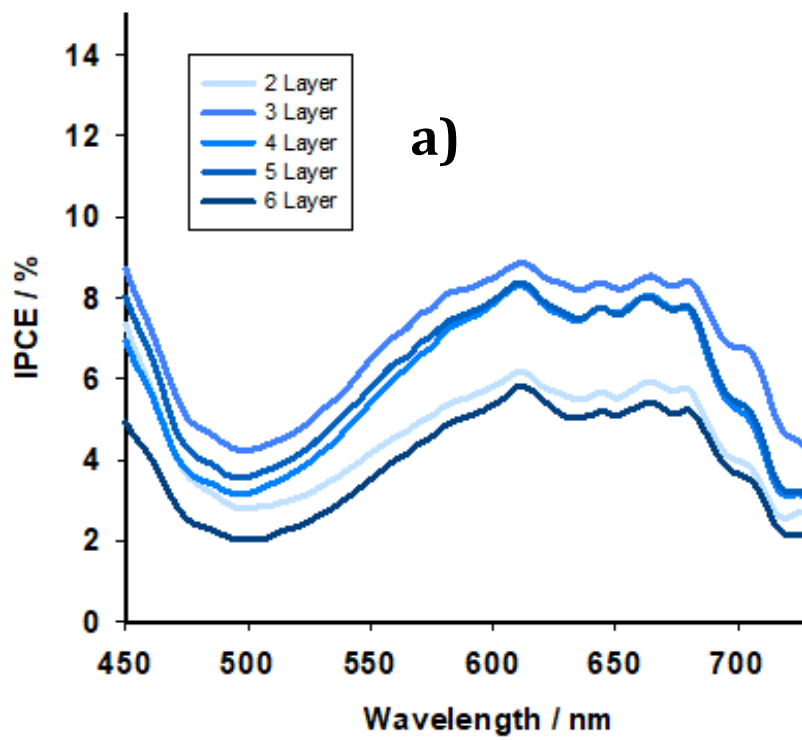


Figure 25: IPCE spectra of p-type NiO-DSSCs using a) RJ3 and b) P1 dyes with a series of NiO film layer quantities.

Dye	V_{oc} / mV	J_{sc} / mA cm ⁻²	FF / %	η / %
D35 ^{a)}	540	4.32	57	1.34
TANDEM- pRJ3-nD35 ^{b)}	540	0.66	44	0.15
TANDEM- pRJ3-nD35 ^{c)}	420	3.26	11	0.14
TANDEM- pP1-nD35 ^{b)}	430	0.69	40	0.12
TANDEM- pP1-nD35 ^{c)}	580	1.89	34	0.37

Table 14: Photovoltaic parameters, including open circuit voltage (V_{oc}), short circuit current (J_{sc}), fill factor (FF) and efficiency (μ) of champion a) current- matched TiO_2 n-DSSC using **D35** dye b) tandem DSSCs illuminated through the NiO photocathodes and c) tandem DSSCs illuminated through the TiO_2 photoanodes.

Results from tandem devices constructed with these dyes are presented in Table 14. In all cases, the efficiency of the devices was lower than that of the individual n-DSSC. IPCE measurements of the devices illuminated via the photoanode can be seen in Figure 28 and are noticeably ‘jagged’. Figure 26 shows the effect on IPCE upon illumination of the **RJ3-D35** device on each side consecutively. Upon illumination of the devices through the photocathode, performance decreases as the intensity of light reaching the photoanode decreased. This could be the result of competing absorption processes by the NiO, p-type dye and electrolyte, or scattering effects by the NiO and additional interfaces.

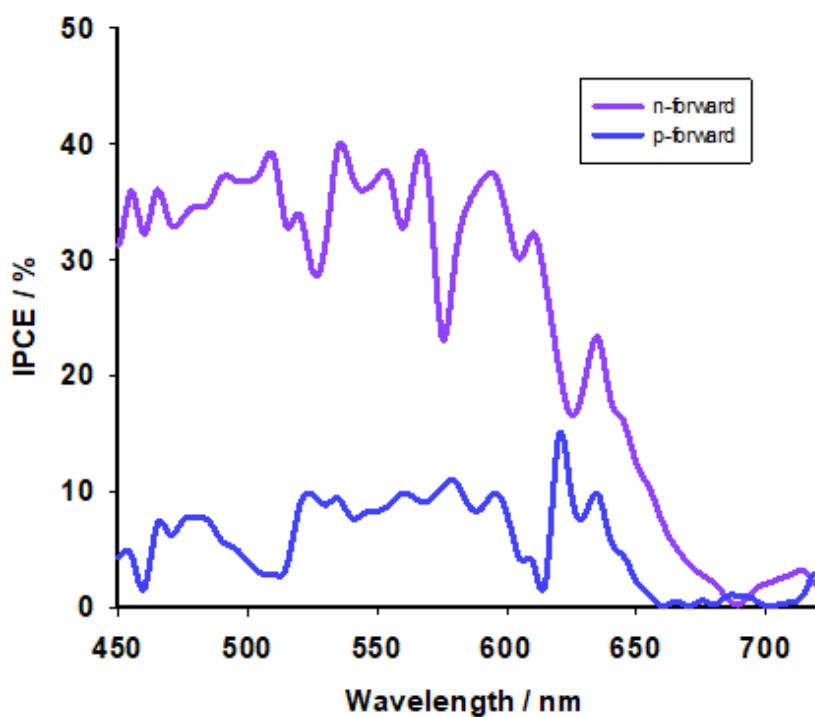


Figure 26: IPCE spectra of the tandem- pRJ3-nD35 device, illuminated from each side consecutively.

While **RJ3** promised improved spectral coverage compared to **P1** in a tandem arrangement, the poor current matching (as evidenced by low fill factors) did not allow for appropriate comparison in the systems. Further optimisation of the photocathode, as well as modification of electrolyte composition is in order complete this study.

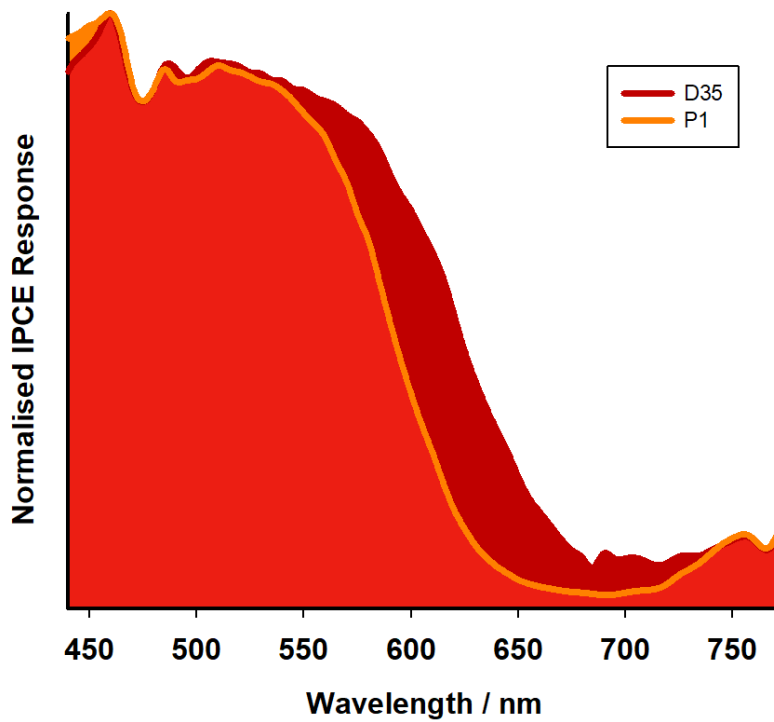
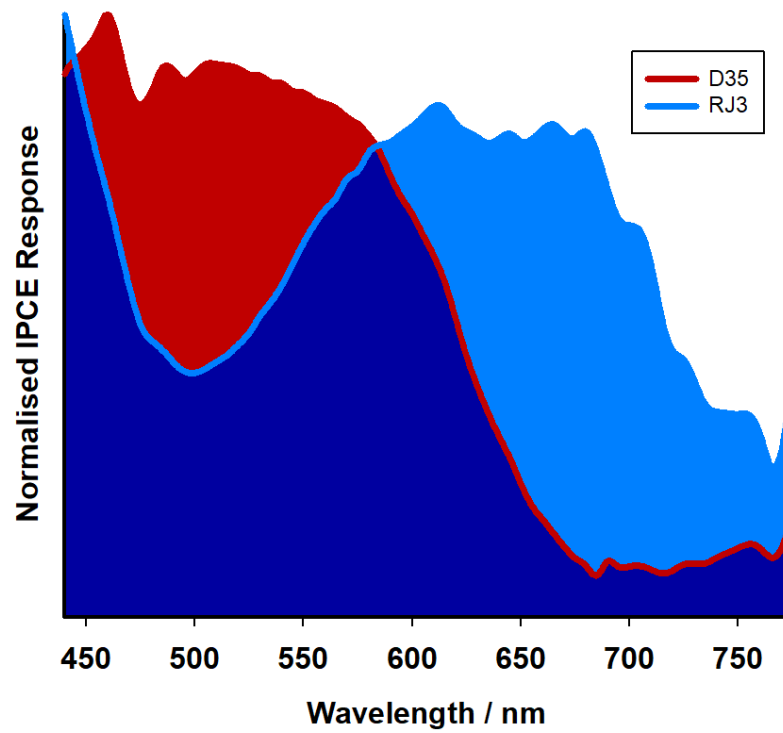


Figure 28: IPCE spectra from preliminary tandem devices constructed with $\text{TiO}_2/\text{D35}$ photoanodes and NiO/dye photocathodes illuminated through the photoanode.

4.2.3 Conclusions

The application of NiO electrodes into tandem devices calls for the creation of red shifted absorbers to fully utilise the entirety of the solar spectrum. These absorbers require strong binding groups and extended charge separated lifetimes to reduce recombination and increase current flow within the device. A trio of BODIPY dyes was developed using a strongly electronegative SF₅ group affixed to the meso position. The molecules are synthesised using room-temperature procedures and boast high yields, making them excellent candidates for up-scalability. The chromophore **RJ3** was applied to NiO-based p-DSSC's which gave a power conversion efficiency (0.104 %), through a short circuit photocurrent (J_{sc}) of 3.02 mA cm⁻², open circuit voltage (V_{oc}) of 85 mV and fill factor of 41 %.

While the current output of **RJ3** was lower than the benchmarking **P1** devices, there was an increase in open-circuit voltage and fill factor. This, combined with the red-shifted spectral response observed in both the absorbance of the dye on the film and the measured IPCE, demonstrated the dye's suitability for incorporation into tandem devices. In preliminary tandem devices, poor current matching between photoelectrodes meant that there was a significant loss of fill factor and therefore performance, however further testing of this dye in tandem devices may yet yield promising results.

4.3 Experimental

Materials were purchased from Fluorochem and Sigma unless otherwise stated

P1 dye was received as synthesised via previous literature procedure.

Sol gel NiO precursor was prepared by dissolving anhydrous NiCl₂ (1 g) and a tri-block co-polymer, F108 (poly(ethylene glycol)-block-poly(propylene glycol)-block-poly(ethylene glycol) (1 g) in a mix of EtOH (6 ml) and deionised water (5 ml). The solution was left to age for 14 days and centrifuged to remove remaining solids before use. To prepare the electrodes, the doctor blade method was used to apply the precursor solution over a Scotch Magic tape spacer to form films with an active area of 0.2 cm². The films were sintered in a Nabertherm B150 Chemical Oven in air at 450 °C for 30 minutes, and the process was repeated, giving 3-layer NiO films with an average thickness of 1.2 μm (measured with Dektak³ST Surface Profile Measuring System). The resulting electrodes were submerged in 0.3 mM dye solutions in ethanol (for **JF1-3**) or MeCN (**P1**, **RJ3**) for 24 hours at room temperature.

The as-prepared counter electrode and photocathode were sandwiched together using a thermoplastic frame (Surlyn, 25 μm thickness) as a spacer. An iodine electrolyte containing LiI (1 M) and I₂ (0.1 M) in dry acetonitrile was introduced into the device via vacuum backfilling through the pre-drilled hole. Another Surlyn piece and a glass cover slip was then used to seal the cell.

Dye loading experiments were carried out by submerging NiO films in a 0.1 mM solution of the dye in DMF. Absorbance spectra were taken on the solutions over time and the difference in concentration calculated by using the dyes' molar extinction coefficient to give a mean dye loading for each film.

To measure the photovoltaic parameters of devices, an Ivium CompactStat potentiostat was used in conjunction with a Xenon light source (Newport, 300 W) calibrated to 100 mW cm⁻² with a Si diode. A black aperture was used to mask the device working area and the current was measured at applied bias between 0.1 V and -0.05 V at a rate of 5 mV s⁻¹. Incident photon to current conversion efficiency (IPCE) measurements were conducted by filtering the source lamp through a monochromator (Oriel Cornerstone 130 1/8m) and measuring the current output at 5 nm increments between 400-800 nm, using a Si photodiode as a baseline.

4.4 References

- 1 A. Morandeira, J. Fortage, T. Edvinsson, L. Le Pleux, E. Blart, G. Boschloo, A. Hagfeldt, L. Hammarström and F. Odobel, *J. Phys. Chem. C*, 2008, **112**, 1721–1728.
- 2 P. Qin, H. Zhu, T. Edvinsson, G. Boschloo, A. Hagfeldt and L. Sun, *J. Am. Chem. Soc.*, 2008, **130**, 8570–8571.
- 3 P. Qin, M. Linder, T. Brinck, G. Boschloo, A. Hagfeldt and L. Sun, *Adv. Mater.*, 2009, **21**, 2993–2996.
- 4 I. R. Perera, T. Daeneke, S. Makuta, Z. Yu, Y. Tachibana, A. Mishra, P. Bäuerle, C. A. Ohlin, U. Bach and L. Spiccia, *Angew. Chemie - Int. Ed.*, 2015, **54**, 3758–3762.
- 5 K. A. Click, D. R. Beauchamp, B. R. Garrett, Z. Huang, C. M. Hadad and Y. Wu, *Phys. Chem. Chem. Phys.*, 2014, **16**, 26103–26111.
- 6 Z. Ji, G. Natu, Z. Huang and Y. Wu, *Energy Environ. Sci.*, 2011, **4**, 2818–2821.
- 7 Q. Q. Zhang, K. J. Jiang, J. H. Huang, C. W. Zhao, L. P. Zhang, X. P. Cui, M. J. Su, L. M. Yang, Y. L. Song and X. Q. Zhou, *J. Mater. Chem. A*, 2015, **3**, 7695–7698.
- 8 C. J. Wood, M. Cheng, C. A. Clark, R. Horvath, I. P. Clark, M. L. Hamilton, M. Towrie, M. W. George, L. Sun, X. Yang and E. A. Gibson, *J. Phys. Chem. C*, 2014, **118**, 16536–16546.
- 9 C. J. Wood, G. H. Summers and E. A. Gibson, *Chem. Comm.*, 2015, 3915–3918.
- 10 F. A. Black, C. J. Wood, S. Ngwerume, G. H. Summers, I. P. Clark, M. Towrie, J. E. Camp and E. A. Gibson, *Faraday Discuss.*, 2017, **198**, 449–461.
- 11 J. Cui, J. Lu, X. Xu, K. Cao, Z. Wang, G. Alemu, H. Yuang, Y. Shen, J. Xu, Y. Cheng and M. Wang, *J. Phys. Chem. C*, 2014, 16433–16440.
- 12 A. R. Marri, F. A. Black, J. Mallows, E. A. Gibson and J. Fielden, *Dye. Pigment.*, 2019, **165**, 508–517.
- 13 L. Zhang and J. M. Cole, *ACS Appl. Mater. Interfaces*, 2015, **7**, 3427–3455.
- 14 H. Klifout, A. Stewart, M. Elkhalfa and H. He, *ACS Appl. Mater. Interfaces*, 2017, **9**, 39873–39889.

- 15 M. Poddar and R. Misra, *Coord. Chem. Rev.*, 2020, 421, 213462.
- 16 A. Treibs and F.-H. Kreuzer, *Justus Liebigs Ann. Chem.*, 1969, **721**, 116–120.
- 17 R. W. Wagner and J. S. Lindsey, *Pure Appl. Chem.*, 1996, **68**, 1373–1380.
- 18 S. Hattori, K. Ohkubo, Y. Urano, H. Sunahara, T. Nagano, Y. Wada, N. V Tkachenko, H. Lemmetyinen and S. Fukuzumi, *J. Phys. Chem. B*, 2005, 109, 19402.
- 19 Y. Kubo, D. Eguchi, A. Matsumoto, R. Nishiyabu, H. Yakushiji, K. Shigaki and M. Kaneko, *J. Mater. Chem. A*, 2014, **2**, 5204–5211.
- 20 C. Qin, A. Mirloup, N. Leclerc, A. Islam, A. El-Shafei, L. Han and R. Ziessel, *Adv. Energy Mater.*, 2014, **4**, 1400085.
- 21 J. F. Lefebvre, X. Z. Sun, J. A. Calladine, M. W. George and E. A. Gibson, *Chem. Commun.*, 2014, **50**, 5258–5260.
- 22 Y. Higashino, S. Erten-Ela and Y. Kubo, *Dye. Pigment.*, 2019, **170**, 107613.
- 23 P. Qin, J. Wiberg, E. A. Gibson, M. Linder, L. Li, T. Brinck, A. Hagfeldt, B. Albinsson and L. Sun, *J. Phys. Chem. C*, 2010, **114**, 4738–4748.
- 24 W. A. Sheppard, *J. Am. Chem. Soc.*, 1960, **82**, 4751–4752.
- 25 T. Umemoto, L. M. Garrick and N. Saito, *Beilstein J. Org. Chem.*, 2012, **8**, 461–471.
- 26 J. M. W. Chan, *J. Mater. Chem. C*, 2019, **7**, 12822–12834.
- 27 S. Altomonte and M. Zanda, *J. Fluor. Chem.*, 2012, 143, 57–93.
- 28 G. Zhang, Y. J. Lee, P. Gautam, C. C. Lin, C. L. Liu and J. M. W. Chan, *J. Mater. Chem. C*, 2019, **7**, 7865–7871.
- 29 H. R. A. Golf, H. U. Reissig and A. Wiehe, *J. Org. Chem.*, 2015, **80**, 5133–5143.
- 30 P. Gautam, C. P. Yu, G. Zhang, V. E. Hillier and J. M. W. Chan, *J. Org. Chem.*, 2017, **82**, 11008–11020.
- 31 P. Gautam, Y. Wang, G. Zhang, H. Sun and J. M. W. Chan, *Chem. Mater.*, 2018, **30**, 7055–7066.
- 32 Y. Derin, R. F. Yılmaz, İ. H. Baydilek, V. E. Atalay, A. Özdemir and A. Tutar,

Inorganica Chim. Acta, 2018, **482**, 130–135.

- 33 G. H. Summers, J. F. Lefebvre, F. A. Black, E. Stephen Davies, E. A. Gibson, T. Pullerits, C. J. Wood and K. Zidek, *Phys. Chem. Chem. Phys.*, 2015, **18**, 1059–1070.

Chapter 5 Alternative Architectures for Efficient Tandem Quantum Dot Sensitized Solar Cells

5.1 Background

While the work in Chapters 3 and 4 focussed on applying molecular light harvesters to DSSC, the work in this section will turn to the sensitisation of NiO with Quantum Dots (QDs) and nanocrystalline materials.

5.1.1 Quantum Dot principles and applications

A quantum dot (QD) is a nanoscale particle of a semiconducting material. When the nanoparticle radius (R) is similar to the Bohr radius of the exciton (a), the particle is known as a quantum dot, as shown in Figure 1, and can be described using the equation below:

$$R = a = \frac{4\pi\epsilon\epsilon_0\hbar^2}{m_e^*e^2}$$

Where ϵ_0 is the permittivity of a vacuum, m_e^* is the rest mass of an electron and e is the charge of an electron.

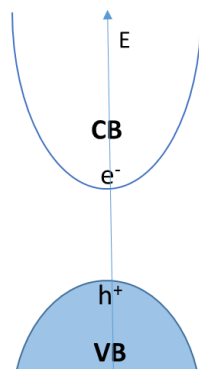


Figure 1: Simplified schematic showing bandgap in a quantum dot structure.

In fields such as nanoelectronics,¹ labelling in medicine,² or wastewater management,³ highly coloured, often fluorescent quantum dots are established as effective materials for their application. Quantum Dots benefit from unique quantum confinement effects which allow the material properties to be drastically altered in accordance with particle size. Smaller nanoparticles will have a greater difference in energy between their valence and conduction bands, which shifts their absorption and emission maxima to the blue region.⁴ Work from Schmitt-Rink *et al.* in the '80s describes the ratio between particle size and its Bohr radius as a fundamental factor in the control of quantum confinement.⁵ For example, the absorption onset of a PbS quantum dot can be modified between 800 and 2000 nm by varying the nanoparticle diameter between 4.3 and 8.4 nm.⁶ This unique property makes them particularly effective materials for optoelectronic devices^{7,8} or photovoltaics,⁹⁻¹² due to their capacity for energy level and light absorption matching. Another exciting characteristic of QDs is that they may undergo multiple exciton generation (MEG) under intense illumination,^{13,14,15} where a single, high energy photon theoretically generates more than one electron-hole pair in the QD sensitiser. Ultrafast transient absorption spectroscopy of a colloidal solution of PbSe quantum dots showed the generation both of three excitons for each photon (of energy 4 times greater than the QD band gap), and the generation of seven excitons per photon (of energy 8 times greater). For high efficiency solar conversion to form two excitons per photon, the band gap of the QD needs to be around 1 eV.¹⁶ MEG is more efficient in QD materials than bulk semiconductor, and the charge carriers could be collected to theoretically increase photocurrent by up to 30 %.¹⁴

5.1.2 Synthesis of Quantum Dot materials

Due to the QDs' small size, it exerts a quantum confinement effect across three dimensions, which allows for its properties to be tuned by adjusting size. Modifying the QD size is simple in terms of chemistry, but synthesis can be tricky since the surface area of the nanoparticle is very high. This causes the QDs to become quite reactive and aggregate, which can be prevented by the use of capping groups, which can stabilise the particle. For example, Sapra et al. synthesised CdSe nanocrystals via a 'green' hot injection method using olive oil as a coordinating solvent, eliminating the need for corrosive TOP. The CdO and Se precursors were soluble in the oil at elevated temperatures (200 °C), while oleic acid in the oil acts as a stabilising agent. CdSe crystals ranged in diameter between 2.3-6 nm with peak absorption around 500 nm. Increasing temperatures and heating times allowed the formation of larger crystals with red-shifted absorption spectra.¹⁷

QD materials have versatile and ranging applications, and the sensitiser often reported for QDSSCs include CdS, CdSe, PbS, PbSeS, CdHgTe, CdTe, CuInS₂ and Ag₂Se. CdSe and CdS are most commonly investigated due to their ease of characterisation and fabrication.⁴ Metal chalcogenides are generally utilised as QD materials because of their high photostability (compared to some organic dyes) and high absorption coefficients.⁸ PbS in particular has strong light absorption in UV region as well as a peak in the near-IR wavelengths.¹⁸ It also has a longer excited state lifetime (~2.6 μs) than CdS or CdSe dots. PbS QDs may be synthesised under N₂ in basic conditions, or most commonly, via a hot-injection synthesis,¹⁹ and have a narrow band gap suitable for application in p-type systems.²⁰ Until now, the majority of high performance QD based PV have relied on lead-based materials. PbX (where X= S or Se) and lead perovskite based QD structures have yielded devices with efficiencies up to 13.8²¹⁻²³ and 16.6 %²⁴⁻²⁶) respectively. The structures of these materials allow for excellent charge mobility and strong light absorption properties, which are attributed to the presence of Pb 6p orbitals within their electronic structures.²⁷

5.1.3 Integration of QDs into QDSSC

QDSSCs work on the same principle as DSSCs, except the molecular sensitiser is replaced by inorganic nanoparticle Quantum Dots.⁴ PCEs of QDSSCs are generally lower than those presented by DSSCs due to the narrower absorption profiles of the QD materials or

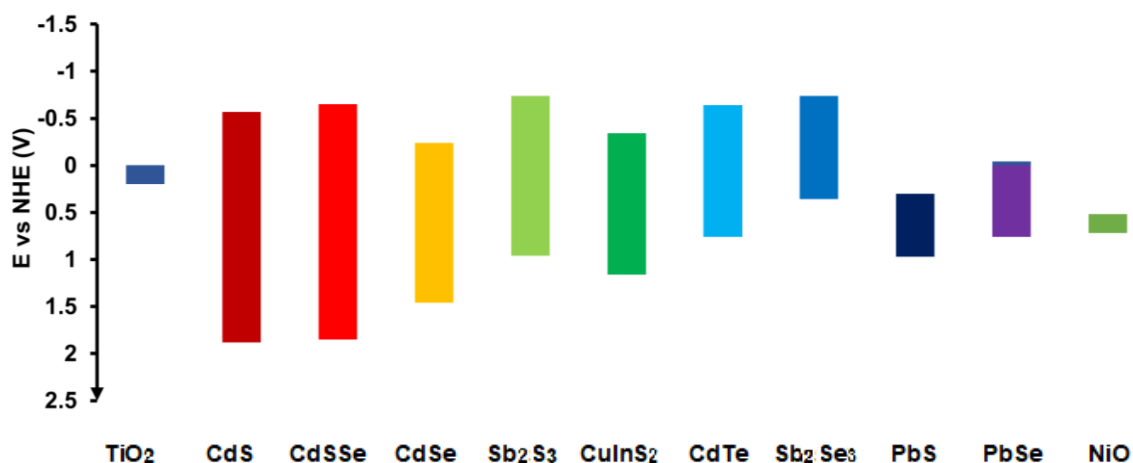


Figure 2: Simplified schematic showing relative bandgap energies vs NHE for a selection of quantum dot materials, in relation to the TiO₂ CB and NiO VB.

recombination processes occurring at the interfaces between QD, linker, or semiconductor.⁴ It is therefore imperative to select materials with appropriate absorption properties and configure device architecture to reduce these recombination pathways. The band gaps of several QD materials can be seen in Figure 2, compared to the VB of NiO and CB of TiO₂.

There are several methods used to apply QD materials in PV, but these techniques can be described as either in-situ (where nanocrystals are synthesised through growth on the semiconductor framework) or ex-situ (where QDs are synthesised in a separate reaction process and later incorporated into the device). Some of these methods are discussed below.

5.1.3.1 In-situ growth

A commonly used method of incorporating nanoparticles in situ is through a successive ionic layer adsorption and reaction (SILAR) procedure. Precursor solutions are prepared and separated so that the electrode can be dipped into each, one after the other. Each dipping step is followed by rinsing and drying. This method can be used in continuous cycles to 'build up' QDs on the surface.^{28,29} SILAR is a simple and inexpensive technique that would be suitable for larger scale applications, allowing the size and quantity of QDs to be modified by changing the number of SILAR cycles, concentration, and composition of the precursor solutions.³⁰ The effect of repeated deposition cycles has been investigated elsewhere and shown to give improved photoelectrochemical (PEC)

performance when CdSe QDs were applied to a p-type NiO film. A film treated with 12 successive SILAR cycles gave a significantly enhanced p-type PEC response because of higher QD loadings and more effective light absorption at longer wavelengths. However, cycles beyond 15 began to show reduced performance, even though light absorption in longer wavelengths increased. It was suggested that recombination reaction was facilitated through pore blocking by accumulating CdSe, suppressed ion transport, poor charge transfer, and an increase of non-active QDs. The higher coverage by CdSe also reduced the IPCE of shortly penetrating photons.²⁸

Both this technique and others such as chemical bath deposition (CBD)³¹ are excellent for creating highly loaded films, which is critical for preventing recombination processes between the electrolyte and un-sensitised semiconductor, and therefore key to improving performance of p-QDSSCs.³² However, while these deposition methods do yield high coverage of QDs on NiO compared to TiO₂, they still lack the finer control of particle size and crystallinity.

5.1.3.2 Ex-situ synthesis

QDs synthesised at high temperatures form highly regular, crystalline particles which can be integrated onto a film in several ways. Methods such as direct deposition, linker-assisted attachment or electrophoretic deposition have been investigated in n-type cells.^{33,34,35} The capping groups used to stabilise the QDs can also be used to modify the QD properties and bind them to other materials. In cases where QDs are synthesised separately to the semiconductor rather than grown directly upon it, the capping groups chosen must be compatible for surface binding. For example, the direct deposition of QDs onto the surface of NiO films requires the transfer of crude QDs from the organic to aqueous phase, which can be achieved by exchanging the organic QD ligands for others such as ligands with hydrophilic 'tails' and thiolate capping groups to stabilise the QD and link it to the film (Figure 7).³² Gomez et. al. suggested that sensitization routes based on pre-synthesized QDs show better results than the in situ growth techniques.³⁶ Capping groups can be utilised to bind the QD to the surface of the film, either by direct adsorption via the capping group, or with the assistance of a linker molecule. Examples of molecular wire linker molecules include mercaptopropionic acid (MPA), 11-mercaptoundecanoic acid (MUA), L-cysteine (Cys), or poly-diallyldimethylammonium chloride (PPDA).^{20,37} These molecules can either be incorporated onto the QD surface,

or bound to the film and then washed with QDs to sensitise the electrode. Work by Zhang et. al using CdSe QDs with MPA (mercaptpropionic acid) capping groups resulted in record efficiencies of 5.4 %.³⁰ Odobel et. al also demonstrated the sensitisation of NiO films with MPA-capped PbS QDs. The QDs were bound to the NiO using a linker deposition method- capped with oleic acid, treated with TBAI, and linked via MPA on the NiO surface. The surface was then washed with CTAB to substitute the OA ligands with halides and make room for more QDs. The extent of the washing and ligand replacement was monitored using IR spectroscopy and the resulting cells gave reasonable IPCEs up to the 950 nm range, with higher PCEs than reported for the **P1** dye.³² Photophysical studies have shown that hole injection from linker-attached QDs occurs with a high rate constant ($1.2 \times 10^9 \text{ s}^{-1}$), much greater than that of the radiative decay of the QD excited state ($6.7 \times 10^7 \text{ s}^{-1}$), however charge recombination is also very quick.³⁸

Electrophoretic deposition has also been used as a method to deposit TiO₂ nanoparticles in both solar cell and photocatalytic applications.³⁹ It can also be used for pre-synthesised QDs and involves high voltage deposition of QDs onto electrodes. Capping and finishing layers are added via SILAR deposition.⁴⁰ As a technique, it is relatively quick and simple, taking hours rather than the days needed for linker assisted or direct absorption of colloidal QDs. One example of this method involved the submersion of TiO₂ FTO electrodes in a PbSe QD solution diluted with toluene. A steady voltage of 200 V was applied to the electrodes for various amounts of time, followed by washing and deposition of a coating layer via SILAR that was later shown to passivate the surface and stabilise performance. Maximised performance was found to be achieved after one hour of applied voltage with efficiencies of up to 2.1 %.⁴⁰ Films such as these are characterised by p-XRD to determine the presence and form of CdSe on the surface. However applying this technique, which employs high voltage and specialised equipment, is not practical on a small scale in our laboratory, so direct deposition methods such as those described by Calzada et al.⁴¹ must be investigated instead.

5.1.4 Optimisation of QDSSC

5.1.4.1 Requirements for the Electrolyte and CE for QDSSC

The iodine redox couple commonly used in DSSC systems is not appropriate for use with p-type QD electrodes. Not only are the QDs unstable in the presence of the redox couple, but the iodide/triiodide potential is close to that of the NiO band edge, limiting the theoretical V_{oc} of the cell.³⁶

Alternative electrolyte systems are required, otherwise a protective layer such as passivation may be required to reduce degradation. Cobalt based electrolytes have proven successful,^{42,43} as they are generally weakly absorbing in the visible spectrum, and $Co^{II/III}$ redox mediators can have a more negative potential than I^-/I_3^- , improving the potential of the cell.⁴⁴

Polysulphide electrolytes have also been found to be very stable under irradiation, and are often chosen for use in QDSSCs.^{11,34,40} However, they are incompatible with the commonly used platinum-based counter electrode catalysts. As reported by Mora-Sero et al., the polysulfide electrolyte corrodes the platinum CE surface, decreasing the electrode's activity and conductivity.⁴⁵ Metal sulphides have been found to be efficient alternative counter electrode materials for QDSSCs due to their low charge transfer resistance and high electrocatalytic activity. They are also compatible with common polysulphide electrolytes, making them ideal for optimisation of QDSSCs.²⁹ CuS is a good candidate for work with CdSe and the optimisation of single-photoelectrode cells. CuS counter electrodes were prepared via a CBD methodology, with deposition times optimised in the experiment. $TiO_2/CdS/CdSe/ZnS$ QDSSCs that used the CuS counter electrodes exhibited a J_{sc} of 14.31 mA cm^{-2} , V_{oc} of 0.603 V , and FF of 0.49 , after a deposition time of 2 hours ($\eta = 4.27 \%$). This improvement from the values of Pt electrodes demonstrated the reduced charge recombination and low resistance required to synthesise efficient QDSSCs.²⁹

Other counter electrodes tested in CdS/CdSe QDSSCs in particular include graphite, carbon, and RGO (reduced graphene oxide). Greater efficiencies and FF values are obtained using Graphene and Pt electrodes for CdS, while CuS and Pt worked best for CdSe.⁴⁵

5.1.4.2 Modification of QD structures

One method investigated to combat charge recombination in QDSSC involved the passivation of the QD surface with a ZnS coating (in the case of CdSe and CdS) to suppress the surface trapping of excited states by the QD. The passivation layer would be a material with a higher band gap than the QD material, which forms a core-shell structure.³¹ This wider-band gap semiconductor may also protect the QDs from photodegradation. The dynamics of electron and hole injection in core-shell $\text{Cd}_x\text{Se}_y\text{Zn}_{1-x}\text{S}_{1-y}$ QD sensitised NiO was studied using ultrafast fluorescence and X-ray spectroscopy by Abdellah et. al. Hole injection was found to be slower than the corresponding electron injection rates and was influenced less by the passivation layer thickness. Their investigations found that the hole's effective mass was much smaller in the protective layer than the 'core' material, concluding that the wavefunction of the hole must extend more easily through the gradient shell than that of the electrons.⁴⁶

Another challenge for nanoparticle based solar cells is to take advantage of quantum confinement effects to improve light harvesting, without the drawback of hindering later charge transport to the electrodes. Some binary QDs that have been tested in quantum dot solar devices have resulted in low efficiency, due to the poor charge transport between the nanocrystals.

The synthesis of 'ternary' structured QDs could also be advantageous. Binary compositions of PbS and PbSe crystals of similar bandgap were investigated, with PbS giving larger V_{oc} and PbSe crystals producing larger short circuit photocurrent.⁴⁷ By creating a variable ternary $\text{PbS}_x\text{Se}_{1-x}$ alloy structure within each nanocrystal, QDs could be engineered to optimise both carrier transport and voltage. These nanocrystals can be synthesised in a one-pot hot-injection reaction where the ratio of Se to S can be modified to change the stoichiometry of the product crystals. These 'alloy' QDs perform well due to the reduced effect of surface traps on recombination. The larger size of the crystals encouraged greater electronic coupling between QDs, facilitating charge transport.⁴⁷

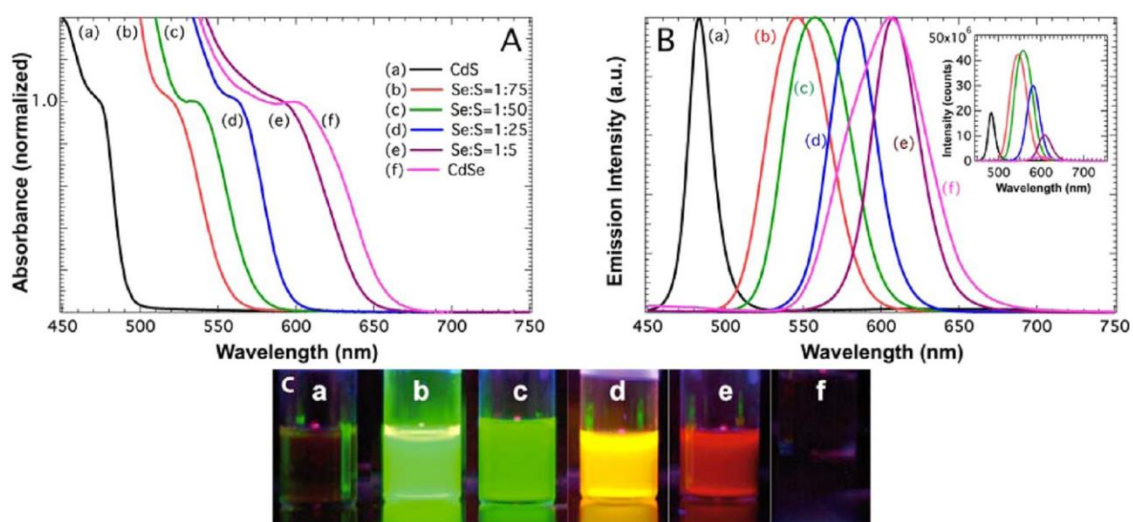


Figure 3: **A)** Absorption spectra (normalised at 1 to excitonic peak), **B)** emission spectra (recorded at 400 nm and normalised to emission peak) and (inset) relative emission intensity variation, and **C)** photographs under UV light of CdSe_xS_{1-x} QDs with different Se:S ratios.³⁵

Kamat et al. also synthesised ternary QDs based on a CdSe_xS_{1-x} structure, giving an array of opportunities for tuning the QD photoresponse beyond modifying size.³⁵ Lead chalcogenides were also investigated for use as semiconductors in solar cell applications. Their large exciton Bohr radii (PbS 18 nm, PbSe 47 nm, and PbTe 150 nm) meant that when the nanocrystals were one tenth of the diameter, electrons and holes could tunnel through the crystals thin organic surface coating. This resulted in strong electronic coupling between the particles, facilitating good charge transport.

Kamat et al. also prepared highly luminescent CdSe_xS_{1-x} quantum dots, with a gradient structure that allowed for tuning absorption and emission bands without modifying the particle size, as seen in Figure 3. Electrophoretic deposition techniques were used to sequentially layer the cadmium chalcogenides within a TiO₂ film. These tandem layers gave overall efficiencies higher than that of the individual layer performance. Power conversion efficiencies of up to 3.2 % were obtained for two tandem layers, resulting in an increase of over 30 % from the expected efficiency of 1.91%.³⁵ TEM images showed very little change in the QD size between each gradient alloy, therefore changes in the spectra couldn't be attributed to size changes. This offers more flexibility in the tuning of QD properties to suit the application. By layering the various QD stoichiometries in a system where larger band gaps decrease to smaller ones as they approach the substrate, high energy photons can be captured, while lower energy photons filter through and are

trapped by the next layer down. This vastly increases the range of wavelengths at which the cell can operate.

5.1.5 Aims for this Chapter

As described above, the optical bandgap (E_g) of an absorber material is defined as the difference in energy between conduction and valence bands. By modifying the size and composition of the quantum dots, the power conversion efficiency of a solar cell could have the potential to significantly increased by using absorbers with different E_g values together. The band gap of the absorbing materials will dictate the output voltage and current. Therefore, initial choice of QD material is key to tailoring the range of spectral response that the device operates under. Research is currently focussed on attempting to increase η by improving light harvesting efficiency and electron transfer rate within QDSSCs. Different approaches to this problem include the use of multi-layered QDs (on TiO_2), modifying QD size, changing deposition methods, and the use of passivation layers. Passivation layers aim to fix defects such as unsaturated surface atoms in order to reduce the number of alternative decay pathways.⁴ Blocking layers may also be used to improve device performance, in which materials such as Al_2O_3 or SiO_2 can be grown on NiO surfaces before sensitisation to reduce recombination of the hole with both the electrolyte and excited QD.³⁶ The work in this Chapter will cover both the ex-situ synthesis of monodisperse, red absorbing PbS QDs, and the direct, in-situ growth of CdS nanocrystal films to apply to NiO films. The surface coverage of the QDs is key to reduce recombination between the NiO and electrolyte and improve device efficiencies when using the films. Once a deposition protocol has been established, then alternative materials can be applied for use in p-QDSSC and tandem configurations, with a focus on non-toxic, heavy-metal free materials as sustainable sensitising materials.

5.2 Direct Deposition of PbS Quantum Dots

5.2.1 Synthesis and Characterisation of PbS

Lead Sulphide (PbS) nanocrystals were synthesised via a hot injection approach.³² Briefly, two solutions of bis(trimethylsilyl) sulfide (TMS) in octadecene and PbO, and oleic acid (OA) in octadecene were prepared and heated separately to 120°C. Once heated, the TMS solution was quickly injected into the PbO-OA solution and allowed to react for 2 minutes, before rapid quenching and cooling. Upon removal of the PbS-OA QDs and re-suspension in toluene, they were taken for further analysis. Details for this synthesis can be found in Section 5.6.

The dispersion of PbS QDs in toluene was dropcast for imaging via high-resolution transmission electron microscopy (TEM) with the resulting images shown in Figure 4. The discrete nanoparticles can be seen to be uniform in shape and diameter, with the inset showing that the diameter of the PbS QDs can be estimated from these images to be roughly 3 nm.

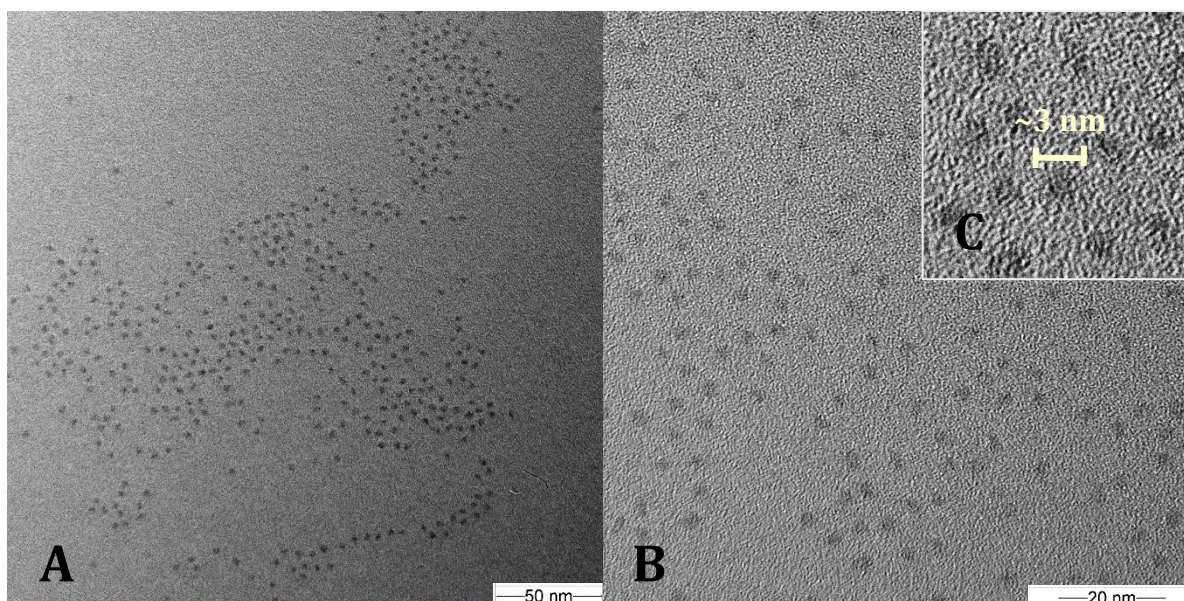


Figure 4: TEM images of PbS QDs measured with 200 kV accelerating voltage **A)** at 100000 x magnification, **B)** at 250000x magnification and **C)** (inset) scaled up image from 250000x magnification annotated with the estimated size of the QD.

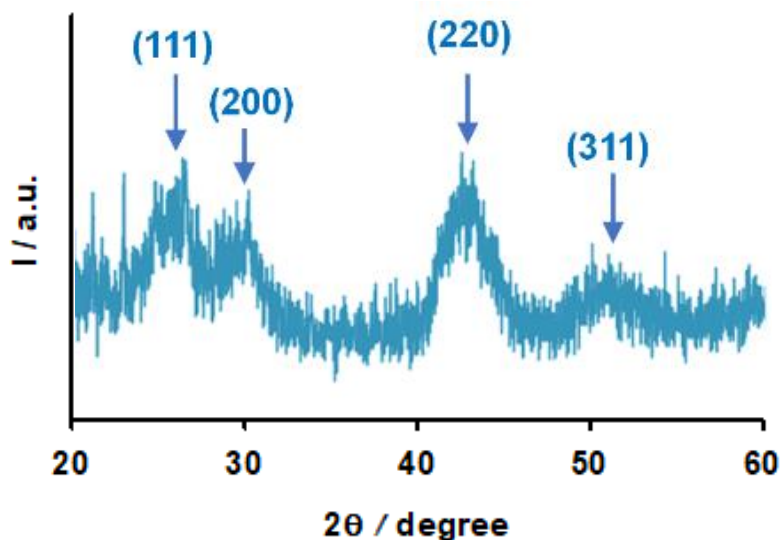


Figure 5: XRD pattern for drop casted PbS nanocrystals.

The XRD pattern for the PbS nanocrystals is shown in Figure 5, and contains broad peaks at 2θ values of 26° , 30° , 43° , and 51° . These correspond to crystal diameters corresponding to $d = 3.42$, 2.97 , 2.09 and 1.79 \AA respectively, matching with the (111), (200), (220) and (311) planes of a PbS fcc crystal lattice (JCPDS file no. 77-0244).

Sensitization of NiO was achieved via immersion of the films in a bath of PbS QDs for 24 hours. One method to improve loading of the QDs onto the film, as highlighted previously, is to exchange the capping ligands of the QD material to alternatives that may facilitate

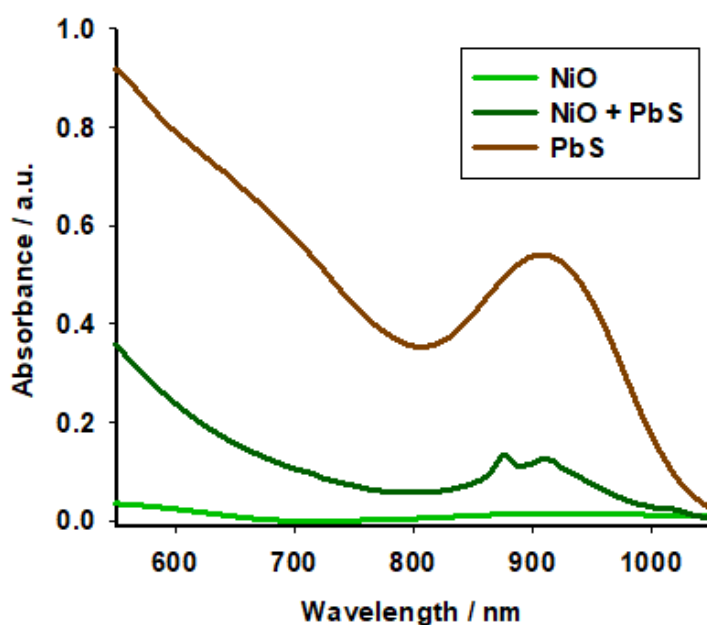


Figure 6: UV-Visible spectra of PbS-sensitised NiO films and the PbS QDs in stock toluene solution.

charge transfer or enable binding to the semiconductor surface. In this case, a short chain molecule, mercaptopropionic acid (MPA), was used to replace the fatty oleic acid capping groups. By pre-treating the NiO film with the acid group, an increase in chemisorption of PbS nanocrystals may be possible.

UV-Visible spectroscopy of the stock PbS solution highlighted a characteristic peak at 873 nm. Loading of PbS onto NiO was poor, with and without the MPA pre-treatment, as seen by the weak characteristic peak for the QD on the sensitised films.

5.2.2 Device Results

To assess the efficacy of the MPA pre-treatment, devices were constructed using the as-fabricated NiO-PbS photocathodes, a $[\text{Co}(\text{dtb-bpy})_3]^{2+/3+}$ redox electrolyte and platinum counter electrodes. The J/V profiles of the resulting champion devices can be seen in Figure 7, and the corresponding device parameters are listed in Table 1.

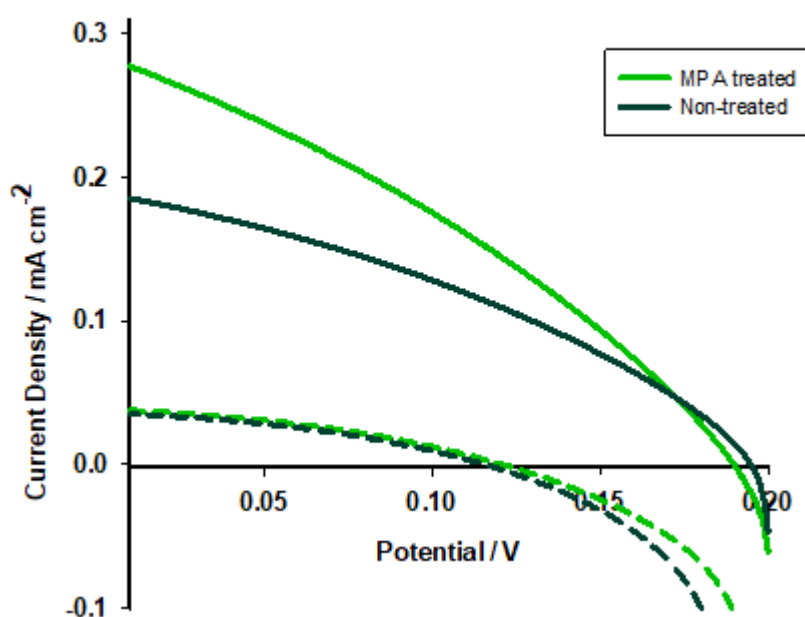


Figure 7: Plot of current density against voltage for the champion 2 layer NiO devices containing deposited PbS both with and without MPA pre-treatment. Electrolyte composition: 1 M $\text{Co}(\text{dtb-bpy})_3(\text{ClO}_4)_3$, 1 M $\text{Co}(\text{dtb-bpy})_3(\text{ClO}_4)_2$, 0.1 M LiClO_4 in 3-methoxypropionitrile. Dotted lines indicate measurement without light.

Material	J _{sc} / mA cm ⁻²	V _{oc} / V	FF	η/%
MPA treated	0.248	0.176	0.31	0.013
Non- treated	0.154	0.18	0.33	0.009

***Table 1:** Summary of the performance of 2L-NiO/PbS devices tested in this section.*

Treatment of the films with MPA consistently improved performance of the devices, but poor loading of the QDs produced limited the device photoresponse, particularly when compared to the dark response of the devices.

Similar to dye-sensitisation, ligand-assisted deposition techniques have an element of specificity in terms of their application to a surface. The dependence of device performance on ligand binding and surface chemistry is beyond the scope of this work but would be key in understanding the optimal binding methodology for upscaling ligand-assisted deposition. In terms of the aims of this work, a more ‘one size fits all’ method of sensitizer application is required for the screening of alternative materials and architectures of tandem devices.

5.2.3 Integration into Anodes for Photo-Electrochromic devices

While the direct and linker-assisted deposition techniques have been deemed unsuitable for the scope of this work, they have been used to good success in applying complementary absorbers in other contexts. The QDs prepared for this work were applied into photoelectrochromic devices (PECs) constructed using TiO₂/CdS or co-sensitised TiO₂/CdS/PbS photoanodes, an aqueous 0.1 M Na₂S electrolyte, and an electrochromic CE, an Ag-V₂O₅ film. The devices were tested as solar cells to determine their potential as PECs using the same configurations, and the parameters are listed in Table 2. The J/V response of the TiO₂/PbS photoanode with the Ag/V₂O₅ 'CE' film gave an efficiency of 2 %, with a high J_{sc} of 9.64 mA cm⁻², a value comparable to previously reported PbS QDs grown via SILAR on mesoporous TiO₂.⁴⁸ While the performance of the individually sensitised CdS and PbS photoanodes produced these reasonable results, combining the two sensitisers produced a complementary spectral response that further boosted the efficiency of the device.

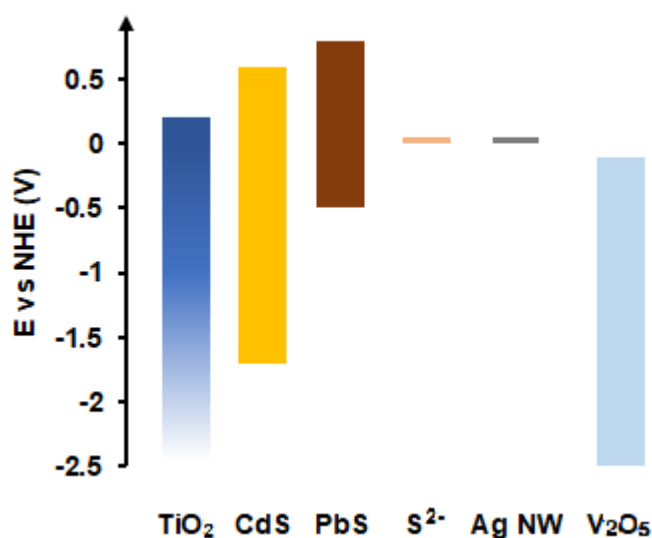


Figure 8: Relative energy levels of the CdS and PbS band edges relative to the TiO₂ CB.

Material	$J_{sc} / \text{mA cm}^{-2}$	V_{oc} / mV	FF	$\eta / \%$
TiO ₂ /CdS–Ag/V ₂ O ₅	7.72	999	0.48	3.74
TiO ₂ /PbS–Ag/V ₂ O ₅	9.64	578	0.36	2.00
TiO ₂ /CdS/PbS–Ag/V ₂ O ₅	9.02	1134	0.51	5.21

Table 2: Solar cell parameters of the listed combinations of photoanodes and CEs with 0.1 M Na₂S electrolyte, under 1 sun illumination (100 mW cm⁻², AM 1.5G); exposed cell area: ~0.15 cm²

Additionally, the coating of the TiO₂/CdS photoanode with the narrow-band gap PbS produces a cascade-effect for electron transfer from the PbS CB to the TiO₂ as shown in Figure 8, which boosted the photovoltage output without compromising photocurrent. Figure 9a shows the absorption profiles of the co-sensitised photoanodes, with two key absorption bands; one below 500 nm attributed to the SILAR-grown CdS, and another peak at 879 nm from the presence of the PbS QDs.

Figure 9b also shows the IPCE response for the TiO₂/CdS photoanode both with and without the additional PbS material. While the response between 400-500 nm remained similar at ~50 % for both, the additional increase to ~9 % at just under 900 nm for the PbS-sensitised anode indicates harvesting of some red photons by the PbS QDs.

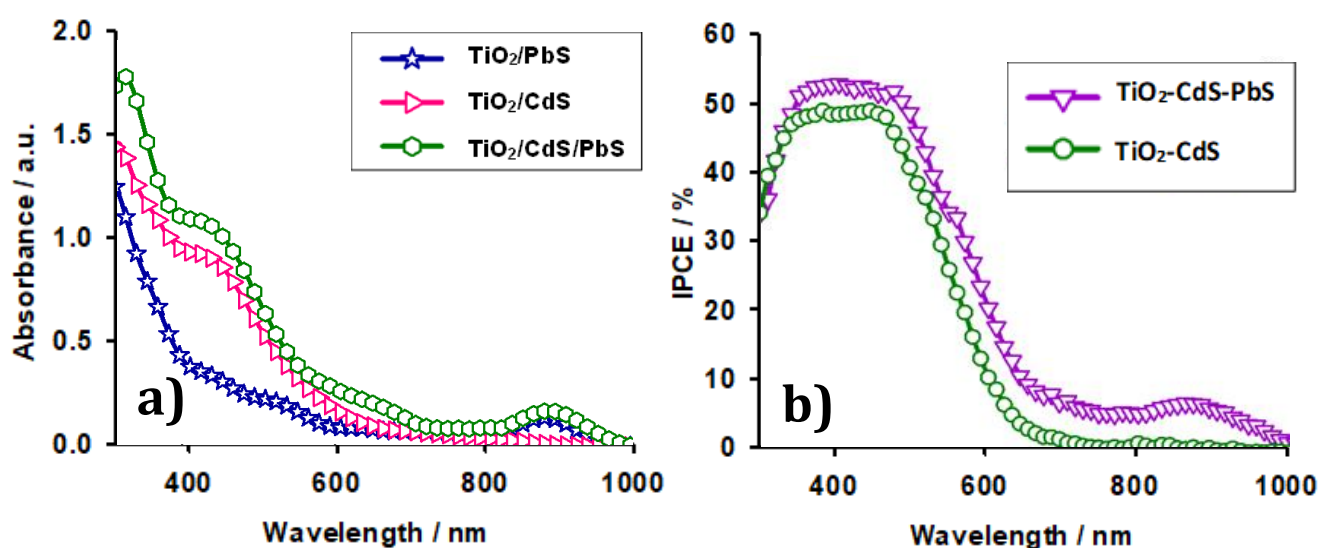


Figure 9: a) UV-Visible spectra of CdS and PbS-sensitised TiO₂ films and b) IPCE response of devices discussed in this section. Modified from Paper 3

5.3 Automation of CdS nanocrystal deposition via SILAR

5.3.1 Automation of SILAR technique

To improve loading of material upon the semiconductor surface, an alternative deposition method was employed. A Successive Ionic Layer Adsorption and Reaction (SILAR) mechanism was employed to deposit discrete layers of nanocrystalline material. For cadmium sulphide, the procedure runs as follows; firstly, the film was submerged in a solution of CdNO_3 in water. After a washing step, the films were dipped into a solution of Na_2S in 1:1 H_2O and MeOH and washed again to complete a single cycle of SILAR. Experimental details for this process can be found in Section 5.6. When performing this reaction by hand, each cycle can take up to 10 minutes. In small batches, performing this procedure manually is feasible and repeatable. However, for large quantities of film preparation, operator fatigue and human error can begin to compromise the quality and integrity of samples. Automation of this reaction is key for the application of these materials into upscaled or screening processes. While there are some commercial options available for SILAR deposition of QD materials, they can be costly or require a large footprint.⁴⁹ To reduce operator input and increase the quality of resulting films, an automated setup was designed, built and implemented to generate QD films. Using commercially available LEGO pieces (LEGO® MINDSTORMS® EV3 Kit no. 31313), two moveable robot arms were built and programmed to perform the dipping steps within the SILAR cycle.

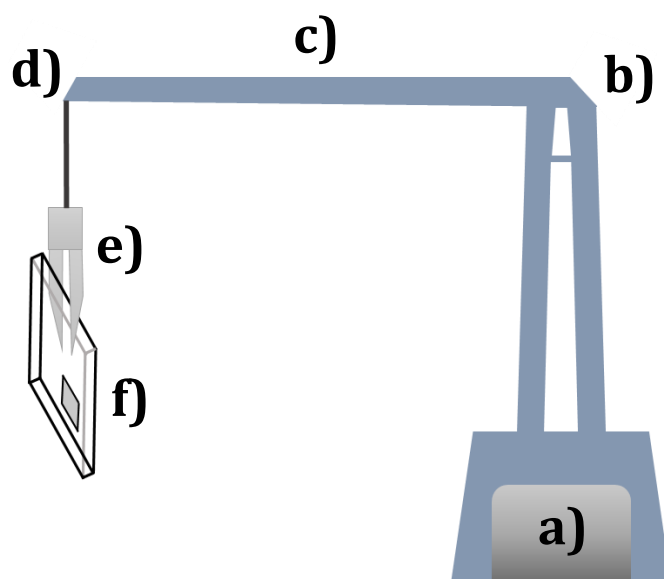


Figure 10: Simplified diagram representing the LEGO armature robot used to automate the SILAR process, with key components a) Power source b) 'left-right' rotation point c) extending arm d) 'up-down' rotation point, e) clamp and f) sample.

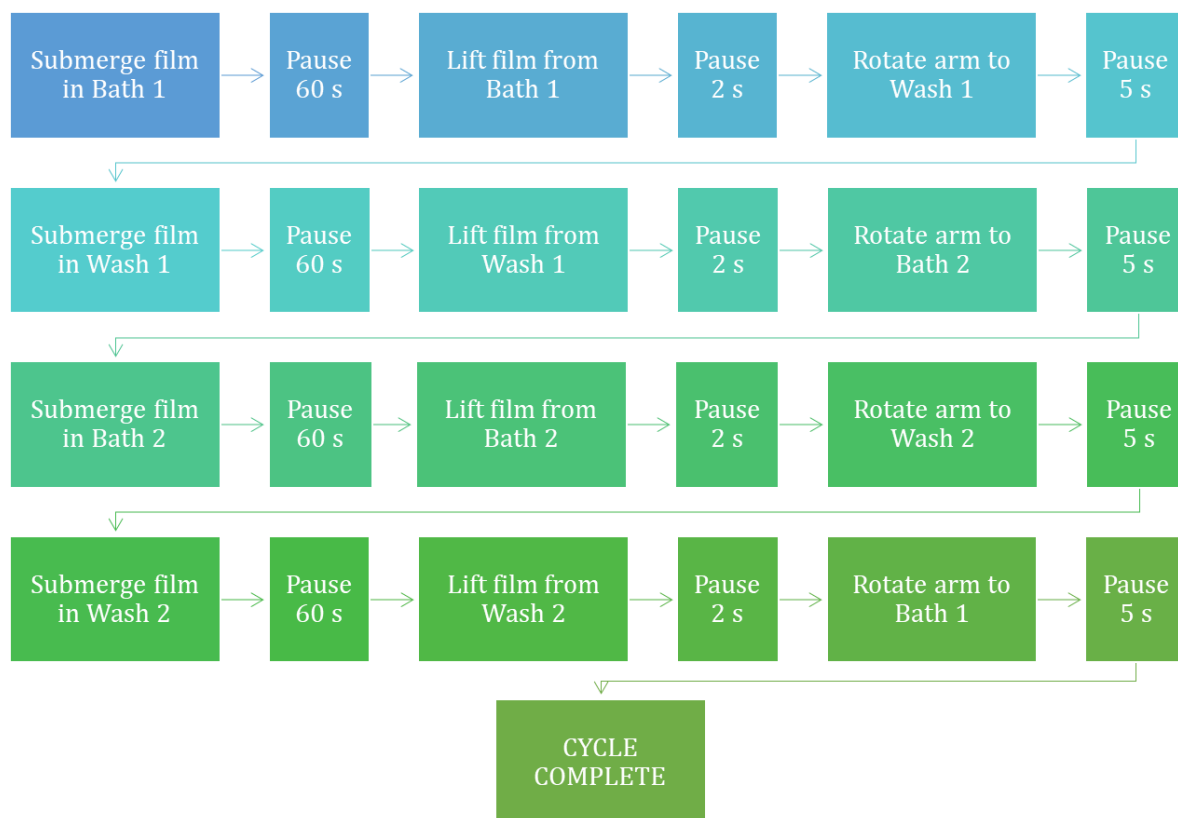


Figure 11: Simplified flowchart schematic of the programmed actions for the automated SILAR process. Total elapsed time for each cycle is less than 5 minutes.



Figure 12: Photograph of the one of the first iterations of the LEGO SILAR robot.

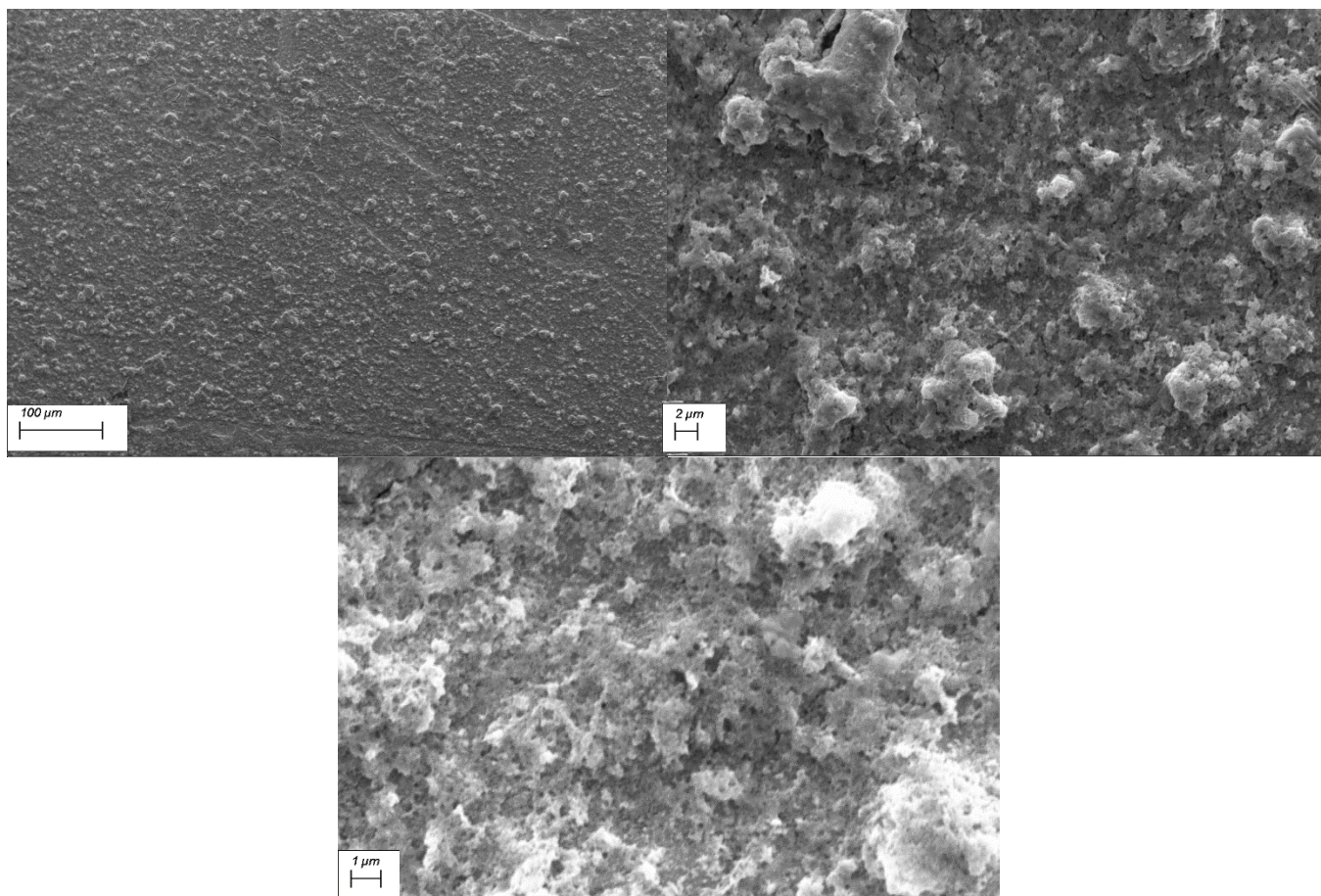


Figure 13: SEM Images of 16 cycle CdS films on FTO under 15 kV accelerating voltage and 6mm working distance with **a)** 375 x **b)** 4950 x and **c)** 13,280 x magnifications.

Figure 10 shows a simplified diagram of the principal components of the robot arm, while Figure 11 shows a flowchart of the subroutine program used to accomplish a single cycle of SILAR. The completed robot, shown in Figure 12, was used to prepare films of CdS using SILAR cycles in multiples of 8.

5.3.2 Material Properties

Upon addition of multiple layers of reacted CdS, the colour of the screen-printed NiO films changed from a pale grey to a vibrant yellow. As the number of cycles increased, this yellow coloration increased in intensity and saturated to a bright orange. SEM images of the films in Figure 13 show clusters of sub-micron crystallites that agglomerate into larger structures.

XRD analysis of NiO- CdS films on FTO gave the pattern shown in Figure 14. Peaks at 26.5, 30.8, 43.9, and 52.1° indicate the presence of cubic CdS nanocrystals.⁵⁰ Figure 16 demonstrates the increase in intensity of absorption upon addition of multiple layers of

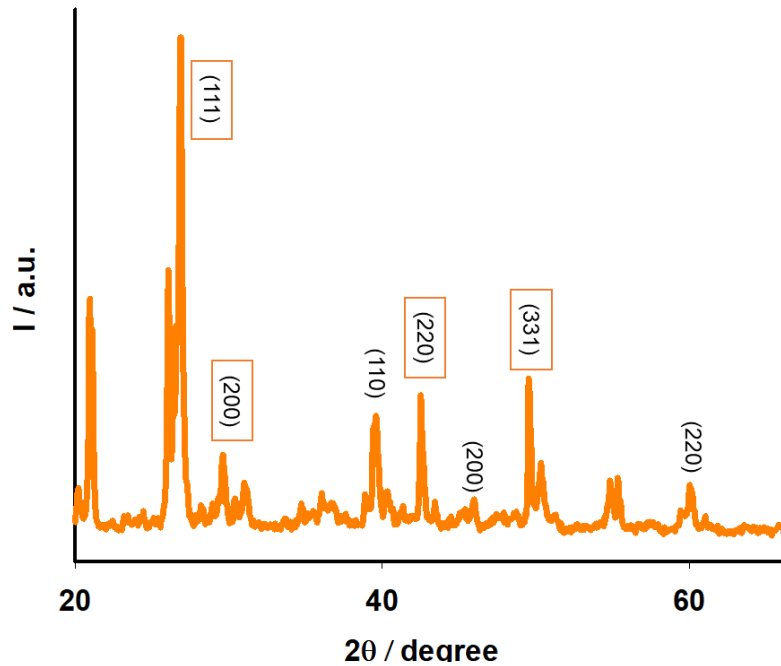


Figure 14: XRD pattern of the as-prepared 2 layer NiO + 16 cycle CdS film. Peaks in boxes correspond to the assigned to the cubic phase structure of CdS, while other peaks are attributed to the NiO phase.

CdS with SILAR. The absorption peaks at around 500 nm increase in intensity with the addition of each group of layers. Diffuse reflectance of the thin films was also used and the resulting Tauc plot in Figure 15 interpreted to determine a change in bandgap with the additional SILAR cycles. Thanks to Dr John Mallows for his assistance in running this experiment and interpretation of the results. This showed that an increase in the number of applied cycles increased the band gap of the CdS within the expected range, from 2.41 to 2.64 eV.⁵¹ While an increase in cycles would be expected to decrease the bandgap of the QDs as they grow, the results here could indicate uneven growth, causing the formation of a mixture of particle sizes during the SILAR process.

Number of SILAR cycles	Band Gap (eV)
8	2.41
16	2.55
24	2.61
32	2.62

Table 3: Calculated bandgaps for each SILAR cluster from the plot in Figure 15

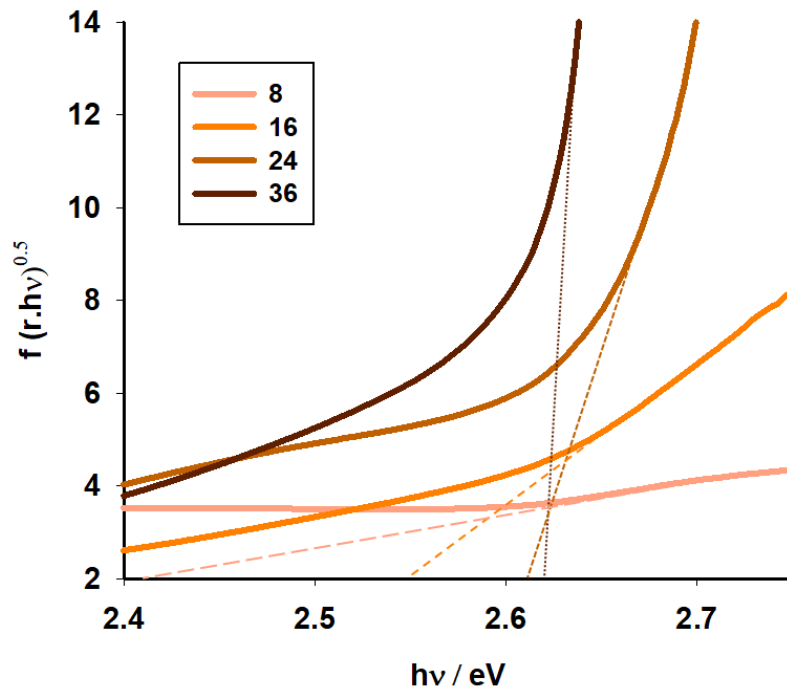


Figure 15: Tauc plot derived from diffuse reflectance spectra. Dashed lines illustrate the extrapolation of band edges from each peak.

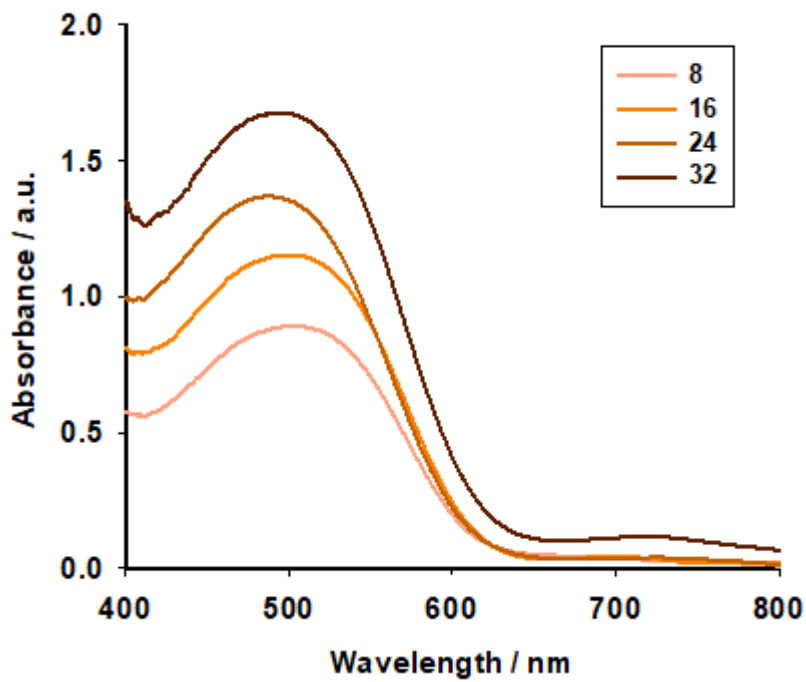


Figure 16: UV-visible absorption spectra of CdS thin film on FTO+2L NiO for each number of SILAR cycles.

5.3.3 Device Results

Devices containing 2 layer commercial NiO films and varying quantities of SILAR-deposited CdS material were prepared. The sandwich cells contained an electrolyte composed of 0.1M Na₂S in H₂O, thickened with silica to form a gel. The J/V curves in Figures 17 and 18 and device results in Table 4 for the sandwich cells show that increasing the number of CdS SILAR cycles used improved the device performance. The increase in current density between 8 and 16 cycles is significant. The change in dark current is also large, with a decrease in recombination and dark current indicating improved coverage of the NiO film with the CdS material. The addition of an extra set of cycles, taking the number to 24, increased the efficiency yet again. However, increasing the number of CdS deposition cycles to 32 or even 40 resulted in devices with highly variable results, making them unreliable. Further testing of these devices could be an area of exploration. The results from these devices are very promising, matching the current outputs of p-DSSCs constructed in earlier chapters, but with improved V_{oc} values. Device efficiencies for 24 cycles are, to the best of the authors knowledge, a record for the comparatively unexplored area of p-QDSSC.

Number of cycles	J _{sc} / mA cm ⁻²	V _{oc} / V	FF	η/%
8	0.803	-0.389	0.32	0.100
16	2.98	-0.523	0.35	0.545
24	4.07	-0.589	0.35	0.839

Table 4: Solar cell parameters of 2L NiO devices sensitized with varying numbers of CdS SILAR cycles, using 0.1 M Na₂S gel electrolyte under 1 sun illumination (100 mW cm⁻², AM 1.5G); exposed cell area: 0.15 cm²

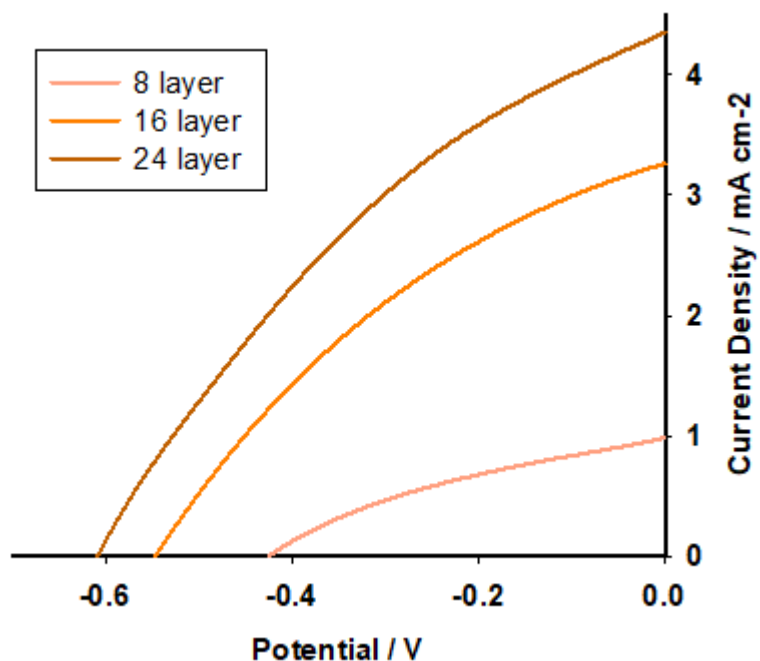


Figure 17: Plot of current density against voltage for illuminated champion 2L NiO devices sensitised with CdS nanocrystals applied with varying numbers of deposition cycles.

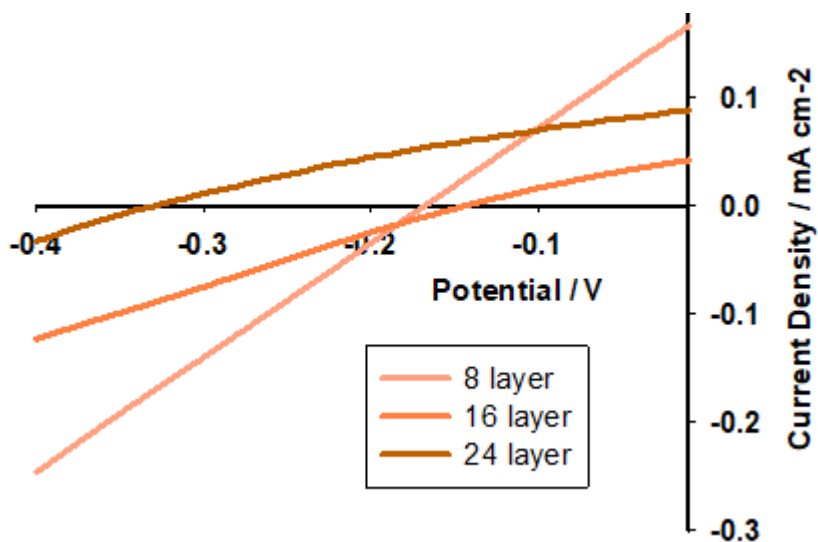


Figure 18: Plot of current density against voltage for champion 2L NiO devices sensitised with CdS nanocrystals applied with varying numbers of deposition cycles in the dark.

5.3.4 Examination of CE Materials

Three varying counter electrode materials were evaluated as candidates for investigation of CdS and other varieties of QDs. These materials included an established carbon-fabric CE comprised of woven, conductive carbon fibres. The second CE tested was a CuS counter electrode prepared on TEC 8 FTO as described in Section 5.6. The last material was a novel, microporous, and flexible nickel-based material known as nickel foam (Ni-foam). Figure 19 shows the microstructure of the foam under magnification via SEM. While the porous nature of both this film and the C-fabric prevent the use of purely liquid electrolytes in device testing, a gel-based polysulphide electrolyte was used to good effect to investigate these materials. Use of the porous CE also meant that the devices couldn't be fully sealed, limiting the amount of characterisation pathways available.

Sandwich cells were constructed using CdS nanocrystals deposited during 16 SILAR cycles, a gel polysulphide electrolyte and architecture described in Section 5.6. 16 cycle films were chosen as a compromise between the elapsed time for sample preparation and device performance. The JV curves and calculated efficiencies can be seen in both Figure

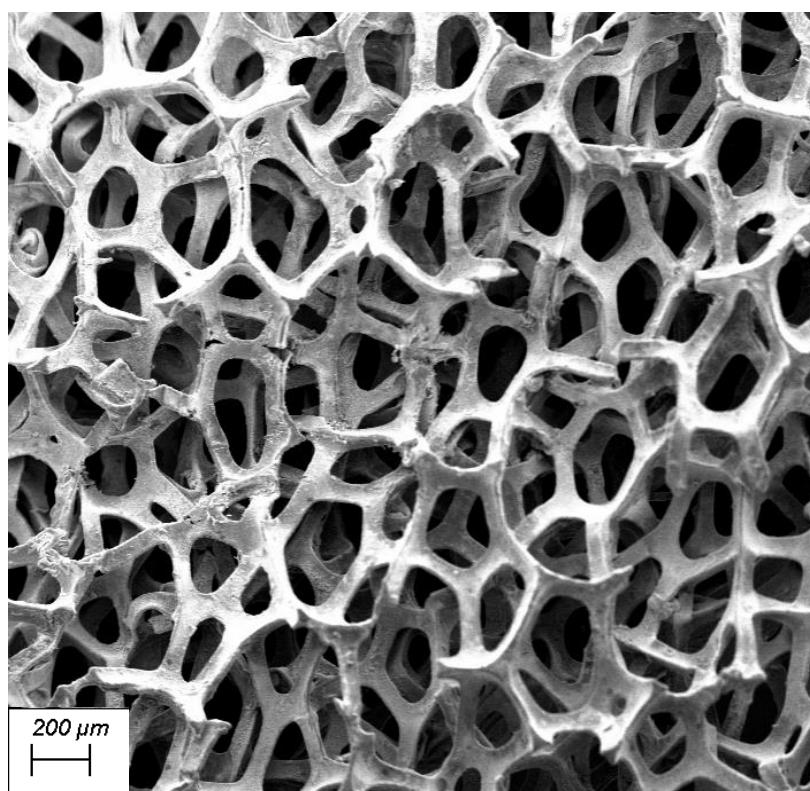


Figure 19: SEM Image of nickel foam under 15 kV accelerating voltage and 8.5mm working distance with a 71 x magnification.

Counter Electrode	$J_{sc} / \text{mA cm}^{-2}$	V_{oc} / V	FF	$\eta/\%$
C Fabric	4.07	-0.59	0.35	0.84
Ni foam	2.98	-0.52	0.35	0.54
CuS	0.47	-0.32	0.27	0.04

Table 5: Solar cell parameters of devices using varying CEs with 0.1 M Na_2S gel electrolyte, under 1 sun illumination (100 mW cm^{-2} , AM 1.5G); exposed cell area: 0.15 cm^2

Figure 20 and Table 5 respectively. C-fabric based devices consistently gave high current output, but FF values varied from device to device, based on the tightness of the weave or amount of permeation of the gel through the fibres. CuS devices performed badly in line with their poor conductivity. The Ni foam devices performed well, and were the most consistent in their performance, and were consequently the CE of choice for both the previously described optimisation of SILAR cycle quantity, and subsequent testing in this chapter. There is room for further examination and comparison of these materials, as well as the exploration of methods to seal devices made with these CEs. Impedance spectroscopy of devices constructed with these materials and investigation into the

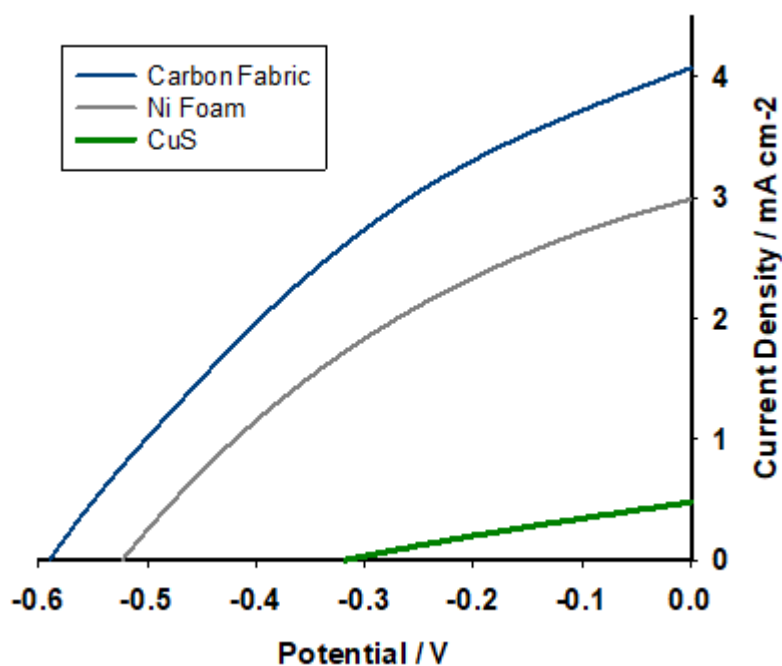


Figure 20: Plot of illuminated current density against voltage for 2 layer NiO devices using varying CE materials, sensitised with CdS nanocrystals (16 SILAR cycles).

interaction of these CE with other redox electrolytes may be good directions to follow in further work.

5.3.5 Co-sensitisation with RJ3

While the CdS films generate promising current output when applied to p-type devices, the narrow spectral response of the QDs is a limitation to device performance. One experimental pathway used to improve the spectral response was a co-sensitisation with the red shifted p-type dye discussed in Chapter 4. As-prepared CdS films were tested in sandwich cells, cleaned, and submerged in a dyebath containing **RJ3** for 24 hours before reassembly and retesting. UV-Visible spectra of the NiO films before and after co-sensitisation, can be seen in Figure 21. The high coverage of NiO by CdS before

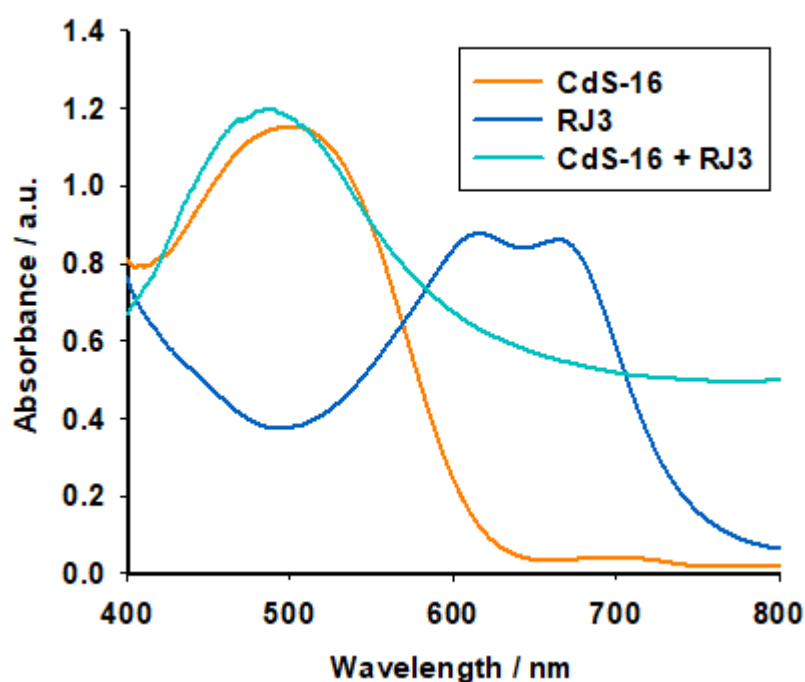


Figure 21: UV-visible absorption spectra of thin films of RJ3 co-sensitised CdS on FTO

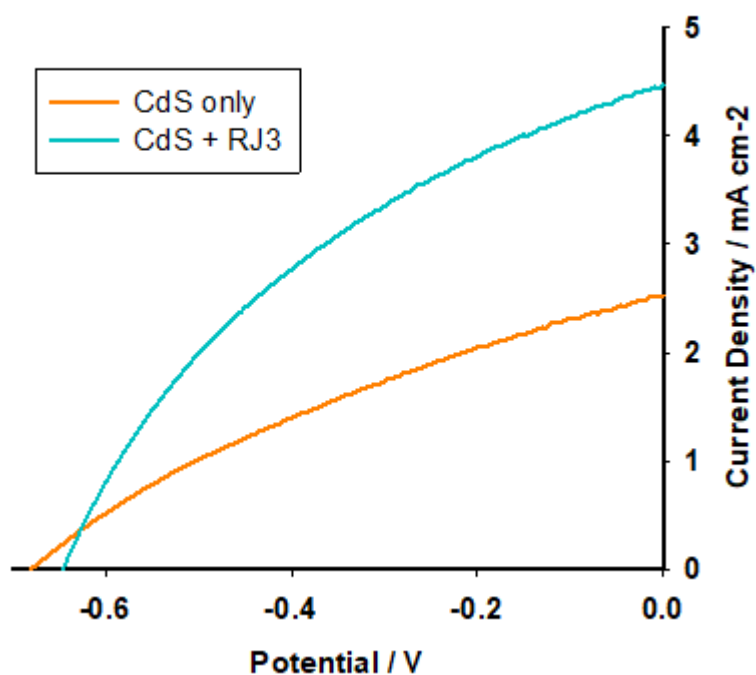


Figure 22: Plot of illuminated current density against voltage for CdS-sensitised 2L NiO devices both with and without the RJ3 co-sensitiser.

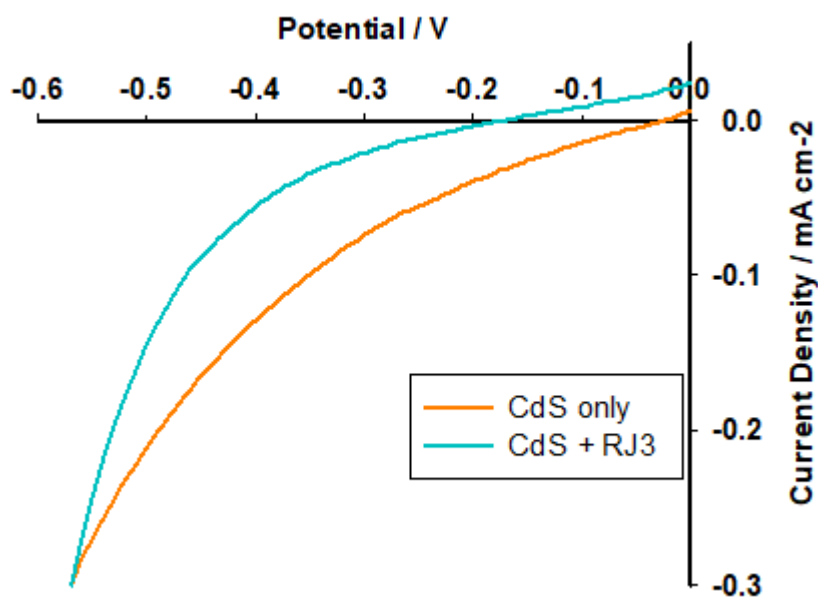


Figure 23: Plot of dark current density against voltage for CdS-sensitised 2L NiO devices both with and without the RJ3 co-sensitiser.

co-absorption suggests that **RJ3** is directly bound to the CdS nanocrystal layer. The absorption of the films is seen to extend further towards

Sensitiser	$J_{sc} / \text{mA cm}^{-2}$	V_{oc} / V	FF	$\eta/\%$
CdS	3.77	-0.68	0.33	0.84
CdS + RJ3	4.44	-0.65	0.38	1.10

Table 6: Solar cell parameters of NiO-CdS devices with and without the RJ3 co-sensitiser, using Ni foam CE and 0.1 M Na₂S gel electrolyte under 1 sun illumination (100 mW cm⁻², AM 1.5G); exposed cell area: 0.2 cm²

the infra-red region upon co-sensitisation with the red-shifted dye. Improved absorption capabilities seemed to increase the performance of the devices, examples of the J/V curves for which can be seen in Figures 22 and 23. The improved FF values and increased current highlight the benefits of adding the co-sensitising dye to performance under illumination. The dye may also act as a conduit for hole transfer from the CdS to the redox electrolyte, reducing recombination pathways and improving the fill factor. Further study of the charge transfer mechanisms within the device could be an interesting route for further understanding of the working principles of these devices. This work coincides with the findings by Kamat et al. in their study of co-sensitisation of CdS with red-shifted dyes on TiO₂.⁵¹

The work demonstrated in this section sets a benchmark for QD devices studied in this Chapter that is comparable to the very few other p-type QDSSC in literature, and often surpasses the performance of dyes for p-DSSC. The electrolyte composition, SILAR automation process and novel Ni foam counter electrode are all subsequently used for further exploration of QD materials and optimisation of device architecture in the next section.

5.4 Investigation of Alternative Architectures and Materials

5.4.1 Synthesis and Characterisation of Bi_2S_3

The use of heavy-metal based materials is common in the development of QDSSCs due to their ease of synthesis and establishment in literature. One alternative material used fairly recently in TiO_2 based n-QDSSC is Bi_2S_3 , a narrow band gap, near-IR absorber containing earth abundant, non-heavy metal elements.⁵²⁻⁵⁴ Photoanode based device efficiencies using QDs of this material have reached 0.8 % through the optimisation of the deposition route.⁵⁵ The red shifted absorption and simple synthesis of these QDs make them an interesting candidate for inclusion into p-QDSSCs.⁵⁶ Bismuth sulphide QDs were therefore investigated as a lead-free Near-IR absorber material that could be used as light harvesters for p-type and tandem QDSSCs.

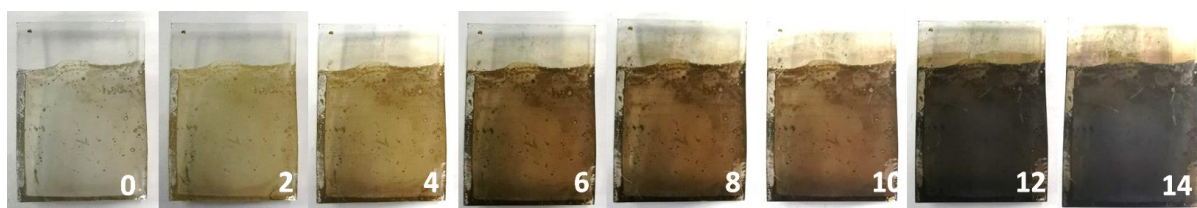


Figure 24: Images of Bi_2S_3 thin films on NiO after every other number of SILAR cycles.

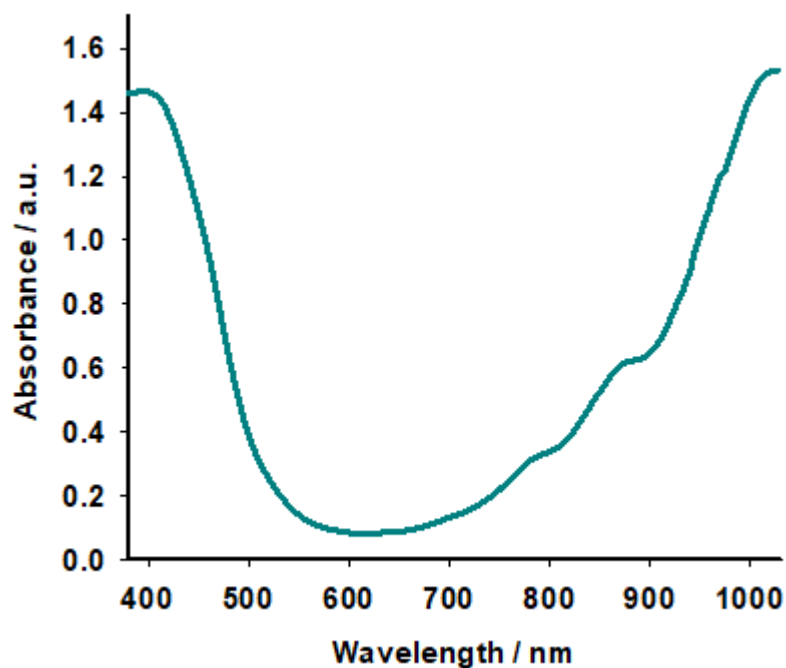


Figure 25: UV-visible absorption spectra of a 10 cycle thin film of Bi_2S_3 on NiO.

By utilising the deposition techniques and CE material investigated earlier in this chapter, Bi_2S_3 thin films were rapidly synthesised and incorporated into devices. The automated SILAR technique was used to prepare the photocathode using solutions of $\text{Bi}(\text{NO}_3)_3$ and Na_2S as the bismuth and sulphur sources respectively. Due to the speed of each dipping cycle, with only 10 seconds of submersion for each chemical bath, the robot proved invaluable to ensure timing was consistent throughout the SILAR process. Figure 22 shows the rapid change in colouration of the NiO films between zero and fourteen cycles of deposition. Figure 25 shows the absorption spectrum of the Bi_2S_3 sample after 10 cycles. Samples reacted further than this point were unstable in that any minor abrasion of the film, or more than gentle washing steps, would remove the outer layers of reacted material, making them unsuitable to the application. It was also observed that the porous NiO acted as a 'seed' for accelerated growth of the Bi_2S_3 nanocrystals. When performing the same SILAR procedure on bare FTO, only a thin, reflective layer of Bi_2S_3 seemed to

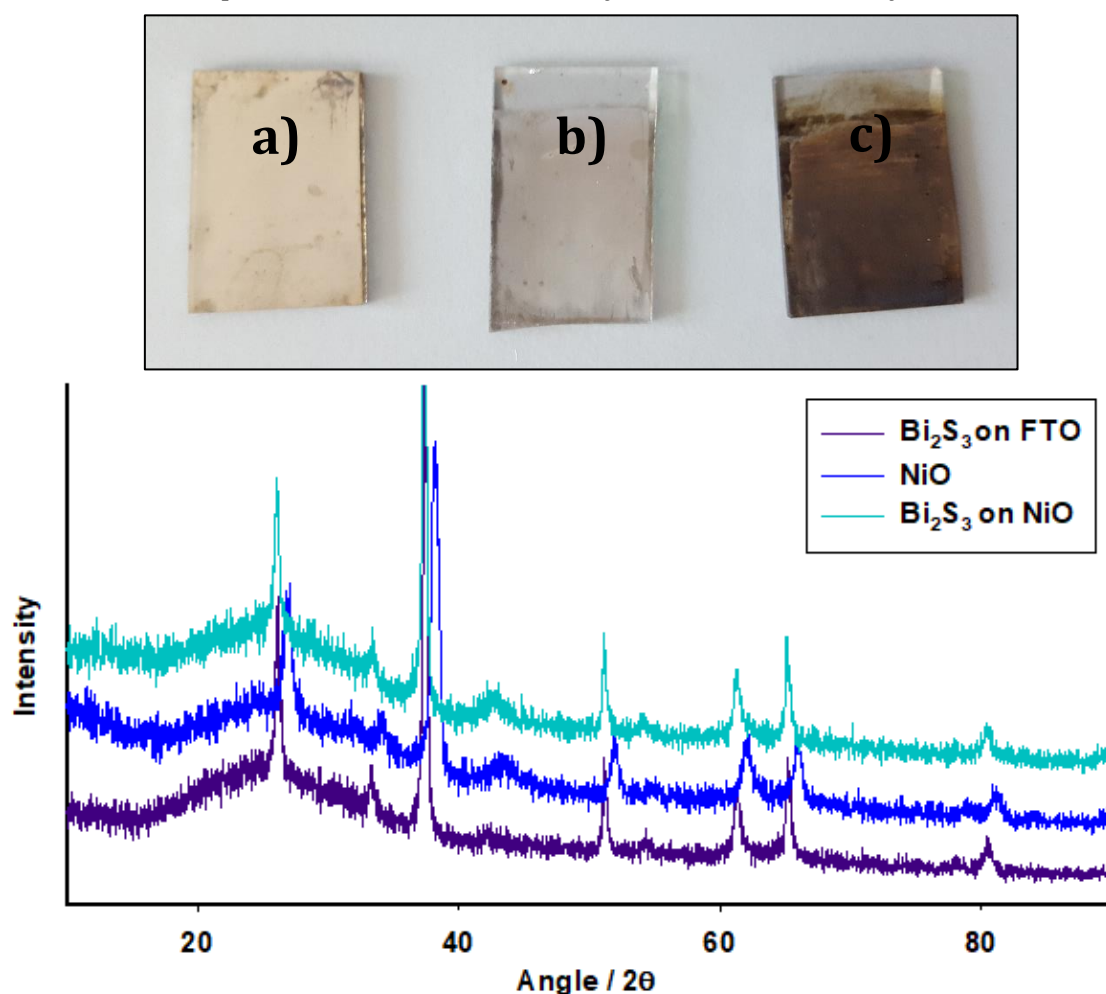


Figure 26: (top) images of films of a) Bi_2S_3 on FTO, b) NiO and c) 10 cycles of Bi_2S_3 deposition on NiO and (bottom) XRD patterns from the same samples.

grow. Figure 26 shows both photos and the XRD patterns of the Bi_2S_3 layers on both bare FTO and the NiO film. The diffraction patterns show no obvious change with the application of the layers of both NiO and Bi_2S_3 , showing only the pattern for the FTO substrate. Analysis of the Bi_2S_3 films with SEM (Figure 27) highlighted uniform deposition of the material with some localised clusters. Kelvin Probe Force microscopy (KPFM) was also used to discern particle size, with the average heights and diameter for the Bi_2S_3 nanocrystals reaching ~ 80 nm, as shown in Figure 28. This agrees with the observed particle sizes within the SEM images of clusters.

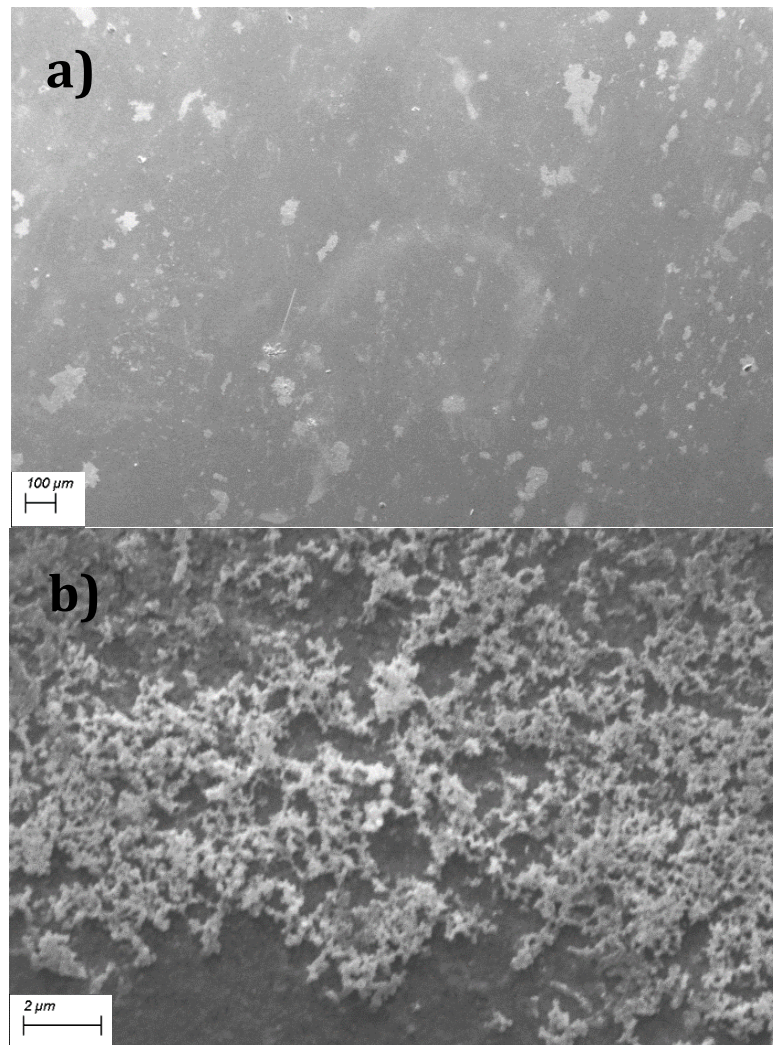


Figure 27: SEM Image of Bi_2S_3 films on FTO under 15 kV accelerating voltage and 7 mm working distance with **a)** a 120 x and **b)** a 15,530 x magnification.

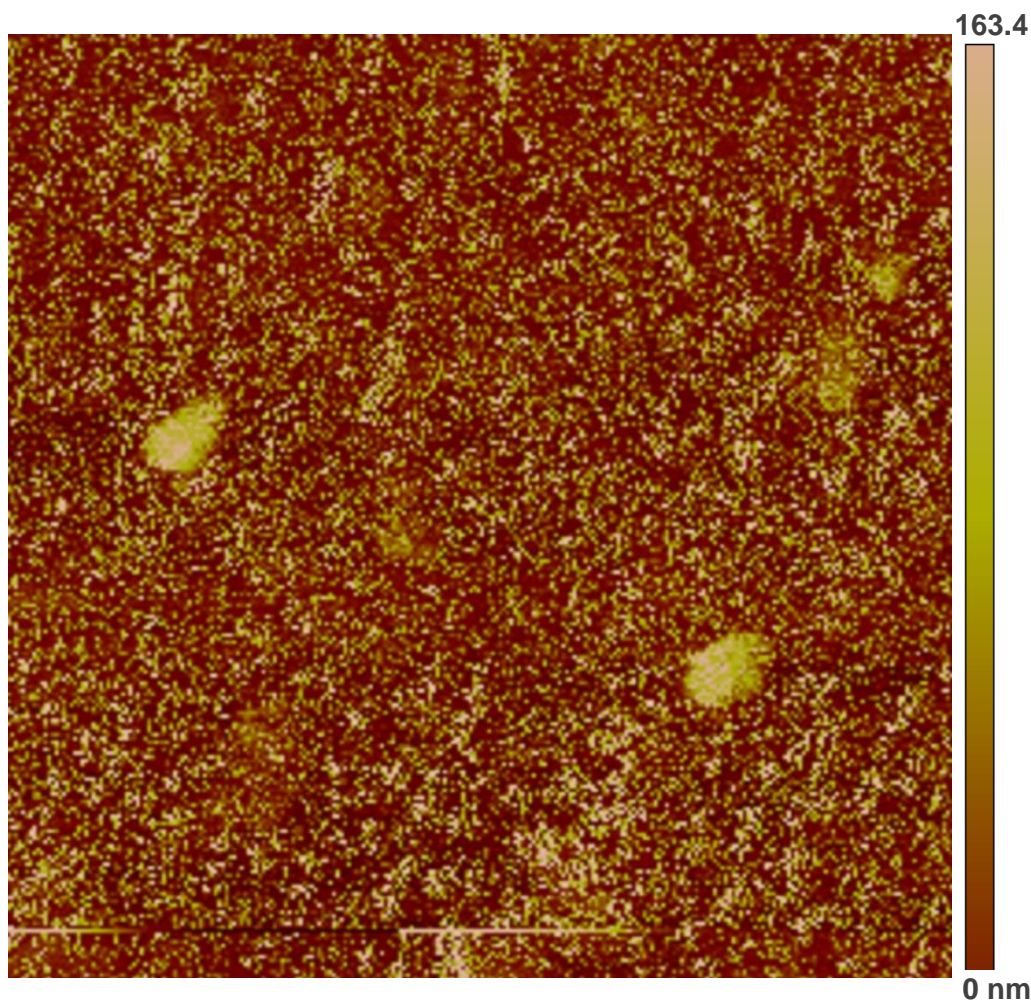


Figure 28: KPFM profile of Bi_2S_3 deposited material on FTO in a $10\ \mu\text{m}$ viewing window.

5.4.2 Single junction device and preliminary tandem device results

Devices were prepared using the as-synthesised Bi_2S_3 on screen-printed NiO films. Additionally, a corresponding CdS based device was used as a comparison. When applied to sandwich cells with polysulphide gel electrolyte and Ni foam CE, significant current was generated for the CdS based device. In the case of the Bi_2S_3 device, the dark current almost matches the generated current when the device is illuminated.

Material	$J_{sc} / \text{mA cm}^{-2}$	V_{oc} / V	FF	$\eta/\%$
FTO/NiO/ Bi_2S_3 – Ni-foam	2.13	-0.21	0.41	0.18
FTO/NiO/ CdS – Ni-foam	4.69	-0.63	0.35	1.05

Table 7: Solar cell parameters of QD-sensitised devices with a Ni-foam CE, using gel based aqueous 1 M Na_2S and 1 M Sulfur electrolyte under 1 sun illumination (100 mW cm^{-2} , AM 1.5G); exposed cell area: 0.15 cm^2

This, along with discoloration of the electrolyte upon application of the film in sandwich devices, could indicate the presence of current-generating side reactions independent of illumination. A critical work by Zeinert et al. investigated the deposition routine of Bi_2S_3 QDs suggested that the use of Na_2S resulted in side reactions forming NaBiS_2 nanocrystals

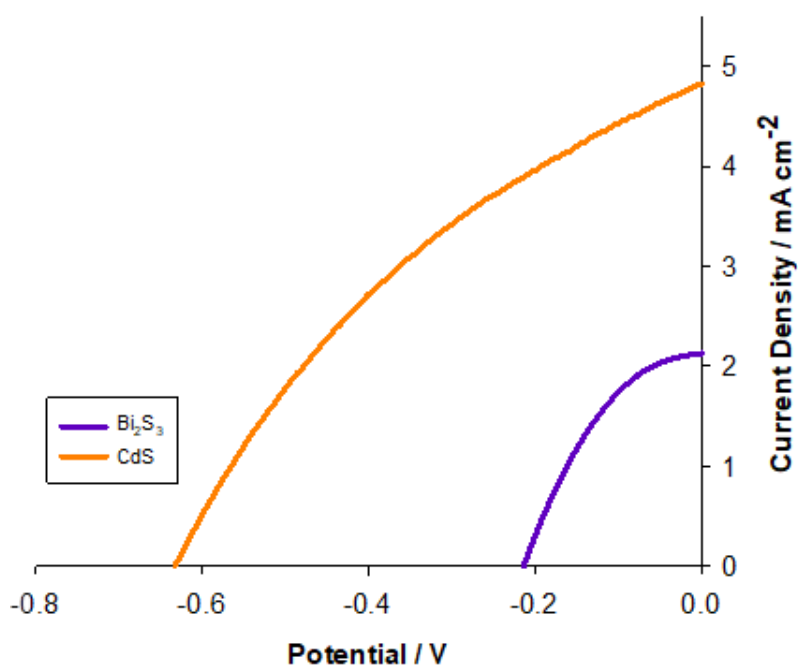


Figure 29: Plot of illuminated current density against voltage for FTO/NiO devices containing deposited CdS (16 cycles) and Bi_2S_3 (10 cycles) with Ni-foam CE. Electrolyte: gel based aqueous 1 M Na_2S and 1 M Sulfur.

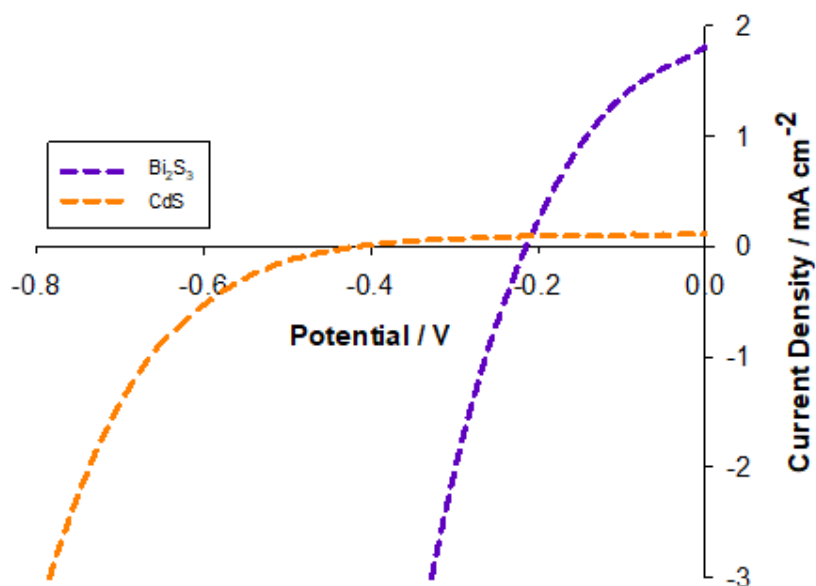


Figure 30: Plot of dark current density against voltage for FTO/NiO devices containing deposited CdS (16 cycles) and Bi₂S₃ (10 cycles) with Ni-foam CE. Electrolyte: gel based aqueous 1 M Na₂S and 1 M Sulfur.

that degrade quickly.⁵⁵ An investigation into the energetics of the devices was also performed. Correlating reported literature with the estimated particle size of the Bi₂S₃, the relative energy levels of the Bi₂S₃ thin film and the NiO VB were visualised. Figure 31 shows that the offset of the Bi₂S₃ VB edge is more negative than the NiO VB edge. This limits the transfer of holes to the NiO, affecting the population of charge in the Fermi level for the semiconductor. When applying bias to the device, the dark current could be the result of

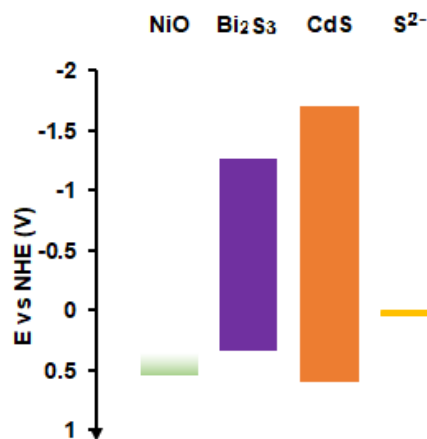


Figure 31: Relative energy levels of the Bi₂S₃ and CdS QDs discussed in this section relative to the VB energy of NiO and the redox potential of the polysulphide electrolyte.

Ohmic contact between the electrolyte and semiconductor. Characterisation of the electrochemical processes involved at this junction could help identify the problems at this interface, but the band alignment of the components makes the material unsuitable for integration into NiO- based p-QDSSC.

While the photovoltaic performance of the individual Bi₂S₃ devices was limited and the band alignment of the QD VB deemed unfavourable, for the sake of comparison to future materials, the performance of the material in proof-of-concept tandem devices was evaluated. Yet firstly, the performance of the photoanode was optimised. To a CdS-sensitised TiO₂ film on FTO, trigonal selenium sub-microtubes were added as co-sensitising charge carriers to facilitate effective hole transfer from the sensitiser to electrolyte. The change in device performance through the addition of the Se microtubes is shown in Table 8, while the current-voltage curves are shown in Figures 29 and 30. The co-sensitised photoanodes were taken on to combine with the Bi₂S₃ sensitized photocathode to create tandem devices.

Material	J _{sc} / mA cm ⁻²	V _{oc} / V	FF	η/%
TiO ₂ /CdS	12.64	0.61	0.28	2.16
TiO ₂ /CdS/Se	13.28	0.67	0.33	2.94

Table 8: Solar cell parameters of TiO₂ QD-sensitised devices with a Ni-foam CE, using gel based aqueous 1 M Na₂S and 1 M Sulfur electrolyte under 1 sun illumination (100 mW cm⁻², AM 1.5G); exposed cell area: 0.15 cm²

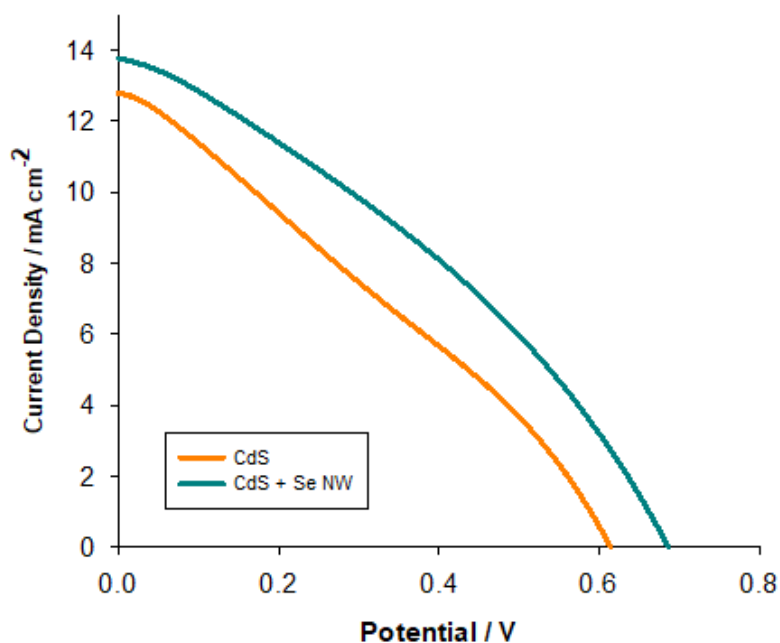


Figure 32: Plot of illuminated current density against voltage for FTO/TiO₂ devices containing deposited CdS (3 cycles) both with and without the addition of Se nanowires, using a Ni-foam CE. Electrolyte: gel based aqueous 1 M Na₂S and 1 M Sulfur.

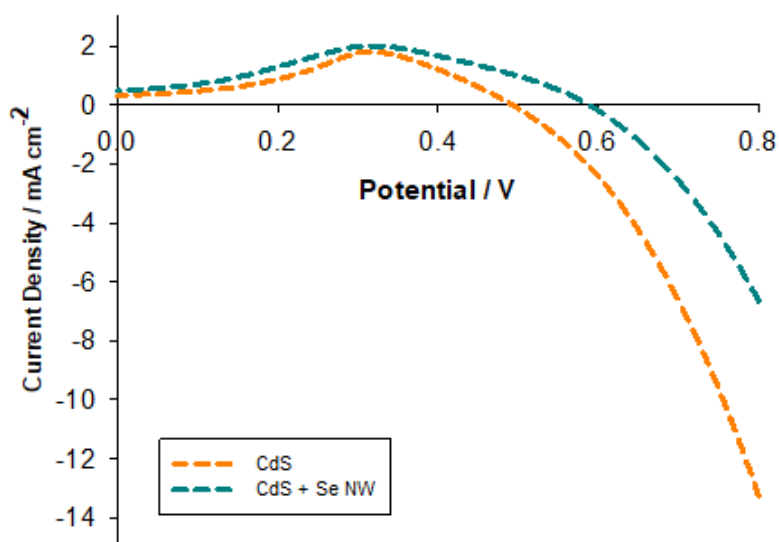


Figure 33: Plot of dark current density against voltage for FTO/TiO₂ devices containing deposited CdS (3 cycles) both with and without the addition of Se nanowires, using a Ni-foam CE. Electrolyte: gel based aqueous 1 M Na₂S and 1 M Sulfur.

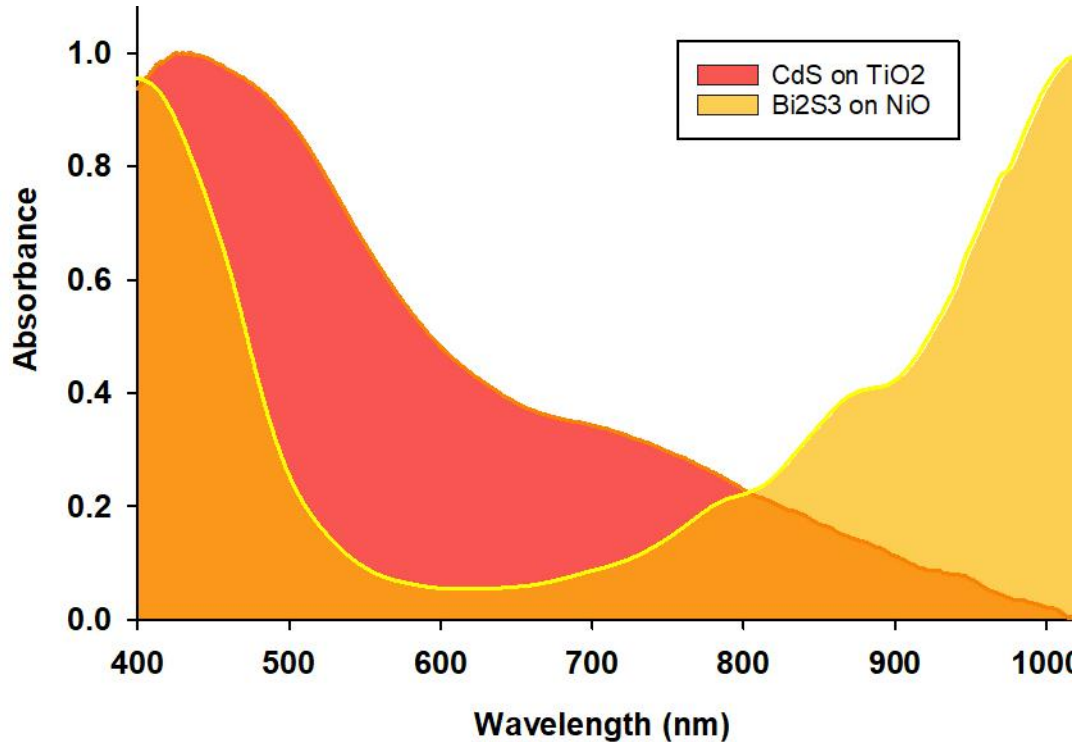


Figure 34: Overlay of absorbance spectra of both CdS sensitised TiO₂ and Bi₂S₃ sensitised NiO.

Figure 34 shows the absorbance spectra of the TiO₂/CdS/Se films overlaid with that of the Bi₂S₃/NiO/FTO films. The use of Bi₂S₃ as a near-IR absorber limits the spectral overlap between the photoanode and photocathode and highlighting its potential for use in tandem QDSSC. Preliminary sandwich devices with the construction TiO₂/CdS/Se - Bi₂S₃/NiO/FTO produced low efficiencies ~0.8 compared to the individual n-type component (~5 %). Poor fill factor was one contributing factor, as shown by the reflex curve in the current density vs voltage profile.

Material	J _{sc} / mA cm ⁻²	V _{oc} / V	FF	η/%
TiO ₂ /CdS/Se - Bi ₂ S ₃ /NiO/FTO	5.72	-0.51	0.27	0.79
TiO ₂ /CdS/Se - Bi ₂ S ₃ /NiO/Ni-Foam	12.73	-0.66	0.24	2.02

Table 9: Solar cell parameters of tandem QD-sensitised devices with TiO₂/CdS/Se NW photoanodes, and Bi₂S₃ -sensitized photocathodes with either FTO or Ni-foam based CE, using gel based aqueous 1 M Na₂S and 1 M Sulfur electrolyte under 1 sun illumination (100 mW cm⁻², AM 1.5G); exposed cell area: 0.15 cm²

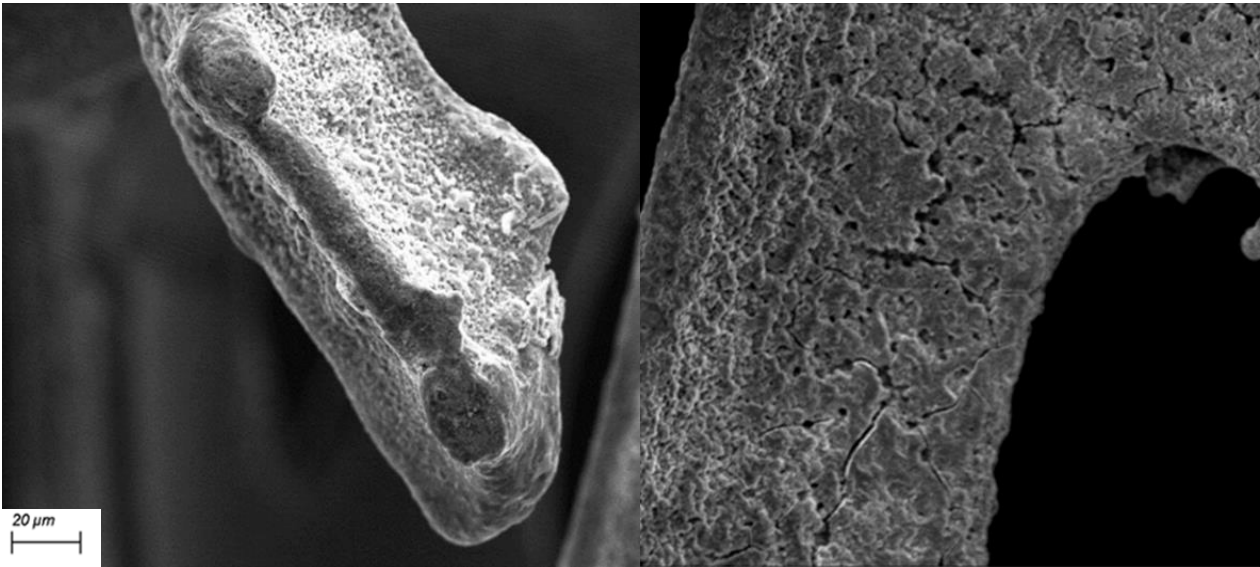


Figure 35: SEM Images of Bi_2S_3 -sensitized NiO on Nickel foam under a) 15 kV accelerating voltage and 7 mm working distance with a 1280 x magnification, b) 5 kV accelerating voltage and 11 mm working distance with a 2430 x magnification.

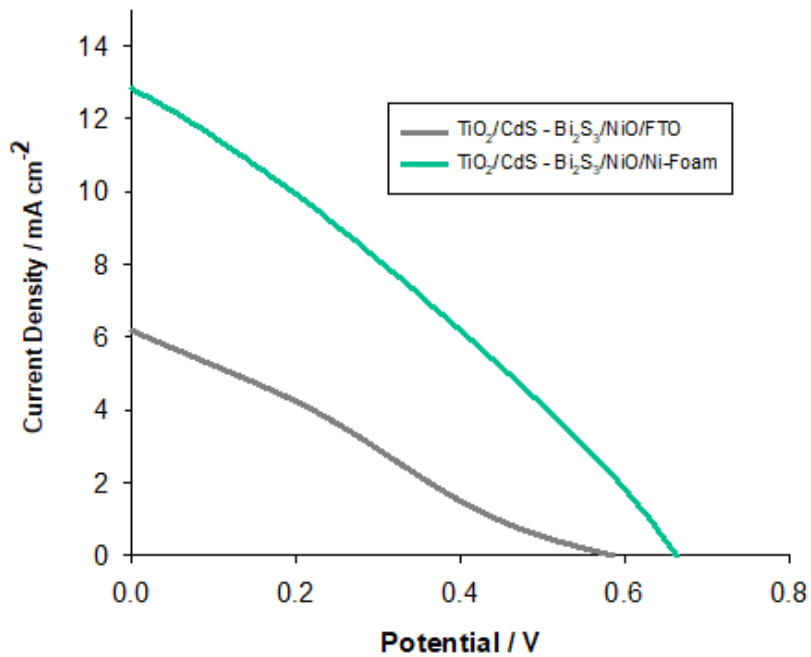


Figure 36: Plots of current density against voltage for tandem devices with $\text{TiO}_2/\text{CdS}/\text{Se}$ NW photoanodes, and Bi_2S_3 -sensitized photocathodes with either FTO or Ni-foam based CE. Electrolyte: gel based aqueous 1 M Na_2S and 1 M Sulfur.

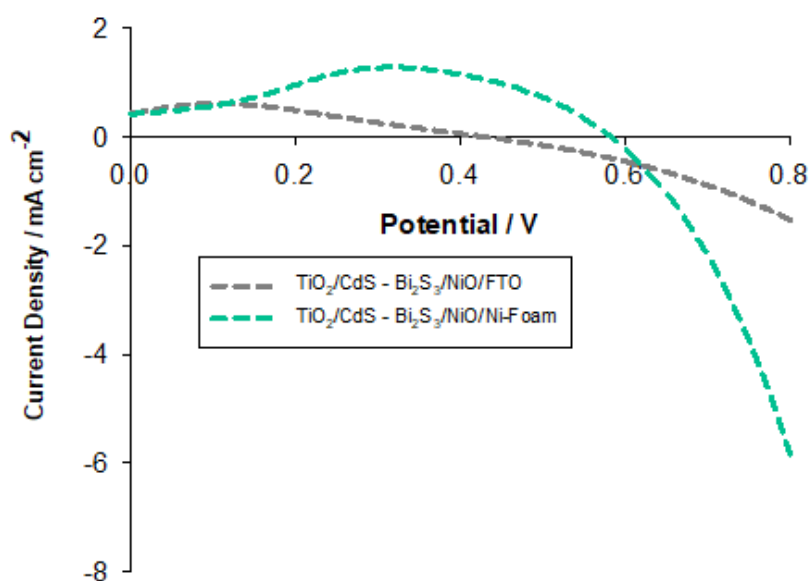


Figure 37: Plots of dark current density against voltage for tandem devices with $\text{TiO}_2/\text{CdS}/\text{Se}$ NW photoanodes, and Bi_2S_3 -sensitized photocathodes with either FTO or Ni-foam based CE. Electrolyte: gel based aqueous 1 M Na_2S and 1 M Sulfur.

The second approach to tandem devices, was to use the same material for the photocathode that was used as the CE in the single-junction devices. The NiO semiconductor was applied to the Ni foam substrate as a pre-synthesised paste via screen-printing. The films were then treated via SILAR to build up a layer of Bi_2S_3 . SEM images of the Ni foam after deposition of the NiO and QD layers shows entire coverage of the bare metal mesh, preventing interaction of the electrolyte with uncoated Ni metal. Devices constructed with these photocathodes produced greater current output and almost doubled overall efficiency. While promising results were obtained with these preliminary devices, the use of Bi_2S_3 within the photocathode structure is a limitation to device performance and longevity. The understanding and findings generated from the work in this section were used in the next part of the study, in which an alternative QD sensitizer, AgBiS_2 , was applied to tandem QDSSCs with an identical environment.

5.4.3 Integration of AgBiS₂ into Tandem Devices

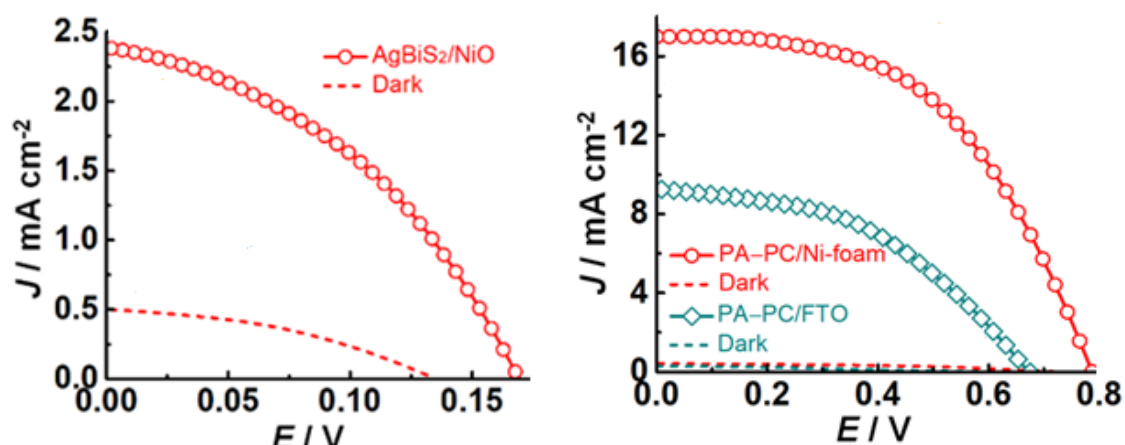


Figure 38: Plots of current density against voltage for **(left)** FTO/NiO devices containing AgBiS₂ with Ni-foam CE. **(right)** Tandem devices with TiO₂/CdS/Se NW photoanodes and Ni-foam based CE or AgBiS₂-sensitized photocathodes with FTO CE. Electrolyte: gel based aqueous 1 M Na₂S and 1 M Sulfur.

In collaboration with A. Kolay at IITH, another sensitising material was studied within this device architecture. The new material, AgBiS₂, has been used as a CE material for QDSSC and in other applications, but only recently as a sensitiser for photovoltaics.^{23,57,58} Its high absorption coefficient and narrow band gap made it a good candidate for study. Incorporation of AgBiS₂ into single junction p-QDSSC produced significantly more photogenerated current compared to Bi₂S₃ devices with the same architecture. The reduced efficiency reported is due to the lower V_{OC} of devices containing AgBiS₂, yet lower dark current indicates that the device is working as intended. Tandem devices were also constructed. Using the same architecture as described earlier, a Ni foam photocathode was prepared, with SEM images in Figure 39 showing complete coverage of the metal by the NiO and AgBiS₂. Investigation of these devices agreed with the results obtained with the Bi₂S₃ QDs. With the addition of Ni foam as a substrate for the photocathode,

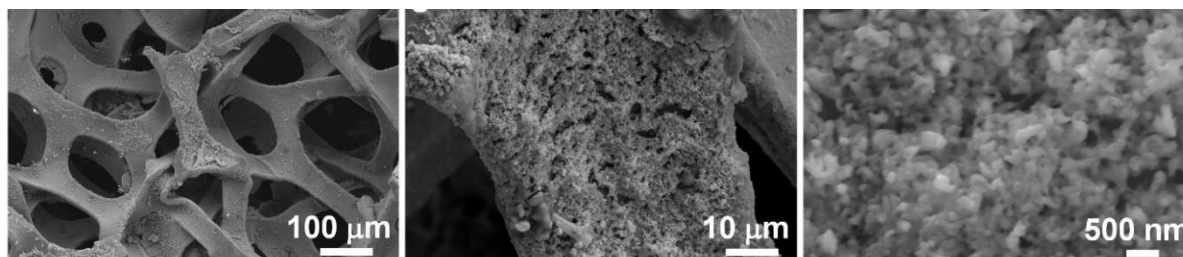


Figure 39: SEM Images of AgBiS₂ sensitized NiO on Nickel foam

Material	V_{oc} / mV	J_{sc} / mA cm ⁻²	FF	η /%
FTO/NiO/AgBiS ₂ -Ni-foam	168	2.39	40.6	0.16
TiO ₂ /CdS/Se-Ni-foam	730	14.18	47.4	4.91
TiO ₂ /CdS/Se-AgBiS ₂ /NiO/Ni-foam	787	16.99	51.5	6.88
TiO ₂ /CdS/Se- AgBiS ₂ /NiO/FTO	675	9.28	44.4	2.79

Table 10: Solar cell parameters of tandem QD-sensitised devices with TiO₂/CdS/Se NW photoanodes, and AgBiS₂-sensitized photocathodes with either FTO or Ni-foam based CE, using gel based aqueous 1 M Na₂S and 1 M Sulfur electrolyte under 1 sun illumination (100 mW cm⁻², AM 1.5G); exposed cell area: 0.15 cm²

performance of the tandem cell was improved. In this case, however, the performance of the AgBiS₂ photocathode may be beneficial rather than hindering, allowing the device performance to reach 6.88 % for the champion sample.

5.5 Conclusions and Future Outlook

Quantum dots are a versatile, unique class of materials that find uses ranging from the commercial sectors to the niche application. The field of study of these materials is vast, and in this work, yet another application for these materials has been established.

In Section 5.2, PbS nanocrystals were synthesised via a hot-injection process to generate monodisperse, near-IR absorbers for use as sensitisers for p-QDSSC. However, when integrating the QDs with the film, loading of the material onto NiO was poor, and devices generated small photocurrents and resulted in low efficiencies (<0.01 %). Even with pre-treatment of the NiO films with MPA, the results only increased marginally. While these QDs were not fit for their initially intended purpose, they found use as a co-sensitiser for photoelectrochromic devices, expanding the absorption properties of TiO₂-CdS photoanodes into the Near- IR region and improving device efficiencies from 3.7 to 5.2 %.

Section 5.3 focussed on an alternative deposition technique for material deposition that gave improved coverage of semiconductor films. SILAR was used to deposit CdS, and the user-intensive process was automated using robotics constructed with cheap, easy to build and program LEGO pieces. Comparison of the effect of deposition cycle numbers on the performance of NiO-CdS sandwich cells resulted in devices reaching just over 1.4 % efficiency. For QDSSCs containing polysulphide electrolytes, the commonly used platinised FTO CE is not viable due to degradation of the CE by the redox couple. As part of the study of the CdS photocathode, three alternative CE materials were also studied. Nickel foam, a flexible, highly conductive alternative, proved promising, and subsequent studies in this chapter used this material as a CE. The next aspect of this work investigated the **RJ3** dye presented in Chapter 4 as a co-sensitiser for the NiO-CdS-Ni foam device architecture. The addition of the near-IR absorber extended the spectral response of the photocathode, allowing for improved light harvesting by the device. The efficiency of co-sensitised devices tested in this section reached 1.05 %, a substantial, and potentially record result for a co-sensitised p-QDSSC.

With a device architecture established and an automated method established for the preparation of QD thin films on NiO, there arose the possibility for investigation of alternative materials. Section 5.4 described one such material, Bi₂S₃, which promised

near-IR absorption with heavy-metal free chemistry. However, the integrity of the thin films was poor, and competing reactions between the material and electrolyte caused devices to generate current in both the light and the dark. The lack of noticeable generated photocurrent limited the performance of tandem devices, but it was found that using Ni-foam as the photocathode substrate in the tandem device architecture improved performance drastically compared to using FTO. Tandem devices using Bi_2S_3 as the p-sensitiser produced up to 2.11 % efficiency, a reduction compared to the photoanodes' individual performance. In a continuation of the work a secondary material, AgBiS_2 , was prepared and analysed using the same device parameters. In this case, there was a reduction in dark vs photogenerated current for the single junction p-devices. When applied in tandem devices, the $\text{AgBiS}_2/\text{NiO}/\text{Ni-foam}$ electrode used in conjunction with an optimized $\text{TiO}_2/\text{CdS}/\text{Se}$ photoanode generated a photocurrent of 16.99 mA cm^{-2} , equating to a tandem device performance of 6.88 %.

The work in this chapter has established a methodology for the automated deposition of thin films synthesised via SILAR. This can be invaluable in screening of various QD materials as p-sensitisers for tandem QDSSC, or indeed as a way of rapidly investigating various substrates or semiconductors for p-type devices using QDs as a control sensitiser. Additionally, in collaboration with colleagues at IITH, a novel device architecture has been established based on a Ni-foam CE that highlights an opportunity to introduce flexibility as a property of QDSSC devices.

5.6 Experimental

A standard hot-injection approach was used to make colloidal QDs (**PbS-OA**). Typically, 0.210 mL bis(trimethylsilyl) sulphide was mixed with 10 mL of 1-octadecene and introduced in a Schlenk tube. The solution was degassed for 2 hours at room temperature using argon (Ar). In a second Schlenk tube, PbO (0.45 g) was suspended in 15 mL of 1-octadecene, and 1.5 mL of oleic acid was added. The mixture was degassed and heated at 95 °C under Ar. The solution became colourless after 1 hours (formation of lead oleate). Then, the temperature of solution was increased to 120 °C, and maintained at this temperature for 2 h under Ar flow. Finally, the Schlenk temperature was lowered to 110 °C and the TMS/octadecene mixture was injected quickly and after 2 minutes of reaction, the solution was cooled down to room temperature. PbS QDs were precipitated with 50 mL of acetone and centrifuged. The supernatant was removed and the QDs were dispersed in toluene. Then, the QDs were precipitated again in acetone (30 mL) and centrifuged. Finally, the PbS nanocrystals were dispersed in toluene (50 mg/mL).⁵⁹

MPA (mercaptopropionic acid) treatment of NiO films was achieved by immersion of the films in a 1 mmol MPA in IPA (isopropanol) solution for 2 hours.

Synthesis of [Co(dtb-bpy)₃(ClO₄)₂]- 0.422 g of 4,4' tertbutyl dipyriddy ligand and 0.121 g CoCl₂.6H₂O were dissolved in 20 ml methanol to produce a tawny brown solution. This was heated to 50°C with stirring for 30 minutes, causing a colour change to a light yellow, after which the reaction was cooled to RT. 0.542 g LiClO₄ in methanol was added dropwise and the reaction stirred for another 40 minutes. A fine yellow precipitate formed which was isolated with vacuum filtration and washed with methanol and diethyl ether.

Synthesis of [Co(dtb-bpy)₃(ClO₄)₃]- Two solutions; 0.253 g CoCl₂.6H₂O in water and 0.928 g 4,4' tertbutyl dipyriddy ligand in methanol were prepared separately and mixed together to form a dark brown solution. Another solution of 0.14 g bromine in methanol was added carefully, producing a large quantity of yellow precipitate. This was removed, and to resulting deep yellow solution an excess of LiClO₄ was added. Immediately, large amounts of fine, pale-yellow precipitate formed, which was filtered away and washed with water.

For **CdS SILAR**, the cadmium source solution was 5.9 g CdNO₃ in 250 ml water, and the sulphur source was 1.9 g Na₂S in 250 ml of a 1:1 mixture of H₂O and ethanol. Films were

deposited for 60 seconds into each bath and wash solution and allowed to dry after each washing.

Polysulphide electrolyte was prepared by vigorous mixing of 1 M Na₂S and 1 M elemental sulfur powder in 10 mL de-ionised water until a transparent dark-yellow solution was formed. 4 wt. % of fumed silica was dispersed by stirring to form a homogeneous polysulfide gel.

Sandwich Cells were constructed by taking the as-prepared electrodes and assembling with active sides facing each other. A 1 mm thick parafilm spacer with a hole cut to the dimensions of the film was inserted between the two and the electrolyte applied into the space. The device was clipped together with binding clips and a mask cut to the same working area was applied.

CuS CE preparation followed the procedure by Chaki et al.⁶⁰ Briefly, a chemical bath deposition technique was used to prepare the counter electrodes. The bath contained 5 ml of 1 M copper (II) chloride solution, which was mixed with 4 ml of triethanolamine. Then, 10 ml of 25 % aqueous ammonia solution was added with continuous stirring for 10 minutes. Next, 10 ml of 1 M NaOH was added with additional stirring for another 5 minutes, before 6 ml of 1 M thiourea solution was added. After another 5 minutes of stirring, the solution was diluted to 100 ml with DI H₂O. Thanks go to AK for pre-preparing the solution. To prepare the electrodes, FTO (TEC 8) glass slides were immersed vertically in the solution for 4 hours at room temperature, before removal and washing with DI water.

Nickel foam was prepared by cleaning before sensitisation by sonication in acetone for 20 minutes.

For co-sensitisation of films with **RJ3**, preprepared CdS films were submerged in dyebaths of **RJ3** for 24 hours before removal and washing.

SILAR of **Bi₂S₃** used two bath solutions; solution 1 contained 0.1M Bi(NO₃) in acetone, while solution 2 contained 0.1M Na₂S in methanol. The wash baths were acetone and methanol for each solution respectively. Dipping times were 10 seconds for the chemical baths, and 1 minute for each wash step, with time allowed to dry after each washing step.

SILAR of **AgBiS₂** was achieved via a two phase method described by Huang et al.⁵⁸ Thanks go to AK for preparing and testing these films. The first phase involved the growth of Ag₂S QDs on the NiO electrode (via SILAR dipping in baths of 0.1 M AgNO₃ in ethanol for 20 seconds, washing, and dipping into 0.1 M Na₂S in methanol for 40 seconds, before washing again), while the second phase involved the deposition of Bi₂S₃ QDs using the method described earlier. The number of cycles of SILAR for both phases was identical, and the film was subsequently annealed (250 °C in Ar for 1 hour) to transform the double layered structure into the AgBiS₂ phase.

5.7 References

- 1 F. Van Riggelen, N. W. Hendrickx, W. I. L. Lawrie, M. Russ, A. Sammak, G. Scappucci and M. Veldhorst, *Appl. Phys. Lett.*, 2021, **118**, 044002.
- 2 W. Liu, S. C. Hak, J. P. Zimmer, E. Tanaka, J. V. Frangioni and M. Bawendi, *J. Am. Chem. Soc.*, 2007, **129**, 14530–14531.
- 3 X. Qu, P. J. J. Alvarez and Q. Li, *Water Res.*, 2013, **47**, 3931–3946.
- 4 M. Kouhnavard, S. Ikeda, N. A. Ludin, N. B. Ahmad Khairudin, B. V. Ghaffari, M. A. Mat-Teridi, M. A. Ibrahim, S. Sepeai and K. Sopian, *Renew. Sustain. Energy Rev.*, 2014, **37**, 397–407.
- 5 S. Schmitt-Rink, D. A. B. Miller and D. S. Chemla, *Phys. Rev. B*, 1987, **35**, 8113–8125.
- 6 P. R. Brown, D. Kim, R. R. Lunt, N. Zhao, M. G. Bawendi, J. C. Grossman and V. Bulović, *ACS Nano*, 2014, **8**, 5863–5872.
- 7 M. M. Tavakoli, *Procedia Eng.*, 2016, **139**, 117–122.
- 8 D. Sharma, R. Jha and S. Kumar, *Sol. Energy Mater. Sol. Cells*, 2016, **155**, 294–322.
- 9 P.-N. Li, A. V Ghule and J.-Y. Chang, *J. Power Sources*, 2017, **354**, 100–107.
- 10 P. Subramanyam, P. Naresh Kumar, M. Deepa, C. Subrahmanyam and P. Ghosal, *Sol. Energy Mater. Sol. Cells*, 2017, **159**, 296–306.
- 11 P. V Kamat, *Acc. Chem. Res.*, 2011, **45**, 1906–1915.
- 12 O. E. Semonin, A. J. Nozik and M. C. Beard, *Science (80-.)*, 2013, **1530**, 1530–1534.
- 13 M. A. Halim, *Nanomaterials*, 2013, **3**, 22–47.
- 14 O. E. Semonin, O. E. Semonin, J. M. Luther, S. Choi, H. Chen, J. Gao, A. J. Nozik and M. C. Beard, 2011, **1530**, 1530–1534.
- 15 S. Jiao, Q. Shen, I. Mora-Seró, J. Wang, Z. Pan, K. Zhao, Y. Kuga, X. Zhong and J. Bisquert, *ACS Nano*, 2015, **9**, 908–915.
- 16 P. Yu, K. Zhu, A. G. Norman, S. Ferrere, A. J. Frank and A. J. Nozik, *J. Phys. Chem. B*, 2006, **110**, 25451–25454.
- 17 S. Sapra, A. L. Rogach and J. Feldmann, *J. Mater. Chem.*, 2006, **16**, 3391.
- 18 X. Zhang, G. E. Eperon, J. Liu and E. M. J. Johansson, *Nano Energy*, 2016, **22**, 70–78.
- 19 S. V. Kershaw, A. S. Sussha and A. L. Rogach, *Chem. Soc. Rev.*, 2013, **42**, 3033.
- 20 W. X. Dai, L. Zhang, W. W. Zhao, X. D. Yu, J. J. Xu and H. Y. Chen, *Anal. Chem.*, 2017, **89**, 8070–8078.
- 21 B. Sun, A. Johnston, C. Xu, M. Wei, Z. Huang, Z. Jiang, H. Zhou, Y. Gao, Y. Dong, O. Ouellette, X. Zheng,

- J. Liu, M. J. Choi, Y. Gao, S. W. Baek, F. Laquai, O. M. Bakr, D. Ban, O. Voznyy, F. P. García de Arquer and E. H. Sargent, *Joule*, 2020, **4**, 1542–1556.
- 22 S. Chen, Y. jie Wang, Q. Liu, G. Shi, Z. Liu, K. Lu, L. Han, X. Ling, H. Zhang, S. Cheng and W. Ma, *Adv. Energy Mater.*, 2018, **8**, 1–9.
- 23 D. Becker-Koch, M. Albaladejo-Siguan, Y. J. Hofstetter, O. Solomeshch, D. Pohl, B. Rellinghaus, N. Tessler and Y. Vaynzof, *ACS Appl. Mater. Interfaces*, 2021, **13**, 18750–18757.
- 24 M. Hao, Y. Bai, S. Zeiske, L. Ren, J. Liu, Y. Yuan, N. Zarrabi, N. Cheng, M. Ghasemi, P. Chen, M. Lyu, D. He, J. H. Yun, Y. Du, Y. Wang, S. Ding, A. Armin, P. Meredith, G. Liu, H. M. Cheng and L. Wang, *Nat. Energy*, 2020, **5**, 79–88.
- 25 M. J. Choi, S. W. Baek, S. Lee, M. Biondi, C. Zheng, P. Todorovic, P. Li, S. Hoogland, Z. H. Lu, F. P. G. de Arquer and E. H. Sargent, *Adv. Sci.*, 2020, **7**, 1–7.
- 26 D. A. Hines and P. V. Kamat, *ACS Appl. Mater. Interfaces*, 2014, **6**, 3041–3057.
- 27 L. Duan, L. Hu, X. Guan, C. H. Lin, D. Chu, S. Huang, X. Liu, J. Yuan and T. Wu, *Adv. Energy Mater.*, 2021, 11.
- 28 F. Safari-Alamuti, J. R. Jennings, M. A. Hossain, L. Yue, L. Yung and Q. Wang, *Phys. Chem. Chem. Phys.*, 2013, **15**, 4767–4774.
- 29 C. D. Sunesh, C. V. V. M. Gopi, M. P. A. Muthalif, H. J. Kim and Y. Choe, *Appl. Surf. Sci.*, 2017, **416**, 446–453.
- 30 H. Zhang, K. Cheng, Y. M. Hou, Z. Fang, Z. X. Pan, W. J. Wu, J. L. Hua and X. H. Zhong, *Chem. Commun.*, 2012, **48**, 11235.
- 31 Y. L. Lee, B. M. Huang and H. T. Chien, *Chem. Mater.*, 2008, **20**, 6903–6905.
- 32 M. Raissi, Y. Pellegrin, S. Jobic, M. Boujtita and F. Odobel, *Sci. Rep.*, 2016, **24908**, 1–7.
- 33 S. Itzhakov, H. Shen, S. Buhbut, H. Lin and D. Oron, *J. Phys. Chem. C*, 2013, **117**, 22203–22210.
- 34 V. Chakrapani, D. Baker and P. V Kamat, *J. Am. Chem. Soc.*, 2011, **133**, 9607–9615.
- 35 P. K. Santra and P. V. Kamat, *J. Am. Chem. Soc.*, 2013, **135**, 877–885.
- 36 I. Barceló, E. Guillén, T. Lana-Villarreal and R. Gómez, *J. Phys. Chem. C*, 2013, **117**, 22509–22517.
- 37 Z. Pan, H. Zhang, K. Cheng, Y. Hou, J. Hua and X. Zhong, *ACS Nano*, 2012, **6**, 3982–3991.
- 38 F. Odobel and Y. Pellegrin, *J. Phys. Chem. Lett.*, 2013, **4**, 2551–2564.
- 39 A. Cheruvathoor Poullose, S. Veeranarayanan, S. Hanna Varghese, Y. Yoshida, T. Maekawa and D. Sakthi Kumar, *Chem. Phys. Lett.*, 2012, **539–540**, 197–203.
- 40 N. Parsi Benekohal, V. González-Pedro, P. P. Boix, S. Chavhan, R. Tena-Zaera, G. P. Demopoulos and

- I. Mora-Seró, *J. Phys. Chem. C*, 2012, **116**, 16391–16397.
- 41 R. Calzada, C. M. Thompson, D. E. Westmoreland, K. Edme and E. A. Weiss, *Chem. Mater.*, 2016, **28**, 6716–6723.
- 42 E. A. Gibson, A. L. Smeigh, L. Le Pleux, L. Hammarström, F. Odobel, G. Boschloo and A. Hagfeldt, *J. Phys. Chem. C*, 2011, **115**, 9772–9779.
- 43 P. Salvatori, G. Marotta, A. Cinti, E. Mosconi, M. Panigrahi, L. Giribabu, M. K. Nazeeruddin and F. De Angelis, *Inorganica Chim. Acta*, 2013, **406**, 106–112.
- 44 E. A. Gibson, A. L. Smeigh, L. Le Pieux, J. Fortage, G. Boschloo, E. Blart, Y. Pellegrin, F. Odobel, A. Hagfeldt and L. Hammarström, *Angew. Chemie - Int. Ed.*, 2009, **48**, 4402–4405.
- 45 H. Kiat Jun, M. Abdul Careem and A. Kariem Arof, *Nanoscale Res. Lett.*, 2014, **9**, 7.
- 46 M. Abdellah, F. Poulsen, Q. Zhu, N. Zhu, K. Zidek, P. Chabera, A. Corti, T. Hansen, Q. Chi, S. E. Canton, K. Zheng and T. Pullerits, *Nanoscale*, 2017, 12503–12508.
- 47 W. Ma, J. M. Luther, H. Zheng, Y. Wu and A. P. Alivisatos, *Nano Lett.*, 2009, **9**, 1699–1703.
- 48 S. Wang, T. Shen, H. Bai, B. Li and J. Tian, *J. Mater. Chem. C*, 2016, **4**, 8020–8026.
- 49 Holmarc Opto-Mechatronics, 2019.
- 50 I. O. Oladeji, L. Chow, J. R. Liu, W. K. Chu, A. N. P. Bustamante, C. Fredricksen and A. F. Schulte, *Thin Solid Films*, 2000, **359**, 154–159.
- 51 H. Choi, R. Nicolaescu, S. Paek, J. Ko and P. V. Kamat, *ACS Nano*, 2011, **5**, 9238–9245.
- 52 L. Lu, D. Yang, W. Liu and Z. Jin, *Mater. Technol.*, 2016, **31**, 160–165.
- 53 Z. H. Ge, P. Qin, D. He, X. Chong, D. Feng, Y. H. Ji, J. Feng and J. He, *ACS Appl. Mater. Interfaces*, 2017, **9**, 4828–4834.
- 54 D. Esparza, I. Zarazúa, T. López-Luke, R. Carriles, A. Torres-Castro and E. D. La Rosa, *Electrochim. Acta*, 2015, **180**, 486–492.
- 55 I. Zumeta-Dubé, V. F. Ruiz-Ruiz, D. Díaz, S. Rodil-Posadas and A. Zeinert, *J. Phys. Chem. C*, 2014, **118**, 11495–11504.
- 56 A. J. Maclachlan, F. T. F. O'Mahony, A. L. Sudlow, M. S. Hill, K. C. Molloy, J. Nelson and S. A. Haque, *ChemPhysChem*, 2014, **15**, 1019–1023.
- 57 N. Liang, W. Chen, F. Dai, X. Wu, W. Zhang, Z. Li, J. Shen, S. Huang, Q. He, J. Zai, N. Fang and X. Qian, *CrystEngComm*, 2015, **17**, 1902–1905.
- 58 P. Huang, W. Yang and M. Lee, *J. Phys. Chem. C*, 2013, **117**, 18308–18314.
- 59 M. Raissi, Y. Pellegrin, S. Jobic, M. Boujtita and F. Odobel, *Sci. Rep.*, 2016, **6**, 1–7.

60 S. H. Chaki, M. P. Deshpande and J. P. Taylor, *Thin Solid Films*, 2014, **550**, 291–297.

Chapter 6 Conclusions and Future Outlook

The work in this thesis has focussed on the development of sensitisers for DSSC and QDSSC, to facilitate screening of p-type semiconductors for tandem solar cells. In order to achieve this, a multi-faceted approach was undertaken. In the first two results chapters, dye sensitisation was studied in the context of both p- and n- type devices.

Chapter 3 encompasses the implementation of several different dye structures into n-DSSC. Since n-DSSC have been extensively studied and optimised in other work, focus was on sustainability. By reducing reliance on rare-earth metals or improving the accessibility of the technology, the applications of DSSCs can be expanded. Firstly in this chapter, an iridium complex containing a diethyl [2,2'-bipyridine]-4,4'-dicarboxylate (deeb) ligand, Complex **1**, was developed by collaborators at the University of St. Andrews, and presented an extended, panchromatic absorption response and red shifted emission. Complex **1** was characterised and the deeb ligand was found to facilitate LLCT processes. Complex **1** was applied into TiO₂ DSSC to assess its capability as a sensitiser. Devices optimised with both blocking and scattering layer treatments on the TiO₂ semiconductor reached efficiencies of ~ 0.5 %, which, while low in comparison to the devices containing the ruthenium sensitiser N719, is a competitive result for an iridium-based sensitiser.^{1,2} The second part of the chapter focusses on the extraction of dye from a natural source.

Seeds from a native Peruvian prickly pear were harvested and the dye extracted. Previous study of similar species indicated that the natural dye components within the seeds were based on betalains. Using 'green' solvents and gentle extraction processes, highly pigmented solutions from the fruit were obtained. Detailed characterisation of these solutions was minimal, but the extracts were integrated into TiO₂ DSSC architectures that had been optimised previously in the chapter to produce preliminary devices with ~0.5 % efficiency. Efficiency was then improved through the use of an acid stabilising group. In this case, citric acid was added to increase the pigments' resistance to photodegradation. Devices constructed with the stabilised dye produced improved efficiencies of up to 1.4 %, comparable with other published devices based on betalain dyes.^{3,4} The development of 'green' sensitiser from sustainable sources is key to the future lifetime of the technologies in development today,⁵ and it is important that the environmental impacts of research are considered as it is undertaken.

The work in Chapter 4 turns attention to sensitiser for p-DSSCs. Key requirements for these dyes include enhanced absorption in the near infra-red region, an extended charge separated state, and appropriate band alignment of the HOMO (by a minimum of 0.8 eV to the Fermi level of the NiO). The first half of Chapter 4 describes a series of dyes prepared by collaborators at the University of East Anglia, composed of triarylamine cores, indolium acceptors and pyridine anchors. The dyes, **JF1**, **JF2** and **JF3** were designed with a 'push-pull' structure in mind, with the indolium acceptor theoretically withdrawing charge and extending the lifetime of the charge separated state of the dye. The dyes also showed intense absorption at 500 – 600 nm, due to the electron withdrawing effect of the indolium, and the electrochemical characterisation of the dyes placed the HOMO of each in sufficient range for favourable hole transfer to the NiO VB. However, low molar extinction coefficients and poor dye loading by the series onto NiO, possibly due to the use of the pyridine anchoring group, limited overall device performance. However, compared to studies undertaken with similar dye structures, the efficiency of p-DSSCs containing dyes **JF2** and **JF3** surpassed those reported, with the former reaching efficiencies of 0.097 %.⁶ The second part of Chapter 4 focusses on a 4,4-difluoro-4-bora-3a,4a-diaza-s-indacene (BODIPY) core structure for dyes in p-DSSCs. The red shifted chromophore **RJ3** was synthesised by R. James, which contained an electron withdrawing SF₅ moiety, a BODIPY core, and an extended styryl group to red shift the

absorption, which was seen to extend to a peak at 642 nm. The dye contained two carboxylic anchoring groups, and was highly emissive, retaining its fluorescence in the solid state. In order to evaluate its performance in p-DSSCs, the dye was applied to 3 layer NiO devices, which gave efficiencies of up to 0.104 %. While this value was lower than that from the devices containing **P1** used as a benchmark, the red-shifted absorption of **RJ3** proved it a promising dye for its application. It was therefore integrated into preliminary tandem devices with **D35**-sensitised TiO₂. However, poor current matching between the electrodes reduced fill factors, limiting the overall output of the tandem device. Optimisations of these devices can be done to improve current matching and produce tandem DSSCs with increased efficiency. Further work is required to optimise the **RJ3**-sensitised NiO in tandem DSSCs. By matching the current of the n-photoanode to the output of the p-photocathode, improved fill factor can be obtained, and the performance of the dye can be appropriately assessed in a tandem configuration.⁷ Additionally, the dye would be an excellent candidate for screening alternative materials for p-DSSC due to its excellent absorption properties and complementary spectral response.

Chapter 5 covers the use of quantum dot and nanocrystalline materials as absorbers for p-QDSC. Quantum dots make excellent candidates as light harvesters due to their size-dependant band gaps and versatile loading methods. Initially, lead sulphide (PbS) quantum dots with a near infra-red photoresponse and synthesised in an ex-situ process were incorporated onto NiO photocathodes via ligand exchange. However, loading of the QDs was very low, resulting in low device efficiencies. A secondary approach was taken, relying on the well documented successive ionic-layer adsorption and reaction (SILAR) process. To speed up the process and allow for upscale within the laboratory, automation was introduced, using relatively cheap and widely available LEGO pieces. A robot arm was constructed and programmed to perform the reaction, including the washing and drying steps needed. Using the automated procedure, CdS nanocrystals were grown on the NiO films, resulting in thick layers of deposited material. The films were incorporated into sandwich p-QDSC with Ni foam, a novel counter electrode material, to produce efficiencies of up to 1.4 % for a NiO-CdS device made with 24 cycles of SILAR, an improvement over literature values for other p-QDSC.^{8,9} To further boost the photoresponse of the devices, the dye **RJ3** studied in Chapter 4 was used to co-sensitise

the NiO-CdS film. Device efficiencies for films reacted with 16 cycles of SILAR were improved from 0.8 % to 1.1 %, through a reduction in recombination and expansion of spectral response. The automation process also opened up opportunities to trial other QD materials. Further work could include the assembly of a library of alternative materials, including lead and cadmium free alternatives that can be synthesised via the automated SILAR procedure.^{10,11} One of the materials tested, Bi₂S₃, was chosen due to its red-shifted photoresponse and heavy-metal free chemistry. This collaboration with colleagues from IITH yielded poor results as the deposited Bi₂S₃ was found to react with the polysulphide electrolyte used within the devices. High dark currents meant that the response of the device to light was negligible and preliminary tandem devices constructed with CdS/TiO₂ photoanodes and Bi₂S₃ photocathodes were limited by the performance of the p-type electrode. Replacement of the Bi₂S₃ with AgBiS₂ improved the photocurrent, and, with the replacement of the photocathode FTO substrate with Ni foam, the performance of the tandem QDSSC was boosted to almost 6.9 %. Use of this alternative, highly conductive material could be key to the development of alternative, flexible photovoltaics,¹² which again opens up a plethora of applications.

While there have been some developments in the field of tandem DSSC in the course of this work, they have been limited to small modifications to the NiO morphology and mixture, or alternative dye systems.¹³⁻¹⁵ The only way to achieve the required step change in efficiency for these devices is to modify the p-semiconductor.¹⁶ The work in this thesis has produced a set of candidates for sensitisers, enabling the screening of p-type semiconductors for tandem DSSCs. It has also established novel architectures for the design of these devices and has opened avenues for further exploration of quantum dots as sensitisers in p-DSCs.

References

- 1 A. Sinopoli, C. J. Wood, E. A. Gibson and P. I. P. Elliott, *Dye. Pigment.*, 2017, **140**, 269–277.
- 2 C. Dragonetti, A. Valore, A. Colombo, S. Righetto and V. Trifiletti, *Inorganica Chim. Acta*, 2012, **388**, 163–167.
- 3 G. Calogero, G. Di Marco, S. Cazzanti, S. Caramori, R. Argazzi, A. Di Carlo and C. A. Bignozzi, *Int. J. Mol. Sci.*, 2010, **11**, 254–267.
- 4 C. Sandquist and J. L. McHale, *J. Photochem. Photobiol. A Chem.*, 2011, **221**, 90–97.
- 5 G. P. Smestad and M. Grätzel, *J. Chem. Educ.*, 1998, **75**, 752–756.
- 6 A. R. Marri, F. A. Black, J. Mallows, E. A. Gibson and J. Fielden, *Dye. Pigment.*, 2019, **165**, 508–517.
- 7 C. J. Wood, M. Cheng, C. A. Clark, R. Horvath, I. P. Clark, M. L. Hamilton, M. Towrie, M. W. George, L. Sun, X. Yang and E. A. Gibson, *J. Phys. Chem. C*, 2014, **118**, 16536–16546.
- 8 F. Safari-Alamuti, J. R. Jennings, M. A. Hossain, L. Yue, L. Yung and Q. Wang, *Phys. Chem. Chem. Phys.*, 2013, **15**, 4767–4774.
- 9 M. Raissi, Y. Pellegrin, S. Jobic, M. Boujtita and F. Odobel, *Sci. Rep.*, 2016, **24908**, 1–7.
- 10 H. Song, Y. Lin, M. Zhou, H. Rao, Z. Pan and X. Zhong, 2021, 6137–6144.
- 11 L. Duan, L. Hu, X. Guan, C. Lin, D. Chu, S. Huang, X. Liu, J. Yuan and T. Wu, 2021, **2100354**, 1–23.
- 12 L. Fagiolari, E. Varaia, N. Mariotti, M. Bonomo, C. Barolo and F. Bella, *Adv. Sustain. Syst.*, 2021, 5, 32.
- 13 T. B. K, D. N. Joshi and V. Dutta, *Sol. Energy*, 2021, **223**, 318–325.
- 14 M. Bonomo, E. J. Ekoi, A. G. Marrani, D. P. Dowling, D. Dini and A. Y. Segura, 2021, 4736–4748.
- 15 S. Zhang, H. Ye, H. Ding, F. Yu and J. Hua, *Sci. China Chem.*, 2019, **62**, 14.
- 16 O. Langmar, E. Fazio, P. Schol, G. De Torre, R. Ø. D. Costa and D. M. Guldi, 2019, 4056–4060.